2013

BINDING ENERGIES AND SOLVATION OF ORGANIC MOLECULAR IONS, REACTIONS OF TRANSITION METAL IONS WITH, AND PLASMA DISCHARGE IONIZATION OF MOLECULAR CLUSTERS

Isaac Kwame Attah
Virginia Commonwealth University

BINDING ENERGIES AND SOLVATION OF ORGANIC MOLECULAR IONS, REACTIONS OF TRANSITION METAL IONS WITH, AND PLASMA DISCHARGE IONIZATION OF MOLECULAR CLUSTERS

A dissertation submitted in partial fulfillment of the requirements for the degree of doctor of philosophy at Virginia Commonwealth University

by

Isaac Kwame Attah
B.Sc., Kwame Nkrumah University of Science and Technology, Ghana, 2006

Director: M. SAMY EL-SHALL
Professor, Department of Chemistry

Virginia Commonwealth University
Richmond, Virginia
May, 2013

Acknowledgement

I will like to thank the Almighty God for His protection and sustenance throughout this period of my life. I have been blessed by Him, and His handiworks are evident in my life.

I will also like to thank my family, my beautiful wife Dorcas Attah, for her support, encouragement, and care. You were my inspiration, and forever will be. FOREVER. I also acknowledge my two “heart beats” Caleb and Faith for their love. Thanks to my parents Isaac Kwasi Attah, and Rebecca Ayitso Pappoe. They encouraged me to always reach to the heights, and never give up. I also acknowledge my brother and sisters for their support and also encouraging me to do my best in every endeavor.

I want to express my truly sincere gratitude to Professor M. Samy El-Shall for the time and patience he gave me. I am a much better individual than I was five years ago, and I credit you for this. Your training has given me the discipline I will need to succeed in life.

Thanks to Dr. Pramod Sharma for his time in training me with such a high standard in scientific inquiry, and teaching me how to persevere till the I get the right results. I am forever grateful. I also show appreciation to Dr. Michael Meot-Ner and for his discussion and help in the final stretch of my PhD journey. Finally, thanks to Drs. Abdel Soliman and Ahmed Hamid for their training on the QMS-IM-QMS system.

Table of Contents

List of Figures

List of Tables

Abstract

BINDING ENERGIES AND SOLVATION OF ORGANIC MOLECULAR IONS,
REACTIONS OF TRANSITION METAL IONS WITH AND PLASMA DISCHARGE
IONIZATION OF MOLECULAR CLUSTERS

Isaac Kwame Attah, Ph.D.

A dissertation submitted in partial fulfillment of the requirements for the degree of Doctor of Philosophy at Virginia Commonwealth University

Virginia Commonwealth University, 2013

Director: M. SAMY EL-SHALL
Professor, Department of Chemistry

In this dissertation, different approaches have been employed to address the quest of understanding the formation and growth mechanisms of carbon-containing molecular ions with relevance to astrochemistry. Ion mobility mass spectrometry and DFT computations were used to investigate how a second nitrogen in the pyrimidine ring will affect the formation of a covalent bond between the benzene radical cation and the neutral pyrimidine molecule, after it

was shown that a stable covalent adduct can be formed between benzene radical cation and the neutral pyridine. Evidence for the formation of a more stable covalent adduct between the benzene radical cation and the pyrimidine is reported here.

The effect of substituents on substituted-benzene cations on their solvation by an HCN solvent was also investigated using ion mobility mass spectrometry and DFT computations were also investigated. We looked at the effect of the presence of electron-withdrawing substituents in fluorobenzene, 1,4 di- fluorobenzene, and benzonitrile on their solvation by up to four HCN ligands, and compared it to previous work done to determine the solvation chemistry of benzene and phenylacetylene by HCN. We report here the observed increase in the binding of the HCN molecule to the aromatic ring as the electronegativity of the substituent increased. We also show in this dissertation, DFT calculations that reveal the formation of both hydrogen-bonded and electrostatic isomers, of similar energies for each addition to the ions respectively.

The catalytic activity of the 1st and 2nd row TM ions towards the polymerization of acetylene done using the reflectron time of flight mass spectrometry and DFT calculations is also reported in this dissertation. We explain the variation in the observed trend in C-H/C-C activity of these ions. We also report the formation of carbide complexes by Zr^+, Nb^+, and Mo^+, with the acetylene ligands, and show the thermodynamic considerations that influence the formation of these dehydrogenated ion-ligand complexes.

Finally, we show in this dissertation, a novel ionization technique that we employed to generate ions that could be relevant to the interstellar and circumstellar media using the reflectron time of flight mass spectrometry.

CHAPTER 1. **Introduction**

Interstellar chemistry started in the 1930's with the detection of the simple diatomic molecules CH, CH^+, and CN,[1,2] but since the discovery of complex organic molecules in the late 1960's [3], a lot of research has been conducted to gain insight into the origin and occurrence of these molecules in outer space. Although the chemistry of formation of these molecules in the ISM is still not well understood,[4] several mechanisms have been proposed by research groups for interstellar molecule formation[5-7]

A large portion of all the detected molecules in the interstellar medium(ISM) contain at least one carbon,[8] and polycyclic aromatic hydrocarbon (PAH) along with Polycyclic aromatic nitrogen heterocyclics (PANH) formation are considered to be an important part of the interstellar carbon cycle.[8,9] PAHs based on their local environment in the ISM, are postulated to include ions (a relevant fraction), heteroatoms (such as PANH) , and partially dehydrogenated forms, and several electronic states other than singlet and doublet (radical ion).[9,10]

Several Unidentified Infrared (UIR) bands and diffused interstellar absorption bands (DIB) have been linked to PAHs and PANHs,[9,11-13] but attempts to identify and assign these bands have proven quite challenging.[9,14] Laboratory work to better understand the physicochemical nature of these compounds is thus very important since by isolation of the relevant species in high enough density in laboratory experiments followed by concrete spectroscopic characterization is the best approach in the attempt to understand the chemistry of the ISM.

PAHs and PANHs are also by-products of several combustion processes of organic matter, and have been linked to health concerns including cancer[15-19], due to their ability to form PAH-DNA complexes.[20,21] This fact also makes their chemistry very relevant. A lot of work has been done in our lab in the attempt to understand the formation mechanism of PAHs and PANHs,[22-26] and part of this dissertation will talk about further work done in this direction.

Non-covalent intermolecular bonds such as hydrogen bonds are one of the most important intermolecular forces in nature[21,27-29], and understanding and characterizing them is seen as an essential step in comprehending several phenomena in contemporary drug discovery and chemical synthesis, crystal and material engineering, molecular recognition and supramolecular chemistry, biological processes, electrochemistry and polymerization in the condense phase, and astrochemistry. [30-41]Although a lot of work has been done to better understand the nature of non-covalent interactions between aromatic systems and both protic and aprotic solvents, a huge majority of them have been done computationally,[42] with very little experimentation to corroborate these studies[35,43]. IR or Raman vibrational spectroscopy, solid state neutron diffraction and X-ray diffraction are among a few other methods have been used to identify the presence of hydrogen bonds in compounds, with a large part of these experimental studies done in the gas phase, which are able to yield reliable quantitative information.[34,35, 44,45] The interactions of the π electrons of conjugated and aromatic molecules with atoms like hydrogen similar to a regular hydrogen bond (H_2O---H or HN---H), but in the case the "so called" weak π--h hydrogen bond is well known.[46-48] To further understand the nature of these interactions many experimental and theoretical studies have been carried out to investigate the interactions between benzene, a simple prototype of an aromatic system[28,49] having a well understood π-electron system and several protic and aprotic solvents. [50] For example, the formation of hydrogen bonds between the π-electrons of benzene (C_6H_6) with the O-H hydrogen of the water molecule to yield the π-hydrogen bonded cluster has been extensively studied, and this cluster has been shown to exist in a geometry where the water molecule is symmetrically bonded to the benzene ring with the hydrogen atoms of the water molecule pointing into the plane of the benzene ring. [46,48,51,52] Similar studies have been done on the radical cation of benzene with water[47,49,53-57], and other polar solvents[49,58-60]. Work on the hydration of other aromatic cations such as cyclic $C_3H_3^+$ [41] , phenylacetylene[61] , pyridine, 2-fluoropyridine, and protonated pyridine[62], acetylene monomer[61], dimer[63] and trimer[64] have also been reported. Although a considerable amount of work has been done in the effort to understand these interactions, very little work has been done to investigate comparatively the effect of substituents on the benzene ring towards the nature of the interaction between the π-electron system and the solvent molecule. This is surprising since the π-hydrogen bond system between benzene and several ligand molecules have been extensively characterized, thus making the effect of X/H substitution on the benzene ring less cumbersome to elucidate. In this work, substituent effect of on the nature of non-covalent hydrogen bonding between substituted benzenes with HCN, a molecule that is able to bond using either through its hydrogen or by using the lone pairs of electrons on its nitrogen. HCN is also an important solvent due to its observation and chemistry role in the atmospheric[65] and interstellar[66] media.

The study of transition metal-olefin complexes has impacted the field of catalysis and organometallic chemistry to a great extent,[67-69] and continues to play an important role in this field[70].

The formation of benzene and its analogs from small organic molecule precursors like acetylene and ethylene has been extensively researched in the gas-phase and is now proved beyond any reasonable doubt.[71] Even after such strides have been made, a detailed mechanism as to how these processes occur is still lacking.[72] Polymerization of unsaturated hydrocarbons has been found to have large kinetic barriers when the reactant molecules are not activated, albeit these reactions are exothermic.[73] The presence of certain transition metals has been shown to initiate and facilitate these reactions by overcoming the energy barrier. Knowledge about the processes and mechanisms of these reactions do not only aid in the elucidations of the occurrence of PAHs in the ISM, but are also important in the fields of catalysis and material engineering for the designing of catalysts with high specificity and efficiency.

Extensive gas phase and theoretical studies have been carried out on the interactions between transition metal ions and unsaturated hydrocarbon compounds, [25,67,74] leading to polymerization reactions between the hydrocarbons molecules and/or complexation between the transition metal ions and the hydrocarbon molecules. Most of these studies have shown that these reactions proceed through a C-H bond activation leading to dehydrogenation,[25,75] or C-C bond activation[69] leading to the dissociation then addition reactions or insertion reactions[76].

Knowledge of the structures of the intermediates and product ions involved in these reactions and also thermochemical characteristics of these processes is a very important and necessary step towards the formulations of mechanisms for these processes.[70]

Gas-phase chemistry presents researchers with the ability to study the intrinsic properties of ions and molecules without interference from neighboring species, [77] as is the case with studies done in the solid phase or liquid phase, where effects due to neighboring molecules and counter ions have to be considered. This also makes it possible for researches to exclusively study effects contributed by a molecule’s environment, by comparative analysis of the gas-phase data and the solid/liquid phase data. Here we utilize the Ion Mobility Mass Spectrometry and Reflectron Time-Of-Flight Mass Spectrometry techniques to study several ion chemistry of interest.

CHAPTER 2. Experimental Instrumentation

All work and results discussed in this dissertation were done using the Virginia Commonwealth University Quadrupole Mass Selected-Ion Mobility-Quadrupole Mass Spectrometer (QMS-IM-QMS)[49,78-80] and a Wiley-McLaren type Virginia Commonwealth University Reflectron-time-of-flight mass spectrometer (RTOFMS) [25].

Both instruments are home built vacuum system, and details about their operation are described below.

2.1 The Vacuum Systems

2.1.1 QMS-IM-QMS vacuum system

The QMS-IM-QMS system is made up of four stainless steel chambers as shown in Figure 1. The first chamber, which serves as the source chamber where the neutral clusters are formed, is pumped using a Varian VHS-6 diffusion pump[3000 L/s (He) pumping speed] and this is backed using an Edwards E2M28 rotary vacuum pump. The normal pressure of the source chamber is $2.0\text{x}10^{-7}$Torr and during an experiment, it is allowed to increase to $6.0\text{x}10^{-5}$Torr to prevent over flooding the second chamber.

The second and fourth chambers, which each contain an electron-impact ionizer assembly coupled to a quadrupole mass filter used for mass selection and ion detection respectively, are each pumped using an Edwards Diffstak 160/700 M diffusion pump [1300 L/s (H_2) pumping speed], and both of these diffusion pumps are backed by a single E2M40 rotary pump.

The normal pressures in the 2 chambersare4.0x10^{-8}Torr, and during an experiment, the second chamber pressure rises to 1.0x10^{-6}Torr, whereas the fourth chamber increases to 6.0x10^{-7}Torr.

The third vacuum chamber which contains a drift cell and 2 sets of ion transport lenses is pumped using an Edwards Diffstak 250/2000P diffusion pump [3000 L/s (H_2)pumping speed], which is backed by an Edwards E2M40 rotary pump. This third chamber setup requires a high pumping speed diffusion pump and a dedicated high capacity rotary pump because it has to continuously rid the chamber of the reagent vapor gas and/or Helium buffer gas which are injected into the drift cell for experimental measurements. The typical chamber pressure during an experiment is 1.0x10^{-5}Torr.

2.1.2 R-TOF vacuum system

The source chamber of this instrument is pumped by a Varian VHS-6 diffusion pump [3000 L/s (He) pumping speed], backed by a Welch Duo-Seal mechanical pump. The normal pressure in this chamber is 1.0x10^{-7} Torr, and is allowed to increase to 1.0x10^{-4} Torr during an experiment.

The second chamber, which contains the acceleration plates, the flight tube, a single stage ion mirror, and a micro channel plate detector, is pumped by a Varian VHS-4 diffusion pump [1500 L/s (He) pumping speed] and is backed by a Welch Duo-Seal mechanical pump. The pressure in this chamber during an experiment is not allowed to increase above 6×10^{-6} Torr. A schematic diagram of the VCU Reflectron Time-of-Flight Mass Spectrometer (RTOF-MS) is shown in figure 2.

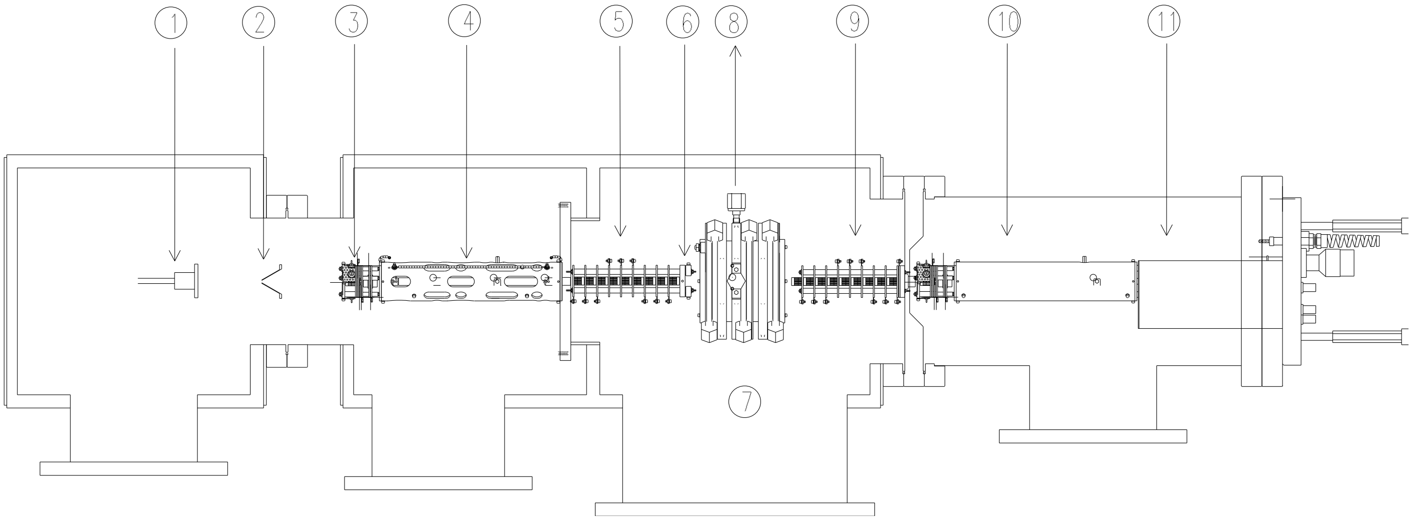

Figure 1: The instrumental setup for mass-selected ion mobility spectrometer. 1) pulsed nozzle; 2) 3 mm skimmer; 3) electron-impact ionizer assembly; 4) quadrupole mass filter; 5) ions transport lenses (Einzel Lenses 1, 2 and 3); 6) steering lens/ion gate; 7) drift cell; 8) to manometer; 9) ions transport lenses (Einzel Lenses 4, 5 and 6); 10) quadrupole mass filter; 11) electron multiplier (detector).

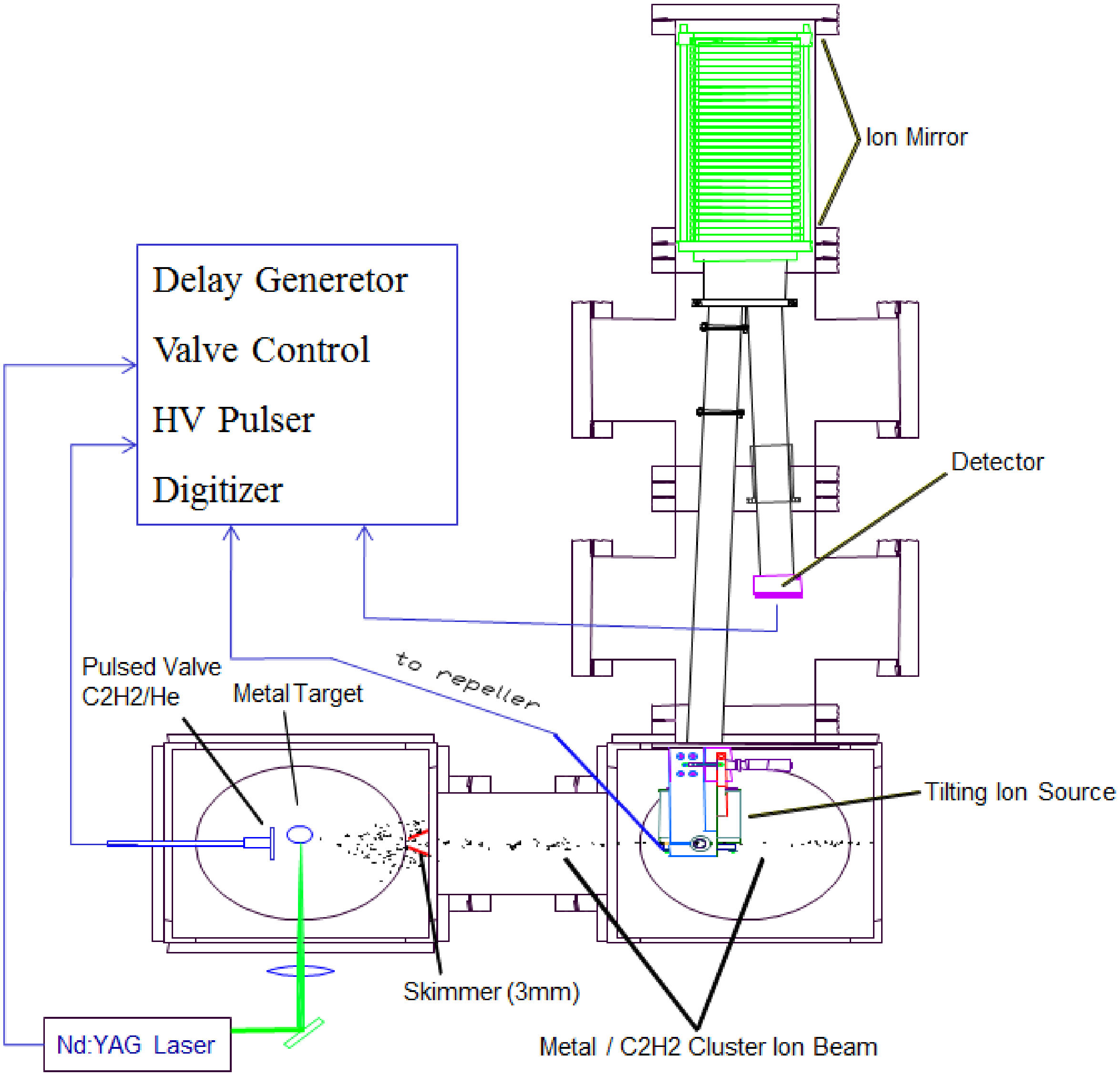

Figure 2: Reflectron Time-of-Flight Mass Spectrometer (RTOF-MS) at VCU.

2.2 Neutral Cluster Generation

A cluster is defined as a finite aggregate of atoms or molecules bound together by van der Waals forces, hydrogen bonds, ionic, metallic, or covalent bonds. A cluster could contain as little as 2 atoms of molecules to as many as a few thousand of them. The study of clusters is a very vital because they possess properties intermediate of a molecule and a bulk solution or material.[81] Clusters are basically formed through condensation of rapidly expanded gases. The method of clusterization used in our laboratory is the pulsed supersonic expansion, where the cluster of interest is obtained by seeding the precursor molecules in an inert gas, usually Helium or Argon. The mixture is then expanded through a micron sized pulsed nozzle (*General Valve* (series 9)) which is operated at a frequency range between 4 to 100 Hz depending on size of cluster that is required.

Seeding is achieved by mixing the sample gas with the inert carrier gas or by passing the inert carrier gas over the sample, in the instance where the sample is liquid or solid at a ratio of ~ 0.5 - 5% (p /p) of the sample vapor in the inert gas. In this case the sample should have an appreciable vapor pressure, which can be induced by heating when the sample is non-volatile.

The pressure before the nozzle (backing pressure, Po) is usually set between 1-6 atm and after the nozzle, is maintained between 1.0×10^{-8} to 1.0×10^{-4}Torr (760 Torr ≈1 atm≈15 psi).

Thermal energy in the high pressure source is converted into directed velocity (u) upon expansion. A simple thermodynamic representation of this process is given by equation 2.1,

$$C_pT_0 = C_pT_1 + \frac{mu^2}{2} \qquad (2.1)$$

where Cp is the heat capacity of the expanding gas, $T_0$the source temperature, T_1 the beam temperature, and m and u the molecular weight and velocity of the expanding gas respectively.[82] T_1 must be lower than the source temperature, T_0 since the kinetic energy term on the right side of the equation is positive.

This natural reduction in temperature leads to clustering (condensation) of the seed molecule due to the low temperature of the cluster beam which has been determined to get as low as 30K. [83] The molecular beam formed has most of the larger sized clusters close to the center axis due to the diffusion of the lighter carrier gas atoms radially away from the beam axis. The expansion of the gas into the collision free region in the vacuum chamber (a few nozzle orifice diameters), creates directed motion of the gas, providing cooling in the vibrational, rotational, and translational temperature coordinates. The quenched temperatures are in the order $T_{vib}> T_{rot}> T_{trans}$. Latent heat released as a result of cluster condensation is extinguished by collision with the inert carrier gas. The gas beam is collimated using a 3 mm cone skimmer which skims the sample cluster beam form a one directional beam entering the second chamber.

This skimmer also serves as conductance limiter which ensures that differential pressures are maintained in the source and ionization chambers.

In experiments where only the monomer ion of the sample is needed, the gas vapor is allowed to flow continuously, carried by the carrier gas, to the first chamber. This process is referred to as continuous flow. In this case, the gaseous mixture flows through a nozzle with our 100 µm orifice which has the poppet removed. Due to the high sensitivity of the vacuum chamber to pressure, we employ a needle valve to finely control the pressure getting to the nozzle to ensure the pressure does not go above 1.0 x $^{-4}$Torr. The resulting molecular beam is collimated by the 3 mm skimmer as described above.

2.3 Ion Generation

The mode of ion generation is important because the energy of the ion depends very much on the way the ion was created. All ions discussed in this thesis were generated by one of three ionization techniques, plasma discharge ionization, laser vaporization ionization (LVI), or electron impact ionization (EI).

2.3.1 Plasma Discharge Ionization

Ions of molecular clusters, Carbon cluster and protonated molecular cluster are created in this study using an electrical discharge from a high voltage-low current power supply applied to discharge source. The source is coupled to the pulsed nozzle (General valve series 9, 250 μm), therefore ions are created in a supersonic expansion.

There are two kinds of sources employed it these experiments, both to be discussed separately.

(i) Plate Plasma Discharge Ionizer (PPDI)

(ii) Needle Plasma Discharge Ionizer (NPDI)

2.3.1.1 PPDI

The PPDI is shown in figure 3. It is made of two brass discs (34.00 mm OD) which have an orifice in the center (2.00 mm ID) that is aligned with the pulsed nozzle orifice. These brass discs are 3.20 mm thick. On each brass disc we welded on a brass rectangle (L=10.80mm, B=5.4mm, H= 3.20mm) to make electrical connections to the discs easier. In addition there are two Teflon discs (1.10 mm and 3.10mm thick respectively) which are placed in between the brass plates for electrical isolation (34.00mm OD, 5.50mm ID).

During operation the 1.00mm thick Teflon disc is placed on the nozzle flange, followed by one of the brass disc. The second brass disc is then placed on the assembly, separated from the first brass disc using the 3.10mm Teflon disc. In this configuration, electrical connectivity between the nozzle and any of the brass discs is prevented.

All four discs have holes drilled close to the outer circumference in a pattern making a square, so that the assembly can be coupled to the nozzle flange of the pulsed nozzle using four plastic threaded shafts, 4 ceramic washers and 8 stainless steel nuts.

Two wires, one connected to each brass plate are used to supply voltage to the plates from a high voltage power supply (Johnson Lab Inc. model-HV4R). The second plate is supplied with 550V, and the first plate is grounded. Due to the electrical isolation, the plates maintain the potential difference till the expansion of the gas mixture by the nozzle, which leads to an instantaneous arc plasma discharge along the cluster beam path creating the ions in the process.

2.3.1.2 NPDI

Figure 4 shows the NPDI, which has a different setup from the PPDI but their principle of operation is the same. The setup is made of a circular teflon block (13 mm thickness, 42mm OD,) the block has an inner orifice (7.5mm ID) which is aligned to the nozzle orifice when it is installed. The teflon block has a hole drilled in the side along the circumference, (1.10mm ID) which holds in place the two needles used for the arc discharge. The needles used are stainless steel hand sewing needles bought from a general store. When installed in the teflon block, the needles are kept ≈2.60mm apart so that there is electrical isolation between the two.

The teflon block has 4 holes drilled in a square pattern, so that the assembly can be coupled to the nozzle flange of the pulsed nozzle using four bolts and nuts.

Two wires, one connected to each needle are used to supply voltage to the needles from a high voltage power supply (Johnson Lab Inc. model-HV4R). One needle has an applied voltage of 500V, and second is grounded. Due to the electrical isolation, the electrodes maintain the potential difference till the expansion of the acetylene gas mixture by the nozzle, which leads to an instantaneous arc plasma discharge along the cluster beam path creating the ions in the process.

2.3.2 Laser Vaporization Ionization (LVI)

Laser induced ionization is widely employed in the formation of atomic, molecular and cluster ions such as laser vaporization ionization of bulk metal to form metal ions in the gas phase[25,84-86], form metal and semiconductor nanoparticles for various applications[87], and initiate ion-induced nucleation[88] or polymerization.[89,90]

Laser vaporization ionization is used here to generate metal ions from a selected metal target. The mechanism of laser vaporization ionization is still not well understood, even though photothermal processes are widely accepted as the mechanism for ionization of the metal ions.[91] For our experiments, the ablation process is achieved using a pulsed second harmonic 532 nm Nd: YAG laser (Surelite-Continuum (SSP-I), ≈10 mJ/pulse, 8-10 Hz, 8-10 ns pulse widths) which is focused through a quartz window on a tiny spot (≈0.01 cm^2) on the metal target located in the source chamber (power density ≈10^7 W/cm2), which results in a sudden and intense increase in temperature at the local surface.

The absorption of photons by the metal target depends on, (i) the absorption coefficient of the metal target, (ii) the wavelength of the laser light, (iii) and laser fluence (J/cm2).

The increase in the local temperature is attributed to the lengthier absorbed-energy dissipation time, as compared to the laser pulse-width. This leads to the formation of a molten layer with an estimated surface temperature of 3000-6000 K[92] and eventually evaporation. The metal vapor absorbs more light which leads to the forming of a plasma/plume. The ionization process creates

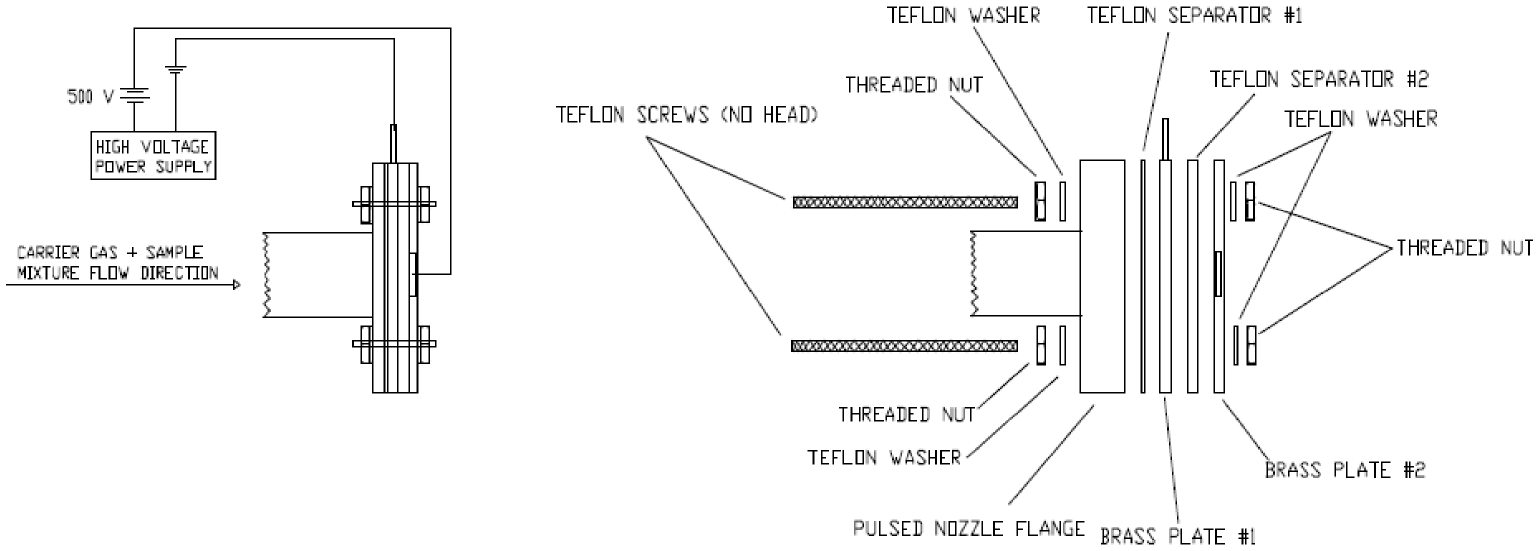

Figure 3: A schematic of the Plate Plasma Discharge ionization assembly used to produce carbon cluster ions. Fig a shows the assembly installed on the nozzle drive, with voltage connections. Fig b. shows the exploded form of fig a, showing all the individual parts in the assembly.

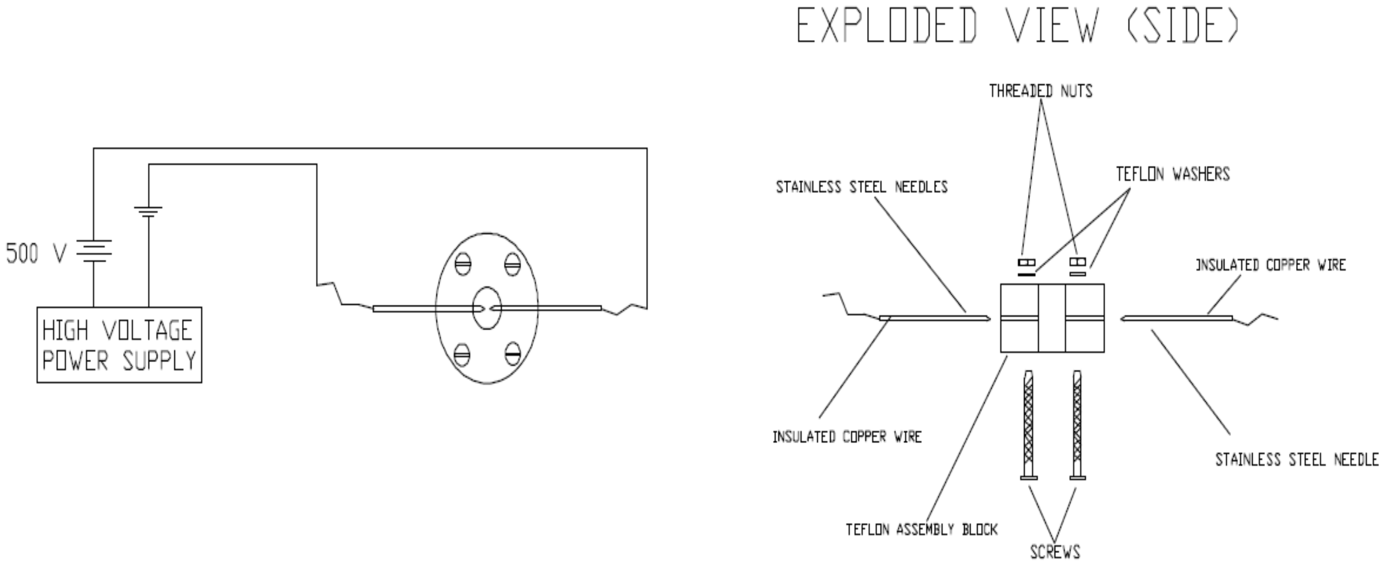

Figure 4: A schematic of the Needle Plasma Discharge ionization assembly used to produce carbon cluster ions. Fig a shows the assembly installed on the nozzle drive, with voltage connections. Fig b. shows the exploded form of fig a, showing all the individual parts in the assembly.

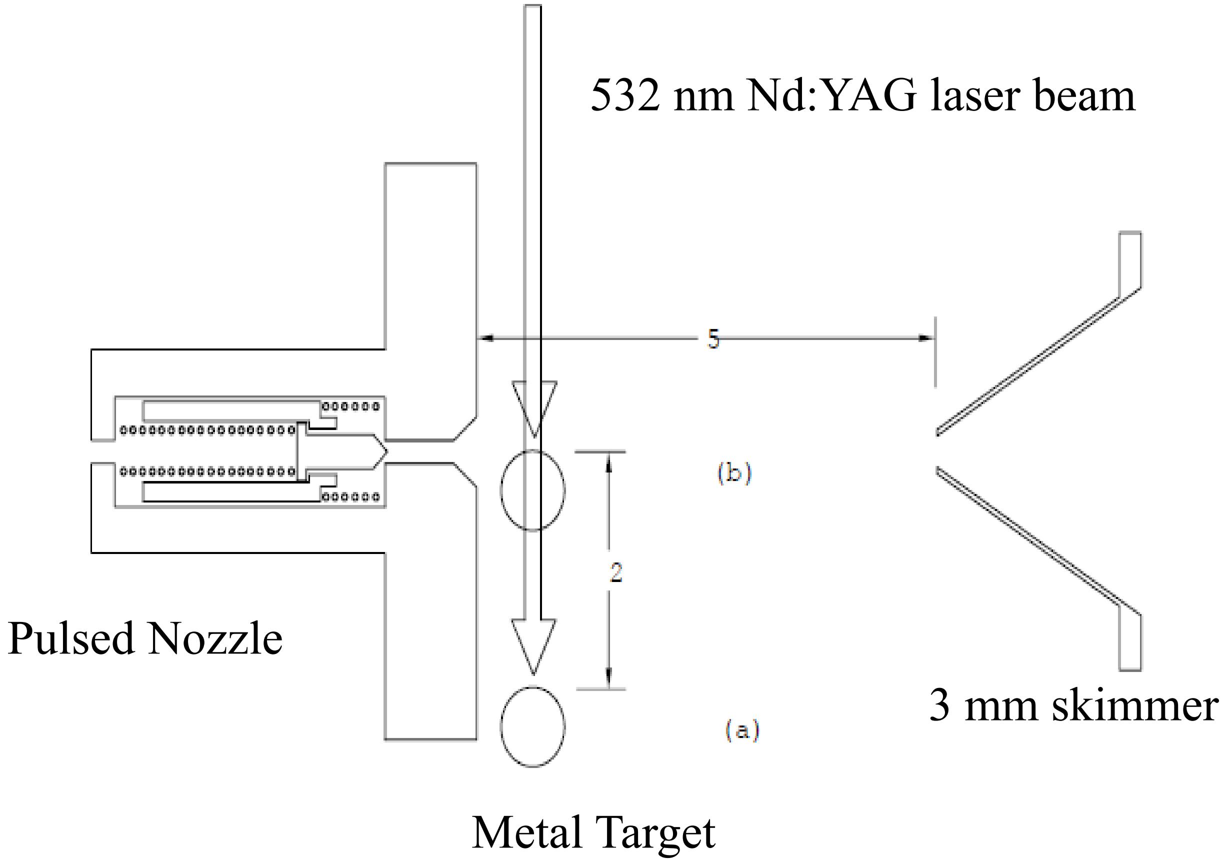
532 nm Nd:YAG laser beam
5
(b)
2
Pulsed Nozzle
3 mm skimmer
(a)
Metal Target

Figure 5: Schematic showing the position of the metal target with respect to the nozzle orifice and laser beam, and skimmer during the laser vaporization/ionization. Distance given in cm.

cations, anions and electrons as well as neutrals. The metal target is affixed on a mechanical motor with a variable RPM, but is operated at2RPM and this translates the metal target relative to the laser spot. This is to ensure the continuous and uniform flux of ions. Figure 5 shows the position of the metal target with respect to the nozzle orifice.

Figure 5also shows the distance the ions travel away from the metal target before being carried by the expanded sample and carrier gas towards the skimmer

2.3.3 Electron Impact Ionization

The quadrupole mass filters used in the QMS – IM- QMS setup are equipped with the Extrel TM axial beam ionizers (model 04-11 and 5221). Electrons responsible for the ionization are thermionically generated by a tungsten filament and then accelerated into the ion region. Ionization occurs in the ionizing volume, which is within the ion region basket shown in figure 6. Collision of the electrons and the neutral cluster beam leads to the ionization of the clusters. The electrons, which are created from the tungsten filament by heating it to a temperature of 1870- 2970 K using on and emission current between 0.05 to 5.0 mA , are extracted using an electrostatic field into the ion region. Ions created here are then extracted from the ion region and focused into the quadrupole mass filter by a set of ion optics.

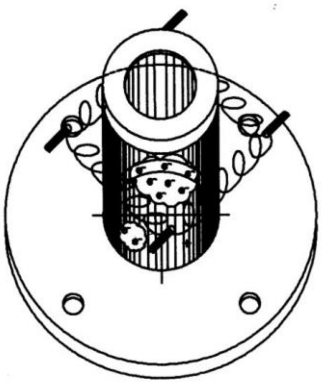

Figure 6: Ion region basket and filament which contains the Ion volume, where electrons ionize the sample molecules

2.4 Quadrupole Mass Selector-Ion Mobility- Quadrupole Mass Selector

2.4.1 Mass filter and ions transport lens system

Ions of interest created by electron impact ionization (EI) of the neutral cluster beam are mass selected using a quadrupole mass filter based on their mass to charge ratio. The quadrupole mass filter assembly consists of 4 stainless steel rods, 3/8” diameter and 7.88” length. The opposite rods in this quadrupole mass filter assembly are connected electrically, and have an effective mass range of 10 – 4000 amu. The mass filter can be used for strict mass selection in the RF-DC mode, and in this case, only an ion with a specific mass to charge ratio will be transmitted though the quadrupole. The mass selection function can be used “loosely” in the RF only mode, where ions within a given mass to charge ration will be allowed to pass through the quadrupole mass filter assembly. In both mass selection modes, fluctuating electric fields are applied to the individual quadrupole rods in a specific frequency and intensity to affect the path of the ions travelling through. The ions that do not meet the specified mass to charge ratio are pushed off axis by the applied voltages and hit the rods of the quadrupole.

This expunging action is achieved by the uniform superimposition of the DC and RF voltage on the quadrupole rods such that the ions of interest and right mass to charge ratio will have a stable trajectory, oscillating on its z-axis and making it through the quadrupole.

The quadrupole assembly has pre and post filters mounted on the main quadrupole rods which serve to collimate the ions entering and exiting the quadrupole mass filter respectively.

During an experiment, the mass selected mode of the quadrupole mass filter is preferred due to its high selectivity, but in the case where the ion count is too low for a reliable measurement, the RF mode is used, provided that there is significantly low or non-existent contamination from ions that are not of interest The ions of interest that are transmitted through the quadrupole mass filter assembly enter the third vacuum chamber, and travel through a set of three Einzel lenses , and then a set of steering lenses, both of which serve to guide the ion beam towards the pin hole orifice of the drift cell (Drift Cell Entrance).

The steering lens assembly is made up of a horizontal and vertical ion-guiding set, each of which is consists of 2 semi-circular nickel plates. One plate from each set is connected to an individual high voltage-low current power supply. The two other plates are both biased by connecting them an independent voltage power supply and also the 3rd Einzel lens which has a set value of -240V. To influence the path of the ion beam into the drift cell entrance, the voltages applied on the unbiased plates are varied with respect to the biased plates to steer the ions in both horizontal and vertical planes. Figure 7 shows the position of the Einzel and steering lenses in the ion optics setup.

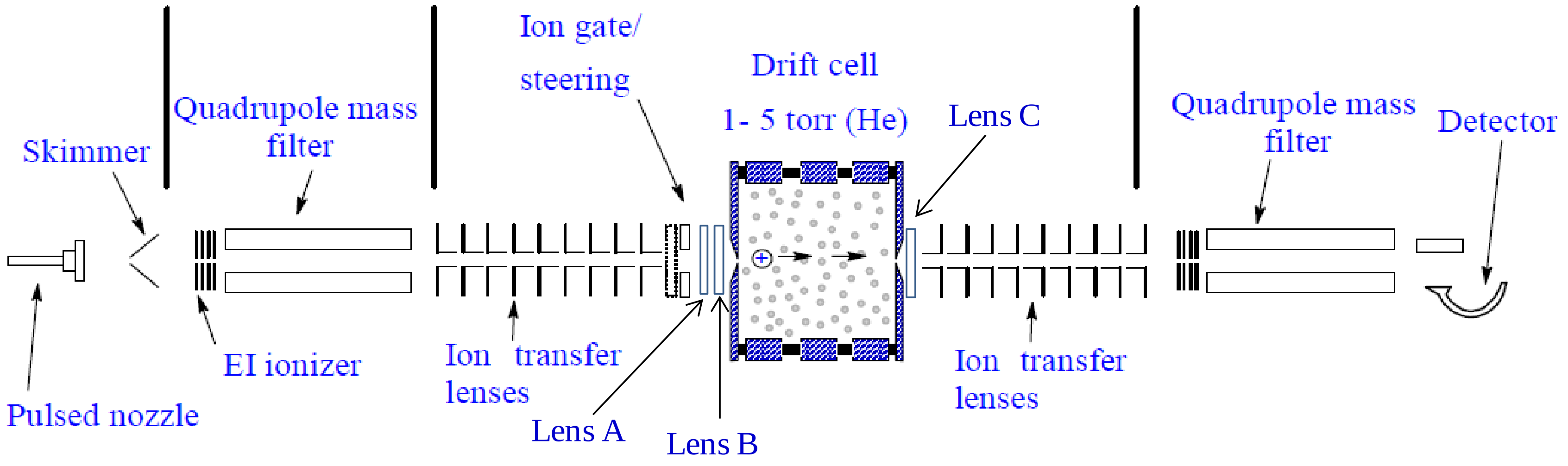

Figure 7 The QMS-IM-QMS setup showing the quadrupole mass filter assemblies, the transport lenses, the drift cell, and electron multiplier ion detector

The vertical steering lens also serves as an ion gate, which “chops” the ion beam into 10- 100μs beam widths for time dependent studies. The gating is triggered by a pulse generator (DEI, PVX-4140) connected to the power supply of the vertical lens, which supplies a + 240V to the plate (i.e. -240V on the biased plate, and +240 V on the second plate) to deflect all ions thus closing the gate. The gate is open when the + 240V is removed and the two plates have the same sign.

2.4.2 DRIFT CELL

The drift cell used in the QMS-IM-QMS system which is shown in figure 1 has been replaced by a new model drift cell designed by Paul Kemper. This new drift cell is made of two main units, the cell body unit and the endcap unit. Their outside dimensions are 3.5" × 3.5" × 2.14" and 3.5" × 3.5" × 0.40" respectively. Both of the units are made of oxygen free high conductivity copper alloy (Alloy 10100 OFHC) which has a high melting point of 1360 K. The inside of the drift cell is machined into a cylindrical shape (1.84" length × 2.0" D). towards the end of the cylinder, the last 0.28" to be exact, the diameter of the tube increased by 0.35" (2.35") to lodge a ceramic ring(2.34" OD, 1.97" ID and 0.40" thickness) electrically isolates the cell body and endcap units from each other. The schematic drawing of the new drift cell is shown in figure 8.

The drift cell entrance lens is made of a stainless steel plate with a 0.254 mm orifice, attached from the inside of the drift cell body and kept in position by a copper retainer. Two lenses sit just before the drift cell entrance, separated by ceramic spacers to help focus the ion beam into the drift cell entrance orifice. The second lens is tapered towards the drift cell entrance to collimate the ion beam. Both lenses are connected to and controlled by different high voltage power supplies.

The endcap also holds an exit lens made of a stainless steel plate with a 0.254 mm orifice and held in position by a copper retainer. The endcap also has mounted on its interior section five drift rings (SS, 1.40" OD, 0.60" ID, and 0.128" thickness) and are held by six ceramic rods as shown in figure 9. After the drift cell exit, an exit lens is mounted unto the exterior of the endcap unit. The exit lens is tapered towards the drift cell exit, as shown in figure 8.

The ion beam are transmitted into a set of three Einzel lenses, which then collimates the ions into the fourth chamber which contains a quadrupole mass filter and an electron multiplier detector, used for ion analysis and detection respectively. The second QMS can be used to monitor an ion of a specified mass (m/z), and in this mode, the arrival time distribution of all ions both reactants and products can be measured. It can also be used to scan a mass range to determine the presence and relative abundance of all ions during an experiment.

Reagent vapor or inert gas used for studies are fed into the drift cell through stainless steel tubes (with ceramic breakers for insulation) and the flow rate of the gas is controlled using mass flow controllers (MKS 1479A) one flow controller and channel for each gas being fed into the cell.

The pressure in the cell is monitored using a capacitance manometer (MKS Baratron type 626). The maximum attainable pressure in the cell is very much dependent on the pumping speed of the diffusion pump and the drift cell entrance and exit orifice diameters. Under our current setup conditions, we are able to attain cell pressures of about 7 Torr He. Thermalization of the ions being studied is completely achieved through collisions of the ions with the escaping gas molecules from the drift cell entrance orifice.[60,80,93]

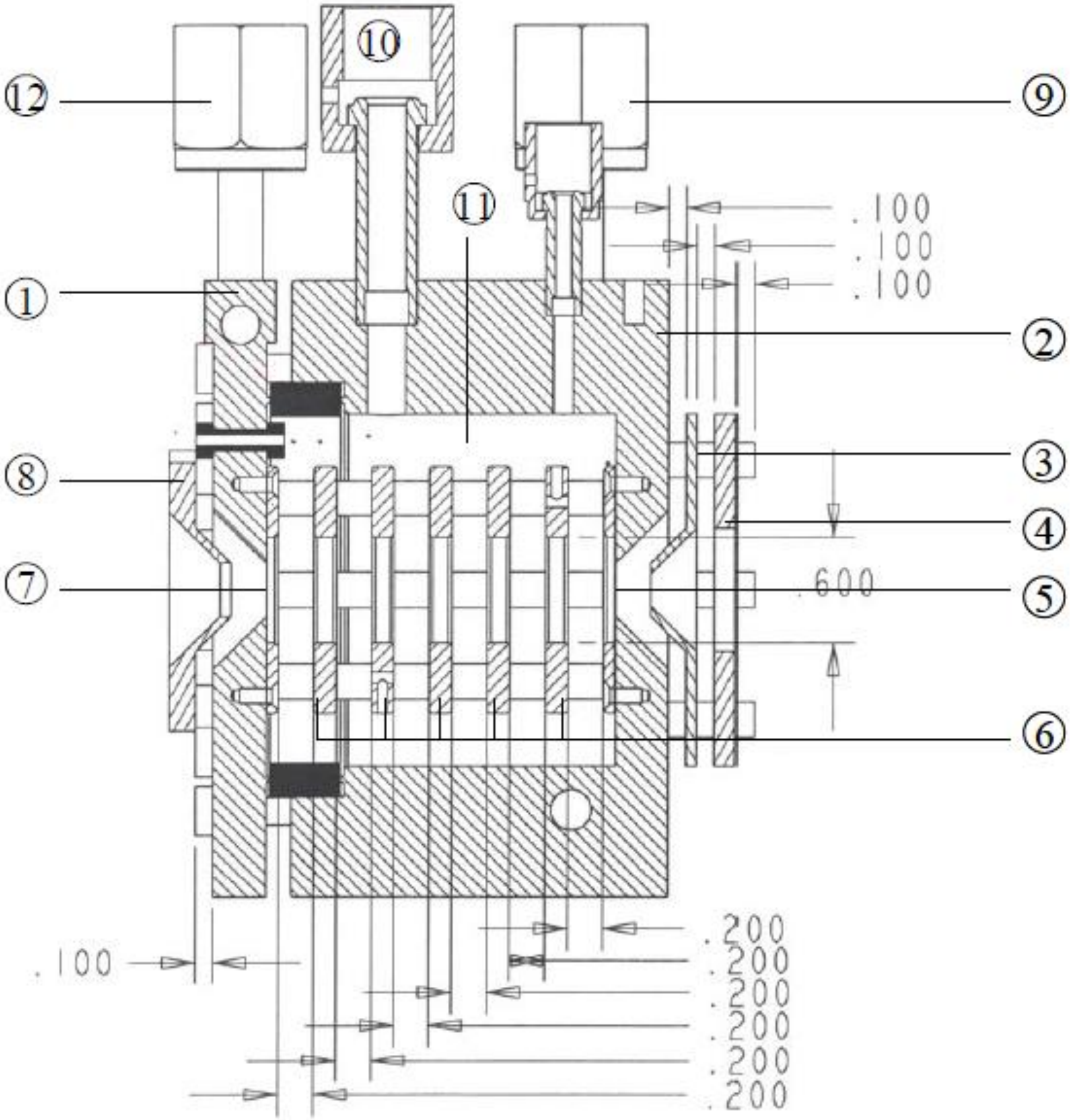

Figure 8: Side view schematic of drift cell. (1) Endcap (2) Drift Cell body (3) Entrance lens (lens B) (4) Tapered entrance lens (lens A) (5) Entrance orifice (0.25 mm) (6) Drift rings (7) Exit orifice (0.25 mm) (8) Tapered exit lens (lens C) (9) Cell body liquid nitrogen inlet (10) Baratron connector (11) Drift cell (12) Endcap liquid nitrogen inlet. Dimensions are in inches, except indicated otherwise

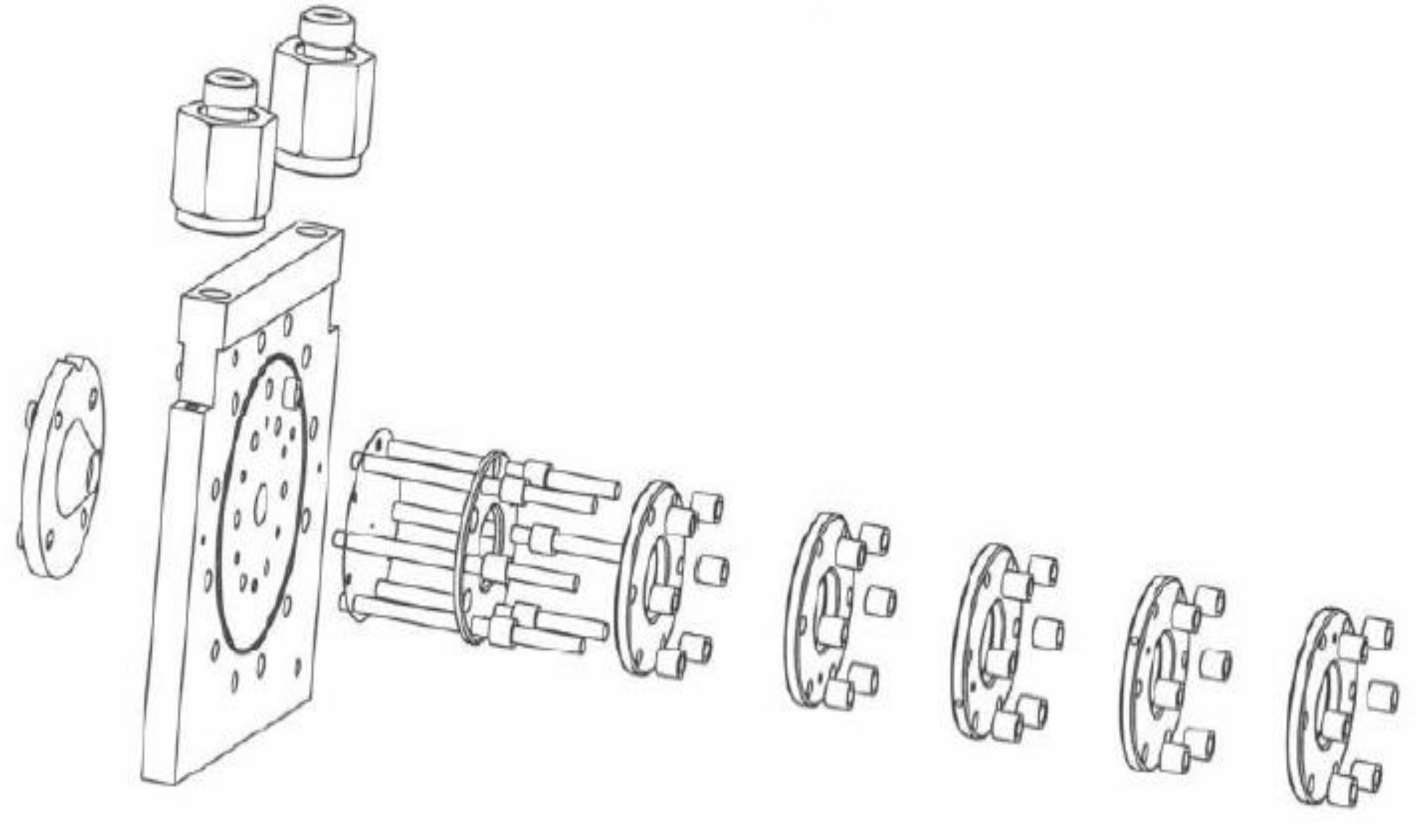

Figure 9: Schematic showing the assembly pattern for mounting the drift rings, ceramic spacers and the exit lens unto the endcap of the Drift Cell.

The drift cell temperature can be controlled either by heating or cooling for temperature dependent studies. Tantalum wires woven through ceramic tubes, inserted into the drift cell (eight in the cell body and 2 in the endcap) is used for heating, and the maximum attainable temperature of the cell using this technique is approximately 500 ^{o}C.

Heating is generated from a DC current obtained from AC current using of a combination of isolation transformers and a dynode bridge rectifier for conversion. The conversion is necessary since ceramic becomes conductive at high temperatures and thus AC current applied to the heating wires could interfere with the voltage applied to the cell. Heating control is done using two controllers (Omega type CN3251) within ±1 ^{o}C. The cell is cooled using liquid nitrogen, and is achieved using two temperature controllers (Omega type CNi3233) coupled to On/Off solenoid valves, one each for the cell body and endcap respectively within ±1 ^{o}C. The lowest attainable temperature is -195 ^{o}C, the temperature of liquid nitrogen. To monitor the cell temperature, two thermocouple wires are connected to the body and the endcap, both connected to omega DP462 readout.

2.4.3 Electron multiplier detector

After mass analysis by the second quadrupole mass filter, the ions are detected by an electron multiplier detector with a conversion dynode (De-Tech; 402A-H), coupled to the QMS.

To detect a cation, the ion strikes the surface of the conversion dynode, which has a high negative voltage applied to it (c.a 5kV), and this leads to the ejection of several electrons. The electrons are accelerated down a multiplier tube due to the potential difference between the dynode and the multiplier tube (less negative voltage applied), and as they strike the surface of the tube, it causes the ejection of a cascade of electrons down the path. This leads to the generation of a short charge pulse at the output terminal, which is detected as a current signal is then processed by Merlin software from ABB Extrel.

The current is amplified by a counting pre-amplifier (MTS-100), which also has an adjustable discriminator, used to increase the signal to noise ratio. This is possible because a signal comes from multi-electron process while noise comes solely from single electron process.

2.4.4 Ion Energy

The definition of an ion's energy (relative to ground) has been well defined[94] as the applied voltage on the ion region lens (where the ion is created) of the axial electron impact ionizer in the first quadrupole mass filter. This makes the energy of the ion less dependent on the energy of the ionizing electron, or the applied potential of the extracting lens. The entire housing of the quadrupole mass filter is floated to a fixed voltage, which adds on to the value of the ion region, and thus the effective ion energy is defined as the sum of the ion region voltage and the floating voltage. The quadrupole mass filter is floated to enable it manage or handle the ion energies more effectively, especially in experiments where very energetic ions are being born.

The resolution of a mass filter depends on the number of oscillations (n) that the ion experiences in the quadrupole mass filter, and the value of n depends on the residence time of the ion being analyzed in the quadrupole field. Thus more energetic ions have less residence time of the ions in the quadrupole, leading to poor resolution. To counter this, there is an applied DC voltage on the z-axis of the quadrupole mass filter, known as the pole bias. The pole bias serves to "slow down" or "speed up" the ions as they travel through the quadrupole, thus increasing or reducing their residence time respectively for optimum analysis and improving the resolution. To this effect, the axial kinetic energy of an ion in the quadrupole mass filter is the difference between the total voltage applied to the ion region and the pole bias voltage, as given in equation 2.2.

$$I.E = (IR + FQ) - PB \qquad (2.2)$$

where I.E is the Ion Energy, IR the Ion Region Voltage, FQ the Floating Quadrupole Voltage, and PB the Pole Bias Voltage. For our studies, the ion energy is maintained between 10 to 30ev. Another important ion energy parameter considered is the injection energy of the ion (kinetic energy) as it enters the drift cell, and is defined as the difference between the Ion Energy and the drift cell entrance voltage. When the injection energy is too low, the ions are not able to penetrate the drift cell entrance orifice due to the high pressure of the helium or reagent gas escaping from the drift cell. This leads to low signal intensity.

In the case where there injection energy is too high, there are two possible effects on a study. Firstly, high injection energies cause the ions to travel too deep into the drift cell before losing their kinetic energy, which makes ion mobility and other drift cell residence time dependent measurement studies inaccurate.

Secondly, high injection energies leads to parent ion fragmentation in the drift cell which not only causes a decrease in ion signal intensity, but more importantly secondary reactions between the fragment ions and the reagent vapor in the drift cell, thus leading to complications in thermochemical and kinetic measurements. For all our studies, the injections energies, except otherwise stated, was kept in the range of 10 - 20 eV. Ions exiting the drift cell are considered to be recreated, and their energy is approximately the drift cell exit voltage.

The second quadrupole mass filter also has the same energy manipulations as the first discussed above. The pole bias of the second quadrupole is adjusted such that the ion energy experienced by the quadrupole rods is between 3 – 10 eV for optimum resolution.

2.5 Reflection Time-of-Flight Mass Spectrometer (RTOF-MS)

The RTOF-MS used for the work described in this dissertation is shown in figure 2. This system has two differentially pumped vacuum chambers. This RTOF-MS can be used to investigate both positive and negative ions.

The first chamber, the source chamber, is where neutral clusters and ions are produced. This chamber has a 250 μm conical nozzle (General valve, series 9) for cluster production. The typical operating pressure of the source chamber is ≈1.0 x 10-5 Torr. The source and TOF chambers are separated by a 3 mm conical skimmer placed at a distance of about 4-7 cm coaxial to the nozzle (the nozzle can be moved back and forth, depending on the experiment for optimum ion transmission to the second chamber). The first chamber is pumped by a Varian VHS-6 diffusion pump [3000 L/s (He)].

The second chamber, the TOF chamber contains the acceleration plates, the flight tube, a single stage ion mirror, and a micro channel plate detector. The TOF chamber is pumped by a Varian VHS-4 diffusion pump [1500 L/s (He)] and with operating pressures kept ≤ 6 × 10-6 Torr. Both diffusion pumps are backed by two Welch Duo-Seal mechanical pumps.

Acceleration of ions towards the detector in the R-TOFMS is based on the de Heer 2nd order space focus principle and also utilizes a single stage ion mirror.[25,95]

The arrangement of voltages are from the bottom, the repeller plate, an accelerator (2nd order space, grounded), and then the entrance of the flight tube. The acceleration process is achieved using a repeller plate (on which acceleration voltage is applied, ≈ ±500 V, same polarity as ions under investigation) which has a field free sub-stage. A middle plate, above the repeller plate, is grounded and functions similar to the repeller plate due to the potential difference created

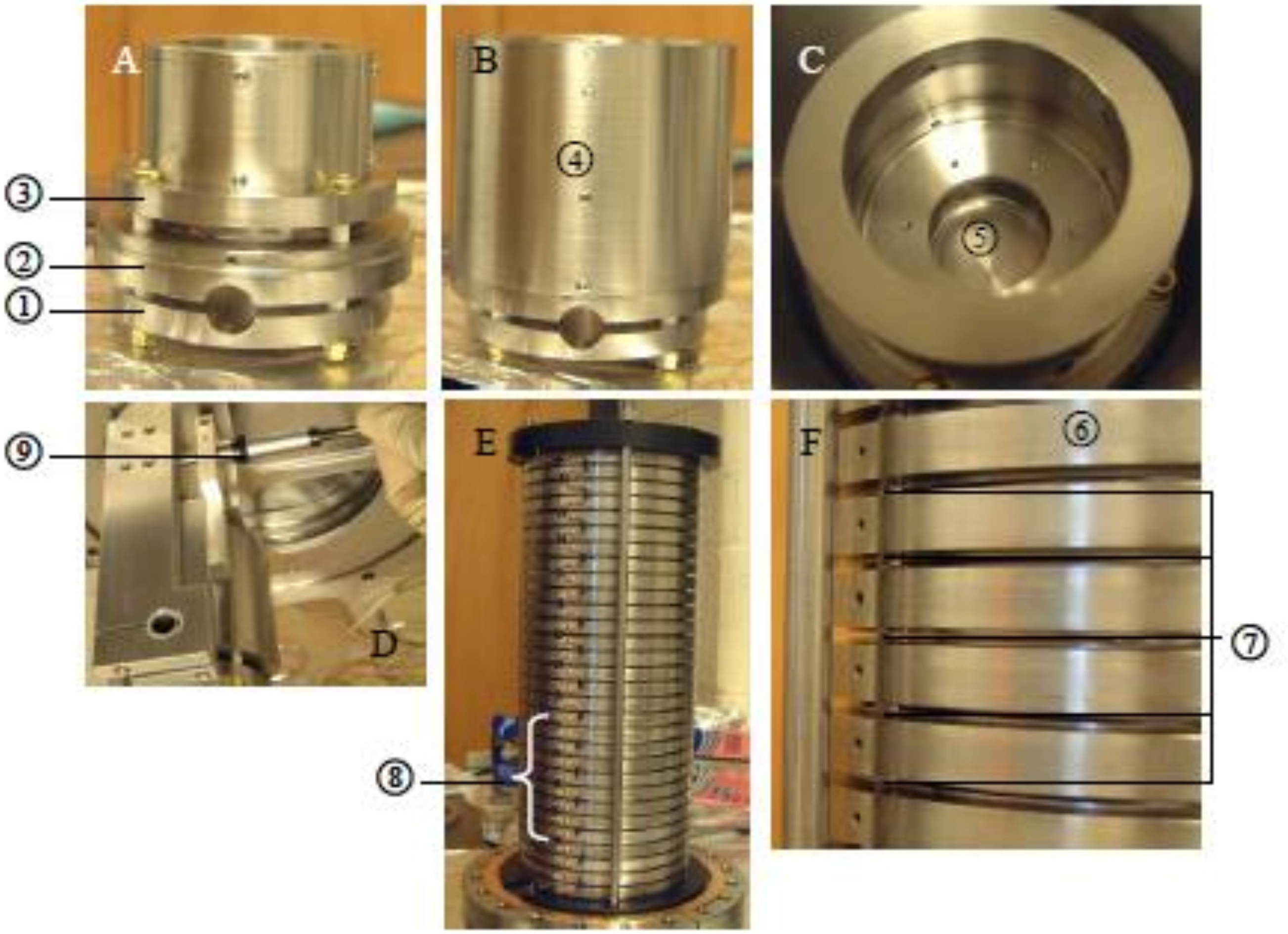

Figure 10: Images of the RTOF ion acceleration source (A – D) and reflectron ion mirror assembly (E and F). (1) Repeller plate (2) Ground plate (3) Flight tube plate (4) Field shield (5) Nickel mesh on the ground plate (6) Ion mirror ring (7) Sapphire bearings (8) Chain of 20 MΩ resistors (9) Manipulator screw for tilting acceleration source (the source is pictured upside down here).

between the repeller plate and the ground plate. There is a 1.27 cm separation between these two acceleration plates. Images of the ion acceleration source and reflectron mirror are shown in figure 10.

From there the ions encounter the entrance of the flight tube (has a high applied voltage, ≈2 KV with polarity opposite to that of the ions under investigation) .Separate high voltage supplies are used for the repeller plate and flight tube, thus eliminating the need for a voltage divider. The repeller plate is pulsed using a pulse generator (DEI GRX-3.0K-H) so as to coincide with the best sampling of the ion beam transmitted from the first chamber. The ion source is equipped with a manipulator flange coupled to a tilting source so that the size of ions reaching the detector can be controlled by changing the orientation of the plates on the horizontal plane.

On exiting the acceleration region and entering the flight tube, the ions are guided into the ion mirror and a second flight tube guides the ions from the ion mirror to the detector (4.1 cm OD × 0.6 m and 0.4 m length respectively).

These flight tubes provide a filed free region for the ions, where separation of the different ions takes place since the speed of the ion is proportional to the inverse square root of the mass-to-charge ratio of the ion.[96,97]

Both flight tubes are supported just below the ion mirror entrance by a mirror shield. The flight tubes have been perforated with several holes (0.74 cm D) for efficient pumping. An insulating cap (3.5" D, also drilled with holes) is also mounted around the flight tube entrance to prevent the tube field from interfering with the acceleration region fields. The detector is clamped unto the end of the flight tube and is insulated from the chamber using ceramic spacers.

The detector used in this RTOF is a Burle Long-Life™ MCP, (40:1 L/D, Chevron style,> 4 x 10^6 gain, 400 MΩ. The detector voltage is floated on the flight tube voltage thus voltage readout of -2.30 kV and -2.10 kV for the flight tube and detector on the power supply respectively is actually, -2.30 kV for the flight tube and -4.40 kV for the detector, even though the detector only "feels" the applied -2.10 kV. The floating is done using a custom-made Portware® voltage supply (Model 5RFTD3-C, ± 5 kV, ± 3 kV float, dual polarity).

The reflectron ion mirror is constructed from 30 stainless steel rings, separated by sapphire bearings (0.32 cm OD), which have been mounted on a 6" stainless steel conflat flange. The reflectron ion mirror is shown in figure 10. The only connection between the rings is a chain of 20 MΩ resistors to maintain desired potential drop-off throughout the mirror. The ion mirror setup is insulated from the flight tube using two delrin rings (4.7" OD) which are mounted above and below the mirror structure. The structural integrity of the reflectron ion mirror is preserved using four 0.25" D rods mounted through the delrin rings on the conflat flange. The first ring is gridded with fine Ni mesh (Buckbee Mears Cortland, 70 lines per inch (LPI), 88-89% transmittance) for entrance field evenness.

The overall ion optics is constructed such that, the flight tube accommodates an ion in the first ion space focal point and the detector is installed to coincide with second focal point.

During an experiment, ions generated in the source chamber are collimated by the skimmer thus creating a narrow width ion beam which travels into the ion source in the second chamber with speeds in the range 400-600 ms^{-1} depending on backup pressure being used. In the TOF chamber, the ions of interest are extracted and accelerated through the first flight tube by the ion source into the reflectron ion mirror. The ion mirror repels the ions out towards the micro channel plates for detection through the second flight tube.

To study cations, the polarity is of the repeller and reflectron ion mirror voltages is positive, whiles the flight tube and detector voltages is set to negative. The polarity configuration is reversed for negative ions experiments. Control of the time sequence is of a very critical importance to ensure optimum sampling and analysis of the product ions during an experiment. Figure 11 shows a typical timing sequence used during the operation of the Reflectron time of flight mass spectrometer. A usual experiment to detect positive ions begins with the opening of the pulsed nozzle leading to the formation of neutral clusters of acetylene, $(C_2H_2)_n$. After a determined delay (≈ 400-500 μs), the laser Q-switch is triggered to initiate lasing, resulting in vaporized metal cations (M^+), anions (M^-), electrons, and neutral atoms and electrons. The cations/anions/electrons subsequently interact with the neutral cluster beam of acetylene forming charged clusters, $M^{\pm}(C_2H_2)_n$.

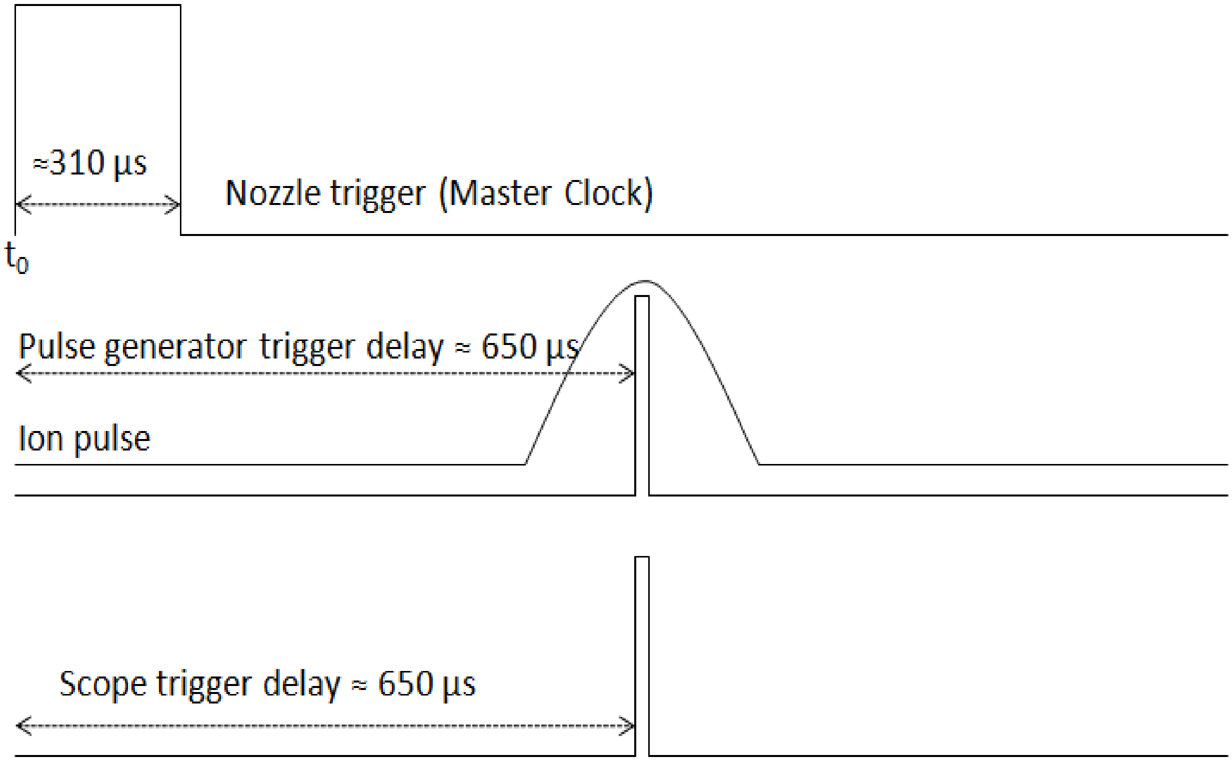

Figure 11: A typical timing sequence for the setup for Reflectron Time-of-Flight spectrometer during operation.

The charged metal-acetylene cluster complexes (both positive and negative) are collimated by a conical skimmer as they enter the detection chamber. At approximately 650 μs after the nozzle opening, the pulse generator is triggered, thus supplying voltage (500 V/cm, 100 μs pulse width) to the repeller plate to accelerate the ions through the flight tube into the reflectron ion mirrors. The flight tube and ion mirror voltages are set at ≈-2.30kV and ≈1.90kV respectively. The ions are reflected out of the reflectron ion mirror towards the MCP detector. The detector voltage is set at -2.10kV.

Signal intensity is optimized by timing the laser delay so that the ions created by the laser interact with the portion of the gas pulse having maximum cluster intensity and also by timing the pulse-generator to pulse the repeller plate at appropriate delay times so as to coincide with the section of the ion packet with the highest ion density and distribution. Delay generation is done using a BNC, model 555 delay/pulse generator. Data acquisition is done on a digital storage oscilloscope (Lecroy 9350A, 500 MHz), which collects and averages a thousand sweeps. The collected spectrum is then transferred to an interfaced computer where the data is processed.

The mass identification of the ions in the collected mass spectrum is done using equation 2.3,

$$t = \left(\frac{m}{2eV}\right)^{1/2}\left(L_1 + L_2 + 4d\right) \qquad (2.3)$$

where t is the time of flight of the ion, m is the mass if the ion, eV is the voltage applied to the repeller plate, L_1 and L_2 the length of the 1st and 2nd flight tubes respectively and d the distance the ion travels into the reflectron ion mirror. Since all the parameters are a constant during an experiment, for two ions with different masses, the equation becomes a ratio of their masses to their time of flight, as shown in equation 2.4,and so if the identity of one ion is known, the other can be determined.

$$\left(\frac{m_1}{t_1^2}\right)=\left(\frac{m_2}{t_2^2}\right) \qquad (2.4)$$

CHAPTER 3. Experimental and Theoretical Methods

3.1 Mobility Measurements

Ion Mobility is a gas phase ion chromatography technique used to measure the drift time of an ion in an inert buffer gas (usually He, Ar or N_2) under the influence of a weak uniform electric field. This measurement is used to determine the ion's most plausible structures by estimating the ion's average collision cross section (Ω). [98,99] The drift time of any ion through a non-reactive buffer gas under the influence of a weak electric field depends on the collisions experienced by the ion's cross section and the buffer gas. [24,79,100] This principle makes it possible to employ this technique to separate structural isomers of and ion. For our studies, helium was used as the buffer gas for mobility studies. Ion pulses (10-100µs width) are injected into the drift cell, with the ions having just enough kinetic energy to enable them overcome the barrier created by the escaping helium gas from the drift cell filled with helium. The ions also are decelerated by frictional forces, and are thermalized through collisions with buffer gas exiting the drift cell before they enter the drift cell entrance orifice.

Inside the drift cell, there are two opposing forces acting on the ion. The first is an accelerating force on the ion imposed by the weak electric field gradient of the drift cell which causes the ion to drift through the cell along the electric field axis. The second force influencing the behavior of the ion within the cell is a deceleration force, arising from the frictional force created through collisions between the ion and the atoms of the buffer gas. Under the right conditions, there will be a long enough drift time, and an appropriate uniform electric field, the forces acting on the ion reach an equilibrium, and the ion transverses the drift cell at a constant velocity, which is then measured as the drift cell velocity $\vec{v}_d$.

The mobility, K, of an ion is defined[101] as the drift velocity of an ion through a buffer gas, $\vec{v}_d$ ($\vec{v}_d = z/t_d$, t_d is the drift time in *s*) divided by the electric field across the drift area of $\vec{E}$ ($\vec{E} = V/z$, *V* is the drift voltage and *z*, the length of the cell (cm), as shown in equation 3.1

$$K = \frac{\vec{v}_d}{\vec{E}} \qquad (3.1)$$

Reduced mobility K_o, is obtained by normalizing the measured mobility K to standard temperature and pressure conditions as shown in equation 3.2, which makes it possible to compare motilities measured under different cell conditions.

$$K_0 = \frac{P}{760}\frac{273.15}{T}K \qquad (3.2)$$

where, *T* is the buffer gas temperature in Kelvin, and *P* is the buffer gas pressure in Torr.

Combining equations 3.1 and 3.2, and substituting $\vec{E}$ yields equation 3.3

$$t_d = \left(\frac{z^2.273.15}{T.760} \frac{1}{K_0} \right) \frac{P}{V} + t_0 \qquad (3.3)$$

with t_o the effective time the ion spent outside the drift cell before it reaches the detector. A plot of t_d against P/V yields a straight line, with the slope

$$slope = \left(\frac{z^2.273.15}{T.760} \frac{1}{K_0} \right) \qquad (3.4)$$

and t_o is the y-axis intercept. To measure the ion mobility of an ion, a mass selected ion pulse is injected into the drift cell, and the arrival time distribution (ATD) of the ion is measured over a range drift cell voltage at a fixed cell temperature and pressure. The drift time of the ion is determined as the highest point on the Gaussian-like distribution of the gated signal, which is obtained by fitting the ATD to a Gaussian equation or smoothing the ATD.

A correction to t_d is applied to account for the distortion of the center of the ion pulse by the drift cell exit orifice. This correction is given by equation 3.5

$$t_d = t_{obs} + 4\frac{D}{\mathrm{v}_d^2} \qquad (3.5)$$

where t_{obs} represents the observed time at peak maximum and D is the diffusion coefficient.[102] When a weak electric field is applied on the cell, the diffusion coefficient D can be related to the ion mobility K by the Einstein equation shown in

$$D = D_L = D_T = K\frac{k_B T}{ze} \qquad (3.6)$$

where D_L and D_T are the longitudinal and transverse diffusion coefficients respectively, K is the mobility, k_B is the Boltzmann constant and z is the number of charges and e is charge of and electron. In the measurement of ion mobility, an important parameter considered is the field intensity expressed as (*E/N*), with E being the electric field and N the number density of the buffer gas,[101] which in effect is a representation of the kinetic energy the ion gains from the applied drift field. Under the weak field conditions essential for ion mobility measurements, the (*E/N*) parameter should be such that (*E/N*) < 6Td (Td =Townsend, where $1\text{Td}=10^{-17}\ \text{V.cm}^2$). Under such conditions, the measured ion mobility is independent of the applied low electric field.[79]

Figure 12 shows the t_d versus P/V plot, where the solid line shows the least square linear fitting to the collect data points. Figure 13 also shows the ATD collected during the ion mobility measurement of $(C_6D_6.C_4H_4N_2)^+$ dimer ions at different drift cell voltages and same ion count duration. The spectrum reveals a distinct distribution spread as the drift cell voltage decreases. This is attributed to the increased drift/dwell time of the ion within the cell which occurs as longitudinal diffusion effect increases.

During ion mobility measurements three assumptions are made, and are discussed as follows[101,103,104]

1. that the measured mobility, *K*, is independent of the applied drift field
2. that the ion drift time, t_d, is represented by the maximum peak intensity of a Gaussian-type distribution

3. that the ions injected into the drift cell do not penetrate significantly before thermalization and loss of excess kinetic energy occur.

To check if the first assumption is satisfied, we calculate the effective temperature of the drifting ions, which is done using equation 3.7,[101,105]

$$T_{eff} = T_g + \frac{M_b v_d^2}{3k_B} \qquad (3.7)$$

where T_g is the buffer gas temperature, M_b, the buffer gas mass, υ_d , the drift voltage, and k_B is Boltzmann constant. Equation 3.7 considers the two sources of the ions temperature, firstly the thermal temperature from the buffer gas, and secondly the drift field effect temperature. An ion mobility done under moderately higher applied drift field conditions at 298K which yielded a K value of 18 cm^2 V^{-1} s^{-1} showed T_{eff} to be only 9 % higher than the thermodynamic temperature and even lower at low applied drift field (E/N <6). This calculated T_{eff} leads to a ≤ 2% change in the measured mobility, K_o.[106]

To satisfy the second assumption, the collected ADT is compared to the ATD predicted by the transport theory for a single ionic species under similar experimental conditions. Under ideal experimental conditions, these two ATDs should match.

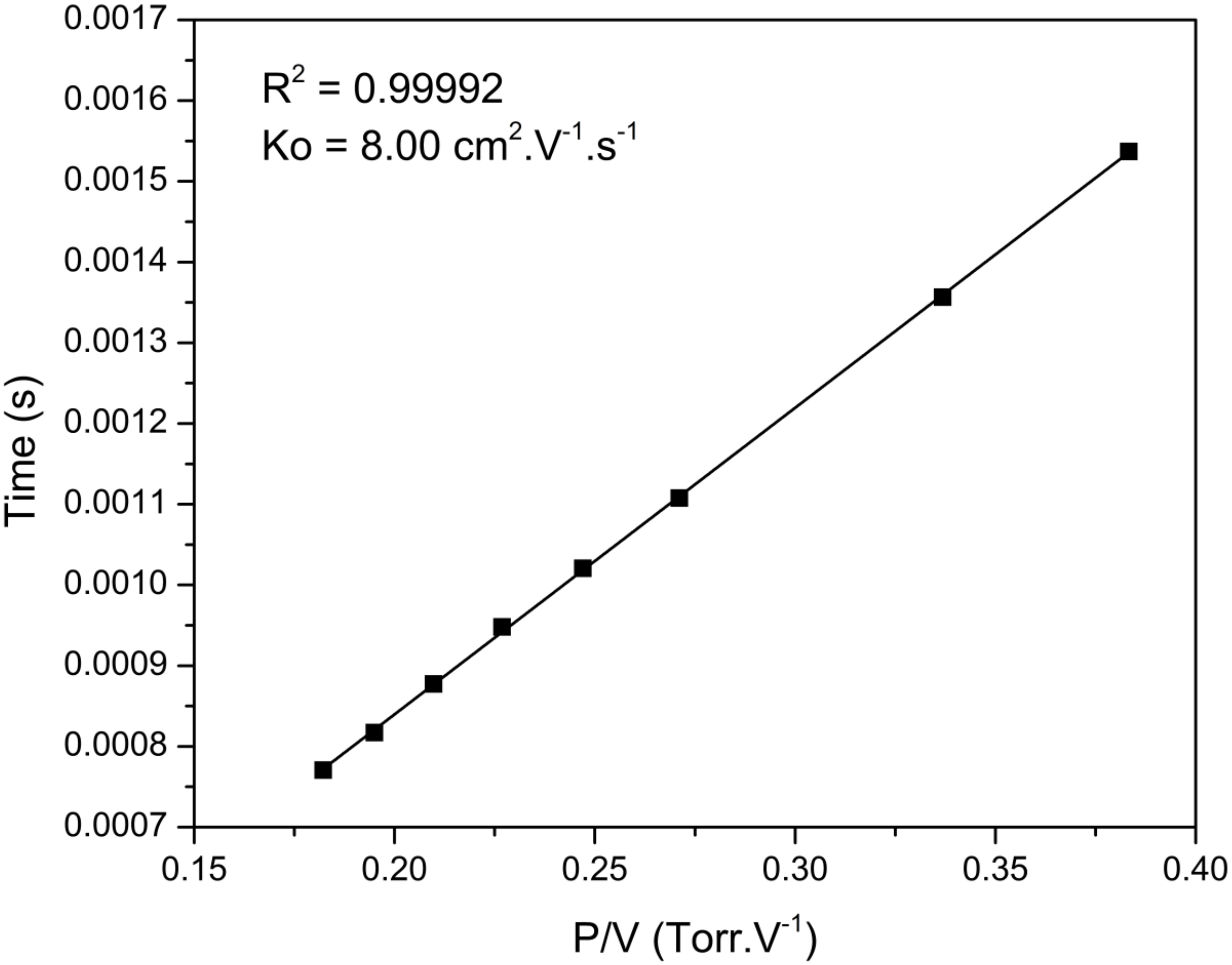

Figure 12: A Plot of the corrected arrival time distributions (ATDs) versus P/V collected after injecting 50 μs $(C_6D_6.C_4H_4N_2)^+$ ion pulse into drift cell filled with 4.5 Torr He at decreasing cell voltages of 2V steps from 29-15 V.

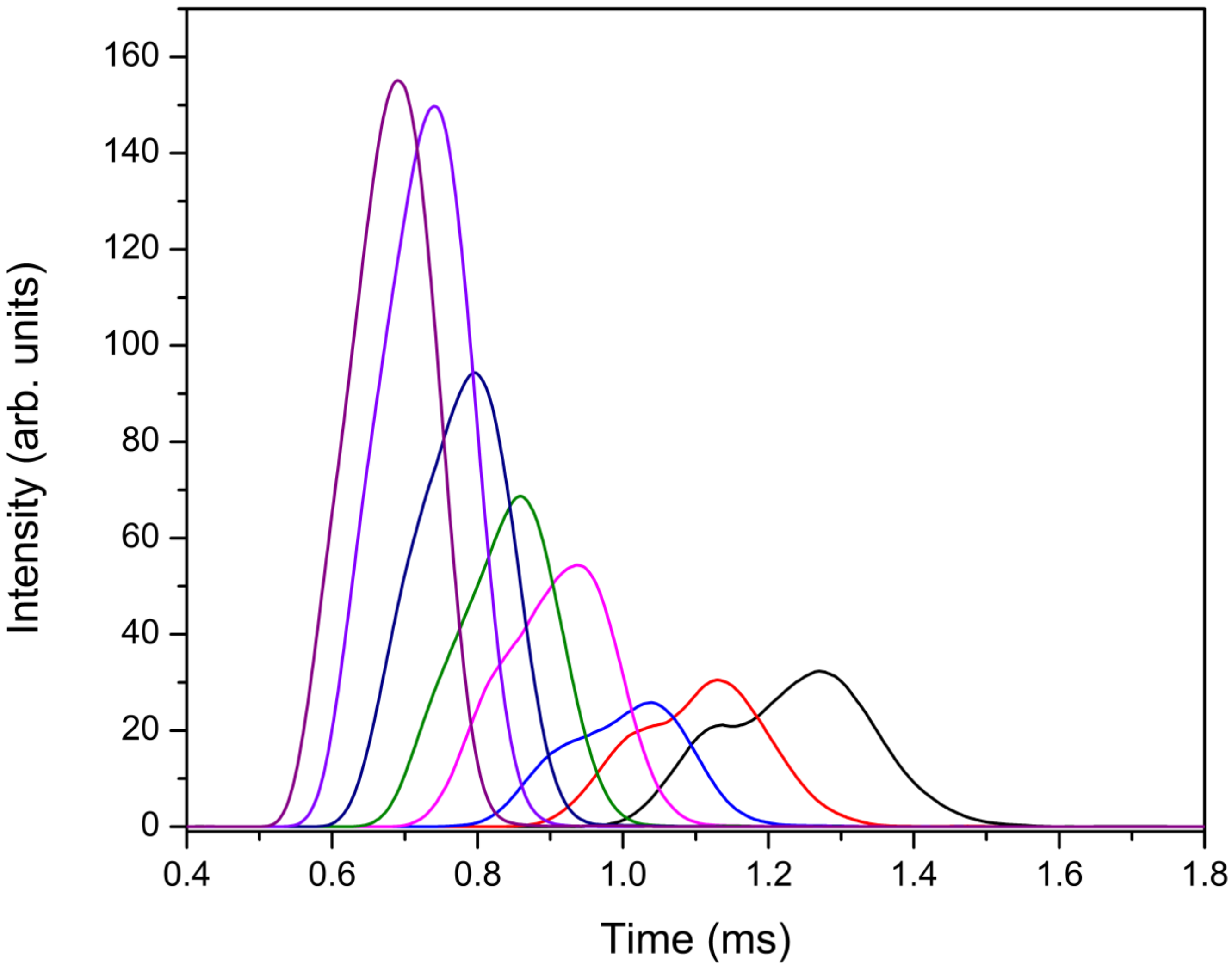

Figure 13: Arrival time distributions (ATDs) of injecting 50 μs $(C_6D_6.C_4H_4N_2)^+$ ion pulse into drift cell filled with 4.5 Torr He at decreasing cell voltages of 2V steps. The earlier ATD corresponds to a drift voltage of 29 V while the later ATD corresponds to a drift voltage of 15 V.

For a mono ionic species drifting through a cylindrical drift tube, the ion flux, φ(t), exiting the drift tube through an orifice of area a is determined using the equation 3.8,

$$\phi(t) = \frac{sae^{-\alpha t}}{4\sqrt{\pi D_L t}}\left(\upsilon_d + \frac{l}{t}\right)\left(1 - \exp\left(-\frac{r_o^2}{4D_T t}\right)\right)\exp\left(-\frac{(l-\upsilon_d t)^2}{4D_L t}\right) \quad (3.8)$$

where *s* and *r* are the surface density and radius of a thin disk of injected ions respectively. The surface density is used as a scaling factor and α is the reaction frequency, which is set equal to zero for the inert buffer gas.

To ensure that the third assumption is satisfied, the depth of penetration into the drift cell before thermalization occurs. The energy of an ion after n collisions (hard sphere) is calculated using the equations 3.9-10,[102]

$$E_f = E_i M^n \quad (3.9)$$

and

$$M = \frac{M_i^2 + M_b^2}{(M_i + M_b)^2} \quad (3.10)$$

where E_f and E_i are the final and initial energy (injection energy) respectively, *M* is the reduced mass as defined in equation 3.10, M_i is the mass of injected ion, and M_b, is the mass of the inert buffer gas. If the injection energy of 13eV and collision rate coefficient of 10^{-9} cm^{3}s^{-1} is used to calculate the final energy, E_f, the number of collisions n, required for thermalization(i.e. $E_f = k_B T$)

is determined to be approximately 24. The time required for the ions to reach thermalization through collisions can be determined using equation 3.11 which is given as

$$t = \frac{n}{N \cdot k} \tag{3.11}$$

With a drift cell pressure of 3.5 Torr helium, and cell temperature of 298K, $n \approx 24$ Collisions, $k = 10^{-9}$ cm^3 s^{-1}, N, the buffer gas number density $\approx 10^{17}$ n/cm^3, the time required for thermalization is found to be $\approx 0.2\ \mu s$.

With this time, we can now calculate the distance the ions can travel into the drift cell before thermalization occurs. This is done using the following equation 3.12

$$d = \int_0^t \upsilon_d + \upsilon_i M^{\frac{n \cdot k \cdot T}{2}} dt \tag{3.12}$$

where υ_d is the drift velocity, υ_i is the initial velocity, and M, the reduce mass according to equation 3.10 , and is determined to be < 2% of the drift cell length.

3.2 Structure Determination

The structure of an ion can be determined from ion mobility measurements, by relating the measured K_0 with the collision cross section integral $\Omega^{(1,1)}$ using the equation 3.13 [107]

$$K_o = \frac{3qe}{16N_o}\left(\frac{2\pi}{k_B T_{eff}}\right)^{\frac{1}{2}}\left(\frac{M_i + M_b}{M_i M_b}\right)^{\frac{1}{2}}\frac{1}{\Omega_{avg}^{(1,1)}} \tag{3.13}$$

where No is the number density of the buffer gas, qe the ion charge, T_{eff}, the effective temperature as defined in equation 3.7, k_B is Boltzmann constant, M_i and M_b are the masses of the ion and buffer gas respectively, and $\Omega_{avg}^{(1,1)}$ is the averaged collision cross section integral over all possible collision orientations. The superscript, (1,1), refers to the pair-wise collision assumption used in the collision cross sectional calculation.

This experimentally determined average collision cross section is then compared to a theoretically derived average collision cross section to determine the best possible structure of the ion. The theoretical average collision cross section is obtained using the Mobcal program, utilizing as its input the geometrical coordinates generated from ab-initio and Density Functional Theory calculations.[79,108] The Mobcal program calculates the theoretical average collision cross section using three methods, which differ mostly based on the interaction potential each methods employs for its computation. All the three methods simulate collisions between the injected ions and the buffer gas atoms.

The three interaction potentials are exact hard sphere, projection approximation and trajectory methods, and are discussed in detail below.

3.2.1 Exact hard sphere approximation

In this method, the collision interaction between the ion and the helium atom are both considered as hard spheres, and the hard sphere potential is used for the computation.[109] The collision cross section in this method is considered to be equal to the sum of the van der Waals radii of the two colliding species, and is given as

$$\Omega^{(1,1)} = \sigma_{HS} \qquad (3.14)$$

To achieve this, the ion is oriented in space randomly and projected into a rectangular plane, and then a circle of hard sphere radius is drawn around each atom of the ion in the plane, before random points are chosen inside this plane. A collision is said to have occurred if a chosen point is located within the sum of the atom hard sphere radius and He hard sphere radius. The process is repeated for randomly chosen points in the projection plane. After this a Monte Carlo function is used to calculate the average collision cross section for all different orientations in space using equation 3.15,

$$\Omega = \frac{\#\text{ of hits}}{\text{Total}\#\text{ of trials}} \times A_{\text{rectangle}} \qquad (3.15)$$

This method however ignores multiple scattering collisions, and also the long range interactions between the polyatomic ion and buffer gas atoms. This method yields temperature independent collision cross sections, since it does not consider the dependence of collisions on temperature conditions.

3.2.2 Projection Approximation

The projection approximation method is similar to the hard sphere method, but uses the 12, 6, 4-interaction potential instead of the hard sphere potential. It also factors in the long-range ion-induced dipole attractive interaction effects.[110] and also considers the temperature dependence of the interactions.

At low temperatures, higher collision cross section values were predicted due to the long range attractive interaction between the individual atoms of the molecule and the bath gas atoms. This model however reveals asymptotic behavior at large *R* values. The interaction potential used in the projection approximation model is given in equation 3.16 as

$$V(R) = \frac{n\varepsilon}{n(3+\gamma) - 12(1+\gamma)} \left[\frac{12}{n}(1+\gamma)\left(\frac{r}{R}\right)^{n} - 4\gamma\left(\frac{r}{R}\right)^{6} - 3(1-\gamma)\left(\frac{r}{R}\right)^{4} \right] \qquad (3.16)$$

where *n* is the exponent that describes the ion-neutral repulsion (usually set at 12 as it is commonly used for Lennard-Jones potentials), ε the depth of the potential well, *r* the position of the potential well, and γ is a ratio that defines the relative contributions of *R-6* and *R-4* terms.

R is the distance between a specific atom in the polyatomic ion and a helium atom. The value of R, where R is defined in equation 3.17, is obtained from a table of collision integrals of atom-atom collisions ($\Omega^{(1,1)}$(T)).

$$R_{coll.} = (\Omega(T)^{(1,1)} / \pi)^{\frac{1}{2}} \qquad (3.17)$$

The potential energy *V(r),* can represented as the sum of $V_{n,6}(R)$ and $V_4(R)$ terms as and are defined in equations 3.18-20 respectively;

$$V(r) = V_{n,6}(R) + V_4(R) \tag{3.18}$$

$$V_4(R) = -\frac{q^2\alpha}{2R^4} \tag{3.19}$$

$$V_{n,6}(R) = \varepsilon_{LJ}\left[\left(\frac{r_{LJ}}{R}\right)^{12} - 2\left(\frac{r_{LJ}}{R}\right)^{6}\right] \tag{3.20}$$

ε_{LJ} and r values are determined by best fitting experimental collision integrals and thus more accurately describing the system under study.

3.2.3 Trajectory calculation

The trajectory method makes use of a potential which comprises of the (12-6) Lennard-Jones and long-range (ion-induced dipole) potentials.[108] The collision cross section integral is estimated by averaging the momentum transfer cross section over the relative velocity between the ion and the neutral atom, and the momentum transfer cross section in turn, is determined by averaging a function of the scattering angle over the impact parameter. Although this method is computationally more expensive, it yields the most reasonable results when compared to the experimentally measured values among all three methods, especially when long range attractive interaction gets more significant and in multiple scattering cases, and thus is the most preferred.

This method gives the most reliable estimates among the three methods.

3.3 Kinetic Measurements

Chemical kinetics refers to the speed with which a chemical reaction proceeds,[111] and is also known as the rate of the reaction. Chemical kinetic studies can be used to study the dependence of the rate of a chemical reaction on concentration of reactants, temperature of the system, and nature of the reactants (i.e. surface area and morphology). Considering the following irreversible second-order charge transfer reaction in equation 3.21,

$$A^+ + B \rightarrow A + B^+ \qquad (3.21)$$

The rate of the reaction can be given as

$$rate = -\frac{d\left[A^+\right]}{dt} = k_2\left[A+\right]\left[B\right] \qquad (3.22)$$

where $-\frac{d\left[A^+\right]}{dt}$ is the rate at which A^+ disappears, k_2 the second-order rate constant, $[A^+]$ and [B] the concentrations of the reactants A and B respectively. A more useful expression of equation 3.22 is given as

$$-\ln\frac{\left[A^+\right]}{\left[A^+\right]_o} = k_2\left[B\right]t \qquad (3.23)$$

where $\left[A^+\right]_o$ is the initial concentration of the reactant A, and t is the reaction time. In the situation where the concentrations of the reactants is such that [B] >> $[A^+]$ (typically 10^{14} to 10^3 respectively) a reaction rate expressed according to equation 3.21 will now be a pseudo-first order reaction, where the pseudo-first order rate constant k_1 is determined by plotting

$-\ln\frac{[A^+]}{[A^+]_o}$ against the reaction time t. With the concentration of [B] known, the second order rate constant can be determined.

The kinetics of irreversible unimolecular dissociation reaction such as a thermally induced dissociation reaction (pyrolysis) of an ionic monomer, dimer, trimer, etc can also be studied under similar conditions as discussed for the bi-molecular reaction. Consider the irreversible unimolecular dissociation reaction

$$A^+ \rightarrow B^+ + C \qquad (3.24)$$

where A^+ is a molecular ion which dissociates into two products, B^+ and C. The reaction is considered a first-order reaction and the rate law is given as

$$rate = -\frac{d[A^+]}{dt} = k_1[A+] \qquad (3.25)$$

where $[A^+]$ is the concentration of the reactant A, $-\frac{d[A^+]}{dt}$ is the rate at which A^+ disappears, and k_1 the first-order rate constant. Equation 3.25 can be rewritten as

$$-\ln\frac{[A^+]_t}{[A^+]_o} = k_1 t \qquad (3.26)$$

where $[A^+]_t$ is the concentration of the reactant A at time t, and $[A^+]_o$ is the initial concentration of the reactant A, at t=0. The first-order rate constant can be determined by plotting $-\ln\frac{[A^+]_t}{[A^+]_o}$ versus t as shown in figure 14, where k is the slope. Experimentally, the initial concentration of the reactant A is determined at any time t, which is the residence time of the ions in the drift cell, by summing the intensities of the reactant and product ions.[98,112]

Since the measured arrival time of the ions is the total time the ions spend both inside and outside the cell, the dwell time, actual reaction time, can be determined by subtracting the time the ion spends outside the cell before reaching the detector t_o from the total time arrival time measured. The time the ions spend outside the cell is determined from mobility experiments of A^+, where the intercept of the plot of t_d vs. P/V as shown in figure 12 corresponds to t_0. The dependence of the rate constant on temperature can be used to calculate the activation energy for the dissociation reaction, E_a, and also the pre-exponential frequency factor A.

This can be achieved using the Arrhenius equation and shown in equation 3.27;

$$k = A\exp\left(-\frac{E_a}{RT}\right) \qquad (3.27)$$

where Ea is the activation energy of the dissociation reaction (in kcal/mol), R the molar gas constant, T the absolute temperature of the system, and A is the frequency factor. A more practical form of equation 3.27 is

$$\ln(k) = \ln A - \frac{E_a}{RT} \qquad (3.28)$$

A plot of ln(k) versus 1/T as shown in figure 15 yields a straight line with the slope of $-E_a/R$, and A, the pre-exponential frequency factor as the y-intercept.

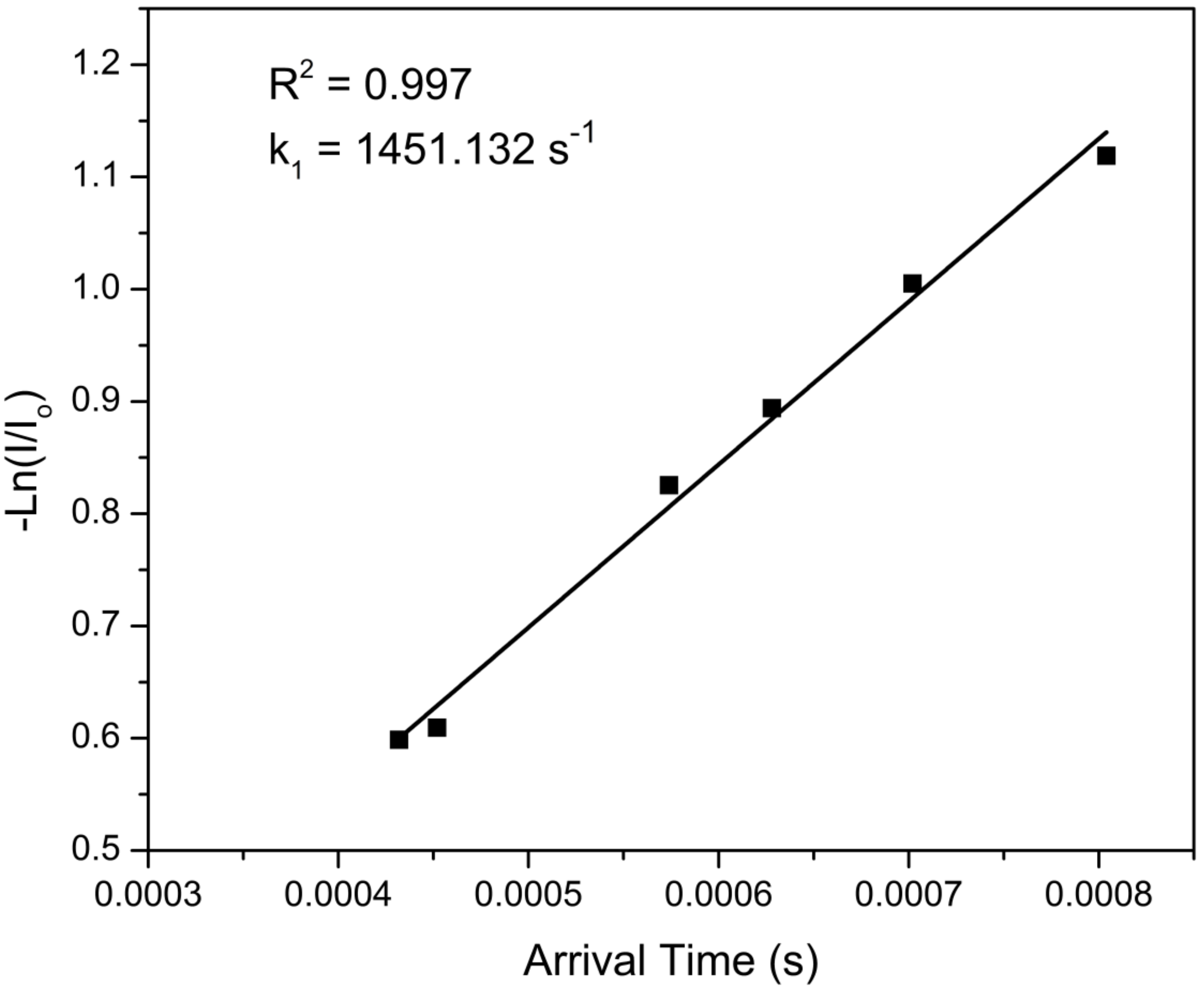

Figure 14: A Plot of –ln(I/I$_o$) versus arrival time for the thermal dissociation of $(C_6D_6.C_4H_4N_2)^+$ in the drift cell filled with 2.64 Torr He at 220 ^oC .The residence time of the ion within the drift cell was varied by decreasing cell voltages in of 3V.

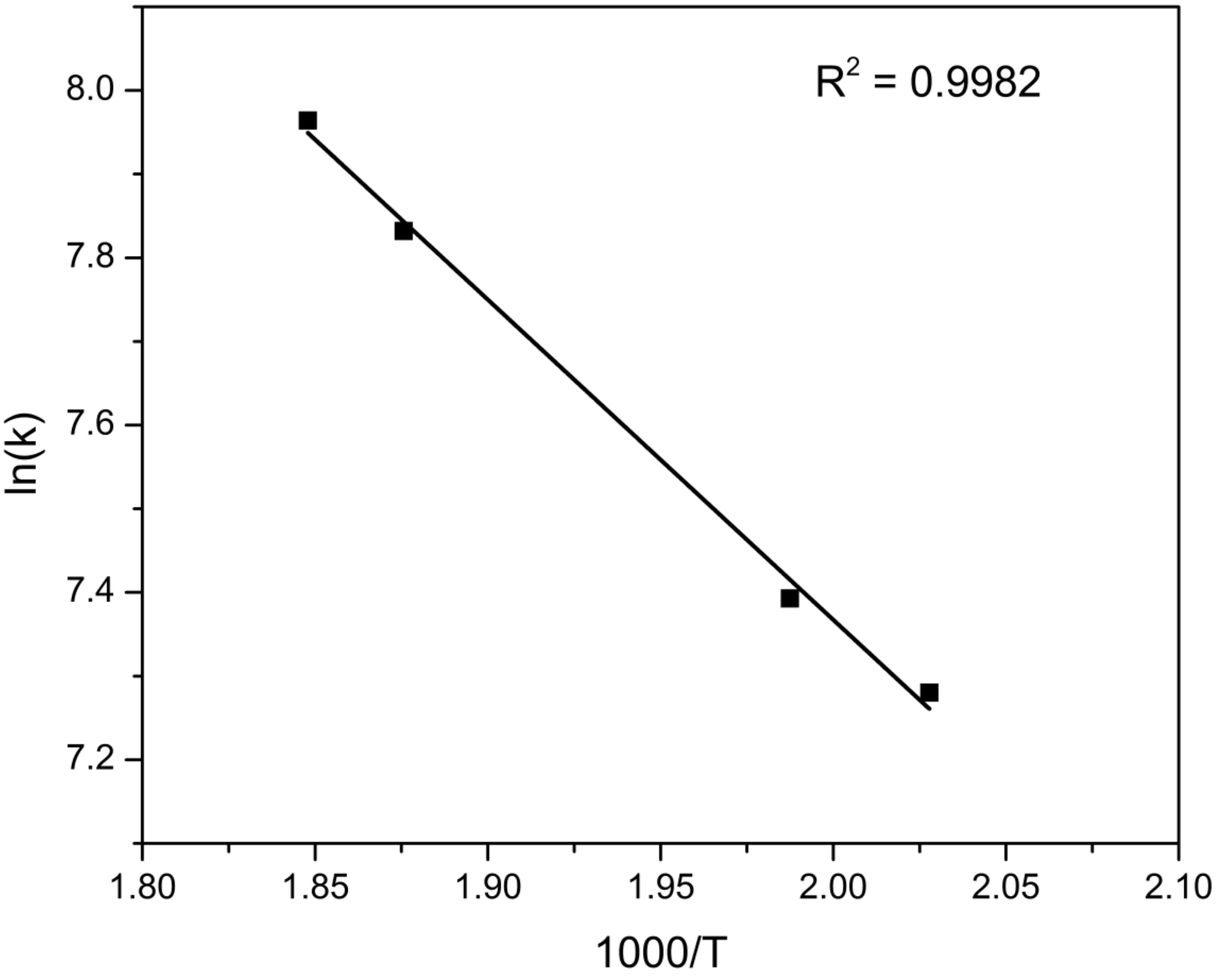

Figure 15: A Plot of ln(k) versus 1/T for the thermal dissociation of $(C_6D_6.C_4H_4N_2)^+$ in the drift cell filled with 2.64 Torr He at 220 ^oC .

3.4 Thermochemistry measurements

Experimental studies which yield important thermochemical information such as ΔH^o and ΔS^o for ion-molecule association reactions can be performed using our QMS-IM-QMS instrument.[26,60,113,114] Consider an association reaction of the form

$$\left[A^+ \cdot (B)_{n-1}\right] + B \rightarrow \left[A^+ \cdot (B)_n\right] \qquad (3.29)$$

where A^+ is the ionic reactant, and B is the neutral reactant gas/vapor, the ΔH^o and ΔS^o for the addition can be determined using the equation

$$\ln K_{eq} = -\frac{\Delta H^\circ}{RT} + \frac{\Delta S^\circ}{R} \qquad (3.30)$$

where R is the gas constant and K_{eq} is the equilibrium constant of the addition reaction. Keq can be calculated using the expression in equation 3.31 given as

$$K_{eq} = \frac{I\left[A^+.(B)_n\right] \times 760}{I\left[A^+.(B)_{n-1}\right] .P_B} \qquad (3.31)$$

where I is the integrated ion intensity derived from the normalized ADT collected for the reactant and product cluster ions, and P_B is the pressure of the reactant vapor in the drift cell. For our studies, in order to do a thermodynamic measurement for an association reaction such as the hypothetical association reaction given in equation 3.29, mass selected A^+ is injected into the drift cell, and the ATD of the injected A^+, and the association complexes, $A^+ \cdot (B)_{n-1}$ and $A^+ \cdot (B)_n$

formed inside the cell, are measured as a function of drift voltage corresponding to different residence (reaction) times. Equilibrium is achieved if the three conditions are satisfied, as discussed below. Firstly, a constant ratio of the integrated intensity of the of $A^+\cdot(B)_n/A^+\cdot(B)_{n-1}$ is observed over the residence time of the ions at constant pressure and temperature. Secondly, the ATDs of the reactant and product ions are identical indicating equal residence times, due to the fact that the product and reactant ions in equilibrium are coupled reactively faster than their movement through the cell. This phenomenon leads to the observation of the similar mean arrival time, t_d, for the injected and association complexes as shown in figure 16. Thirdly, the equilibrium constant K_{eq} should be independent of the neutral reactant concentration (pressure) in the reaction cell.

By combining the well know thermodynamic expressions given in equations 3.32 and 3.33,[115] a useful relationship can be derived, as stated in equation 3.34.

$$\Delta G^\circ = \Delta H^\circ - T\Delta S^\circ \tag{3.32}$$

$$\Delta G^\circ = -RT\ln K_{eq} \tag{3.33}$$

$$R\ln K_{eq} = \frac{-\Delta H^\circ}{T} + \Delta S^\circ \tag{3.34}$$

A plot of $\ln K_{eq}$ versus 1/T yields a straight line, with - ΔH^o as the slope, and ΔS^o as the y-intercept. Figure 17 shows a van’t Hoff plot for an association reaction from which - ΔH^o and ΔS^o are determined experimentally.

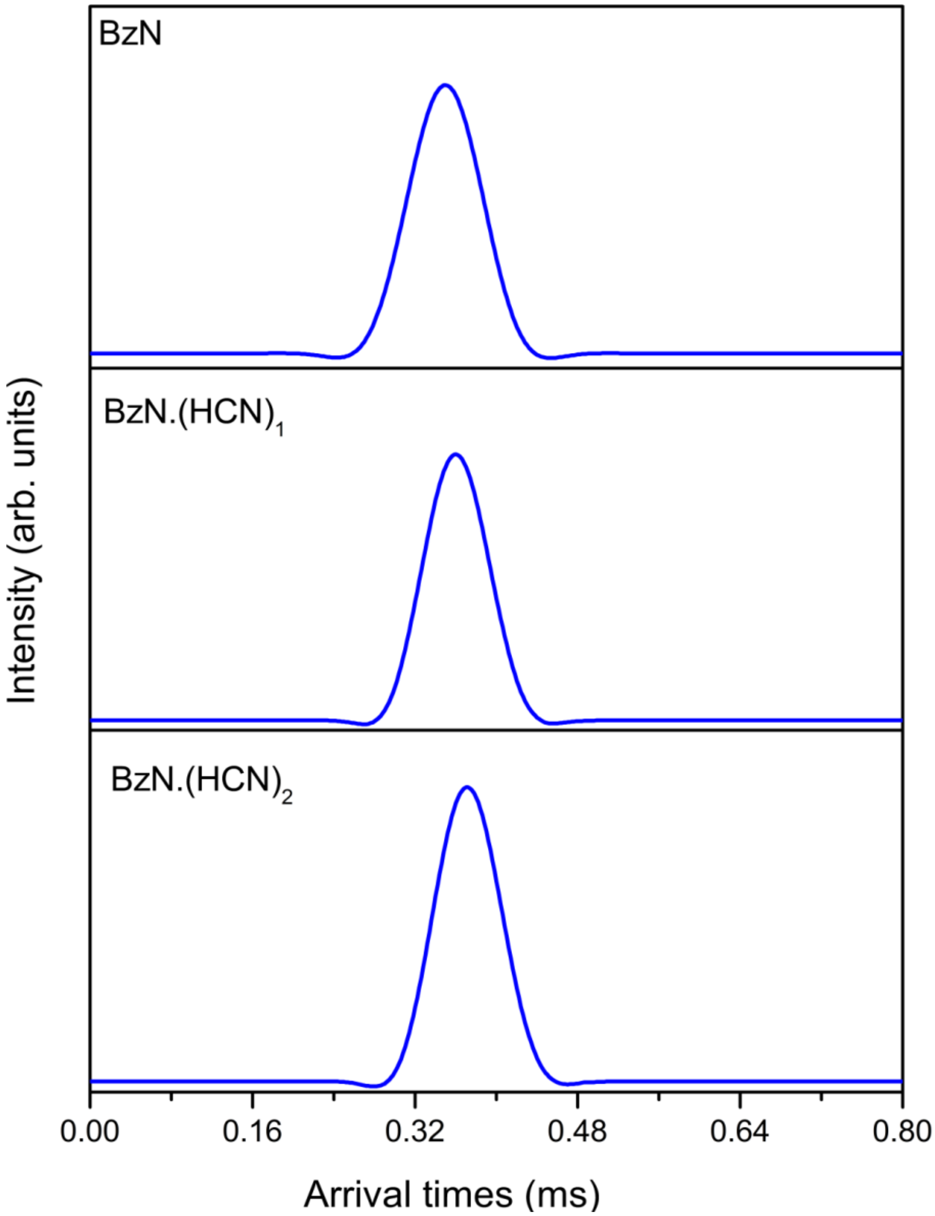

Figure 16: Arrival time matching/coupling for the $C_7H_5N^{\cdot+}(HCN)_{0\text{-}2}$ cluster ions which indicates that the addition reaction is in a true equilibrium.

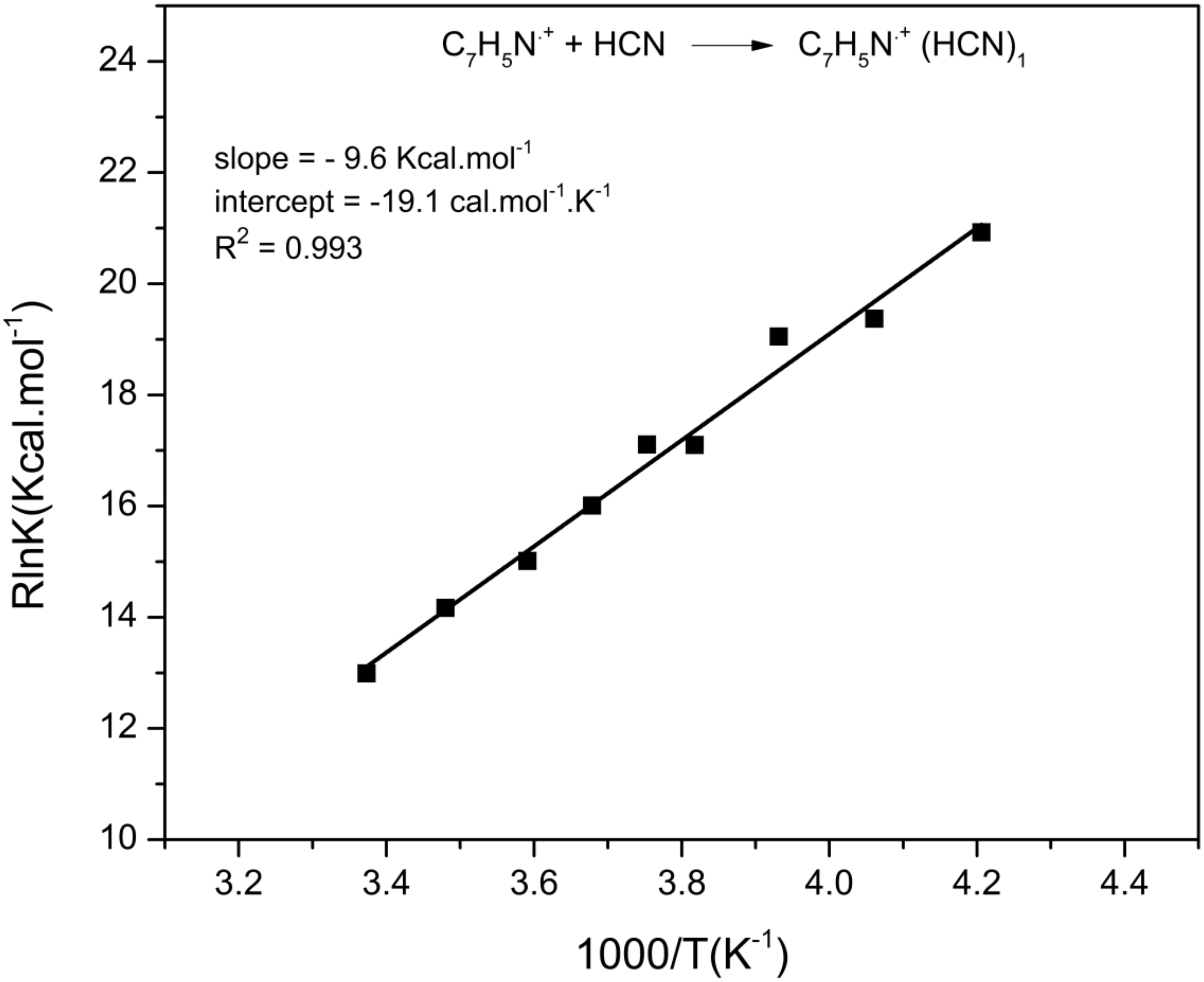

Figure 17: A van't Hoff plot of $R \ln K_{eq}$ versus 1/T for the first addition of an HCN molecule to $C_7H_5N^{\cdot+}$ radical cation. The slope and the intercept of the linear least square line gives the binding energy and entropy of the first addition reaction respectively.

3.5 Theoretical calculations

To corroborate our experimentally measured structural and thermochemical results, density functional theoretical (DFT) computations of the Gaussian 03 package[116] was used to calculate the lowest energy structures of the ionic cluster systems we studied. The calculations were done at the Becke three-parameter, Lee-Yang-Parr (B3LYP) exchange-correlation function level of theory. This level of theory has been proven to yield sufficiently accurate and reliable results in the literature.[26,60,113,114,117]

For hydrocarbon-only geometry optimizations and energy calculations were done using the 6-311++G(d, p) basis sets which includes d-type and p- type polarization functions on non-hydrogen and hydrogen atoms, respectively and also have all electrons are included.[118] For TM-acetylene complex ions studied in this work, optimizations for the 1st row TM ions were done using the 6-31+G(d, p) for the C and H, and the Watchers + f (14s 11p 6d 3f)/[8s 6p 4d 1f] basis set for the metal cations.[25] For the 2nd row TM ions, 6-311++G(d, p) basis set was used for C and H atoms and the Hay-Wadt (n+1) ECP VDZ basis set for metal cations.[119]

To ensure that true lowest energy structures (ground state) were attained, vibrational analysis were used to verify the absence of any imaginary frequencies, which indicate the presence of transition states. In order to be able to do zero point vibrational energy (ZPVE) corrections for all the energies calculated from the optimized geometries, frequency calculations were done at the same level of theory so as to be able to obtain the relative zero point vibrational energy (ZPVE) for correction. Thus all the calculated energies presented in this dissertation are corrected for ZPVE. The total spin $<s^2>$ value in our calculations was 0.75-0.77 which indicates the lack of spin contamination for open shell ions.[116,120]

CHAPTER 4. Reactions Between Aromatic Hydrocarbons and Heterocyclics. 2. The Effect of a Second Nitrogen on Nature of Covalent Bond Formation Between Benzene and Pyrimidine

4.1 Introduction

Formation of Polycyclic aromatic hydrocarbon (PAH) and Polycyclic aromatic nitrogen heterocyclics (PANH) formation are considered as an integral part of in the interstellar carbon cycle, are considered as an essential phase in the interstellar carbon cycle[8,9] , due to the fact that a large portion of all the detected molecules in the interstellar medium(ISM) contain at least one carbon.[8] PAHs based on their local environment in the ISM, are postulated to include the ions (a relevant fraction), heteroatoms (such as PANH) , and partially dehydrogenated forms, and several electronic states other than singlet and doublet (radical ion).[9,10]

PAHs and PANHs are also found many environments, some under ionizing conditions such as in radiation chemistry, flames, and as by-products of several incomplete combustion processes of organic matter. They have also been linked to health concerns including cancer[15-19], due to their ability to form PAH-DNA complexes,[20,21] making the study of their chemistry very important.[121]

Ion chemistry can be important in the formation and reactions of these compounds. [121]In these respects, we investigated mechanisms for the formation of aromatics and nitrogen heterocyclics through ionic association and polymerization reactions. A significant fraction of PAH and PAN molecules in interstellar clouds can be in ionized or protonated, and the ions can interact with neutrals, including PAH and PAN molecules to form various covalent and non-covalent adducts. However, little is known about this chemistry, especially about PAH/PAN ionic cross-reactions.[24] For this reason, we examined recently the prototype benzene/pyridine system. The (benzene/pyridine)$^{\bullet+}$ adduct (denoted as (Bz•Py)$^{\bullet+}$) can form various isomeric non-covalent hydrogen bonded and electrostatically forms.[24] The most stable isomer includes a covalent C – N bond, and has a dissociation energy that we measured experimentally as > 33 kcal/mol and obtained computationally as 38.1 kcal/mol. It is of interest whether similar C-N bond formation is general in other ionized PAH / PANS systems, which can include molecules with fused rings or with several N atoms in the rings.

Forming this covalent C-N bond involves the transfer of an H atom, from the benzene C atom that forms the C-N bond to a pyridine C atom, where it forms a tetrahedral carbon and disrupts the aromatic pyridine π system. Alternatively, the H atom may be transferred to another ring carbon in benzene, where it disrupts the aromatic π system of benzene. In comparison, in benzene/pyrimidine (i.e., 1,3-diazine) a second N is present in the pyrimidine ring, adding a lone-pair donor site that can accommodate the H atom displaced from the benzene carbon without disrupting any stable aromatic π systems. Compared with Benzene•Pyridine$^{\bullet+.}$ This should lower the energy of Benzene•Pyrimidine$^{\bullet+}$ and increase its stability and dissociation energy. We report here, an application of experimental ion mobility studies and computational DFT studies to investigate these systems.

4.2 Experimental Methods

The experiments reported here were done using the VCU mass-selected ion mobility spectrometer. Details of this instrument have been previously discussed in the experimental section, and only a brief description is presented here.

All the molecular ions benzene-d6 ($C_6D_6^{\bullet+}$- *m/z* 84), benzene ($C_6H_6^{\bullet+}$- *m/z* 78), pyrimidinium ($C_4H_4N_2^{\bullet+}$- *m/z* 80) and heterodimer ions (C_6D_6• $C_4H_4N_2^{\bullet+}$- *m/z* 164) and (C_6H_6• $C_4H_4N_2^{\bullet+}$- *m/z* 158) were generated by electron impact ionization (EI) of the respective neutral which is seeded in 3−5 bar of ultra-pure helium carrier gas to make > 1% sample vapor in He mixture . The heterodimer mixture is prepared by mixing the two neutral samples into a heated glass bubbler in a ratio based on their respective vapor pressures [The mixture is expanded through a 500 μm diameter pulsed nozzle (General Valve, Series 9), into the source vacuum chamber (10^{-8} mbar) in short pulses of 150−300 μs duration at 50−100 Hz repetition rates. The protonated pyrimidinium ion C_4 $H_4N_2H^+$ was obtained from mass selecting the protonated monomer arising from self-protonation reactions during the expansion and EI of pyrimidine vapor in He. The monomer or dimer ions of interest were then mass selected using the first quadrupole mass filter and injected through an ion gate (in 5-15 μs pulses) into a reaction drift cell (5cm) with a known set temperature containing pure helium, Benzene or Pyrimidine vapor in He, depending on the system under study. To maintain the pressure of helium or sample vapor in the drift cell within ±1 mTorr of set pressure, flow controllers (MKS # 1479A) were employed. The temperature of the drift cell can be controlled to within ±1K of set value, using four temperature controllers (Omega type CN3251 for heating, and Omega type CNi3233 for cooling).

Injection energies of 10−14 eV (laboratory coordinates) used in this study are just over the minimum energy limit required to introduce the ions into the drift cell so as to overcome the outward flow of He or sample vapor/He gas escaping through the entrance orifice of the drift cell.

Thermalization of the injected ions occurs by collisions with He or sample vapor/He after injection to the mobility cell. For example, at a given cell pressure of 0.8 Torr at 300 K, injected ions encounter over 10^4 collisions with neutral molecules and/ or He atoms at > 1 ms residence time inside the cell. Usually about 10 – 100 collisions are needed for thermalization, which therefore occurs after the ions traverse 1% of the mobility cell after injection.

Mass spectra of the reactant and product ions exiting the reaction cell were obtained using a detector coupled to the second quadrupole mass filter. Arrival time distributions (ATDs) of the various ions were measured by monitoring the signals corresponding to each ion as a function of time after injection into the drift cell. To vary the residence time (mean drift time) of the ions within the drift cell between 200 and 1500 μs after injection, the drift cell voltage was changed accordingly. Time-resolved studies can determine if product ions are formed due to high injection energy at the entrance to the cell, as the normalized intensities of these ions do not change with drift time, or products due to reactions in the cell whose normalized intensities increase with reaction times. Time resolved studies identify primary and secondary reaction products and allow measuring rate coefficients.

Pseudo first-order rate constants were calculated from $\ln I/\Sigma I = -kt$, where I is the integrated intensity of the reactant ATD peak, and ΣI is sum of the integrated intensities of the reactant and all product ion peaks including secondary products, obtained from the areas of their ATD peaks, and t is the mean drift time taken as the center of the ATD peak of the reactant ion.

The pseudo-first-order rate coefficients $k1$ were obtained from the slopes of the plots of $\ln I/\Sigma I$ vs t at variable times. The second-order rate constants $k2$ were then obtained from the equation $k2 = k1/[N]$, where N is the number density (molecules cm-3) of the neutral reactant vapor partial pressure in the drift cell. All the rate coefficients measured were reproduced at least two times, with estimated errors calculated due to the uncertainties in the measurements of the neutral reactant partial pressure, drift cell temperature, fluctuations in ion signal and background noise.

Collision induced dissociation (CID) and high energy reactions channel products upon the injection of the reactant ions into the drift cell were studied. The direct collisions of the high-energy ions with escaping sample vapor near the entry pinhole significantly increases with increasing mole fraction of these reactants in the seeded gas mixtures ion sourceThe collisional energy is varied by varying the injection energy from 10 to 40 eV, depending on the mass of the injected ion.

Equilibrium constants for the association of $C_4 H_4N_2H^+$ with $C_4 H_4N_2$ were calculated from the equation $K = [I(C_4 H_4N_2)_2 H^+ /I(C_4 H_4N_2H^+)P(C_4 H_4N_2)]$, where I is integrated peak intensity and $P(C_4 H_4N_2)$ is the partial pressure of pyrimidine (atm) in the drift cell. Establishment of equilibrium is confirmed by three tests. 1. A constant ratio of the integrated intensity of the of $C_4 H_4N_2H^+ /(C_4 H_4N_2)_2 H^+$ over the residence time of the ions; 2. The ATDs of the reactant and product overlap due to the fact that the product and reactant ions in equilibrium are coupled reactively faster than their movement through the cell; 3. The equilibrium constant K_{eq} is independent of the neutral reactant pressure in the cell.

Structural information was obtained by ion mobility measurements by injecting an ion pulse of 10-50 μs into the drift cell filled with Helium. The ATDs with 2 μs resolution were measured at different P/V values, where P is the He pressure (Torr) and V is the drift voltage (volts), by varying V while keeping P fixed. A mean arrival time versus P/V plot yields a straight line, and the reduced mobility for the ion is calculated from the slope of the equation t) $[(z^2 \times 273.15)/(T \times 760 \times K_0)](P/V) + t0$, where, t is the mean arrival time, z is the drift cell length, T (K) is the cell temperature, K_0 is the reduced mobility, and t_0 is the time that the ions spend outside the cell.[60,101,122] This experimentally determined average collision cross section is then compared to a theoretically derived average collision cross section to determine the best possible structure of the ion. The theoretical average collision cross section is obtained using the Mobcal program,[123] utilizing as its input the geometrical coordinates generated from ab-initio and Density Functional Theory calculations.[79,123]

4.3 Theoretical Methods

Density functional theoretical (DFT) computations of the Gaussian 03 package[116] was used to calculate the lowest energy structures of the all the ions in this study. The calculations were done at the Becke three-parameter, Lee-Yang-Parr (B3LYP) exchange-correlation function level of theory. This level of theory has been proven to yield sufficiently accurate and reliable results in the literature.[26,60,113,114,117]

All geometry optimizations and energy calculations were done using the fairly large 6-311++G(d, p) basis sets which includes d-type and p- type polarization functions on non-hydrogen and hydrogen atoms, respectively and also have all electrons are included.[118]

To ensure that true lowest energy structures (ground state) were attained, vibrational analysis at 298K was performed to verify the absence of any imaginary frequencies, which indicate the presence of transition states. All the calculated energies presented in this study were corrected for zero point vibrational energy (ZPVE).

4.4 Results and Discussion

4.4.1 Injection of the (Benzene•Pyrimidine)$^{\bullet+}$ Dimer Ion into Helium, and the Thermal Stability of the Dimer Ion

Scheme 1 shows all the possible reaction channels for the interaction of benzene radical cation with the neutral pyrimidine molecule, and vice versa. Some of these reactions are endothermic and cannot be observed under normal conditions. Scheme 1 includes the formation and potential reactions of the (Benzene·Pyrimidine)$^{\bullet+}$ (also denoted below as Bz•Pym$^{\bullet+}$) adduct. We did not observe an association/dissociation equilibrium that could yield the dissociation energy of this adduct. However, we can estimate the lower limits of the Bz•Pym$^{\bullet+}$ binding energy from the thermal stability of the adduct and from potential ligand exchange reactions. We performed several types of experiments for these purposes, including the injection of the dimer ion into He at various temperatures to test its thermal stability, and injection of $Bz^{\bullet+}$ into Pym/He or $Pym^{\bullet+}$ into Bz/He to check for ligand exchange reactions. In some of these reactions C_6D_6 was used for the Bz component.

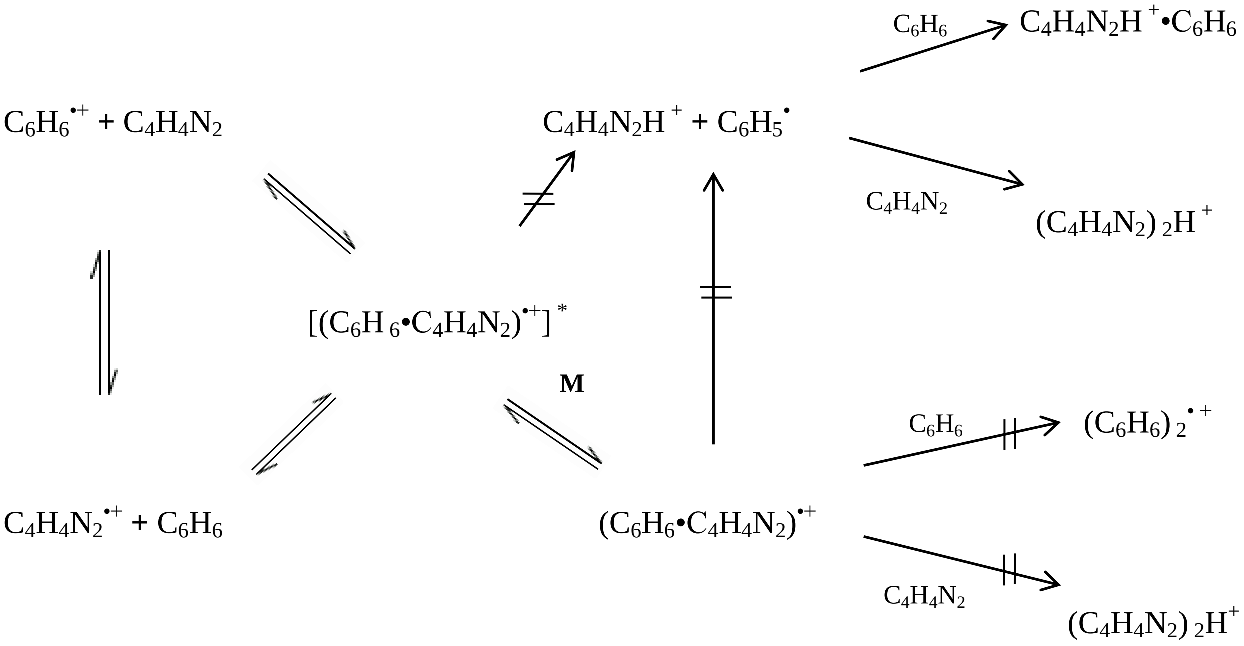

Scheme 1: Potential reactions in the ionized benzene/pyrimidine reaction system. Reactions that were not observed to occur are crossed out.

Figure 18 shows the mass spectra obtained by injecting the $Bz \bullet Pym^{\bullet+}$ heterodimer radical cation, formed by ionizing co-expanded benzene-d6 and pyrimidine vapors into helium in the drift cell. In Figure 18a the $Bz \bullet Py^{\bullet+}$ dimer ion injected to helium at 303 K showed no thermal

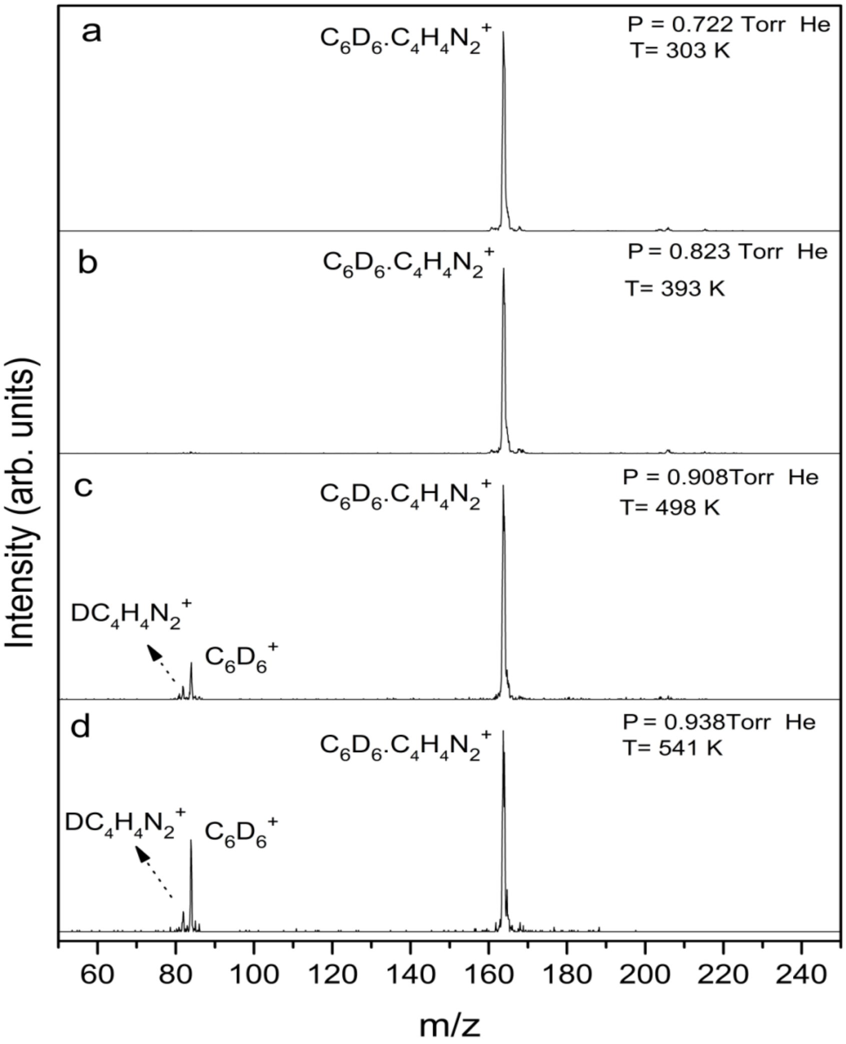

Figure 18: Mass spectra of $(C_6D_6 \bullet C_4H_4N_2)^{\bullet +}$ injected in He, at injection energy of 10.6eV (lab frame)

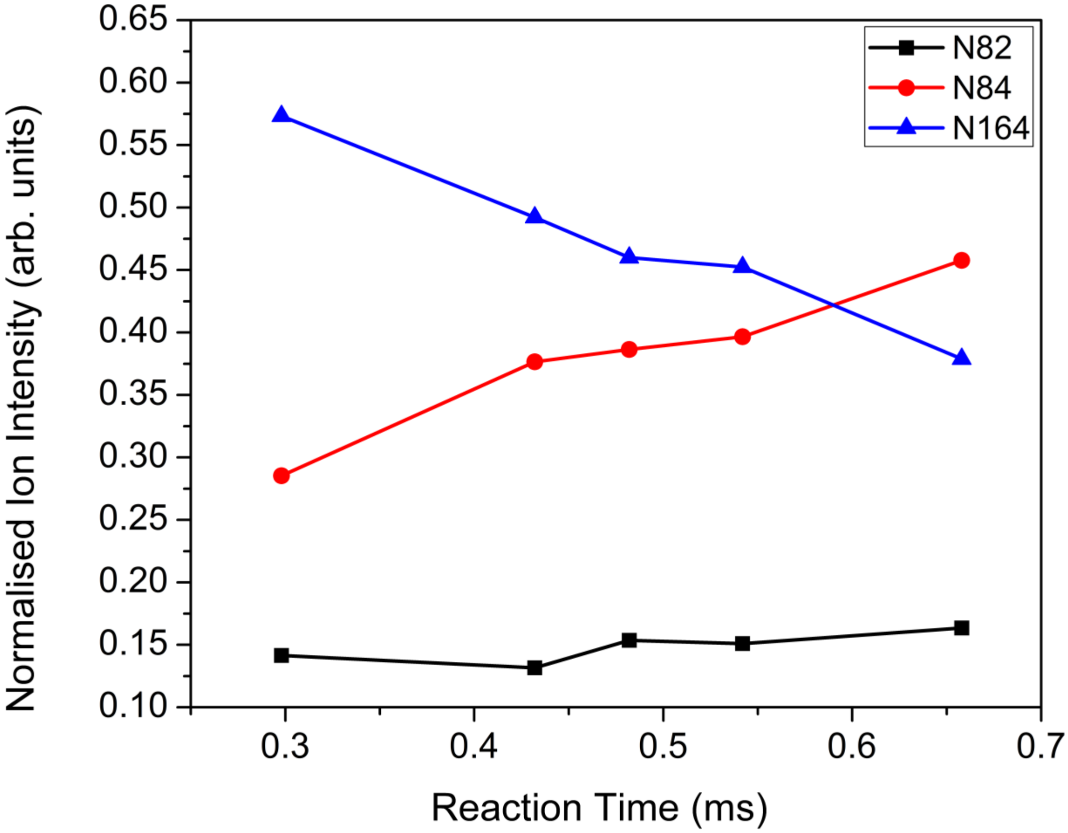

Figure 19: Normalized intensity for the dissociation of the $(C_6D_6{\bullet}C_4H_4N_2)^{\bullet+}$ dimer injected into 2.6 Torr of He at 508 K (injection energy 12.6 eV lab frame)

dissociation products, and similar stability was observed up to about 480 K. Figures 1b-d shows the unimolecular pyrolytic nature of the dimer ion, showing its thermal stability up to 541K. The fragmentation products observed are $C_6D_6^{\bullet+}$ and a small peak of $DC_4H_4N_2^+$.

Figure 19 shows the time resolved study of thermal dissociation of the Bz•Pym$^{\bullet+}$ dimer ion at 508K and 2.6 Torr helium, leading to $C_6D_6^{\bullet+}$. This product increases with reaction time, which

verifies thermal dissociation and allows calculating the unimolecular dissociation rate coefficient. The small $C_4H_4N_2D^{\bullet+}$ dissociation ion in Figure 19 apparently formed upon injection of the Bz•Pym$^{\bullet+}$, most probably through collisional dissociation with He, and it remains constant with reaction time. This fragment ion shows proton transfer from benzene-d6 molecule to pyrimidine. The 82m/z could be the $D^+C_4H_4N_2$ ion or the deuterated phenyl ion, $C_6D_5^+$, both arising from the fragmentation of the dimer ion. To rule out the formation of a phenyl ion and a hydrogenated pyrimidine radical, C_6H_6 was used to form $(C_6H_6.C_4H_4N_2)^{\bullet+}$, and the fragmentation pattern was observed. No fragment corresponding to $C_6H_5^+$ at 77m/z was observed, confirming that the 82m/z ion is $C_4H_4N_2D^+$ ion, thus confirming the transfer of a hydrogen from the benzene ring to the pyrimidine ring.

4.4.2 Thermal Stability and Dissociation Kinetics of the (Benzene•Pyrimidine)$^{\bullet+}$ Ion

An excited complex ion can dissociate for two reasons, the first reason is when there is too much energy within the complex, and it falls apart due to excess inherent energy. The second reason, provided the first reason is eliminated is because enough energy is supplied to the molecule, and this energy if focused in a single bond, could lead to the breaking of the bond. The first cause of dissociation can be eliminated through efficient thermalization using third body collisions, as shown in scheme1. If this is achieved, an estimate of the bond dissociation energy

(BDE) or activation energy (Ea) could be calculated by measuring the rate constant of dissociation, which is then used to determine the activation energy. Due to this mechanism, classical unimolecular thermal dissociation exhibits low-pressure limiting kinetics where collisional activation is rate-limiting and k_{dissoc} is proportional to third-body pressure, and high-pressure limiting kinetics where k_{dissoc} is limited by the dissociation rate of a thermally equilibrated population and k_{dissoc} is independent of third-body pressure, and an intermediate fall-off region.[124,125] Arrhenius activation energies from high-pressure limiting k_{dissoc} yield the energy barriers to dissociation. In the absence of reverse energy barriers, E_a can be equated with the dissociation energy.

Applying these kinetics to the Bz•Pym$^{•+}$ adduct, Figure 20 shows the pressure dependence of k_{dissoc} at 508 K, obtained from plots similar to Figure 19, as a function of the third body He pressure. After a steep rise below 1.6 Torr, k_{dissoc} becomes nearly independent of P(He) at higher pressures.

A unimolecular dissociation rate constant of 1900 ± 500 s^{-1} was measured (at 508K and 2.6 Torr He,) and the activation energy estimated from this result by assuming a usual pre-exponential factor of log A = 15, and the Arrhenius relation $k_{dissoc} = A \exp(-E_a/RT)$ then yields E_a of 28.0±1.0 kcal mol^{-1}. The activation energy was also obtained from an Arrhenius plot at a constant helium pressure of 1.6 Torr. Figure 21shows plots of –ln $[I(C_6D_6•C_4H_4N_2)^{•+}/(I(C_6D_6•C_4H_4N_2)^{•+} + I(C_6D_6^{•+}))]$ as a function of reaction time, and the slope of each curve gives the unimolecular rate constant k_{dissoc} for the dissociation reaction at each temperature respectively.

A plot of the rate constants against the inverse temperature (1/T) at which the k_{dissoc} was measured as shown in Figure 22, gives a straight line with a slope of Ea/R, and the intercept as

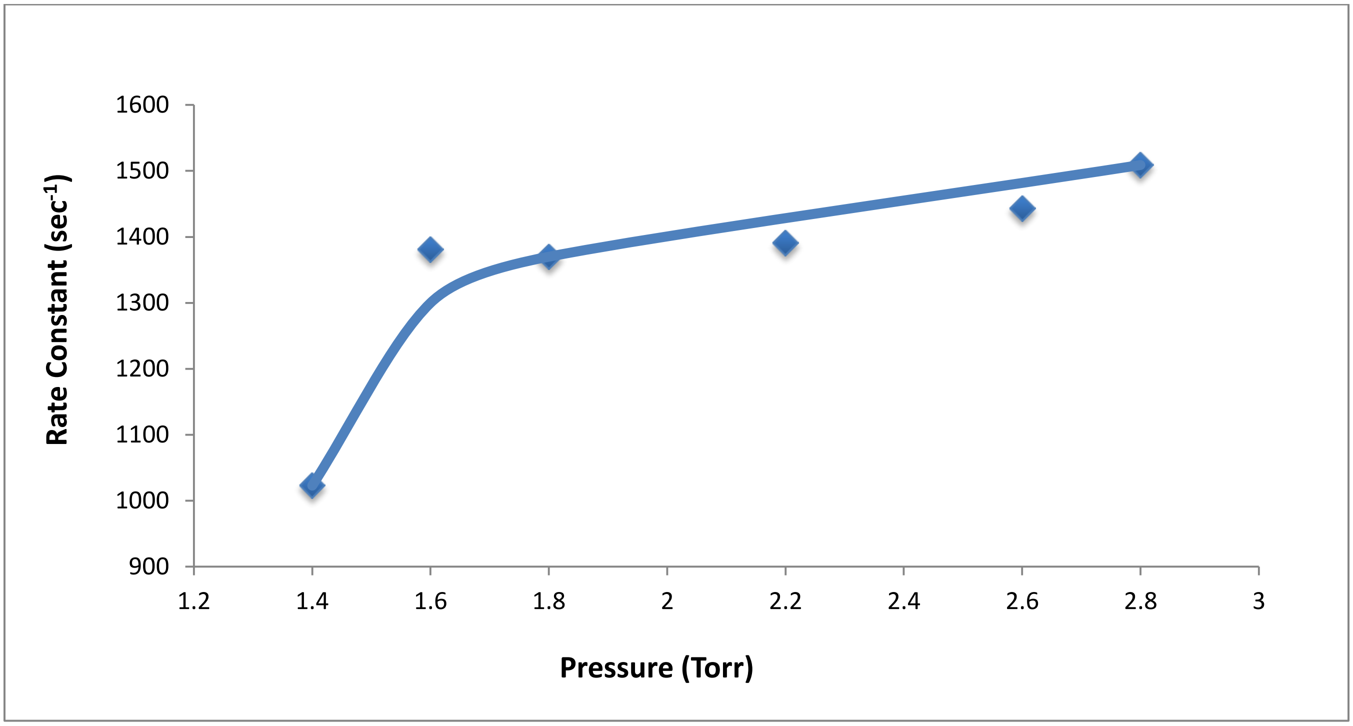

Figure 20: plot of dissociation rate constant versus Helium pressure for the Dissociation of $(C_6H_6 \bullet C_4H_4N_2)^{\bullet +}$ at 508K

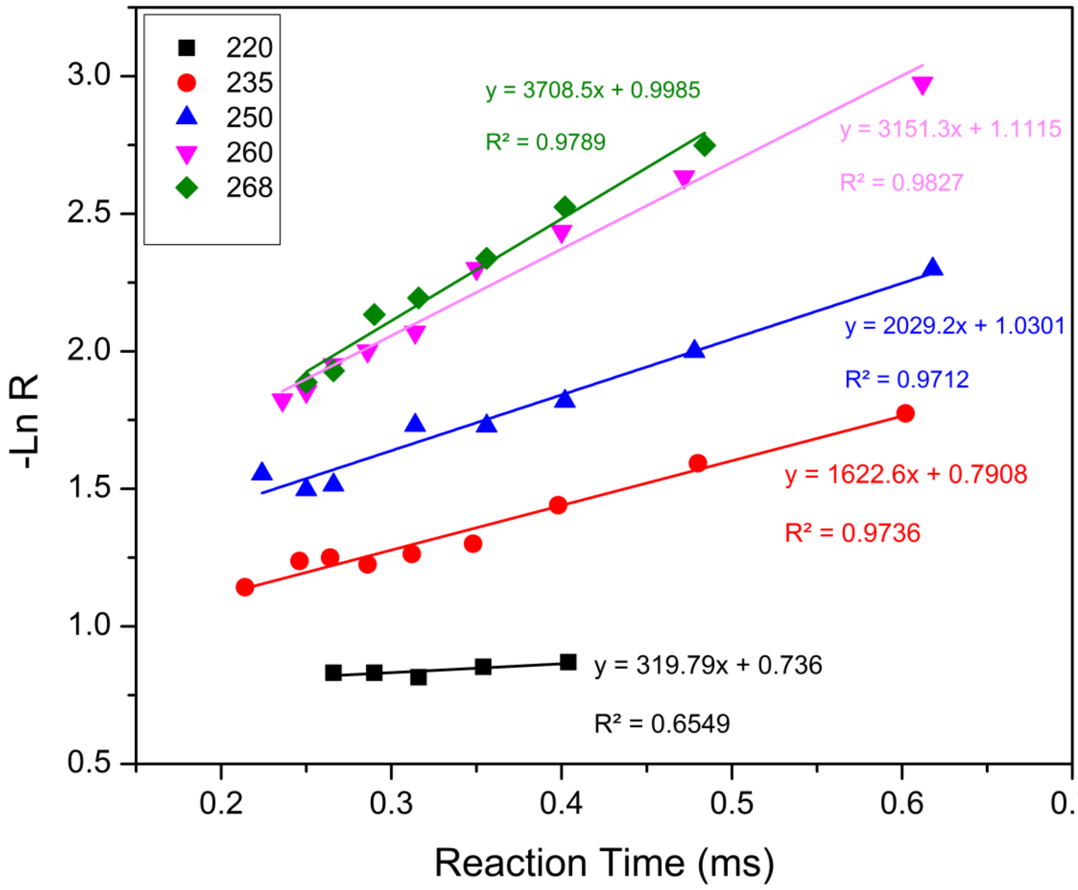

Figure 21: Plot of negative log of ion intensity ratio vs reaction time for the Dissociation of $(C_6H_6{\bullet}C_4H_4N_2)^{\bullet+}$ at different drift cell temperatures using 12.6eV injection energy at 1.6 Torr Helium

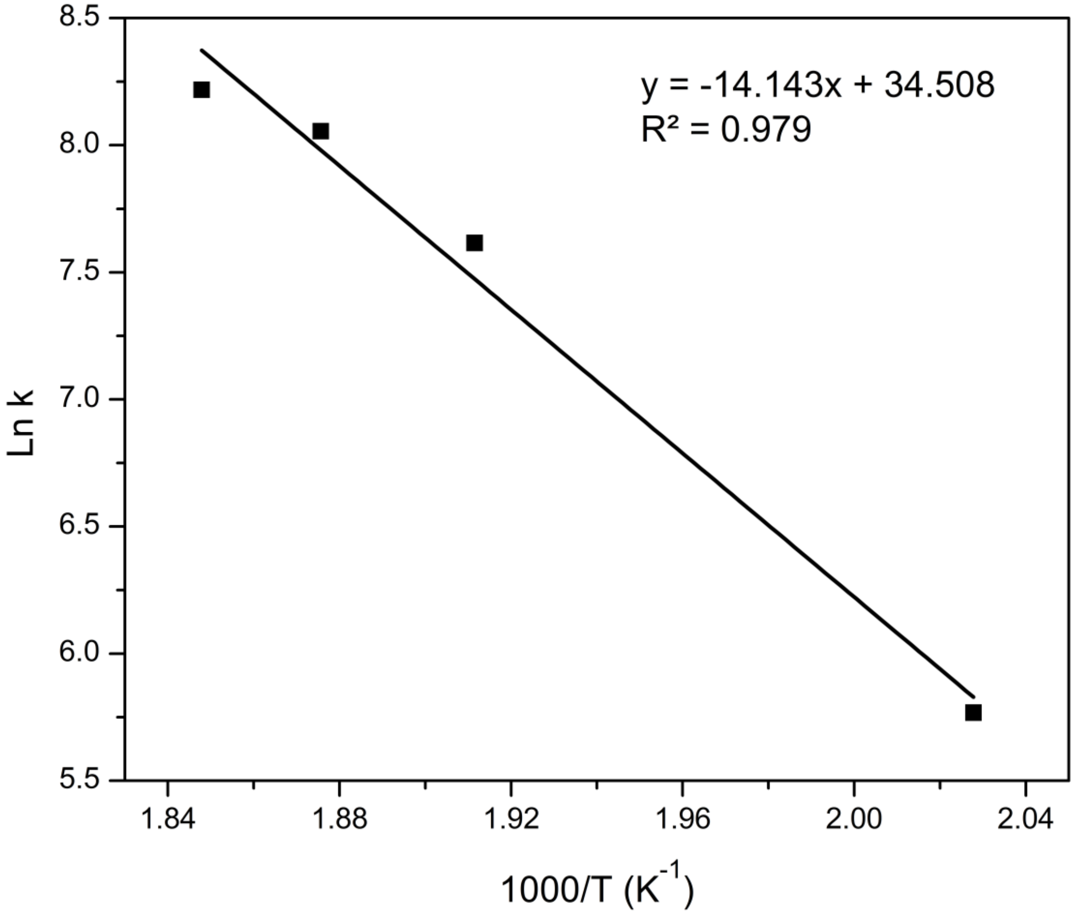

Figure 22: Plot of log of the dissociation rate constant (Ln k) vs 1/ Temperature for the dissociation of $(C_6D_6.C_4H_4N_2)^{\bullet+}$at different drift cell temperatures. The slope gives Ea/R, and the intercept is the log of the Arrhenius factor

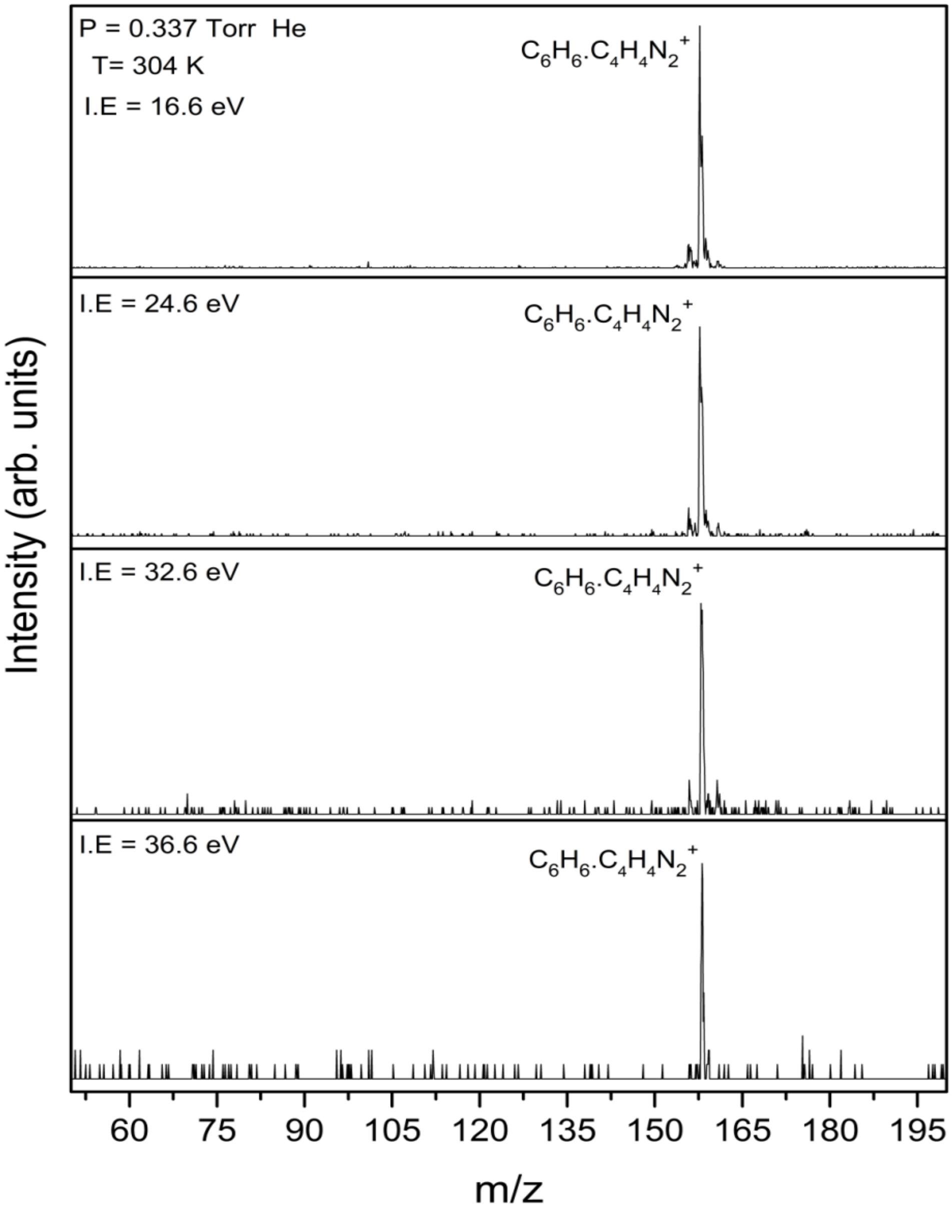

Figure 23: Stability of $(C_6H_6{\bullet}C_4H_4N_2)^{\bullet+}$ against collisional dissociation upon injection into the mobility cell. Mass spectra show no fragmentation at the injection energies indicated (lab frame)

the log of the Arrhenius factor. From this measurement, an Ea of 28.0±1.0 kcal mol^{-1} was measured. In the absence of a reverse reaction, both measurements of Ea being 28 $kcalmol^{-1}$ could indicate this value to be the dissociation energy. If a barrier exists however, the measured Ea will be the upper limit of the dissociation energy of the injected $(C_6D_6{\bullet}C_4H_4N_2)^{\bullet +}$ dimer to $C_6D_6^{\bullet +}$ + $C_4H_4N_2$ monomers.

4.4.3 Collision Induced Dissociation of $(C_6H_6.C_4H_4N_2)^{\bullet +}$

We also tested the stability of the $Bz{\bullet}Py^{\bullet +}$ dimer against collisional dissociation, by injecting the adduct ion into He at 304 K at P(He) = 0.337 Torr at injection energies of 16.6, 24.6, 32.6 and 36.6 eV (lab frame) shown in Figure 23. No dissociation products were observed, although the activated adduct ion could fragment to yield the reactants $C_6H_6^{\bullet +}$ and $C_4H_4N_2$ or $C_4H_4N_2^{\bullet +}$ and C_6H_6 or to fragments of a covalent adduct. In comparison, in a similar experiment with the benzene/pyridine$^{\bullet +}$ we did observe fragmentation to $C_5H_5NH^+$ as the lowest energy fragment and also fragmentation to yield $C_6H_6^{\bullet +}$ increasingly at higher energies. The absence of collisional dissociation of the present benzene/pyrimidine$^{\bullet +}$ suggests that it has a higher dissociation energy than benzene/pyridine$^{\bullet +}$, consistent with the computational results below.

4.4.4 Irreversible Association of Benzene$^{\bullet +}$ with Pyrimidine and an Estimated Binding Energy of the Bz•Pym$^{\bullet +}$ Adduct

The mass spectra displayed in Figure 24 were obtained by injecting $C_6D_6^{\bullet +}$ into pyrimidine vapor in helium buffer gas in the drift cell. The spectrum in Figure 6a shows $C_6D_6^{\bullet +}$ injected into the drift cell containing helium only at 302 K. On adding pyrimidine vapor at 302K we observe the formation of the radical heterodimer cation $(C_6D_6{\bullet}C_4H_4N_2)^{\bullet +}$ as shown in Figure 24b. We also observe a small m/z 161 peak corresponding to $(C_4H_4N_2)_2H^+$ that may be formed

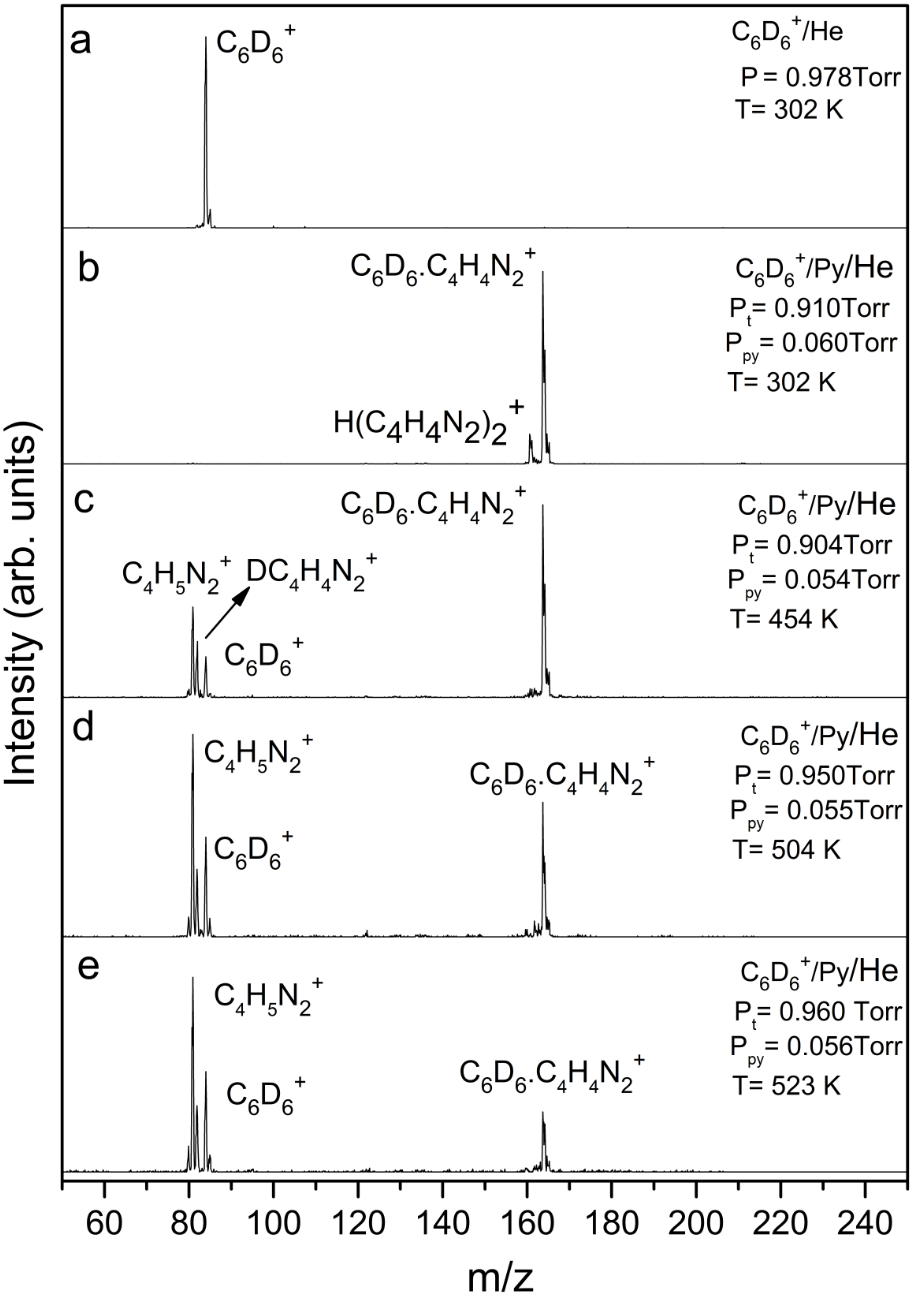

Figure 24: Mass spectra of $(C_6D_6)^{\bullet+}$ injected at 12.6 eV (lab frame) into $C_4H_4N_2$/He, in 2.6Torr of He at drift cell temperatures as indicated.

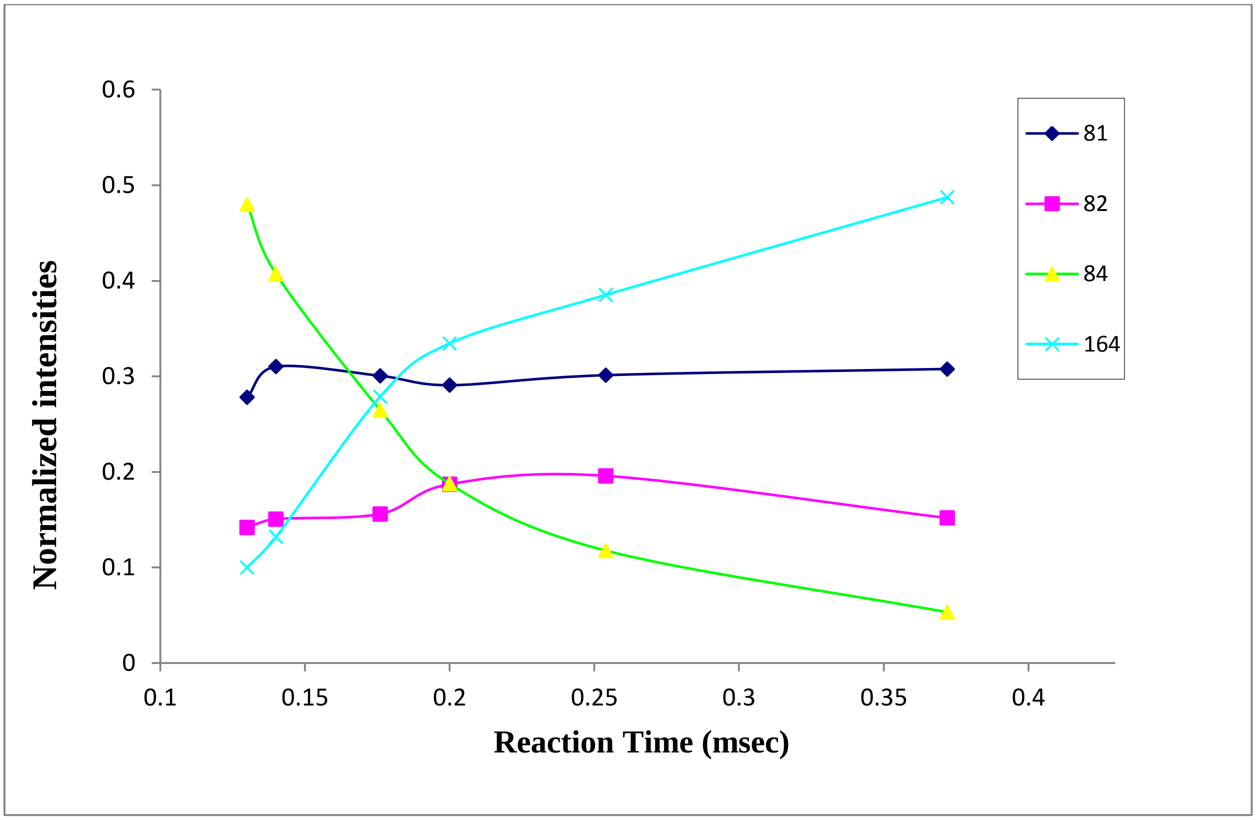

Figure 25: Time resolved mass scan of the association of $(C_6D_6)^{\bullet+}$ (m/z 84) with pyrimidine to form the $(C_6D_6{\bullet}C_4H_4N_2)^{\bullet+}$ dimer (m/z 164), following the injection of $(C_6D_6)^{\bullet+}$ (m/z 84) into Pyrimidine/Helium at 504K. Pyrimidine pressure is 0.055 Torr in 0.9 Torr Helium, injection energy 12.6 eV, lab frame. Note that m/z 81 ($C_4H_4N_2H^+$) and m/z 82 ($C_4H_4N_2D^+$) are independent of reaction time, indicating that they are formed by high energy processes at injection.

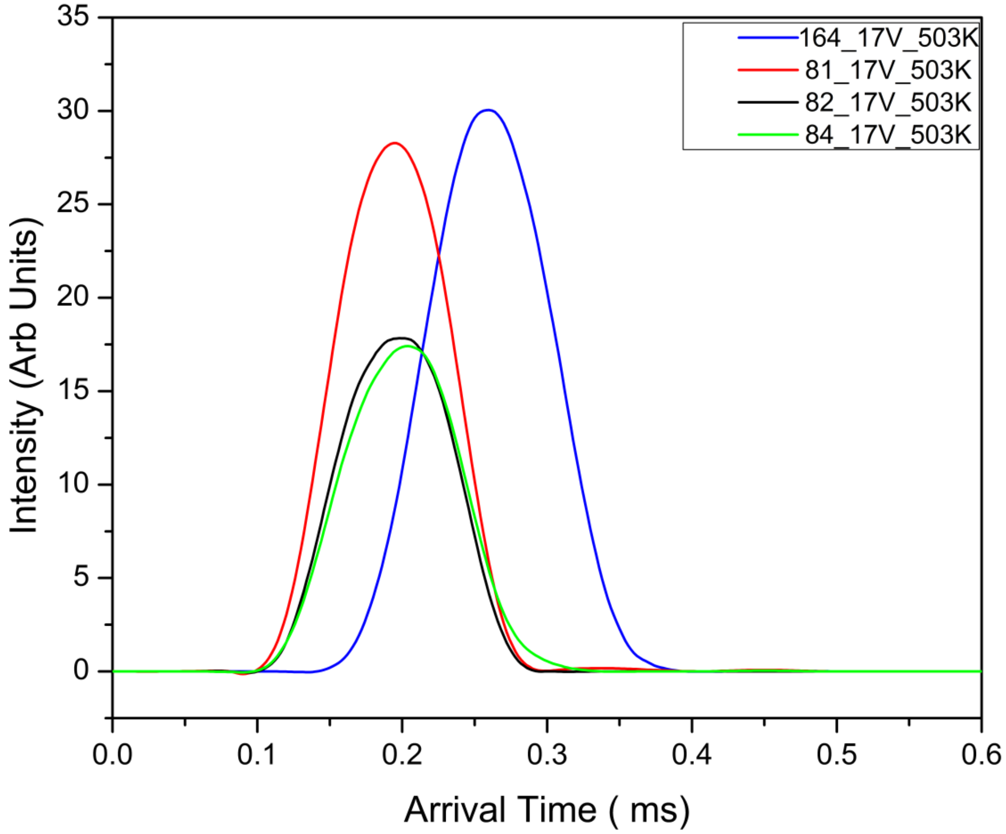

Figure 26:. Arrival time distribution (ATD) collected for the association product C6D6.C4H4N2 dimer obtained from $C_6D_6^{\bullet +}$ into 0.055Torr of $C_4H_4N_2$ at 503K in 0.9Torr Helium.

by charge transfer from $Bz^{\bullet +}$ to Pym followed by self-protonation and dimer formation. We do not observe $(C_4H_4N_2)_2D^+$ that would indicate intra-cluster proton transfer to pyrimidine in $(C_6D_6{\bullet}C_4H_4N_2)^{\bullet +}$ followed by dimer formation. However, at high drift cell temperature (Figure 24c), we observe dissociation products of the dimers into $C_4H_4N_2H^+$ (that may result from dissociation to $C_4H_4N_2H^+$ followed by self-protonation), and $C_4H_4N_2D^+$ and $C_6D_6^{\bullet +}$ that could form by high-energy processes upon injection or produced in the cell by thermal dissociation.

The time-resolved spectrum in Figure 25 shows that $C_4H_4N_2H^+$ and $C_4H_4N_2D^+$ are in fact high-energy products formed at injection, and the only reaction in the cell is the association of the injected $C_6D_6^{\bullet +}$ with pyrimidine to form $(C_6D_6{\bullet}C_4H_4N_2)^{\bullet +}$. At 454 K the injected $C_6D_6^{\bullet +}$ reacted out completely, while at 504 K in Figure 24 it appears to appears to react out more slowly but not completely in 0.4 msec. Arrival time distributions under the conditions of Figure 24 also showed that there was no equilibrium between $C_6D_6^{\bullet +}$ and $(C_6D_6{\bullet}C_4H_4N_2)^{\bullet +}$ as their ATDs did not overlap as shown in Figure 26.

Therefore $(C_6D_6{\bullet}C_4H_4N_2)^{\bullet +}$ is formed irreversibly by the reaction of $C_6D_6^{\bullet +}$ with $C_4H_4N_2$ under our conditions. Note that m/z 82 ($C_4H_4N_2D^+$) does not increase with time in Figure 25, which shows that there is no D^+ transfer followed by dissociation in the dimer ion. This indicates that there is no D^+ transfer in the dimer, or that D^+ transfer in the dimer leads to a stable covalent structure (see below) that does not dissociate thermally.

4.4.5 Estimated Bond Dissociation Energy of $Bz{\bullet}Pym^{\bullet +}$ from the Non-Occurrence of Ligand Exchange Reactions

Another approach to estimating the binding energy in $(C_6D_6{\bullet}C_4H_4N_2)^{\bullet +}$ is to test for ligand exchange reactions. Such reactions occur efficiently in loose non-covalent cluster ions if the reaction is exothermic. As shown in Figure 24b, at 302K we do not observe the formation of $(C_4H_4N_2)_2D^+$ that would be formed by reaction (1).

$$(C_6D_6{\bullet}C_4H_4N_2)^{\bullet+} + C_4H_4N_2 \longrightarrow (C_4H_4N_2)_2D^+ + C_6D_5^{\bullet} \qquad (4.1)$$

The thermodynamics of reaction (1) is a sum of individual steps in a thermochemical cycle of equations (2) – (4).

$$(C_6D_6{\bullet}C_4H_4N_2)^{\bullet+} \rightarrow C_6D_6^{\bullet+} + C_4H_4N_2 \qquad (4.2)$$

$$C_6D_6^{\bullet+} + C_4H_4N_2 \rightarrow C_4H_4N_2D^+ + C_6D_5^{\bullet} \qquad (4.3)$$

$$C_4H_4N_2D^+ + C_4H_4N_2 \rightarrow (C_4H_4N_2)_2D^+ \qquad (4.4)$$

This thermochemical cycle leads to equation. (4.5)

$$\Delta H^o_1 = \Delta H^o_2 + \Delta H^o_3 + \Delta H^o_4 \qquad (4.5)$$

The observed non-occurrence of reaction in equation (1) indicates that $\Delta H^o_1 \geq \Delta H^o_1 + \Delta H^o_2 + \Delta H^o_3 > 0$. The value of ΔH^o_3 can be obtained from well-established thermochemistry [126,127] as 0.4 kcal/mol. Figure 27 shows the mass spectra collected following the injection of $C_4H_4N_2^{\bullet +}$ into Helium (27a), and pyrimidine vapor in Helium at different drift cell temperatures (27b-e) to estimate ΔH_4. After equilibrium conditions were established (i.e. equivalent ATDs for both reactant and product ions due to equilibrium coupling as shown in Figure 28, constant reactant to product ion ratio over reaction time as shown in Figure 29, and finally the non- dependence of the reaction rate constant of the neutral reactant concentration) a binding energy of 22.7 ±1 kcal mol^{-1} ($\Delta S = 27.82 \pm 2$ $calK^{-1}mol^{-1}$) was measured using van't Hoff as shown if Figure 30 (22.4 ±1 kcal mol^{-1} computed at the B3LYP/6-311++G** level of theory). A sum of ΔH^o_3 and ΔH^o_4yield

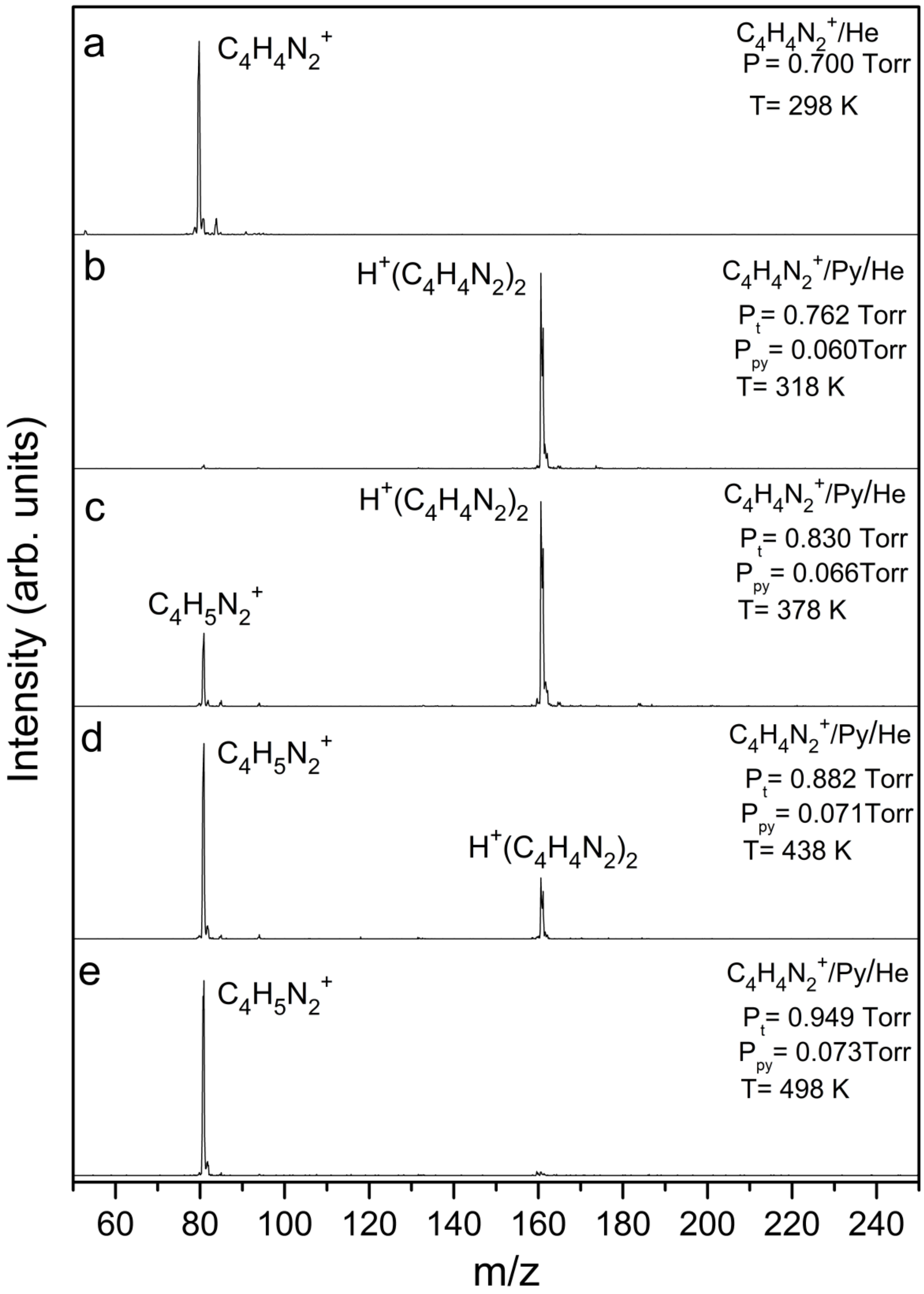

Figure 27: Mass spectra of $C_4H_4N_2^{\bullet+}$ injected at 12.6 eV into $C_4H_4N_2$/He at drift cell temperatures as indicated.

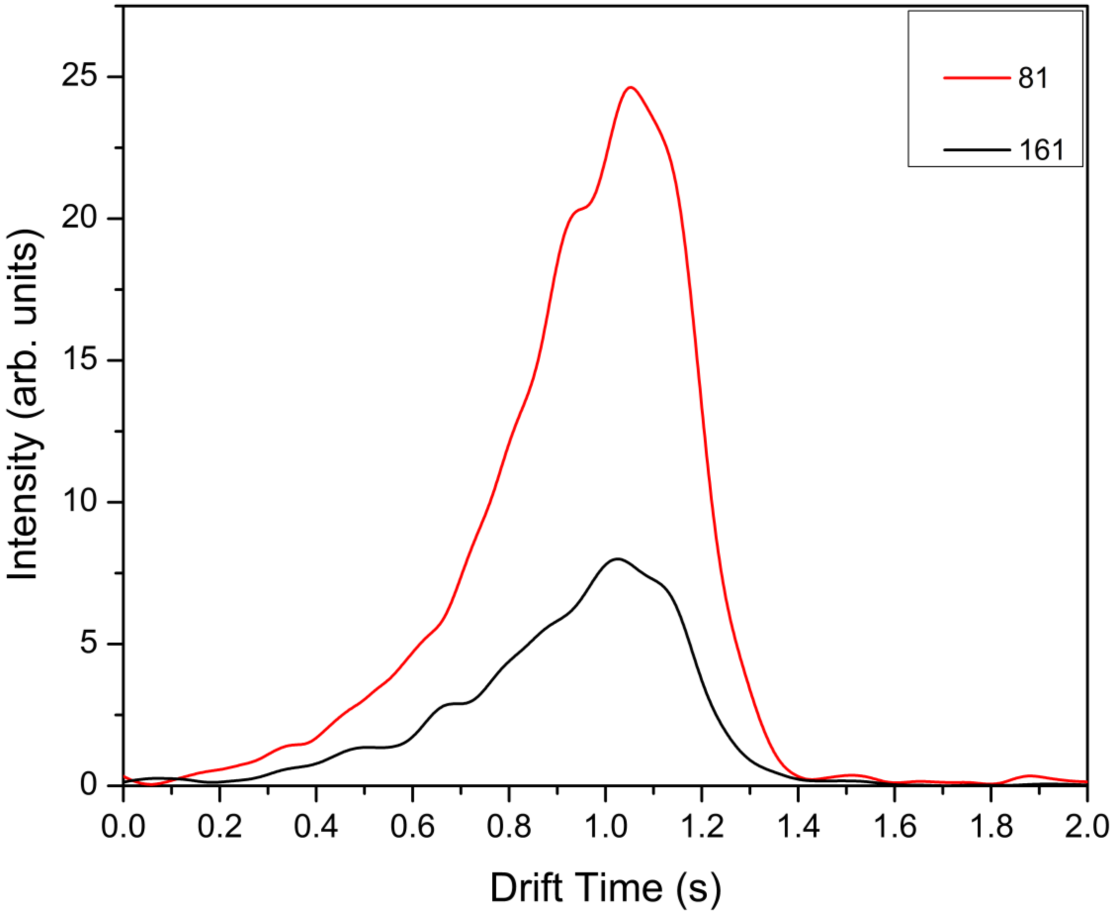

Figure 28: Arrival time distribution (ATD) collected for the dissociation of $(C_4H_4N_2)_2H^+$ into $C_4H_4N_2^{\bullet+}$ in 0.59Torr of $C_4H_4N_2$ at 503K in 1.3 Torr Helium.

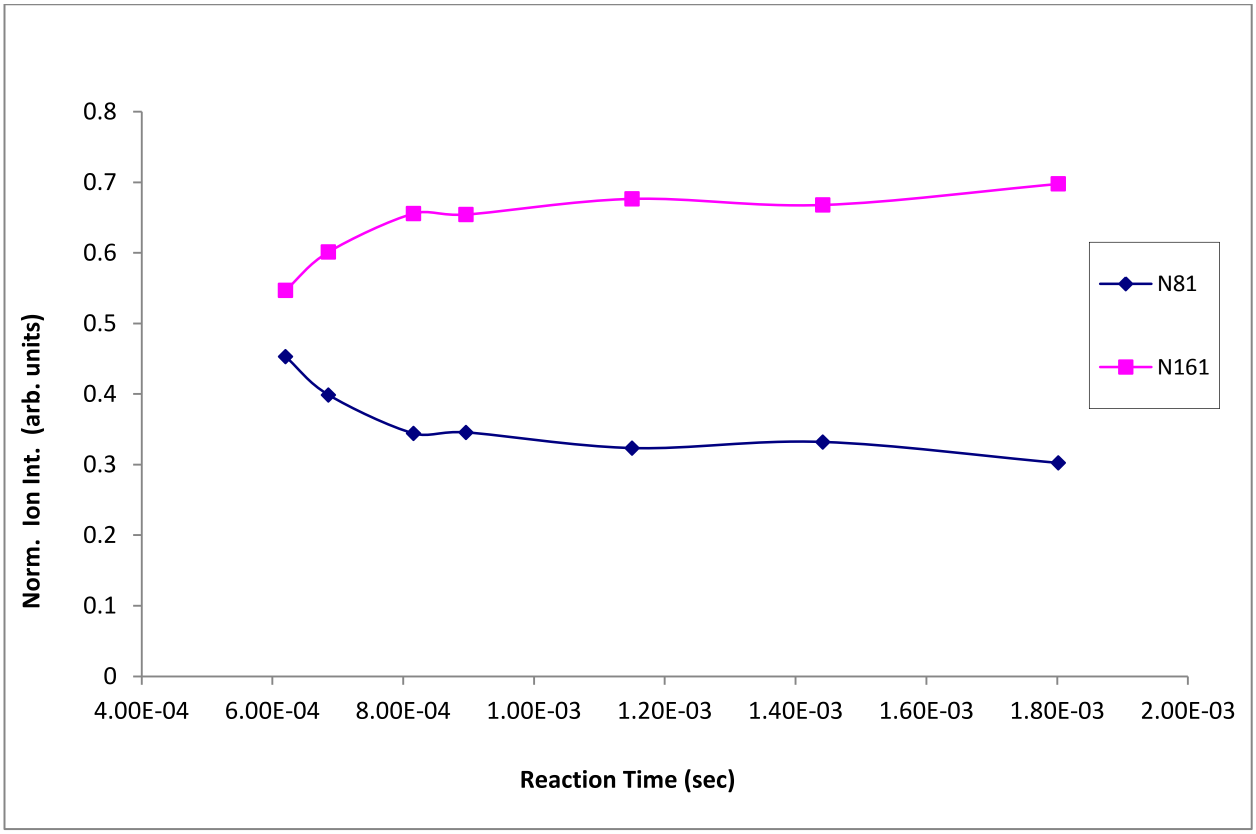

Figure 29: Time resolved mass scan of the dissociation of $(C_4H_4N_2)_2H^+$ into $C_4H_4N_2^{\bullet+}$ in 0.59Torr of $C_4H_4N_2$ at 523K in 1.3Torr Helium showing that the dissociation reaction is in equilibrium.

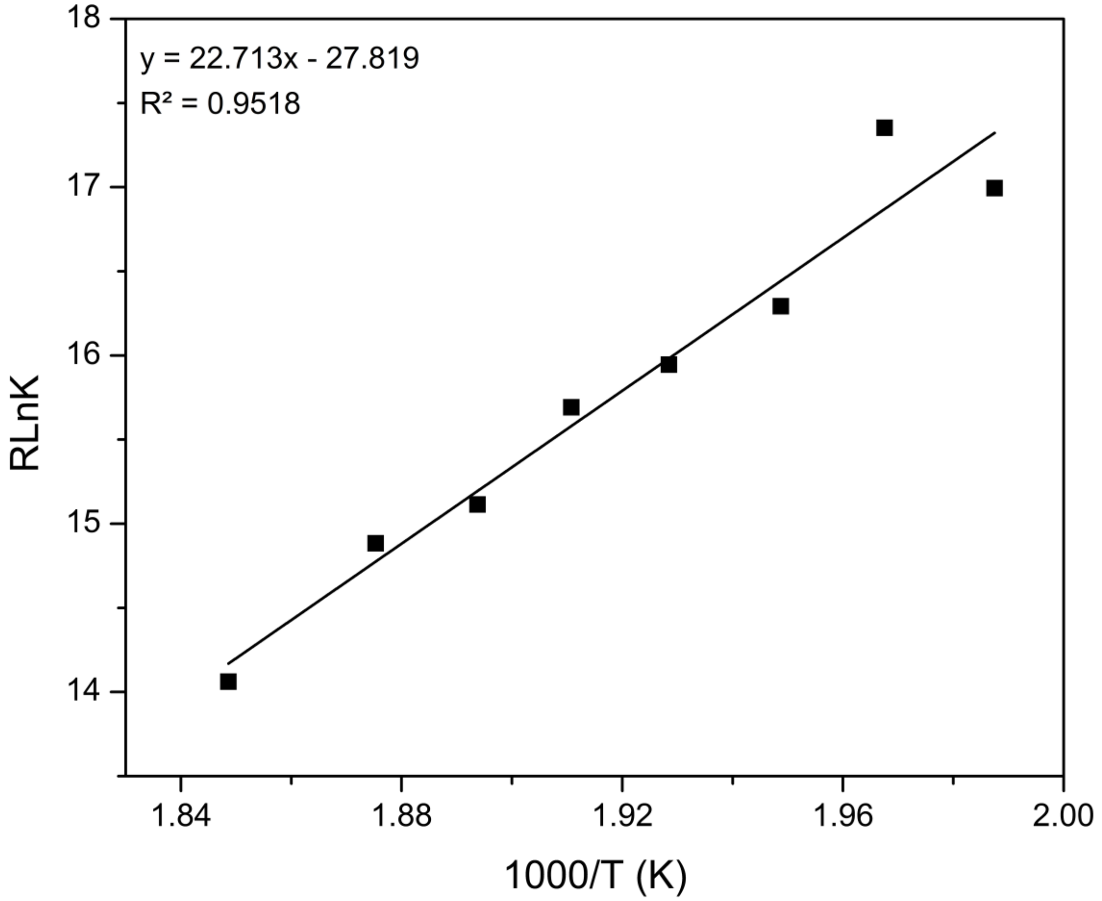

Figure 30: Van't Hoff plot for binding energy measurement of $(C_4H_4N_2)_2H^+$ dimer in 0.58Torr of $C_4H_4N_2$ at different temperatures in 1.3Torr

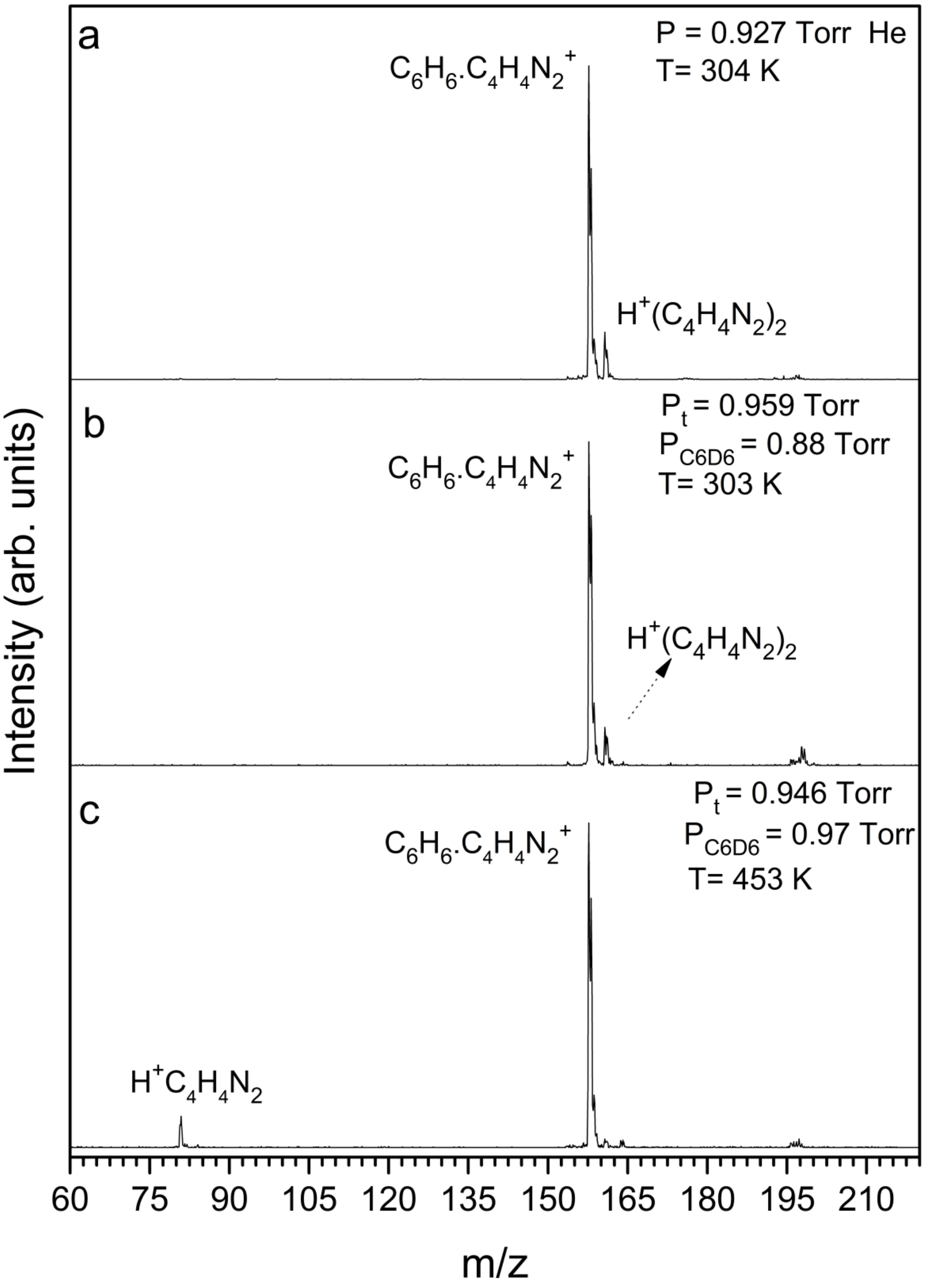

Figure 31: Lack of ligand exchange reactions of $(C_6H_6•C_4H_4N_2)^{•+}$ injected into C_6D_6/He at the pressures and temperatures indicated. Ligand exchange could yield $(C_6D_6•C_6H_6)^{•+}$ (m/z 162) or $(C_4H_4N_2•C_6D_6)^{•+}$ (m/z 164) which are not observed.

a ΔH^o_2 > 23.1kcal mol^{-1}, consistent with earlier estimation of the lower limit of the BDE $(C_6H_6 \bullet C_4H_4N_2)^{\bullet +}$ to be at least 28.1kcal mol^{-1}.

Similarly, no ligand exchange was observed when $(C_6H_6 \bullet C_4H_4N_2)^{\bullet +}$ was injected into the drift cell containing C_6D_6/He. Figure 31a shows the heterodimer radical cation in He only, and also the protonated pyrimidine dimer formed at the ion source. We do not observe any new ions being formed when C_6D_6 is added to the drift cell at 303K and 453K (Figure 31b,c), indicating the absence of ligand exchange reactions. The thermodynamics of this ligand exchange would be given by dissociation (reaction 2, using C_6H_6 instead of $C_4H_4N_2$) followed by $Bz^{\bullet +} + Bz \rightarrow (Bz)_2^{\bullet +}$ ($\Delta H = -17$ kcal/mol) [79,127,128]. Assuming that non-occurrence of ligand exchange indicates endothermicity, then from this cycle $\Delta H_4 - 17$ kcal/mol > 0 and $\Delta H_2 > 17$ kcal/mol consistent with the preceding estimates and the theoretical results below.

4.4.6 Ion Mobilities of the $Bz \bullet Pym^{\bullet +}$ Dimers

Structural information of gas phase ions can be obtained from ion mobility measurements, where the measured reduced mobility K_o, of the ion through a drift cell is proportional to the ion's collision cross-section (Ω),[24,26,79,123,129] which depends on its geometry. To identify the most plausible ion structure, theoretical calculations are performed on the geometry of several isomeric configurations, and the angle-averaged collision cross-sections are computed for the lowest energy isomers, using the trajectory method.[123] The theoretical Ω's are then compared to the experimentally measured values to identify the most likely structure. Figure 32 shows the ion mobility plot of the $(C_6H_6 \bullet C_4H_4N_2)^{\bullet +}$ dimer cation measured at 302.3 and 3.81 Torr helium over different drift cell voltages (lab coordinates). The average experimentally measured reduced mobility and corresponding Ω of the $(C_6H_6 \bullet C_4H_4N_2)^{\bullet +}$ dimer cation in our experiments

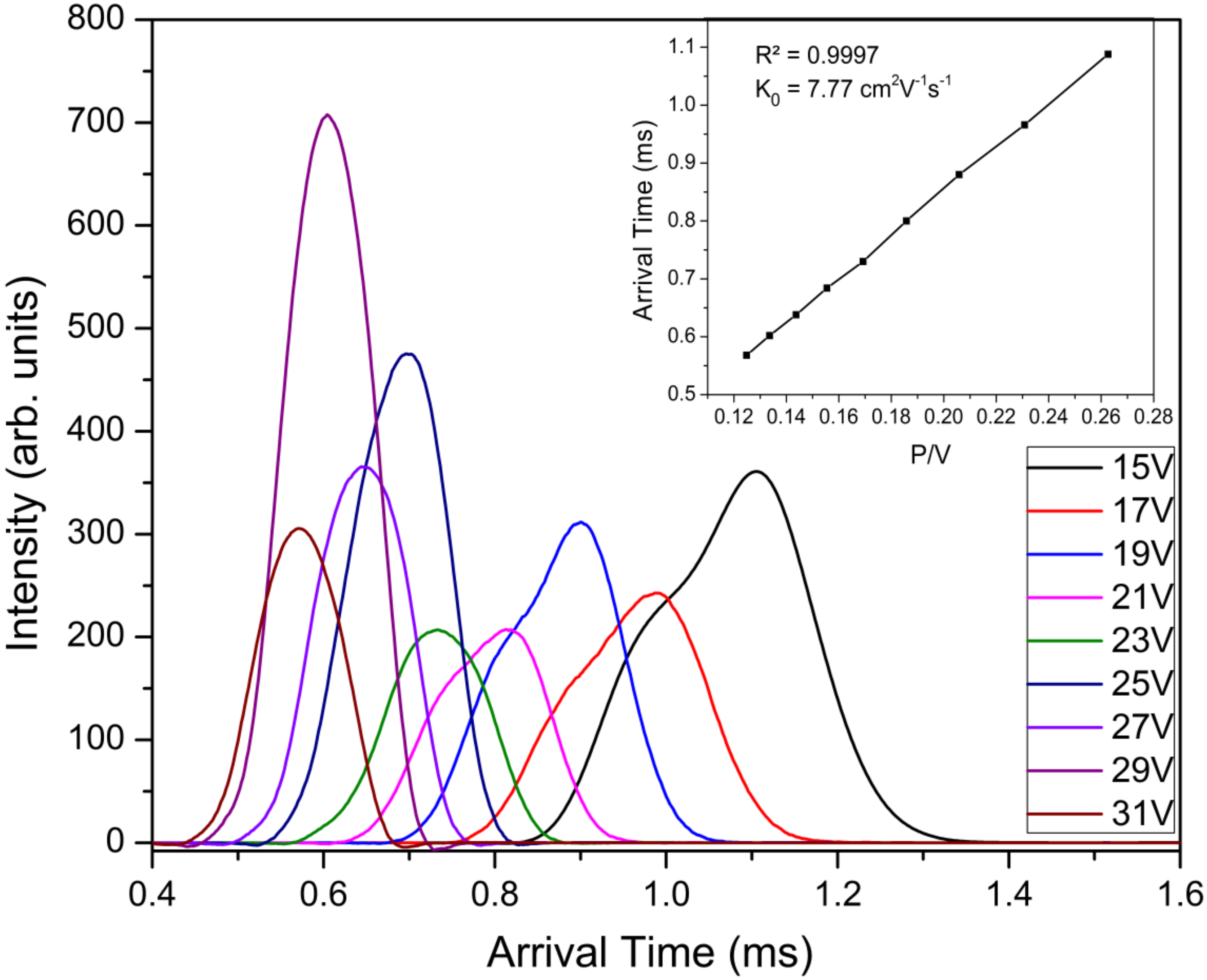

Figure 32: Arrival time distributions of the injected $(C_6H_6 \bullet C_4H_4N_2)^{\bullet +}$ dimer (50μs pulses) into the drift cell containing 3.81Torr He at different cell voltages (15 to 31 V, Lab coordinates) collected 302K. Inset shows the plot of arrival time at different cell voltages vs. P/V which yields K_o as the slope.

are 7.85 ± 0.15 $cm^2 V^{-1} s^{-1}$and 68.55 ± 1.4 $Å^2$. The measured reduced mobility indicates that the Bz•$Pym^{•+}$ structure is more compact than that of the benzene-pyridine radical dimer cation (7.4 ± 0.3 $cm^2 V^{-1} s^{-1}$)[24] and the T-shaped benzene radical dimer cation (7.6 ± 0.3 $cm^2 V^{-1} s^{-1}$)[24].

A comparison of the experimentally measured average K_o and Ω (7.85 ± 0.15 $cm^2 V^{-1} s^{-1}$and 68.55 ± 1.4 $Å^2$ respectively) for the observed ion with the computed isomers structures A-L,

clearly point to the fact that the experimentally observed ions could not be the non-covalent isomers A to D since their average K_o and Ω (7.36 ± 0.10 $cm^2 V^{-1} s^{-1}$ and 73.63 ± 0.97 $Å^2$ respectively) are considerably different from experiment, while the average K_o and Ω of the covalent isomers E-L (7.55 ± 0.12 $cm^2 V^{-1} s^{-1}$ and 71.88 ± 1.08 $Å^2$ respectively) of the covalent isomers E-H are in reasonable agreement with experiment. This difference in ion mobility is not surprising since the non-covalent isomers possess a "T-shaped" configuration and longer C-N bonds, which leads to a larger collision cross-section compared to the two-ring tighter "propeller" shaped covalent isomers.

4.4.7 DFT Computations of the Bz•$Pym^{•+}$ Dimers

DFT computations were done at the B3LYP/6-311++G** level of theory to complement the experimental observations in this study. The accuracy of the B3LYP level of theory along with the 6-311++G** basis set for C, N, and H were tested by calculating the binding energies of the protonated dimers of pyrimidine and pyridine which can be compared to experimental values. The DFT computed binding energy for the protonated dimer of pyrimidine was 22.4 kcal mol^{-1} was which agreed perfectly with experimentally measured binding energy of 22.7 ± 1kcal mol^{-1} measured using the QMS-IM-QMS setup. The binding energy for the protonated dimer of pyridine was calculated at the level of theory to be 24.9 kcal mol^{-1}, which agrees excellently with the reported value of 25.2 ±1kcal mol^{-1} in literature.[127,130]

The calculated BDEs with respect to dissociation to $C_6H_6^{\bullet+}$, $C_4H_4N_2$ and C_5H_5N at 298 K and geometries along with their relative energies in relation to the lowest energy isomer are shown in Figures 33 to 35. The reduced mobility, K_o, and Ω calculated using the trajectory method of the Mobcal[123] program is also given for each isomer. Figure 36 shows the DFT calculated NBO charges for the lowest energy isomers for the non-covalent and covalent isomers respectively.

4.4.7.1 Non-Covalent Bz•Pym$^{\bullet+}$ Dimer Isomers

The lowest energy geometries for the non-covalent electrostatically bonded $(C_6H_6.C_4H_4N_2)^{\bullet+}$ dimer cation are shown in Figure 33, isomers A – D, with the BDEs referenced to $C_6H_6^{\bullet+}$ and a $C_4H_4N_2$ molecule. We observe the formation of a "T-shaped" configuration in all of these isomers, with a nitrogen of $C_4H_4N_2$ pointing to a C atom of the C_6H_6 ring. Geometries of isomers B to D have both nitrogen of the $C_4H_4N_2$ ring directly above the C_6H_6 ring, and have the same calculated energy of 19.14 kcal mol^{-1}, although they have different computed Ω's. In isomer A the second nitrogen is outside the vertical plane of the C_6H_6 ring, which makes it slightly more stable, by 0.14 kcal mol^{-1}, than B to D, which is within computational uncertainty.

4.4.7.2 Covalent Bz•Pym$^{\bullet+}$ Dimer Isomers

The calculated lowest energy isomers for the covalently bonded $(C_6H_6.C_4H_4N_2)^{\bullet+}$ dimer cation are shown in Figure 34, with the BDEs referenced to $C_6H_6^{\bullet+}$ and a $C_4H_4N_2$ molecule. Structural isomer E has the benzene C-H hydrogen displaced by the C-N bond hydrogen situated on the second pyrimidine N atom with a BDE of 40.7 kcal/mol, while in F to H the hydrogen is placed on a different carbon atoms of the pyrimidine ring with BDEs of 22.3 – 26.8 kcal/mol. Isomers K and L with the displaced hydrogen on the benzene ring have even smaller BDEs of 21.4 and 25.4 kcal/mol, respectively. In these covalent adducts the lowest energy isomer G has the displaced hydrogen on the para carbon to the C-N nitrogen, similar to the most stable (benzene/pyridine)$^{\bullet+}$ adduct isomer N, shown in Figure 36, with a BDE of 34.9 kcal/mol (recalculated here at the same level as the other structures in this study). Here also isomer M with the displaced hydrogen added to the benzene ring has a recalculated BDE of 32.9 kcal/mol, smaller by 2.0 kcal/mol than N, similar to the difference in the analogous (Benzene•Pyrimidine)$^{\bullet+}$ isomers G and L of 1.4 kcal/mol. The NBO charge distribution of the lowest energy non-covalent and covalent isomers given in figure 19 shows that 44.3% of the initial charge on the benzene ring is transferred to the pyrimidine ring in the non-covalent isomer, whereas 67.2 is transferred to pyrimidine in the covalently bonded isomer.

The energetics calculated at the same B3LYP/6-311++G** level for the lowest energy covalent isomers can be summarized as follows. The BDE of the (Benzene•Pyrimidine)$^{\bullet+}$ isomer G is smaller by 8.1 kcal/mol than the analogous isomer N of (Benzene•Pyridine)$^{\bullet+}$. This could be because the additional in-ring dipole in the pyrimidine ring repels the positively charged benzene component. On the other hand, the lowest energy covalent (Benzene•Pyrimidine)$^{\bullet+}$ dimer with the displaced H atom on the second pyrimidine N atom has a BDE larger than the most stable (Benzene•Pyridine)$^{\bullet+}$ by 5.8 kcal/mol, presumably because here both components preserve the aromatic stabilization of the π systems. Overall, comparing the covalent (Benzene•Pyrimidine)$^{\bullet+}$ isomers G and E, placing the displaced C-H hydrogen on the second pyrimidine N instead of the para carbon of pyrimidine increases the BDE of the dimer by 13.9 kcal/mol because the aromatic π system of pyrimidine$^{\bullet+}$ is preserved in E but disrupted in G. This difference is substantial but smaller than the estimated 26 kcal/mol aromatic stabilization of

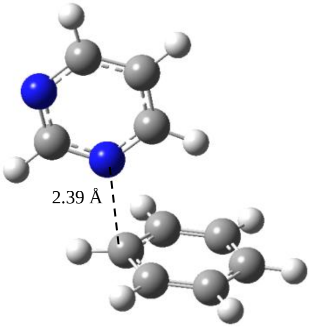

A

BDE = 19.28 kcal mol^{-1}

Rel. E. = 0

K_o = 7.29 $cm^2V^{-1}s^{-1}$

Ω = 73.79 $Å^2$

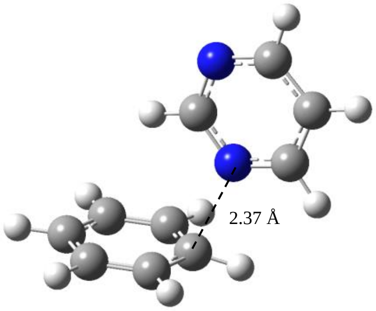

B

BDE = 19.14 kcal mol^{-1}

Rel. E. = 0.14

K_o = 7.44 $cm^2V^{-1}s^{-1}$

Ω = 72.96 $Å^2$

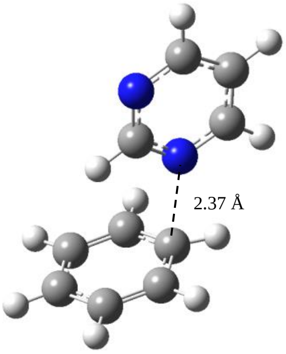

C

BDE = 19.14 kcal mol^{-1}

Rel. E. = 0.13

K_o = 7.22 $cm^2V^{-1}s^{-1}$

Ω = 75.14 $Å^2$

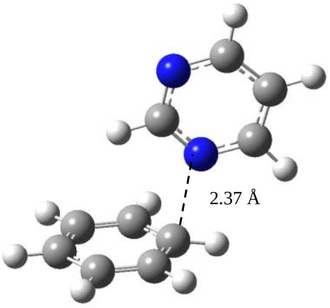

D

BDE = 19.14 kcal mol^{-1}

Rel. E. = 0.14

K_o = 7.47 $cm^2V^{-1}s^{-1}$

Ω = 72.61 $Å^2$

Figure 33: Computed geometries, bond dissociation energies, mobilities and collision cross-sections of non-covalent isomers of (Benzene•Pyrimidine)$^{\bullet+}$ (A – D). C-N bond lengths between the two rings are shown.

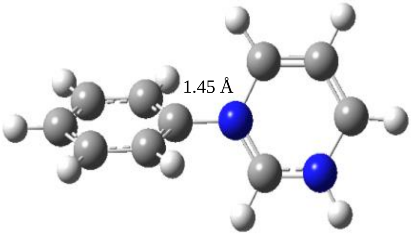

E

BDE = 40.71 kcal mol^{-1}

Rel. E. = 0

K_o = 7.436 cm^{2}V^{-1}s^{-1}

Ω = 72.49 Å^2

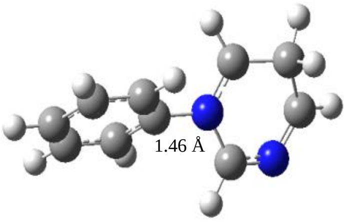

F

BDE = 22.30 kcal mol^{-1}

Rel. E. = 18.41

K_o = 7.50 cm^{2}V^{-1}s^{-1}

Ω = 72.34 Å^2

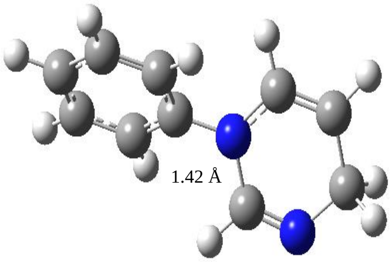

G

BDE = 26.81 kcal mol^{-1}

Rel. E. = 13.89

K_o = 7.80 cm^{2}V^{-1}s^{-1}

Ω = 69.56 Å^2

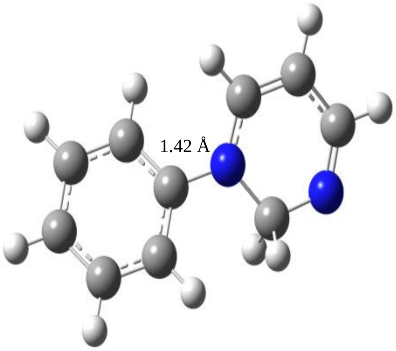

H

BDE = 26.42 kcal mol^{-1}

Rel. E. = 14.28

K_o = 7.38 cm^{2}V^{-1}s^{-1}

Ω = 73.50 Å^2

Figure 34: Computed geometries, bond dissociation energies, mobilities and collision cross-sections of covalently bonded isomers of (Benzene•Pyrimidine)$^{\bullet+}$ (E – H). C-N bond lengths between the two rings are shown. Note that bond assignments by the Gaussian program are determined by the interatomic distances of the optimized geometry. Assignments of bonds, such as carbons in isomer E with five bonds, reflect only these automated assignments.

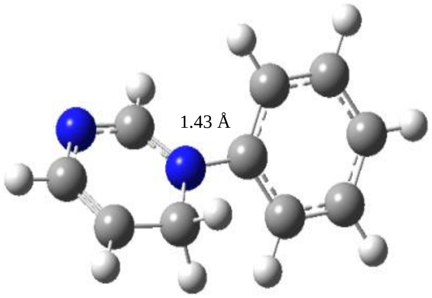

I

BDE = 25.47 kcal mol^{-1}

Rel. E. = 15.24

K_o = 7.55 cm^{2}V^{-1}s^{-1}

Ω = 71.85 Å^2

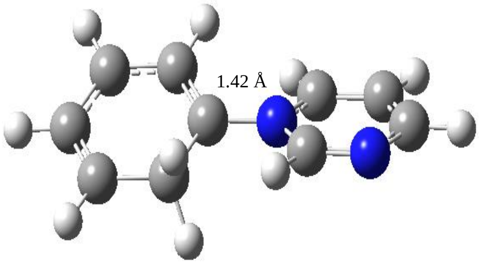

J

BDE = 23.44 kcal mol^{-1}

Rel. E. = 17.26

K_o = 7.64 cm^{2}V^{-1}s^{-1}

Ω = 71.02 Å^2

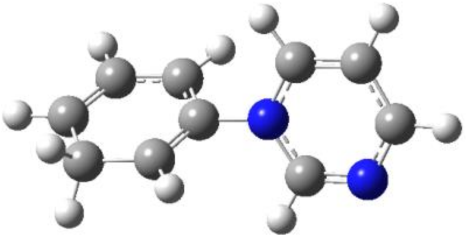

K

BDE = 21.37 kcal mol^{-1}

Rel. E. = 19.34

K_o = 7.44 cm^{2}V^{-1}s^{-1}

Ω = 72.95 Å^2

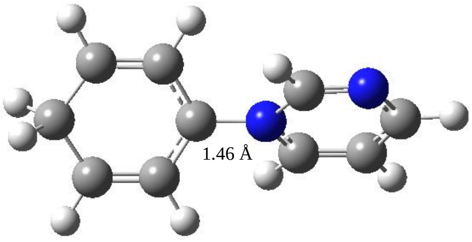

L

BDE = 25.43 kcal mol^{-1}

Rel. E. = 15.28

K_o = 7.57 cm^{2}V^{-1}s^{-1}

Ω = 71.71 Å^2

Figure 34 cont’d: Computed geometries, bond dissociation energies, mobilities and collision cross-sections of covalently bonded isomers of (Benzene•Pyrimidine)$^{•+}$ (I - L). C-N bond lengths between the two rings are shown. Note that bond assignments by the Gaussian program are determined by the interatomic distances of the optimized geometry. Assignments of bonds, such as carbons in isomer E with five bonds, reflect only these automated assignments.

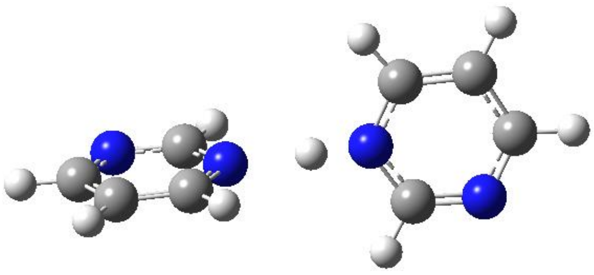

M

BDE = 22.37 kcal mol^{-1}

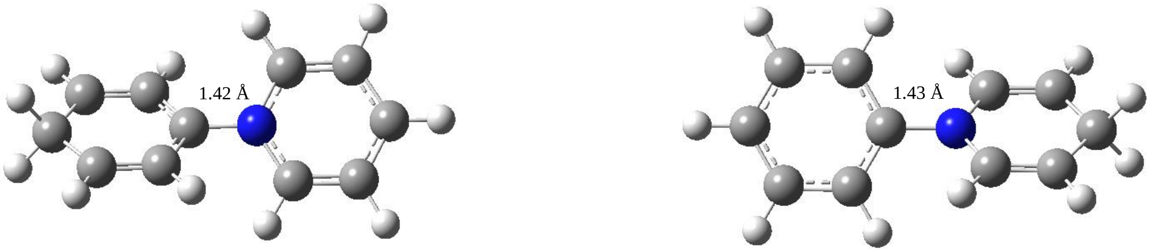

N

BDE = 32.89 kcal mol^{-1}

Rel. E. = 2.0

O

BDE = 34.89 kcal mol^{-1}

Rel. E. = 0

Figure 35: Computed geometries and bond dissociation energies of hydrogen bonded pyrimidine dimer (M), and covalently bonded isomers of (Benzene•Pyridine)$^{\bullet+}$ (N and O). Note that bond assignments by the Gaussian program are determined by the interatomic distances of the optimized geometry. Assignments of bonds, such as carbons in isomer E with five bonds, reflect only these automated assignments.

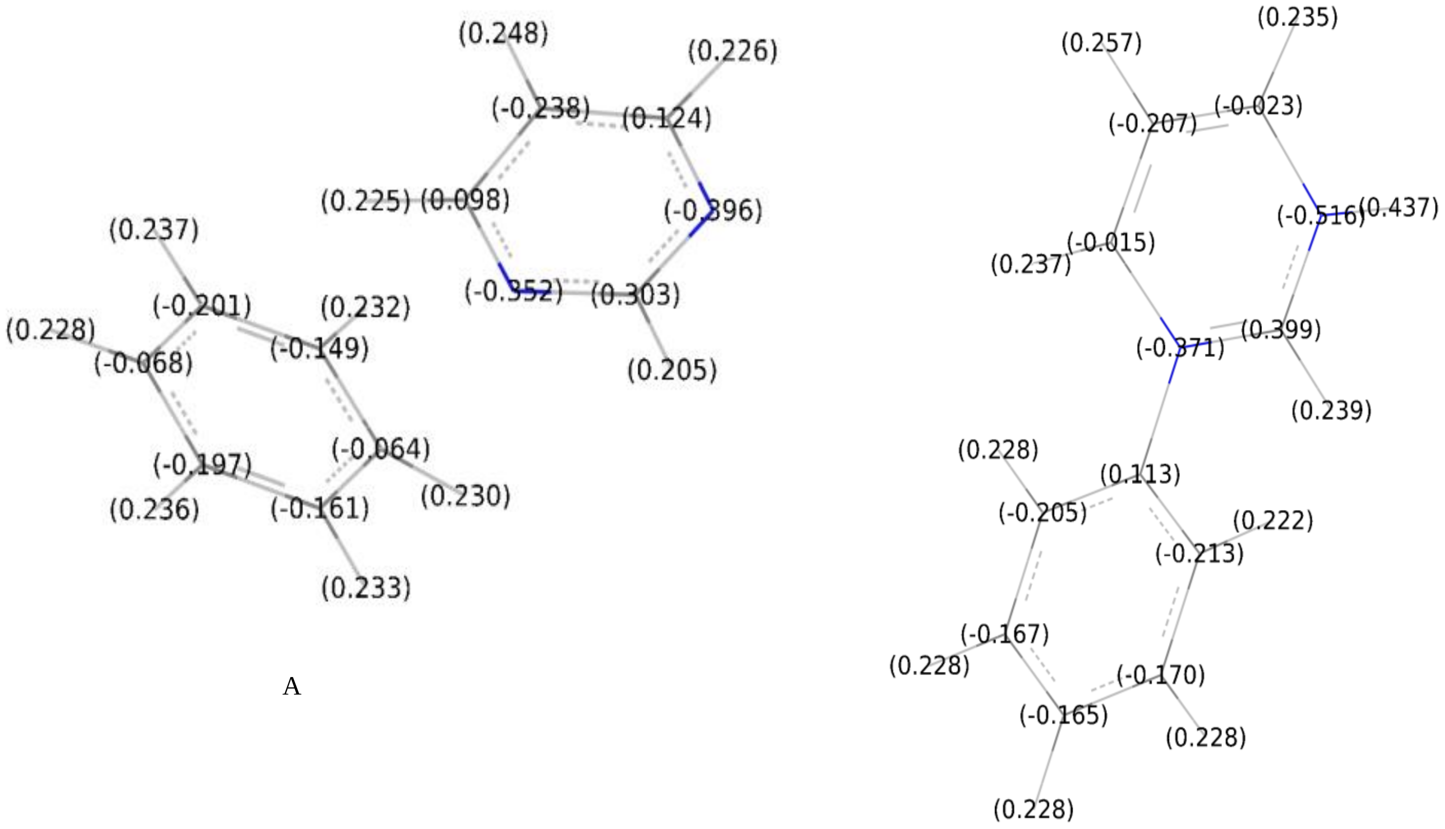

A

E

Figure 36: Computed geometries isomer of the non-covalent isomer A and covalent isomer E, showing NBO charges computed at the B3LYP/6-311++G(d, p) level of theory. Total charge on both rings is +1.

pyrimidine,[131] possibly because the aromatic stabilization is smaller in the radical cation or some aromaticity is preserved in the hydrogenated ring.

4.5 Estimating the bond strength of the $(C_6H_6.C_4H_4N_2)^{\bullet+}$ dimer cation from experimental and theoretical observations.

A lower limit to the dissociation energy can be obtained from the data in Figure 8, assuming that the reaction in the time resolved mass scan approaches equilibrium after 0.37ms. The ratio of $I(C_6D_6\bullet C_4H_4N_2)^{\bullet+}/I(C_6D_6^{\bullet+})$ at 0.37ms is 9.2. Thus $K_{eq}= [(C_6D_6\bullet C_4H_4N_2)^{\bullet+})]/[C_6D_6^{\bullet+}]P(C_4H_4N_2) > 9.2 /P(C_4H_4N_2)$ (atm) = 6962/0.05 giving $\Delta G^o_{assoc} < -11.8$ kcal/mol for forming the adduct from $C_6D_6^{\bullet+}$. For a non-covalent adduct ΔS_{assoc} may be estimated as -30 cal/mol K[24,130] from analogous dimers, and for a covalent adduct -50 cal/mol K[132]. Then from $\Delta G^o_{assoc} = \Delta H^o_{assoc} - T\Delta S^o_{assoc} < -11.8$ kcal/mol at 504 K we obtain $\Delta H_{assoc} < -26.9$kcal/mol for a non-covalent, and $\Delta H_{assoc} < -37.0$ kcal/mol for a covalent adduct. The estimated BDE $(-\Delta H^o_{assoc}) > 27$ kcal/mol for non-covalent adducts is larger than the 19 kcal/mol calculated below for the isomers A to D, while for the covalent adduct the estimated > 37 kcal/mol excludes all the covalent isomers from F to L, except E which has a calculated energy of 40.7 kcal/mol, consistent with the estimated lower limit of the binding energy.

4.6 Conclusion

The present work concerns the adduct radical cation $(\text{Benzene}\bullet\text{Pyrimidine})^{\bullet+}$ and compares it with $(\text{Benzene}\bullet\text{Pyridine})^{\bullet+}$ Thermochemistry and computations show that both form a stable covalent adduct bonded by a C-N bond, whose formation displaces a benzene hydrogen. In $(\text{Benzene}\bullet\text{Pyridine})^{\bullet+}$ this hydrogen is transferred to the para carbon of pyridine, disrupting the aromatic π system of pyridine. In comparison, in the pyrimidine (1,3-Diazine) adduct the N lone pair of the second ring nitrogen can accommodate the hydrogen without disrupting an aromatic π system. This lowers the energy of the adduct by 13.9 kcal/mol compared with the isomer where the hydrogen is on the carbon para to the C-N bond nitrogen. The overall effect is that the (Benzene•Pyrimidine)$^{\bullet+}$ adduct is more stable (i.e., the BDE is higher) by 5.8 kcal/mol than (Benzene•Pyridine)$^{\bullet+}$. In both cases the new C-N bond is in the plane of both rings whose axises are co-linear but the two rings are rotated with their planes perpendicular to each other.

In addition to the covalent adduct, computations also showed stable non-covalent electrostatically bonded adducts (Benzene•Pyrimidine)$^{\bullet+}$. Estimated limits of the BDE from non-reversible association, lack of ligand exchange, and dissociation kinetics is BDE > 22 – 28 kcal/mol, which is higher than the 19 kcal/mol calculated for the non-covalent dimers but in agreement with the calculated 40.7 kcal/mol for the lowest energy C-N bonded covalent dimer.

Comparison of (Benzene•Pyrimidine)$^{\bullet+}$ with (Benzene•Pyridine)$^{\bullet+}$ shows that a second nitrogen in the ring facilitates covalent association by accommodating a displaced hydrogen on the second nitrogen without disrupting an aromatic π system. It would be of interest whether this is a general phenomenon in the association of ionized nitrogen heterocyclics with hydrocarbons, that can occur in ionizing environments including interstellar clouds.

CHAPTER 5. Substituent Effects on Intermolecular Bonds of Ionized Aromatics; Complexes of Ionized Fluorobenzenes and Benzonitrile with Hydrogen Cyanide

5.1 Introduction

Intermolecular forces, including hydrogen bonds,[27-29] are important in chemical synthesis, crystal and material engineering, molecular recognition and supramolecular chemistry, polymerization, biology and astrochemistry.[30-41,133] In ionizing environments, strong hydrogen bonds can form between radical or protonated ions and neutral molecules. In particular, aromatic hydrocarbons form stable molecular radical ions which can interact with polar ligand and solvent molecules, or with other aromatic molecules. It is of interest how substituents on the aromatic molecules affect these intermolecular forces. These effects can be studied experimentally by measuring ion-molecule binding energies, and computationally by calculating the binding energies, structures and charge distributions on the complexes.

Our first studies in this area dealt with dimer cations such as $(\text{benzene})_2^{\bullet+}$ and similar dimers of derivatized and polycyclic aromatic hydrocarbons. These dimers usually have parallel π stacked sandwich structures which allow charge transfer (CT) resonance between the components. This is most effective in homodimers, contributing 7 kcal•mol^{-1} of the 17 kcal•mol^{-1} binding energy in $(\text{benzene})_2^{\bullet+}$. However, CT becomes weaker in heterodimers where the charge is localized on the component with the lower ionization energy. Substituents that affect the ionization energies thereby affect the bond energies in the dimers.[134,135]

Alternatively, different adducts form with non-aromatic polar ligands such as H_2O, HCN, CH_3CN, that bond to $\text{benzene}^{\bullet+}$ through $\text{-CH}^{\delta+}$---N or O hydrogen bonds. Additional ligand molecules can then bond to other unoccupied benzene CH hydrogens, forming internally solvated structures (with the ion inside a solvent cluster), or attach to the first solvent molecules forming an externally solvated cluster (with the ion outside the solvent cluster). Solvation by 3 or more solvent molecules can also form mixtures of such structures. In these cases substituents on the ionized aromatic molecule can affect the charge densities on the ring carbons and on the CH hydrogens and thereby affect the ionic hydrogen bonds.

In addition to the sandwich and hydrogen-bonded adducts, a third type of structure is observed in some cases, where ligand molecules bond electrostatically to charge centers in the ionized aromatics. We found thermochemical indications for such electrostatic complexes in adducts of polar ligands such as CH_3CN and CH_3NO_2 to aniline$^{\bullet+}$.[135] In some cases the thermochemistry indicates that electrostatic complexes are more stable than possible π stacked sandwich complexes, such as in aniline$^{\bullet+}$---benzonitrile or nitrobenzene[135] or in noncovalent non-coplanar isomers of the benzene$^{\bullet+}$---pyridine dimer, where the pyridine N atom points to a partial charge on a benzene carbon in the ring.[24] Substituents can affect such electrostatic dimers by affecting charge centers in the ionized aromatics. In some cases hydrogen-bonded or electrostatic structures are more stable than CT resonance sandwich dimers, such as in the dimers aniline$^{\bullet+}$---benzonitrile and aniline$^{\bullet+}$---nitrobenzene.[135]

There is little information presently on substituent effects on the intermolecular interactions of ionized aromatics. The present work examines the effects of electron-withdrawing substituents on benzene, in complexes of HCN with ionized fluorobenzenes and benzonitrile.

Hydrogen cyanide is a useful probe of non-covalent interactions because it is highly polar, and it can serve both as a hydrogen donor and as a lone-pair hydrogen acceptor in hydrogen bonds. In benzene$^{\bullet+}$(HCN)$_n$ clusters the ligand molecules added to the benzene hydrogens but also formed HCN---HCN---HCN chains by subsequent HCN molecules.[60] In another system, phenylacetylene$^{\bullet+}$(HCN)$_n$, the dominant interactions were hydrogen bonds between the C-H acetylenic hydrogen and the N≡CH nitrogen of the first HCN ligand.[41] Subsequent ligands added to the first HCN molecule to form linear hydrogen bonded HCN---HCN---HCN chains. Such HCN---(HCN---(HCN---H$^+$---NCH)---HCN)---HCN chains were proposed in protonated hydrogen bonded clusters, where binding enthalpies indicated completion of solvent shells by 2 (first shell) or 4 (second shell) HCN molecules about the proton.[1,45]

In aromatic systems, much work has been done on non-covalent interactions between aromatic molecules or ions and both protic and aprotic solvents, but the majority was done computationally.[42] Experimental investigations included IR or Raman vibrational spectroscopy, solid state neutron diffraction and X-ray diffraction, to identify experimentally hydrogen bonds between molecules, largely in the gas phase for quantitative information.[34,35,18,44,45]

In most systems studied, conventional H_2O---H or HN---H hydrogen bonds involve lone-pair electron donors in neutral and ionic hydrogen bonds. However, unconventional NH$^+$--- π and OH$^+$--- π and even weaker CH$^+$--- π bonds were also investigated, where the conjugated π electron systems of aromatic compounds serve as electron donors.[1,46-48]

For example, studies concerned the interactions between benzene, a prototype aromatic system[28,136] and protic and aprotic solvent molecules,[50] such as hydrogen bonds between the π-electrons of benzene (C_6H_6) with the O-H hydrogen of the water molecule to yield π-hydrogen bonded cluster, where the hydrogen atoms of the water molecule point into the plane of the benzene ring.[46,48,51,52] Similar studies have been done on the radical cation of benzene with water[47,53-57,136], and other polar solvents[49,58-60]. Work on the hydration of other aromatic cations such as cyclic $C_3H_3^+$[41] , and ionized phenylacetylene[137] , pyridine, 2-fluoropyridine, and protonated pyridine[62], acetylene monomer[61], dimer[63] and trimer[64] ions have also been reported. In contrast to the neutrals where the π rings are electron donors, the ionized aromatics can serve as hydrogen donors for ionic hydrogen bonds, or form other electrostatic complexes. However, little work addressed the effect of substituents on the aromatic rings on the interaction between the π-electron system and the solvent molecules, especially in ions.

In neutral molecules, Tarakeshwar *et. al* [35] used *ab initio* methods to investigate the nature of binding between fluorobenzene and 1,4-difluorobenzene with water, and discovered several stable conformers with σ or π type of interactions between the binding molecules. Based on the calculated binding energies they concluded that the water molecule binds more tightly to difluorobenzene than to fluorobenzene. In these systems the ligand H_2O molecules were bonded to the hydrogens in the plane of aromatic rings, and the second electron withdrawing fluorine atom could have increased the partial positive charges on the aromatic hydrogens. As we observe below, the second fluorine substation has negligible effects in the ionic clusters.

Investigating substituent effect of aromatic rings on non-covalent interactions with solvent molecules helps a basic understanding of such interactions, and could also help to design molecules with finely tuned non-covalent interactions in drug discovery, enzyme design, and organic electronics and catalysts,[42,138] and other contributions to supramolecular chemistry[42].

We shall present here experimental thermochemical and DFT computational investigation of the non-covalent interactions between the radical cations of fluorobenzene, 1,4-difluorobenzene, and benzonitrile ($C_6H_5F^{\bullet+}$, 1,4-$C_6H_4F_2^{\bullet+}$, and $C_6H_5CN^{\bullet+}$respectively) and hydrogen cyanide (HCN), by studying the stepwise solvation of the organic aromatic ions by HCN to yield $C_6H_5F^{\bullet+}(HCN)_n$, 1,4-$C_6H_4F_2^{\bullet+}(HCN)_n$, and $C_6H_5CN^{\bullet+}(HCN)_n$ for n=1-4. Hydrogen cyanide is interesting due to its observation in the atmospheric[65] and interstellar[66] media, and as a ligand or solvent that has both a hydrogen donor CH and nitrogen lone pair donor (hydrogen acceptor) – N: site. This enable HCN to serve as a ligand for protonated cations (NH_4^+, $HCNH^+$)[1,45,a] [REFS], radical cations ($C_6H_6^{\bullet+}$, $C_6H_5CCH^{\bullet+}$) and also for anions, and to form linear hydrogen bonded chains in these clusters.

In binding to benzene$^{\bullet+}$ HCN serves as a hydrogen acceptor in binding to the benzene$^{\bullet+}$ C-H hydrogens. It will be interesting to know how will the nature of binding be affected by replacing one or two C-H hydrogens with a fluorine atoms or a cyanide group as in fluorobenzene, 1,4-difluorobenzene, and benzonitrile respectively. These electron withdrawing substituents can affect the ionization and protonation energies of benzene, its π electron donor properties, and the partial charges on the C-H hydrogens, and thereby affect the hydrogen bond donor properties of the ions.

Here we measure the binding energies of HCN molecules to substituted ionized benzenes, and use computations to investigate the types of hydrogen bonds and their relative stabilities in these clusters.

5.2 Experimental and Theoretical Methods

The ion association experiments reported here were carried out using the VCU quadrupole mass selector-ion mobility-quadrupole mass spectrometer. Details of the instrument were given in the experimental section. To generate the molecular radical cations $C_6H_4F_2^{\bullet+}$, $C_6H_5F^{\bullet+}$, and $C_7H_5N^{\bullet+}$ respectively, the neutral monomers are generated by the supersonic expansion of 40 psi (2.8 bar) of ultra-high pure helium seeded with about 1−4% of vapor of the compound through a pulsed supersonic nozzle (500 μm) to the vacuum source chamber with 10^{-7} mbar pressure, and ionized by electron impact ionization using electron energy of 60−70 eV. The radical cations are then mass selected using the first quadrupole mass-filter and then injected in 30−50 μs pulses into the drift cell, which has neutral HCN in Helium buffer gas mixture.

To allow a known and constant concentration of HCN and Helium pressure into the drift cell, two flow controllers (MKS # 1479 accurate within ±1 mTorr) are used. The drift cell temperature is controlled within ±1 K using four temperature controllers. Liquid nitrogen flow, controlled using electronic solenoid valves is used to cool down the drift cell. The second quadrupole mass filter is used to scan and detect the product distribution from the reaction after they exit the drift cell. The arrival time distributions (ATDs) are collected by monitoring the intensity of each ion as a function of reaction time, and to vary the reaction time, the drift cell voltage is varied to change the drift time accordingly.

The ions are injected into the mobility cell with injection energies of 8−14eV, laboratory frame, just above the minimum energies required to introduce the ions into the cell against the backward flow of the HCN/He mixture from the drift cell entrance orifice. Most of the thermalization of the injected ion occurs just outside the cell entrance by collisions with the HCN and He vapor escaping from the cell. Further thermalization occurs in the mobility cell. For example, at a given cell pressure of 0.2 Torr at 300 K, ions undergo over 10^4 collisions with neutral molecules at > 1 ms residence time inside the cell, more than sufficient for efficient thermalization of the ions.

The HCN used in our experiment is prepared by adding 8 g of sodium cyanide (NaCN) (Sigma-Aldrich, 97%) into a 500 mL stainless steel bubbler, which is then placed in liquid nitrogen and evacuated. 4 mL of pure sulfuric acid (H_2SO_4) (Aldrich, 99.999%) is then added through a stainless steel tube extension of the inlet valve of the bubbler. To generate the HCN gas, the temperature of the stainless steel bubbler is allowed to increase till room temperature, by which time the reaction of the sulfuric acid with the sodium cyanide salt inside the bubbler will occur. To ensure safety, the pressure of HCN in the closed circuit line is constantly monitored using a Baratron pressure gauge (MKS-26A13TBD) to ensure there is no leakage. Equation one represents the equilibrium reactions being measured during this study.

$$(A^{+\cdot}(HCN)_{n-1} + HCN \longrightarrow (A^{+}(HCN)_{n} \qquad (5.1)$$

where A = $C_6H_4F_2^{\bullet+}$, $C_6H_5F^{\bullet+}$, or $C_7H_5N^{\bullet+}$. The check for the attainment of equilibrium is done by ensuring the following conditions are satisfied,

(i) a constant ratio of the integrated intensity of the product to the reactant ions obtained during the residence time of the ions in the cell; and

(ii) The ATDs of the reactant and product ions are identical indicating that the product and reactant ions in the equilibrium are coupled reactively faster than their movement through the cell.

(iii) The equilibrium constant is independent of the partial pressure of the neutral reactant.

After equilibrium conditions have been established, the equilibrium constant, K_{eq}, can be measured using equation 2.

$$K_{eq} = I(A^{+}(HCN)_{n})/((I(A^{+}(HCN)_{n-1})P_{HCN}) \qquad (5.2)$$

Here $I[A^{+}(HCN)_{n-1}]$ and $I[C6H6^{+}(HCN)_{n}]$ are the integrated intensities of the ATDs of the reactant and product ions respectively, and P_{HCN} is the pressure of HCN in the reaction cell in atm. The equilibrium constant, K_{eq}, is obtained at different temperatures, and the thermodynamic quantities ΔH° and ΔS° are obtained from the slope and intercept, respectively, of the van't Hoff plot. All values measured in this experiment were duplicated at least three times, and the average values are shown in Tables1 and 2 with their corresponding uncertainties.

Density Functional Theoretical calculations of the lowest energy geometries for the various isomers of the cluster ions $A^{\bullet+}(HCN)_n$ [A=$C_6H_4F_2^{\bullet+}$, $C_6H_5F^{\bullet+}$, or $C_7H_5N^{\bullet+}$ respectively] were done at the B3LYP/6-311++G(d,p) level of theory using the Gaussian03 program suite.[139] Frequency calculations were also performed for all the optimized geometries at the same level of theory in order to obtain zero point vibrational energy (ZPVE), to calculate ΔH° values at 298 K, and also to verify the absence of any imaginary frequencies. The ΔH° values at 298 K for the stepwise formation of $A^{\bullet+}(HCN)_n$ [A = $C_6H_5F^{\bullet+}$, 1,4-$C_6H_4F_2^{\bullet+}$, or $C_6H_5CN^{\bullet+}$ respectively], n = 1−4, were also calculated for the lowest energy structures according to thermochemical calculations outlined in the Gaussian03 program.[139]

5.3 Results And Discussion

5.3.1 Mass Spectra and Arrival Times Distributions

Figure 37a shows the mass spectrum collected following the injection of mass selected fluorobenzene radical cation into the drift cell containing 0.598 Torr helium only, at 300K. This spectrum shows that there are no dissociation products of the $C_6H_5F^{\bullet+}$ ion, due to the low injection energy used in our study, (13.1 eV, laboratory frame) which allows the ions to enter the drift cell against the back-flow of the helium gas escaping through the orifice. Figures 37b-d shows the mass spectra obtained when the $C_6H_5F^{\bullet+}$ ion is injected into the drift cell containing HCN vapor at different temperatures. Figure 37b shows the first and second additions HCN to the $C_6H_5F^{\bullet+}$ ion yielding $C_6H_5F^{\bullet+}(HCN)_n$ with n = 1 and 2 respectively at 0.26 Torr HCN in He and 302K. The $C_6H_5F^{\bullet+}$ ion is observed to disappear as the temperature decreases and the equilibrium shifts to the higher addition products of $C_6H_5F^{\bullet+}$ (HCN)$_n$ as shown in figures 37c, d and e. Figure 37c was obtained by injecting $C_6H_5F^{\bullet+}$ into 0.215 Torr HCN at 245 K. The spectrum in figure 37d was collected with 0.194 Torr HCN at 214 K, while figure 37e was collected with 0.115 Torr HCN at 179K, the lowest temperature we were able to attain before HCN vapor froze in the cell. Under this condition we observed $C_6H_5F^{\bullet+}$ $(HCN)_4$ as the most dominant peak.

To verify equilibrium, we collected arrival time distributions (ATD's) for the $C_6H_5F^{\bullet+}$ (HCN)$_{n-1}$, $C_6H_5F^{\bullet+}$ (HCN)$_n$, and $C_6H_5F^{\bullet+}$ (HCN)$_{n+1}$ ions. In principle, reactant and product ions coupled by equilibrium in an association reaction will have identical ATDs, due to the fact that for example, $C_6H_5F^{\bullet+}$(HCN)$_{n-1}$ will exist in a fixed ratio with respect to $C_6H_5F^{\bullet+}$ (HCN)$_n$ and switches back and forth faster than the drift of the ions in the cell.

Figure 38 shows the overlapping of the ATDs of $C_6H_5F^{\bullet+}$ (HCN)$_n$, with n=0-4, indicating that the ions are under equilibrium conditions.

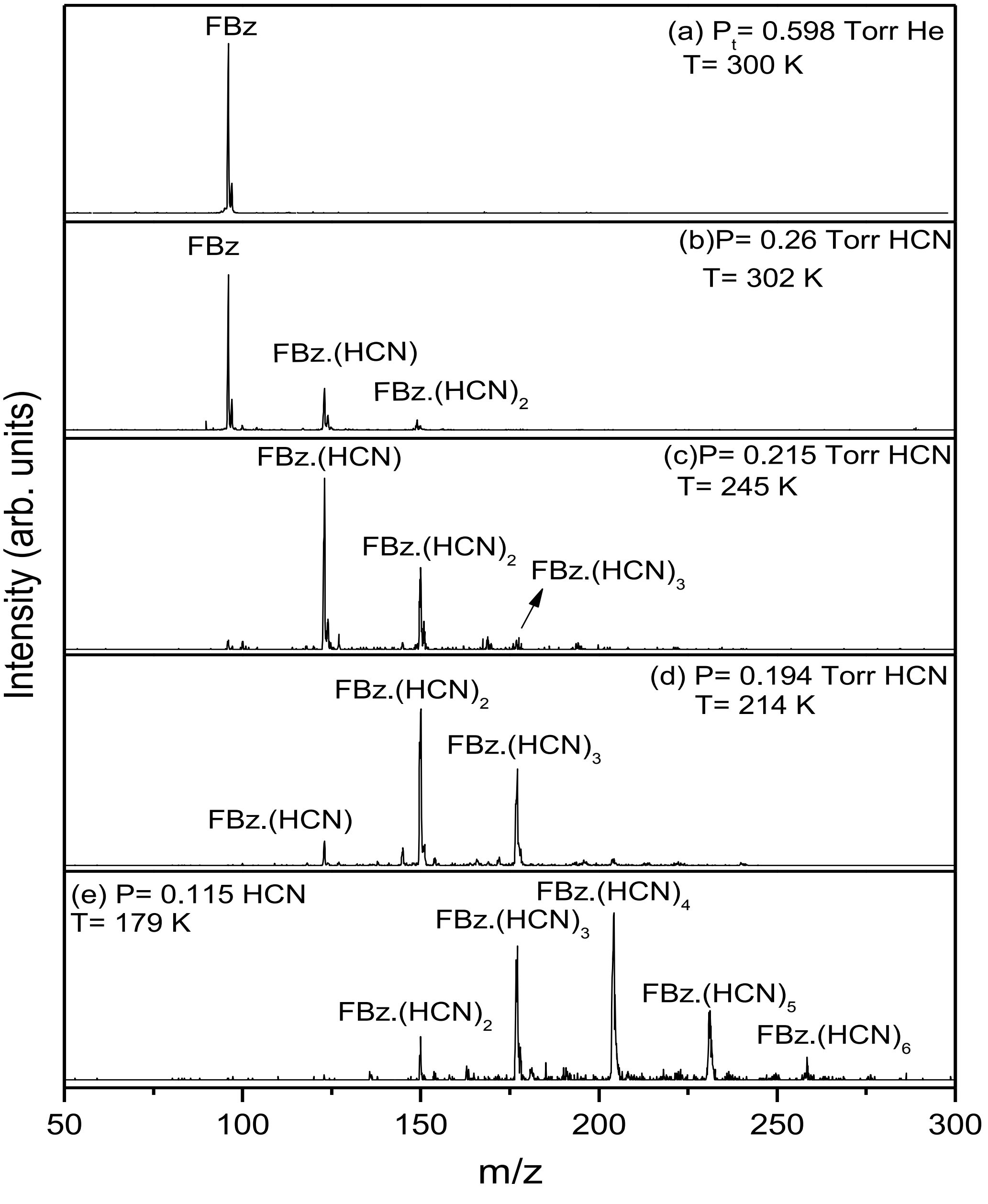

Figure 37: Mass spectra obtained following the injection of the mass selected the $C_6H_5F^{\bullet+}$ (FBz) into the drift cell containing He or HCN vapor at different pressures and temperatures as indicated. Similar mass spectra was obtained for the 1, 4-Difluorobenzene$^{\bullet+}$/HCN system under similar experimental conditions.

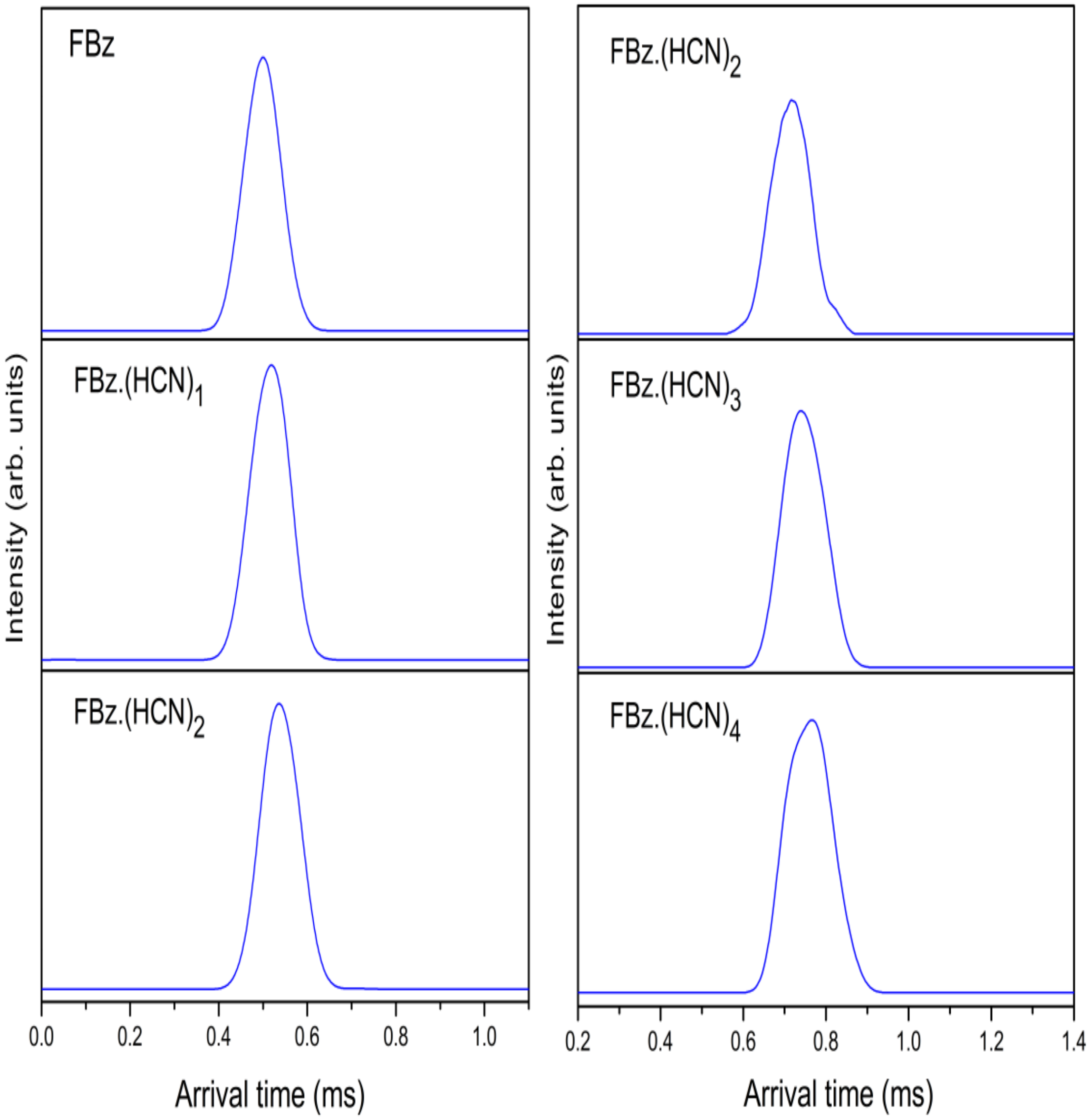

Figure 38: Arrival Time Distributions of the $C_6H_5F^{\bullet+}$ (HCN)n ions with n = 0 − 2 obtained following the injection of mass selected fluorobenzene ions into 0.2 Torr of HCN vapor at 263 K (left) and at 203 K for n = 2−4 (right). Similar ATD overlap was observed for the 1, 4-difluorobenzene$^{\bullet+}$/HCN system under similar experimental conditions.

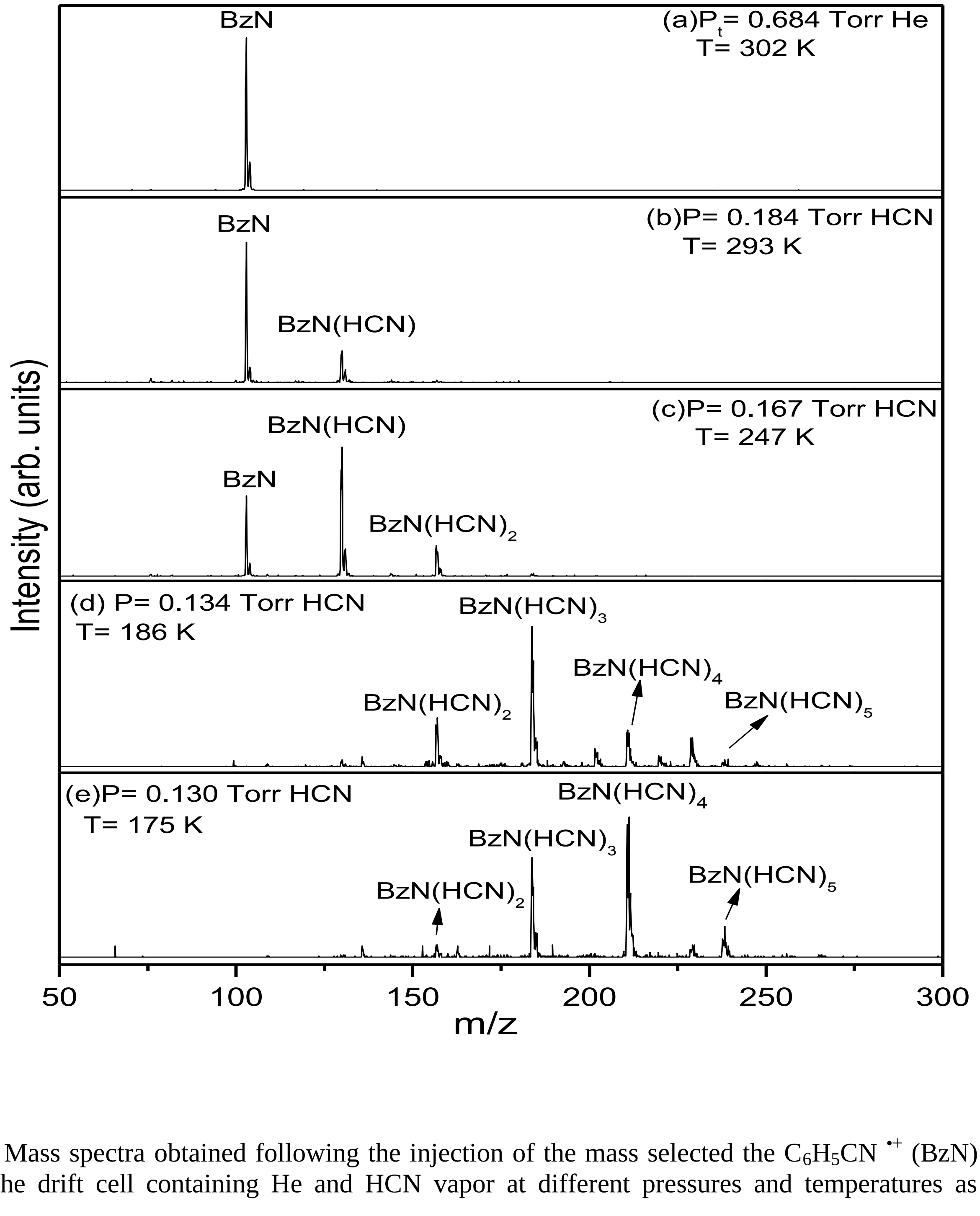

Figure 39: Mass spectra obtained following the injection of the mass selected the $C_6H_5CN^{\bullet+}$ (BzN) ions into the drift cell containing He and HCN vapor at different pressures and temperatures as indicated.

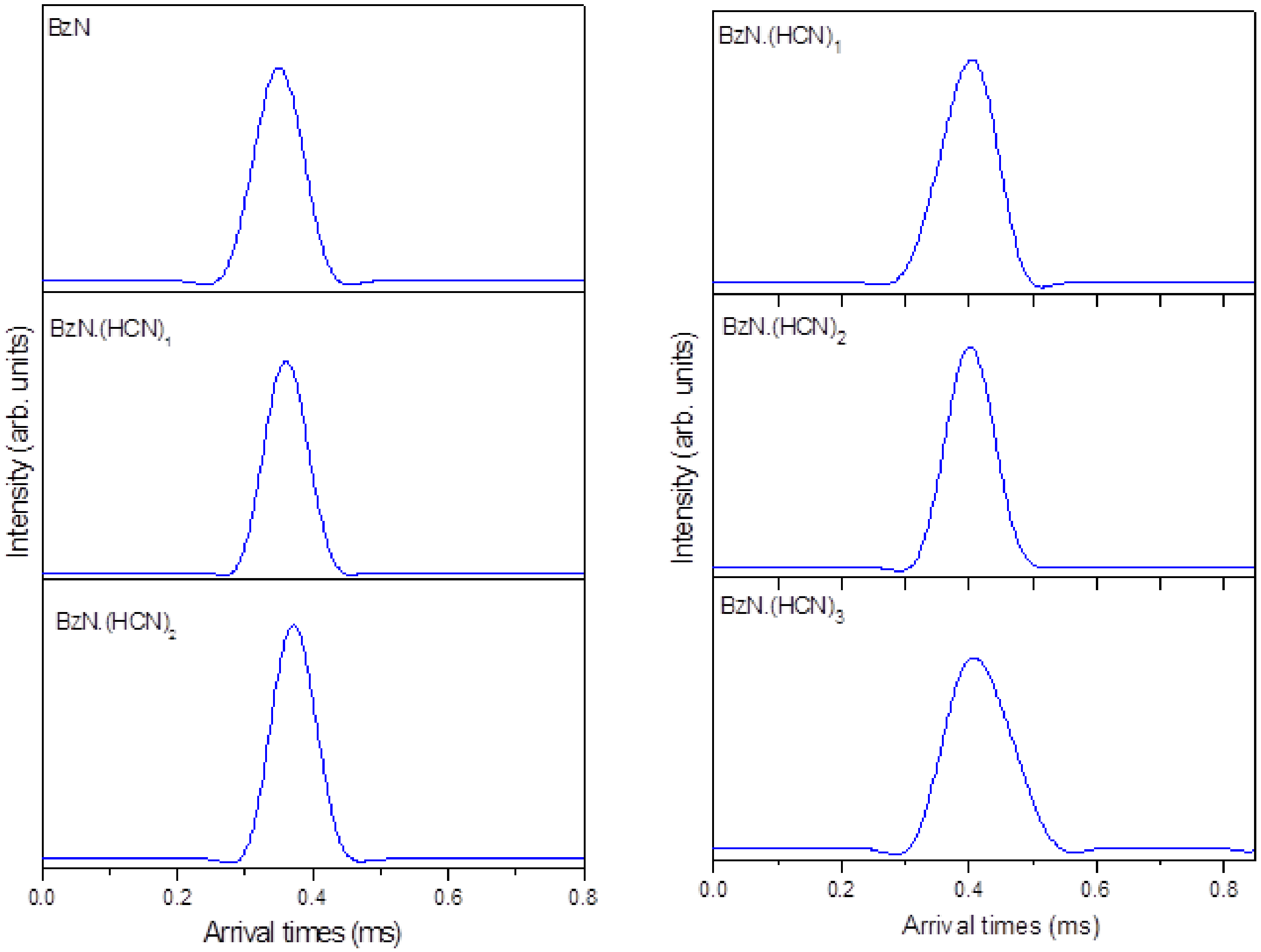

Figure 40: Arrival Time Distributions of the $C_6H_5CN^{\bullet +}$ (HCN)n ions with n = 0 − 2 obtained following the injection of mass selected fluorobenzene ions into 0.15 Torr of HCN vapor at 238 K (left) and at 209 K for n = 2−4 (right).

Mass spectra for the 1, 4-Difluorobenzene$^{\bullet+}$/HCN system were obtained by similar methods as for Fluorobenzene$^{\bullet+}$/HCN system, at 159, 219, 259 and 300 K, and show similar trend of shifting the cluster distributions to higher cluster at low temperatures. Clusters with up to 6 HCN molecules were observed at 159 K. The ATDs were also collected at 269 and 208 K and showed overlap similar to Figure 38 for fluorobenzene$^{\bullet+}$/HCN.

Similar to the above observations, Figure 39a shows the mass spectrum of mass selected benzonitrile radical cation into 0.684 Torr pure helium at 302 K. In figures 39b-d is the mass spectra of $C_6H_5CN^{\bullet+}$ /HCN system obtained by injecting the mass selected $C_6H_5CN^{\bullet+}$into the drift cell containing HCN vapor at different temperatures. Again, as the temperature of the drift cell is lowered, the equilibrium conditions tend to favor the higher $C_6H_5CN^{\bullet+}(HCN)_n$ cluster ions, with gradual diminishing and eventual disappearance of the $C_7H_5N^{\bullet+}$ ion. The ATDs of the $C_6H_5CN^{\bullet+}$ $(HCN)_n$ ions also overlapped giving further evidence for the attainment of equilibrium conditions.

5.4 Thermochemistry, Binding Energies and Structures

The measured equilibrium constants yielded the van't Hoff plots in Figures 41 to 43, and the thermochemical ΔH° and ΔS° values in Tables 1-3, which also present the DFT binding energies ΔE°, calculated at the B3LYP/6-311++G(d, p) at 298K. For all the ions, we were able to measure the ΔH° and ΔS° for up to the fourth addition, i.e. $\Delta H°_{3,4}$ and $\Delta S°_{3,4}$. The experimental binding energies of HCN for the present ions along with $C_6H_6^{\bullet+}$ [60] and $C_6H_5CHCH_2^{\bullet+}$ [114] are summarized in Table 4. The DFT computed structures and the NBO charges for all three ions and the HCN molecule are shown in Figures 44 and 45,

5.4.1.1 Addition of the First HCN Molecule

Comparing theory and experiment, the first HCN molecule binds to the fluorobenzene$^{\bullet+}$ and 1, 4-difluorobenzene$^{\bullet+}$ radical cations with a measured binding energy of 11.2±1 kcal•mol^{-1}, and a calculated binding energy of 9.60 kcal•mol^{-1}and 9.85 kcal•mol^{-1} respectively. These binding energies show that the second fluorine substituent atom at the para position has little effect on the binding to the HCN molecule. This is also confirmed by the calculated DFT optimized lowest energy geometries of the ions, shown in Figure 44, which shows that the first HCN molecule binds to the fluorobenzene radical cation at an angle of 87.1° to the plane of the fluorobenzene ion with a bond length of 2.84 Å, and similar geometries are observed with the difluorobenzene radical cation, with the ion plane-to-molecule angle and bond length of 88.1°, and 2.88 Å respectively. The ΔS° values are also similar within the experimental uncertainty of ±2 cal•mol^{-1}•K^{-1}, consistent with the energetic and structural similarities.

The experimentally measured binding energy of benzonitrile$^{\bullet+}$(HCN) of 9.6kcal•mol^{-1} is in excellent agreement with the calculated binding energy of 9.5kcal•mol^{-1}.The DFT optimized lowest energy geometry of the $C_6H_5CN^{\bullet+}$(HCN) cluster ion shows a bifurcated structure, with the HCN binding to two C-H hydrogen atoms by 2.7Å and 2.4 Å bonds in the same plane, as shown in Figure 44. Hamid *et al*[60], through experimental and theoretical investigations of benzene$^{\bullet+}$(HCN) and benzene$^{\bullet+}$(H_2CCHCN) determined that these clusters have similar bifurcated structures as $C_6H_5CN^{\bullet+}$(HCN), and very similar Δ*H*° and Δ*S*° values.

Further, the measured binding energies of the second HCN to the $C_6H_5F^{\bullet+}$(HCN) and $C_6H_4F_2^{\bullet+}$(HCN) ions in Tables 1 and 2 show a close resemblance of the two ions both in experiment and in theory. The measured BDE for n = 1 and 2 are 9.0 kcal•mol^{-1} and 9.3

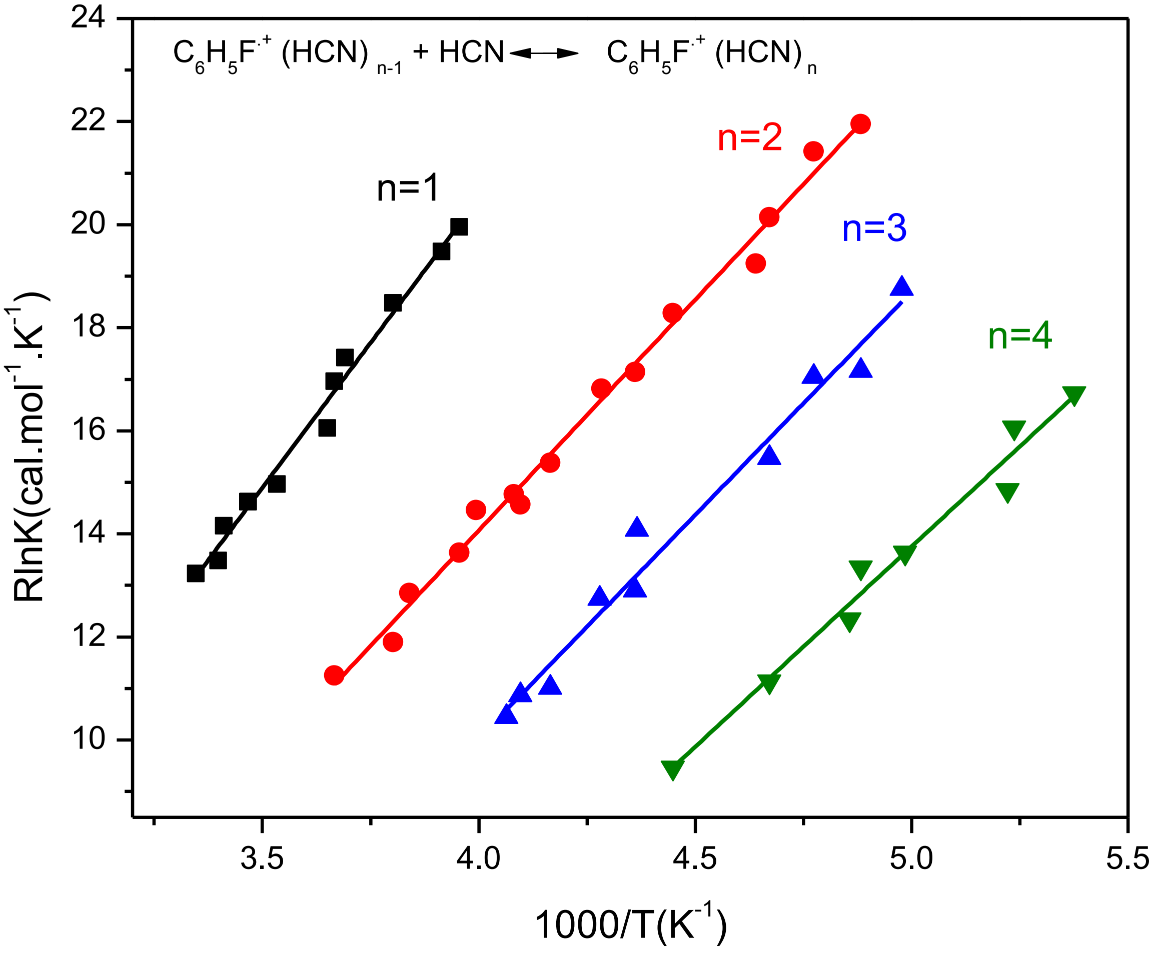

Figure 41: Van't Hoff plots for the $C_6H_5F^{\bullet+}(HCN)_{n-1}$ + HCN ↔ $C_6H_5F^{\bullet+}(HCN)_n$ association reactions for n = 1−4 as indicated.

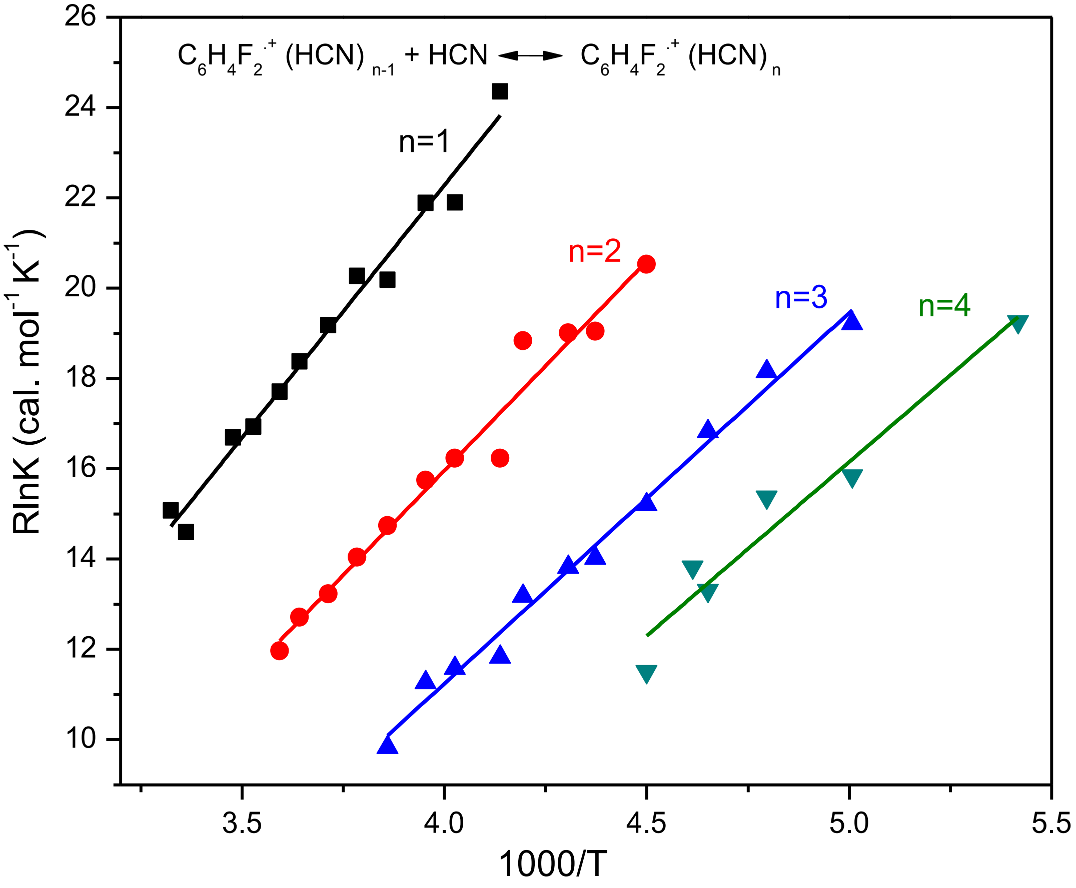

Figure 42: Van't Hoff plots for the $C_6H_4F_2^{\bullet+}(HCN)_{n-1}$ +HCN ↔$C_6H_4F_2^{\bullet+}(HCN)_n$ association reactions for n = 1−4 as indicated.

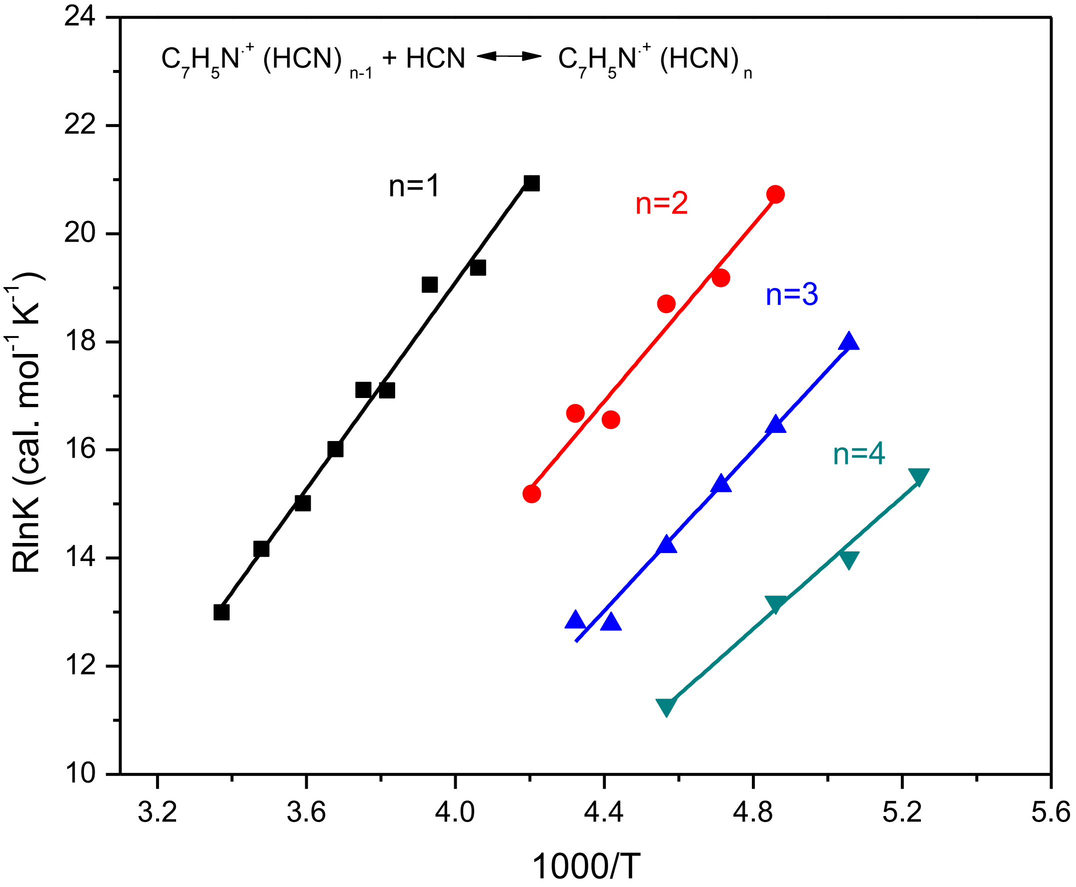

Figure 43: Van't Hoff plots for the $C_6H_5CN^{\bullet+}(HCN)_{n-1}$ + HCN $\leftrightarrow C_6H_5CN^{\bullet+}(HCN)_n$ association reactions for n = 1−4 as indicated.

kcal•mol^{-1} for $C_6H_5F^{•+}(HCN)_n$ and 1,4-$C_6H_4F_2^{•+}(HCN)_n$ respectively, which agree well with the calculated $\Delta E°$ values of 8.5 kcal•mol^{-1} and 8.6 kcal•mol^{-1}, respectively. Based on these observations, the B3LYP/6-311++G (d, p) level of theory yielded satisfactory results for the present systems.

The non-covalent adducts of HCN to the ionized aromatics are bonded primarily by electrostatic forces both in planar hydrogen-bonded structures and in vertical L-shaped structures in Figures 44 and 45. For example, only 0.035 charge is transferred from $C_6H_5F^{•+}$ to the HCN ligand in Figure 44c. Although the results show comparable binding energies of HCN to all the ions, they result from different interactions with different charge centers. The atomic charges on the ions are therefore of interest.

In fluorobenzene, the electronegative F atom is significantly negative and its carbon is has a high partial positive charge (0.410) in the neutral molecule, and even more (0.603) in the ion (Figures 44a, 44b). It appears that fluorine substitution creates a π hole at this carbon. The negative N end of HCN (-0.308) (Figures 44f) can interact attractively with the large positive charge at this carbon, although this can be counterbalanced in part by repulsion with the adjacent F atom (-0.235) and ortho carbons (-0.194). On the other hand, in hydrogen bonding to the ring hydrogens, especially the para hydrogen, HCN interacts with a smaller positive charge (0.240), but is not destabilized by nearby negative charges. These effects balance out fortuitously to lead to practically equal binding energies in the planar and vertical isomers (Figures 45, ions F1a and F1b). Similar charges, interactions and binding energies apply in 1,4-difluorobenzene. (Figures 44d and Fig.45, ions dF1a and dF1b) However, in benzonitrile$^{•+}$, although the CN group is electron withdrawing, there are no large positive charges on the ring carbons, (Figure 44e) and a planar bifurcated hydrogen-bonded structure has the lowest energy, although a vertical electrostatic structure has very similar energy, maybe somewhat fortuitously. (Figure 45, ions B1a and B1c) This is basically similar to benzene$^{\bullet+}$(HCN), which also has lowest energy planar structure, as well as vertical structure with HCN pointing to the center of the ring[60] Moreover, despite the different charge distributions, interactions and structures, the binding energies of all of these dimers are similar, within a small range of 9.2 – 11.2 kcal•mol^{-1} for these ions.

5.4.1.2 Addition of the Second HCN Molecule

In adding further solvent molecules, two types of clusters can build up. In “externally solvated” structures the ligand molecules bind to each other and the ion is outside of the solvent cluster. In “internally solvated” structures the ligand molecules bind directly to the ions and it is inside the solvent cluster. Mixed structures are also possible with several solvent molecules which can have both types of arrangements in one cluster. In the present clusters we observe all three types of structures (Figures 46 and 49)

The DFT optimized lowest energy geometry of the $C_6H_5F^{\bullet+}$ $(HCN)_2$ and $C_6H_4F_2^{\bullet+}$ $(HCN)_2$ (Figure 8) shows that the second addition of the HCN leads to the formation of an “externally solvated” structure where the second solvent molecule binds to the first, rather than binding directly to the ring structure of the ion. For $C_6H_5F^{\bullet+}(HCN)_2$, the second HCN molecule binds to the first in the same plane with a slight increase in the bond angle (2.8°) and a bond length of 2.1 Å. The bond length between the aromatic ring and the first HCN is also reduced upon the second HCN binding. In the case of 1,4-$C_6H_4F_2^{\bullet+}(HCN)_2$, the second HCN molecule binds with a bond

Table 1: Measured and computed thermochemistry of the stepwise clustering reactions of HCN molecules with $C_6H_5F^{\bullet+}$ radical cations (equation 1).[a]

n	$-\Delta H°_{n-1, n}$	$-\Delta S°_{n-1, n}$	$-\Delta E°_{n-1, n}$
1	11.2	24.4	9.6
2	9.0	21.8	8.5
3	8.7	24.6	7.9
4	7.8	25.1	7.4

a. Units: ΔH° and ΔE°, kcal•mol$^-$1, ΔS° cal•mol^{-1}•K^{-1} Error estimate for experimental values from standard deviations of van't Hoff and from usual uncertainties in clustering equilibrium temperature studies: ΔH° ±1 kcal•mol^{-1}, ΔS° ±2 cal•mol^{-1}•K^{-1}.

Table 2: Measured and computed thermochemistry of the stepwise clustering reactions of HCN molecules with 1,4-$C_6H_5F^{\bullet+}$ radical cations (equation 1).[a]

N	$-\Delta H°_{n-1, n}$	$-\Delta S°_{n-1, n}$	$-\Delta E°$
1	11.2	22.5	9.8
2	9.3	21.1	8.6
3	8.2	21.6	7.9
4	7.7	22.3	7.3

a. Units: ΔH° and ΔE°, kcal•mol$^-$1, ΔS° cal•mol^{-1}•K^{-1}Error estimate for experimental values from standard deviations of van't Hoff and from usual uncertainties in clustering equilibrium temperature studies: Δ*H*° ±1 kcal•mol^{-1}, Δ*S*° ±2 cal•mol^{-1}•K^{-1}.

Table 3: Measured and computed thermochemistry of the stepwise clustering reactions of HCN molecules with $C_6H_5CN^{\bullet+}$ radical cations (equation 1).[a]

N	$-\Delta H°_{n-1,\,n}$	$-\Delta S°_{n-1,\,n}$	$-\Delta E°$
1	9.6	19.1	9.5
2	8.2	19.0	8.5
3	7.4	19.6	7.6
4	6.1	16.6	7.3

a. Units: ΔH° and ΔE°, kcal•mol$^-$1, ΔS° cal•mol^{-1}•K^{-1}Error estimate for experimental values from standard deviations of van't Hoff and from usual uncertainties in clustering equilibrium temperature studies: $\Delta H°$ ±1 kcal•mol^{-1}, $\Delta S°$ ±2 cal•mol^{-1}•K^{-1}.

Table 4: Measured association enthalpies for the stepwise solvation of aromatic radical cations $M^{\bullet+}$ by 1-4 HCN molecules (kcal•mol^{-1})

	$-\Delta H°_{n-1,\,n}\,[M^{\bullet+}(HCN)_n]$				
n	$C_6H_6^{\bullet+\,a}$	$C_6H_5CN^{\bullet+}$	$C_6H_5CCH^{\bullet+\,b}$	$C_6H_5F^{\bullet+}$	$1,4\text{-}C_6H_4F_2^{\bullet+}$
1	9.2	9.6	10.5	11.2	11.2
2	8.0	8.2	9.0	9.0	9.3
3	7.5	7.4	8.2	8.7	8.2
4	7.3	6.1	7.2	7.8	7.7

[a] Reference 60
[b] Reference 114

length of 2.1 Å to the first HCN, and the bond length of the first HCN with the difluorobenzene ion slightly reduces by 0.1Å.

For the $C_6H_5CN^{\bullet+}(HCN)_{1,2}$ addition we observe 8.2 kcal•mol^{-1} and 8.5 kcal•mol^{-1} as the experimentally measured and theoretically computed binding energies, respectively, which are in excellent agreement. Unlike the second addition of HCN to $C_6H_5F^{\bullet+}(HCN)$ and $C_6H_4F_2^{\bullet+}(HCN)$ which leads to externally solvated cluster complex, the second addition of HCN to the $C_6H_5CN^{\bullet+}$ (HCN)cluster ion binds directly to a C-H hydrogen at the ortho position on the aromatic ring of the $C_6H_5F^{\bullet+}$ ion with a 2.2Å bond (Figure 46, ion B2a). Comparing the experimental measured and theoretically computed binding energies in Tables 1-3 for the second addition of the HCN ligand to all the three ions shows similar bond strengths between the $M^{\bullet+}(HCN)$ ions and the second HCN ligand, even though $C_6H_5F^{\bullet+}(HCN)$ and $C_6H_4F_2^{\bullet+}(HCN)$ form externally solvated complex ions, whereas $C_6H_5CN^{\bullet+}(HCN)$ forms an internally solvated complex ion. Previous studies in ionized aromatic clusters with HCN also found similar experimental and theoretical binding energies for the second addition of HCN to the $M^{\bullet+}(HCN)$ cluster ion as 8.0 kcal•mol^{-1} and 8.2 kcal•mol^{-1}for benzene radical cation[60], 9.0 kcal•mol^{-1}and 7.6 kcal•mol^{-1}for phenylacetylene radical cation[114] respectively. These binding energies follow the common trend of decreasing binding energies of consecutive ligand molecules to cluster ions due to the increasing charge delocalization in the cluster and consequently, decreasing charge at the binding sites. As in all such clusters, the binding energies converge toward the enthalpy of vaporization of the ligand,[135] here 6.0 kcal•mol^{-1} for $\Delta H^{o}_{vap}(HCN)$ at 298K.

These observations suggests that after the first HCN ligand, the influence of the molecular ion on the strength of the bond formed between the $M^{\bullet+}(HCN)$ and the incoming HCN ligand is reduced, and it depends more on the nature of the incoming ligand. Hamid *et. al* [60] found the second acrylonitrile ligand bound to the $C_6H_6\,^{\bullet+}(H_2CCHCN)$ cluster ions with a binding energy value of 10.7 kcal•mol^{-1}, while Ibrahim and coworkers [122] found a binding energy of a second H_2O molecule to $C_6H_6\,^{\bullet+}(H_2O)$ to be 8.0kcal•mol^{-1}. This trend validates the conclusion reached by Hamid *et. al*[60] that ligands with higher dipole moments will bind more strongly to the $M^{\bullet+}(X)$ [X=HCN, C_3HCN, H_2O, etc.] with less dependence of the identity of the core ions. This could suggest that most of the rearrangement of the charge density of the molecular ion due to adding a ligand occurs after the first addition, while the second addition only alters the charge distribution minimally and has little influence the effective binding energy.

5.4.1.3 Addition of the Third HCN Molecule

The third HCN in $C_6H_5F^{\bullet+}(HCN)_3$ and 1,4- $C_6H_4F_2^{\bullet+}(HCN)_3$ bonds directly to ring hydrogens, forming structures with elements of both internally and externally solvated cluster ions (Figure 47, ions F3a and dF3a). In $C_6H_5F^{\bullet+}(HCN)_3$ (F3a) the third HCN molecule forms a bifurcated structure with the two C-H hydrogens at the meta and para positions of the aromatic ring, while in 1,4- $C_6H_4F_2^{\bullet+}(HCN)_3$ the incoming HCN binds to the C-H hydrogen at the meta position with respect to the first HCN molecule on the aromatic ring (dF3a) . In the case of $C_6H_5CN^{\bullet+}(HCN)_3$, the third HCN binds to the first HCN “externally” (B3a). The measured binding energies for the third addition of HCN unto the three aromatic ions agree excellently with the calculated values, as shown in Tables 1-3. The binding energy of the third addition is still slightly higher for $C_6H_5F^{\bullet+}(HCN)_3$ and 1,4-$C_6H_4F_2^{\bullet+}(HCN)_3$ than for $C_6H_5CN^{\bullet+}(HCN)_3$.

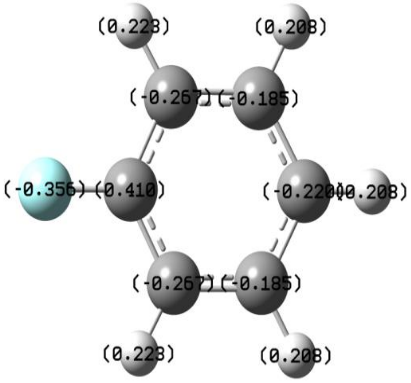

44a

Neutral C_6H_5F

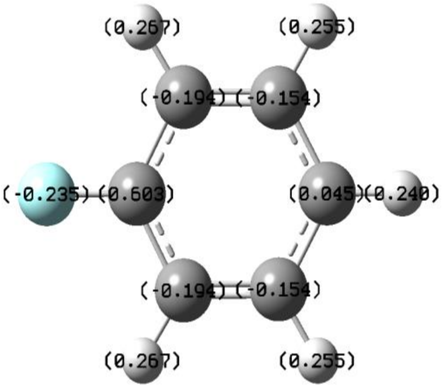

44b

$C_6H_5F^{\bullet+}$

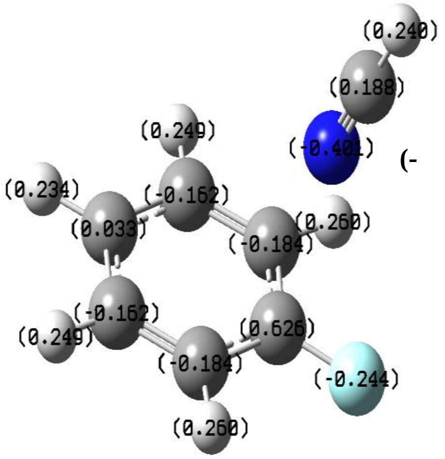

44c

$C_6H_5F^{\bullet+}$(HC

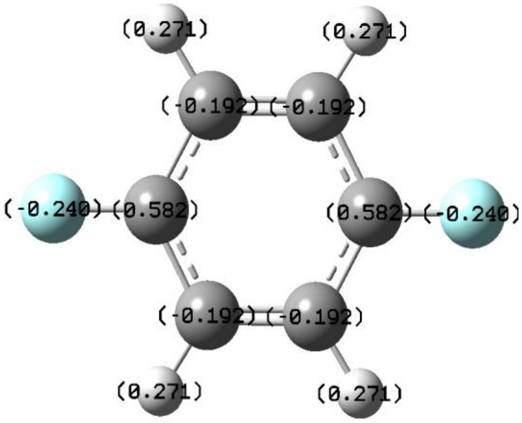

44d

$C_6H_4F_2^{\bullet+}$

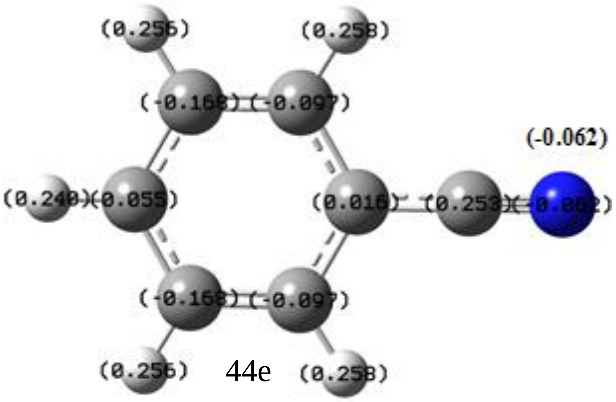

44e

$C_6H_5CN^{\bullet+}$

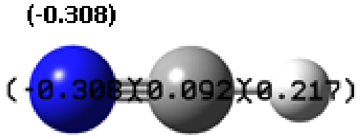

44f

Neutral HCN

Figure 44: DFT computed natural bond orbital charges (NBO) at the B3LYP/6-311++G(d,p) level of theory for (44a) fluorobenzene, (44b) fluorobenzene$^{\bullet+}$, (44c) fluorobenzene$^{\bullet+}$(HCN), (44d) 1,4-difluorobenzene$^{\bullet+}$ and (44e) benzonitrile$^{\bullet+}$, (44f) HCN.

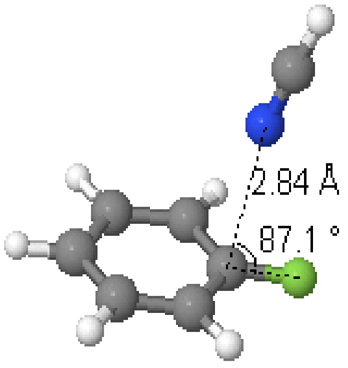

F1a

Rel. E = 0.0

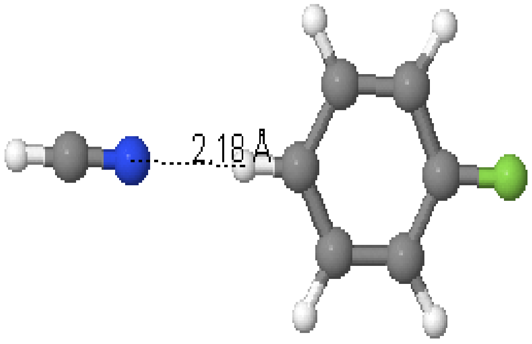

F1b

Rel. E = 0.2385

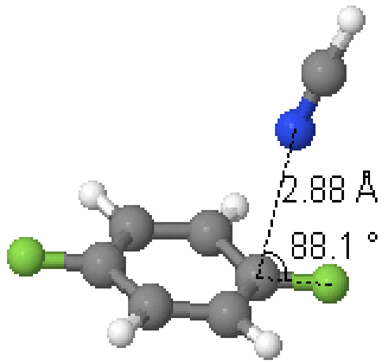

dF1a

Rel. E = 0.0

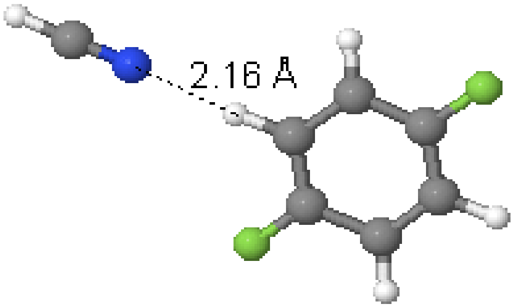

dF1b

Rel. E = 0.3483

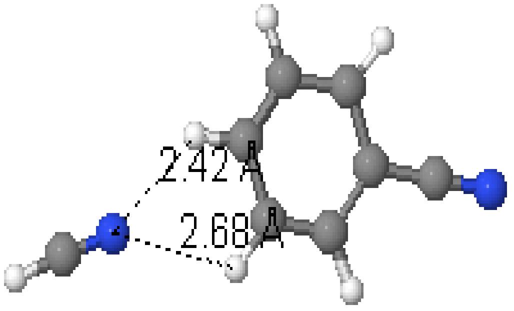

B1a

Rel. E = 0.0

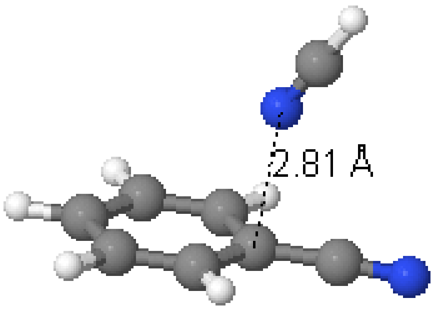

B1c

Rel. E = 0.2981

Figure 45: Selected DFT optimized structures for the $A^{\bullet+}$(HCN) cluster complex ions [A = $C_6H_5F^{\bullet+}$, 1,4-$C_6H_4F_2^{\bullet+}$, or $C_6H_5CN^{\bullet+}$ respectively], showing the relative energies(R.E) in reference to the lowest computed energy given in Tables 1-3. Energies in kcal•mol^{-1}.

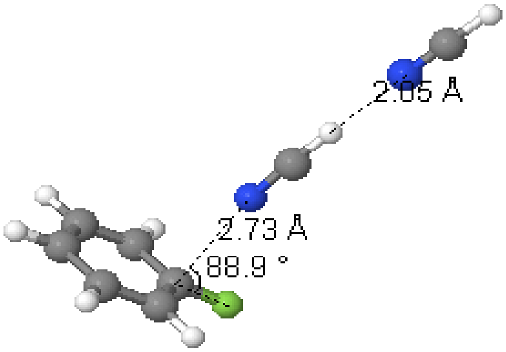

F2a

Rel. E = 0.0

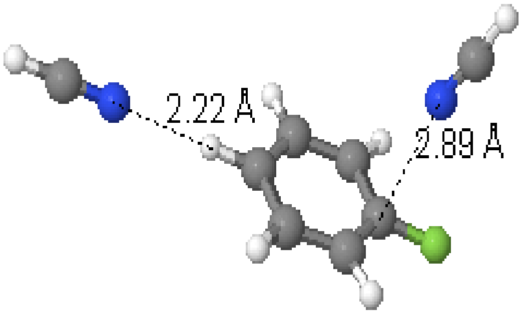

F2b

Rel. E = 0.2560

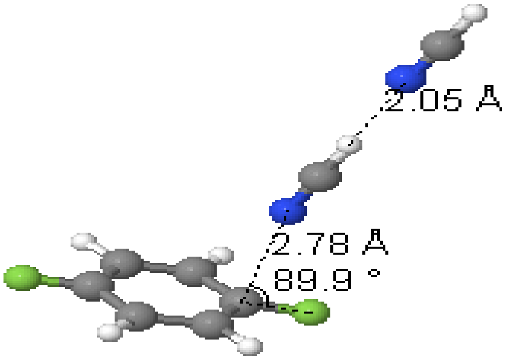

dF2a

Rel. E = 0.0

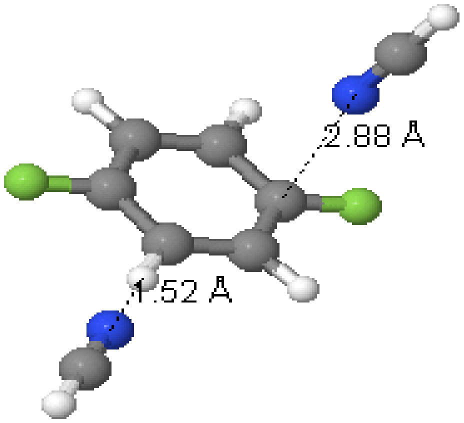

dF2b

Rel. E = 0.1977

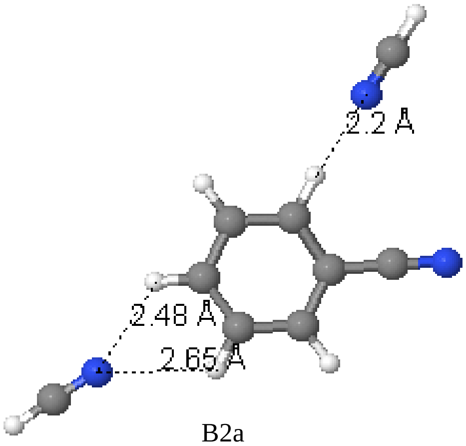

B2a

Rel. E = 0.0

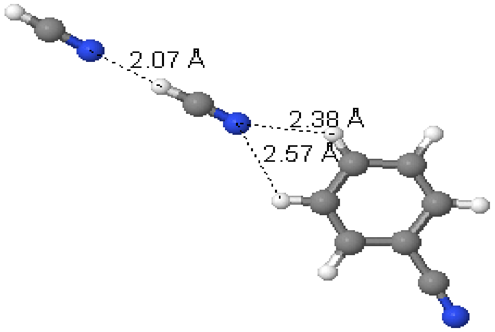

B2d

Rel. E = 0.4826

Figure 46: Selected DFT optimized structures for the $A^{\bullet+}(HCN)_2$ cluster complex ions [A = $C_6H_5F^{\bullet+}$, 1,4-$C_6H_4F_2^{\bullet+}$, or $C_6H_5CN^{\bullet+}$ respectively] showing the relative energies(R.E) in reference to the lowest computed energy given in Tables 1-3. Energies in kcal•mol^{-1}

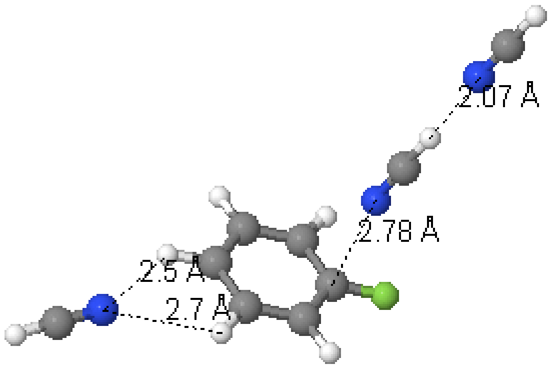

F3a

Rel. E = 0.0

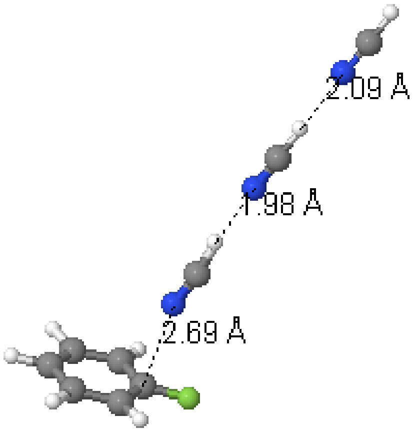

F3d

Rel. E = 0.7166

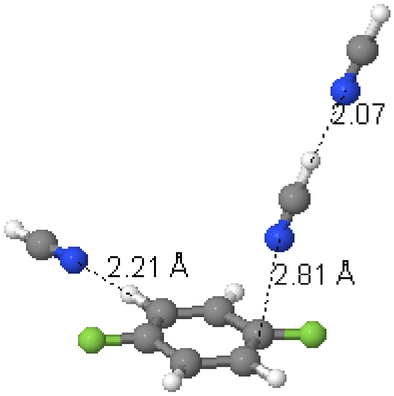

dF3a

Rel. E = 0.0

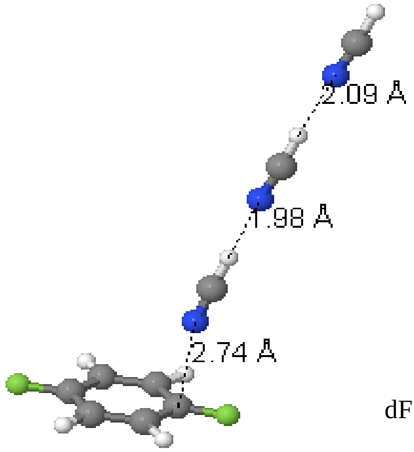

dF3e

Rel. E = 0.7254

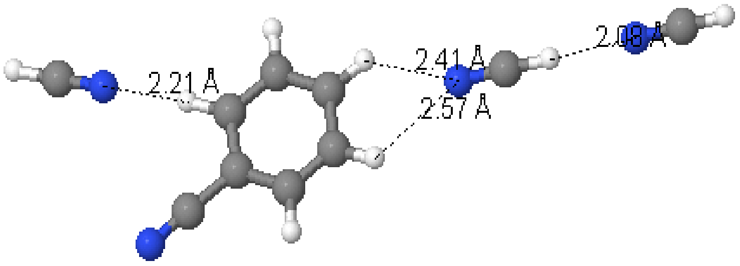

B3a

Rel. E = 0.0

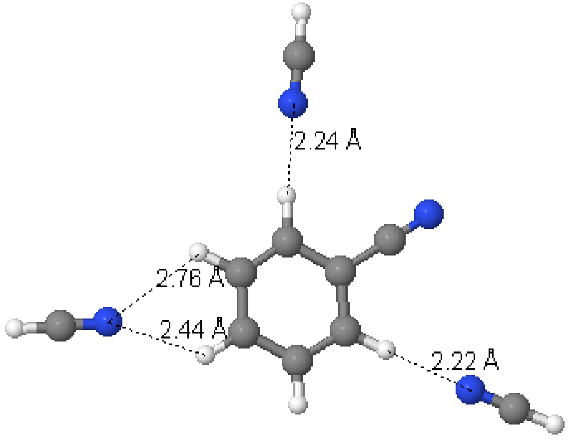

B3b

Rel. E = 0.1970

Figure 47: Selected DFT optimized structures for the $A^{\bullet+}(HCN)_3$ cluster complex ions [A = $C_6H_5F^{\bullet+}$, 1,4-$C_6H_4F_2^{\bullet+}$, or $C_6H_5CN^{\bullet+}$ respectively] showing the relative energies(R.E) in reference to the lowest computed energy given in Tables 1-3. Energies in kcal•mol^{-1}.

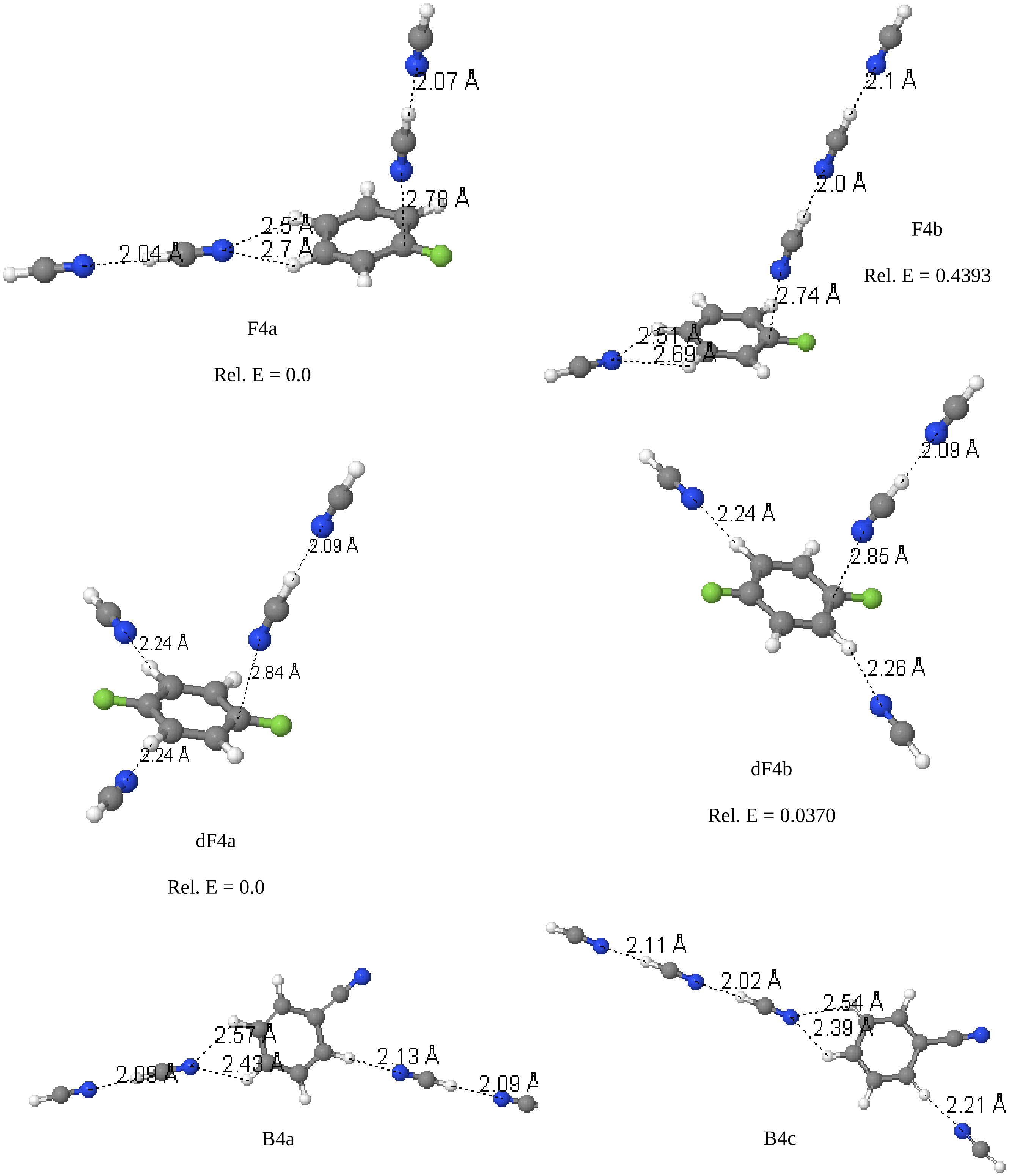

F4a

Rel. E = 0.0

F4b

Rel. E = 0.4393

dF4a

Rel. E = 0.0

dF4b

Rel. E = 0.0370

B4a

Rel. E = 0.0

B4c

Rel. E = 0.5723

Figure 48: Selected DFT optimized structures for the $A^{\bullet+}(HCN)_4$ cluster complex ions [A = $C_6H_5F^{\bullet+}$, 1,4-$C_6H_4F_2^{\bullet+}$, or $C_6H_5CN^{\bullet+}$ respectively] showing the relative energies(R.E) in reference to the lowest computed energy given in Tables 1-3. Energies in kcal•mol^{-1}.

5.4.1.4 Addition of the Fourth HCN Molecule

In $C_6H_5F^{\bullet+}(HCN)_4$, the fourth HCN binds externally to the third bifurcated HCN with a bond length of 2.0Å (ion F4a). The measured binding energy for this addition is 7.8 kcal•mol^{-1} in good agreement with the DFT calculated value of 7.4 kcal•mol^{-1}. The fourth HCN in $C_6H_4F_2^{\bullet+}(HCN)_4$ binds externally to 2nd meta position on the aromatic ring as shown in (ion dF4a), with a bond length of 2.2Å. The measured binding energy of 7.7 kcal•mol^{-1} agrees well with the theoretical value of 7.3 kcal•mol^{-1}. In the benzonitrile cluster ion $C_6H_5CN^{\bullet+}(HCN)_4$ the fourth HCN ligand binds externally to the HCN at the ortho position, with a bond length of 2.1Å (ion B4a). The measured binding energy for this addition is 6.1 kcal•mol^{-1}, which is lower than the DFT lowest energy structure computed value of 7.3 kcal•mol^{-1}, but within the experimental uncertainty range of ±1 kcal•mol^{-1} for clustering equilibrium temperature studies.

5.5 Conclusions: Substituent Effects on the Binding Energies and Structures of Benzene Cations with Hydrogen Cyanide

Thermochemistry of the stepwise solvation of the radical cations fluorobenzene, difluorobenzene, and benzonitrile by 1 – 4 HCN molecules was investigated using the VCU ion mobility mass spectrometer and DFT computations, and with ionized benzene and phenylacetylene in previous studies [60,114]. Compared with $C_6H_6{}^{\bullet+}(HCN)_n$ clusters, the electron-withdrawing substituents increase slightly the ligand binding energies due to larger positive charges on the hydrogen bonding aromatic CH hydrogens, and in fluorobenzenes, by creating high positive charges or π holes on the fluorinated carbons.

However, the binding energies of an HCN molecule to all five ionized benzene derivatives are close, between 9.2 and 11.2 kcal•mol^{-1} The HCN ligand can form linear or bifurcated C-H---N ionic hydrogen bonds to all of the ions studied. With fluorobenzenes, it can form a vertical L-shaped geometry by bonding electrostatically to a positive charge center or π hole on the fluorinated carbon, but this attractive force is partially counterbalanced by repulsive interactions with the adjacent negative charges on fluorine and the ortho carbons. As a result, the in-plane hydrogen bonded and out-of-plane vertical structures have, fortuitously, nearly equal energies. With the other ionized aromatics the in-plane hydrogen bonded structures have lower energies, although stable vertical adducts are also available.

All the computed lowest energy geometries isomers had computed bond lengths of the aromatic ring to HCN of more than 2.0Å, indicating that no covalent bonds are being observed, consistent with the experimental binding energies below 11.2 2 kcal•mol^{-1}.

In higher clusters with 2 – 4 HCN molecules, the further ligand molecules can hydrogen bond to the core ions, or add to the first ligand molecules to form linear HCN---HCN--- chains hydrogen bonded to the core ions. With 3 – 4 HCN molecules both structural types can be found in the same cluster. In general, isomers with various structural types often have energies within 1 kcal•mol^{-1}. Therefore, the observed populations at thermal energies can contain equilibrium mixtures of these isomers.

Together with previous studies, these results show that ionized aromatics can form several different types of complexes, including π stacking and charge resonance, in-plane internally or externally solvated hydrogen-bonded structures or electrostatic out-of-plane complexes. Each type may be affected by substituents or fused ring substitutions on the ionized aromatics, but the present results suggest that these substituent effect may be small in general.

Figure 49: DFT optimized structures calculated B3LYP/6-311++G(d,p) structures of clusters of fluorobenzene$^{\bullet+}$, 1,4-difluorobenzene$^{\bullet+}$ and benzonitrile$^{\bullet+}$ with 1 – 4 HCN molecules. Energies in kcal•mol^{-1}.

BzN(HCN)$_1$

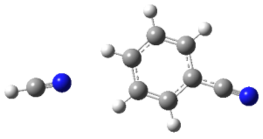

B1a

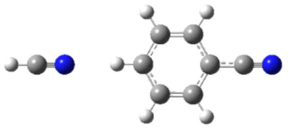

B1b

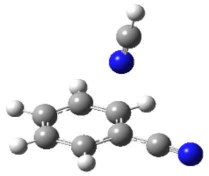

B1c

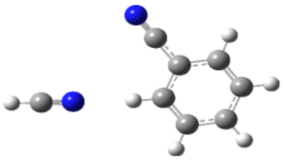

B1d

BzN(HCN)$_2$

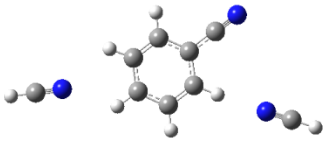

B2a

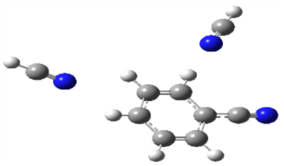

B2b

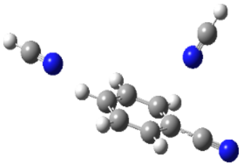

B2c

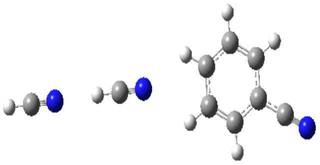

B2d

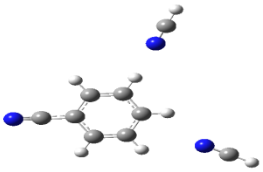

B2e

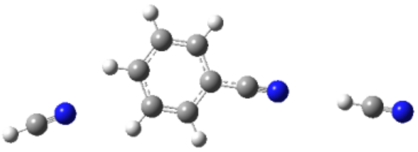

B2f

BzN(HCN)$_3$

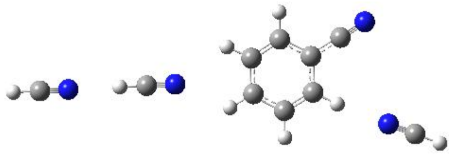

B3a

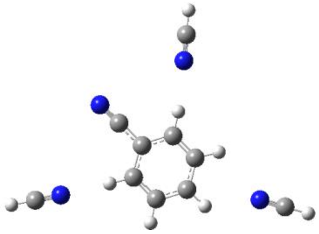

B3b

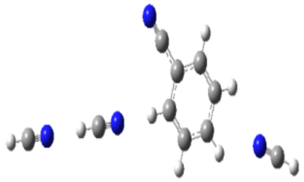

B3c

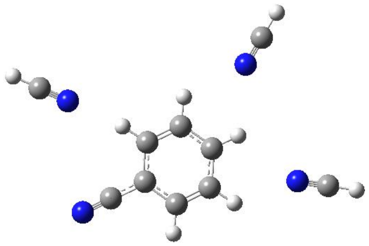

B3d

BzN(HCN)$_4$

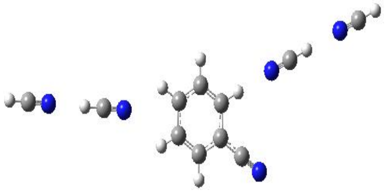

B4a

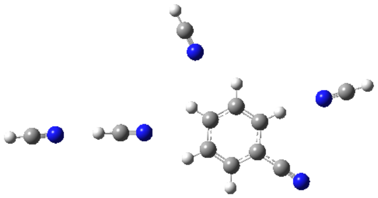

B4b

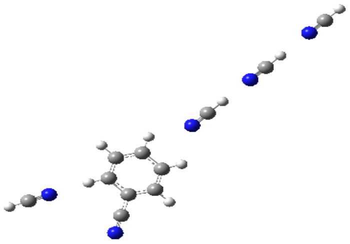

B4c

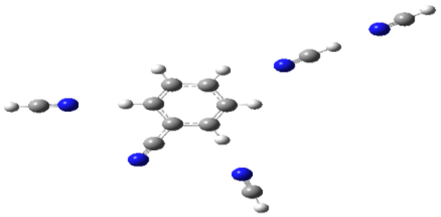

B4d

FBz (HCN)$_1$

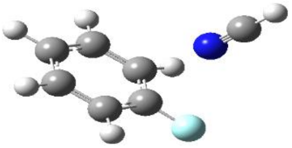

F1a

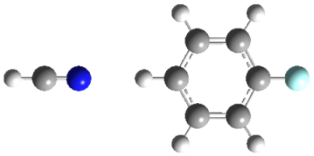

F1b

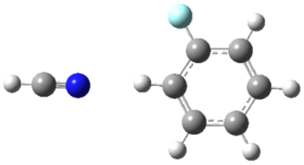

F1c

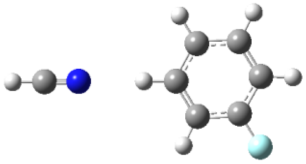

F1d

FBz (HCN)$_2$

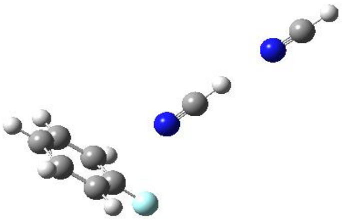

F2a

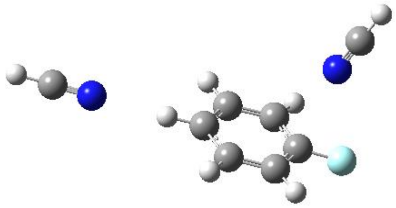

F2b

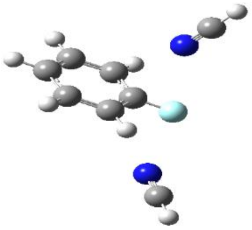

F2c

FBz (HCN)$_3$

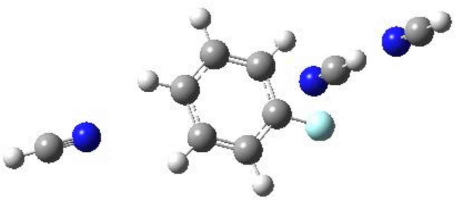

F3a

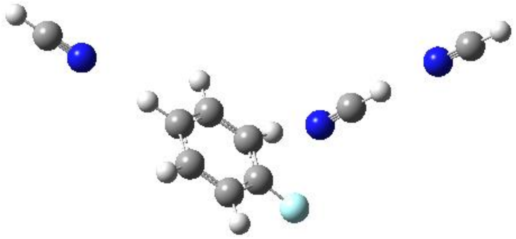

F3b

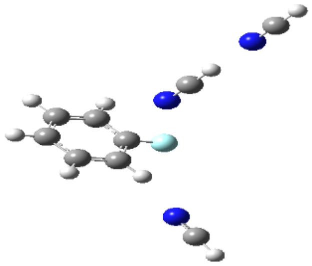

F3c

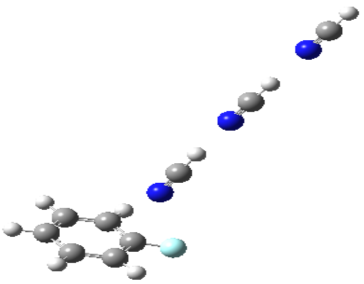

F3d

FBz $(HCN)_4$

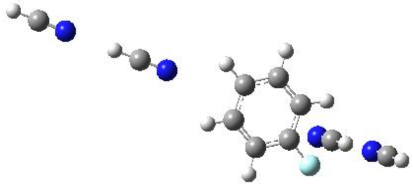
F4a

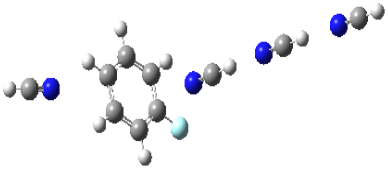
F4b

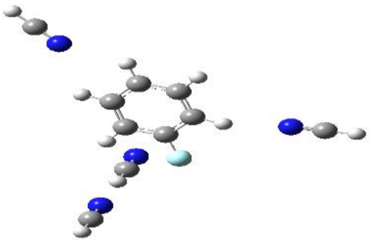
F4c

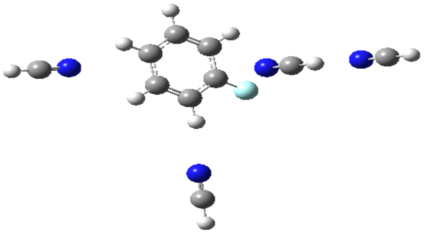
F4d

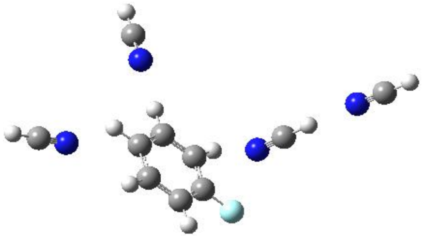
F4e

F2Bz (HCN)$_1$

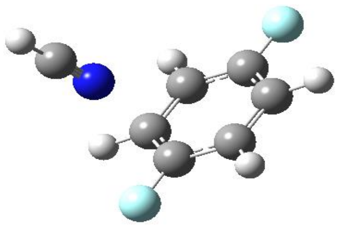

dF1a

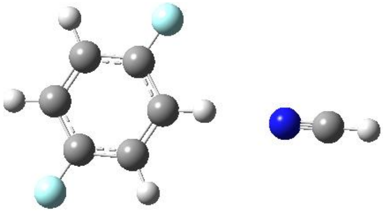

dF1b

F2Bz (HCN)$_2$

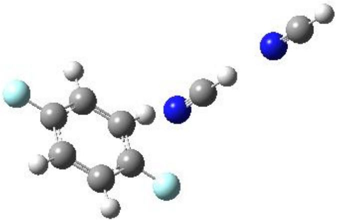

dF2a

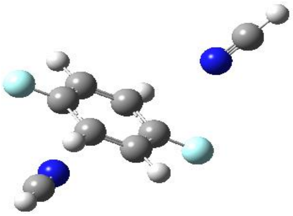

dF2b

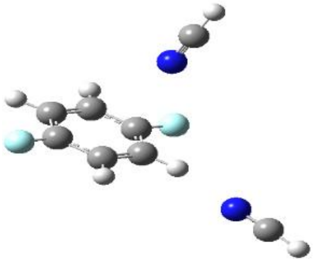

dF2c

F2Bz (HCN)$_3$

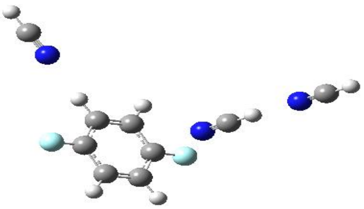

dF3a

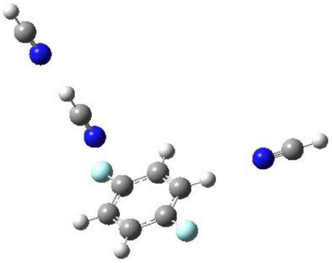

dF3b

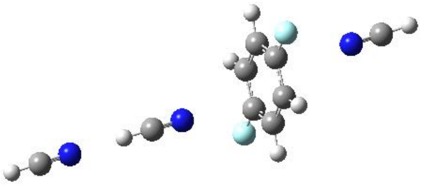

dF3c

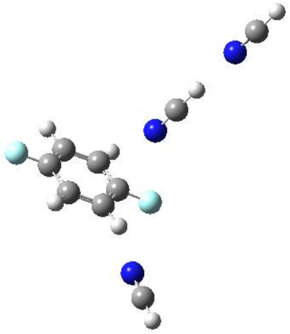

dF3d

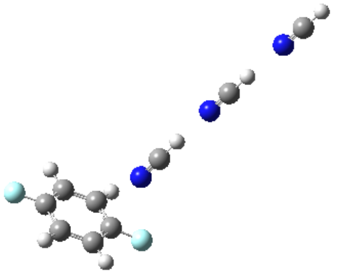

dF3e

F2Bz (HCN)$_4$

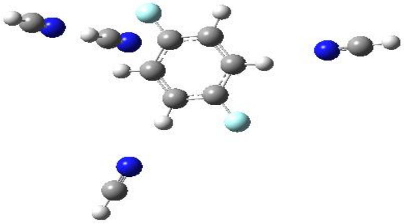

dF4a

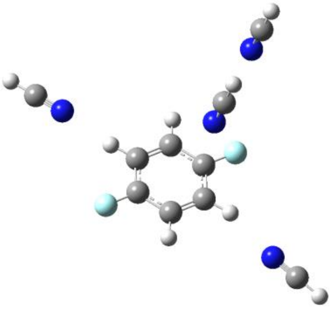

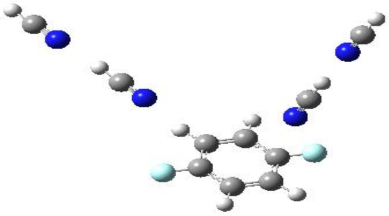

dF4c

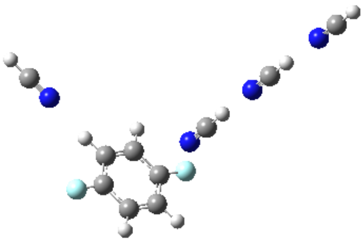

dF4d

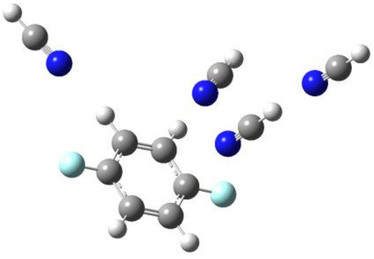

dF4e

CHAPTER 6. Metal Acetylene Cluster Ions $M^+(C_2H_2)_n$ as Model Reactors for Studying Reactivity of Laser-Generated Transition Metal Cations

6.1 Introduction

The reactivity of metal ions with small organic molecules in the gas phase has been a topic of intense investigation over the last few decades.[140-148] Interest in gas phase research of organometallic systems has advanced primarily due to the fact that the fundamental understanding obtained from these studies yields information applicable to a diverse range of fields, ranging from atmospheric chemistry to heterogeneous catalysis and interstellar chemistry. This is possible because gas phase studies can probe elementary reactions under well-defined conditions unperturbed by external factors that prevail in the condensed phase reactions such as the effects of solvent, counter ions, ion pairing, and intermolecular interactions which could lead to modification of the chemical reactions.[78,149,150] Moreover, these gas phase studies are also critical to identify detailed processes and mechanisms in heterogeneous catalysis.[72] For example, the majority of olefinic and acetylenic polymerization processes are catalytic, most often involving a heterogeneous catalyst.[151,152] The study of the analogous processes in the gas phase and within molecular clusters of the monomer molecules is important not only for probing the mechanism of such catalytic processes, but also for the design of new catalysts with tailored reactivity and selectivity. A large number of studies have investigated the reactivity of transition metal (TM) cations with small organic molecules, and dehydrogenation, condensation and/or C-C bond activation have been identified as primary reaction channels.[72,149,150,153-156] These studies have revealed that TM ions are highly reactive in C-H and

C-C bond activation of various hydrocarbons (including alkanes), due to the facile formation of insertion products via oxidative addition.[157,158] Thus a major motivation for these studies is the ability of the TM ions to activate otherwise inert molecules such as alkanes.[159-162] These studies have shown that the first-row groups 8–10 metal ions are more active towards C-C bond cleavage processes, whereas metal ions early in the transition series, as well as second- and third-row-metal ions, referentially activate C H bonds. Cycloaddition of unsaturated hydrocarbons is a useful kind of reaction for the synthesis of aromatic hydrocarbons. Although these cyclization reactions are generally quite exothermic, they are usually hindered by high kinetic barriers as far as unactivated hydrocarbons are concerned. Due to the technological importance associated with the catalytic cycloaddition of unsaturated hydrocarbons leading to the formation of benzene and higher polycyclic aromatics, a large number of studies, both experimental and theoretical, have been carried out.[71,73,163-165] For example, Schroeter *et al.*[73] investigated reactions of butadiene and acetylene complexed with metal ions (Cr^+, Mn^+, Fe^+, Co^+, Cu^+) using ion-beam four-sector and Fourier transform ion cyclotron resonance mass spectrometry.

It was observed that with the exception of Cu^+, for all other metal ions the reaction proceeded as a formal [4+2] cycloaddition involving 1,4-cyclohexadiene/M^+ as an intermediate, which subsequently eliminates molecular hydrogen to generate the corresponding benzene/M^+ complexes or bare M^+ and C_6H_6. Failure of Cu^+ to mediate the cycloaddition reaction was ascribed to its closed-shell s^0d^{10} electronic ground state.

Formation of benzene has also been observed in the gas phase from acetylene on Fe^+ and from ethylene on W^+ and U^+.[73,163,165] Acetylene cyclotrimerization on supported size-selected Pd_n clusters has also been reported.[166] Various hypotheses have been formulated to explain metal ion catalyzed cyclization of unsaturated hydrocarbons leading to the formation of benzene and its analogs, but a detailed generalized mechanism is not available yet.[71,165]

In this dissertation, we have utilized acetylene clusters containing TM atomic ions, $M^+(C_2H_2)_n$, as nano-reactors to assess the reactivity of several metal ions towards acetylene polymerization in the gas phase. The composition and abundance of $M^+(C_2H_2)_n$ as well as the hydrocarbon ions generated as a result of ion–molecule reactions within the clusters were determined using a Reflectron Time-of- Flight Mass Spectrometer (RTOF-MS).TM ions from the first, second and third rows have been studied using the Laser Vaporization Ionization (LVI) technique. Since the metals from the left side of the periodic table, i.e., V^+, Nb^+, Mo^+ and W^+ form very stable oxides, the LVI method provides a suitable and advantageous method for generating pure metal ions in the gas phase. In the present paper, we focus on the reactivity of the first row TM ions particularly Fe^+, Co^+ and Ni^+ incorporated within large acetylene clusters. In addition to the mass spectrometric studies, we also report DFT calculations on $M^+(C_2H_2)_n$, M= Fe, Co, and Ni for n = 1–3 aimed at elucidating and comparing the structures, binding energies, and the nature of bonding of these cluster ions with our experimental findings. These studies have been carried out with an aim to better understand the C_2H_2 cyclotrimerization/polymerization process as well as for screening alternative efficient catalysts for polymerization of C_2H_2 bond activation

6.2 Experimental

The experiments were done using the VCU RTOF-MS, which is based on a single stage ion mirror and 2nd order space focusing principle.[95] The system consists of two differentially pumped vacuum chambers as shown in figure 2. The first chamber, pumped by a Varian VHS-6 diffusion pump (3000 L/s in He), houses a 250µm supersonic nozzle (General valve, series 9) for cluster production as well as a metal target for cation generation by LVI (source chamber). The second chamber (RTOF-MS chamber), pumped by a Varian VHS-4 diffusion pump (1500 L/s in He), contains the acceleration plates, flight tube, ion mirror and a micro channel-plate detector (MCP). The typical operating pressure of the source chamber and the TOF chamber are 1.0 x 10^{-5} Torr and $\leq 2\times10^{-6}$ Torr, respectively. For a typical experiment, the metal target is placed 0.5–1.5cm from the nozzle face and displaced 0.5–1.2cm from the beam axis. Acetylene clusters formed by supersonic expansion of a mixture of ≈ 1% acetylene (BOC GASES®) in helium (ultrahigh purity, Spectra Gases, 99.99%, 4–5 atm, 250–350_s pulse widths, 8 Hz) are interacted with transition metal cations produced by LVI of a metal target utilizing the second harmonic (532 nm) of a Nd-YAG laser (Continuum-Surelite SSP-I, 8–10 ns pulse width). For experiments with a higher seed ratio of acetylene to helium (>5%), acetylene vapor is passed over a dry ice/methanol cooled trap to remove the acetone stabilizer prior to the expansion. Under our experimental conditions the cluster generation source, as well as the laser used to generate the ions are pulsed. In addition, a pulsed high voltage is applied to the repeller plate to accelerate ions towards the detector. Hence synchronization of these different events in space as well as in time is very essential. A typical sequence begins with opening of the nozzle (t_0) which results in the generation of neutral acetylene clusters $(C_2H_2)_n$. After a certain delay (≈ 490–550μs), the laser Q-switch is triggered to initiate lasing, resulting in the generation of metal cations (M^+) along with anions (M^-), electrons and neutral particles. The ions subsequently interact with the neutral cluster beam forming charged clusters, $M^+(C_2H_2)_n$. The charged clusters are collimated by a 3mm conical skimmer placed at a distance of about 4–7cm coaxial to the nozzle. Approximately 1.05 ms after t_0, the pulse generator is triggered to supply voltage (100μs pulses) to the repeller plate to accelerate the ions (300 V/cm) through the ion mirrors guided by the ion optics towards the MCP detector. Signal intensity is maximized by timing the laser delay so that the cations interact with the portion of the gas pulse having maximum cluster intensity and timing the pulse-generator to pulse the repeller plate at appropriate delay times. The delay generator utilized here is a BNC, model 555 generator. Data acquisition is carried out on a digital storage oscilloscope (Lecroy 9350A, 500 MHz), averaged and transferred to a computer for further processing. For our theoretical computations, the B3LYP hybrid functional level of theory[167] of the density functional theory (DFT) within the GAUSSIAN 03 quantum chemical package was used.[139] This functional is known to give yield results for geometries, binding energies, and vibrational frequencies of transition metal complexes.[168,169] Two separate basis sets were used to for the optimization calculations, the 6-31+G(d,p) basis set for C and H atoms and the Watchers + f (14s 11p 6d 3f)/[8s 6p 4d 1f] basis set for all transition metal cations.[170,171] All calculated energies were zero point energy (ZPE) corrected and all C H stretch frequencies were scaled by 0.96.[139]

6.3 Results

6.3.1 Observed trends within small acetylene clusters

In our first set of experiments, studies were carried out on small acetylene clusters containing metal ions of the first row transition series. These transition metals in general are widely used for various catalytic processes and represent a different order of d-shell vacancies as shown in Table 1. Below we first present an overall view of the general trends observed among the reactivity of the first row TM ions followed by a more detailed study of the acetylene clusters containing Fe, Co and Ni ions. We then present the structural calculations of the $M^+(C_2H_2)_n$ clusters for M= Fe, Co and Ni, and n = 1–3.Finally, we discuss the experimental observations in relation to the structural calculations and present a plausible reaction mechanism to explain the observed trends.

Table 5: Low-lying electronic states for the first-row transition metal cations. Ground states are in bold. Energy levels are statistically averaged over J-levels.

Ion	**State**	**Configuration**	**Energy (eV)**	**Ion**	**State**	**Configuration**	**Energy (eV)**
V^+	**${}^5D$**	**$3d^4$**	**0.026**	Cr^+	**${}^6S$**	**$3d^5$**	**0.000**
	${}^5F$	$4s3d^3$	0.363		${}^6D$	$4s3d^4$	1.522
	${}^3F$	$4s3d^3$	1.104		${}^4D$	$4s3d^4$	2.458
	${}^3P$	$3d^4$	1.452		${}^4G$	$3d^5$	2.544
	${}^3H$	$3d^4$	1.566		${}^4P$	$3d^5$	2.406
	${}^3F$	$3d^4$	1.681		${}^4D$	$3d^5$	3.104
	${}^5P$	$4s3d^3$	1.692				
	${}^3G$	$3d^4$	1.807				
Ni^+	**${}^2D$**	**$3d^9$**	**0.075**	Fe^+	**${}^6D$**	**$4s3d^6$**	**0.052**
	${}^4F$	$4s3d^8$	1.160		${}^4F$	$3d^7$	0.300
	${}^2F$	$4s3d^8$	1.757		${}^4D$	$4s3d^6$	1.032
	${}^4P$	$4s3d^8$	2.899		${}^4P$	$3d^7$	1.688
Cu^+	**${}^1S$**	**$3d^{10}$**	**0.000**		${}^2G$	$3d^7$	1.993
	${}^3D$	$4s3d^9$	2.808		${}^2P$	$3d^7$	2.299
	${}^1D$	$4s3d^9$	3.256				

Moore, C. E. Atomic energy levels as derived from the analyses of optical spectra; U.S. National Bureau of Standards; U.S. Govt. Print. Off.: <Washington>, 1971.

Figures 50-52 represent the RTOF-MS spectra obtained upon the interaction of acetylene clusters with the Ti^+, V^+ and Cr^+ ions. The major cluster series observed is $M^+(C_2H_2)_n$ with n up to 8, 7 and 10 for the Ti^+, V^+ and Cr^+ ions, respectively. No other side-products arising as a result of intracluster reactions within the $V^+(C_2H_2)_n$ clusters were observed for Ti^+- and V^+-containing clusters However, for $V^+(C_2H_2)_n$ clusters hydrogen abstraction reactions were observed resulting in the generation of V+C2nH2n−m species (see Figure 51, inset) according to:

$$M^+(C_2H_2)_n \rightarrow c\ M^+(C_2H_2)_{n-m} + \frac{m}{2}\ H_2 \qquad (6.1)$$

A drop in the ion intensity is observed for the $V^+(C_2H_2)_n$ clusters after n = 2, which could be attributed the stability of the n = 2 cluster.

Figures 53-55 display the mass spectra of the $M^+(C_2H_2)_n$ clusters for M= Fe, Co and Ni, respectively. For the three metal cations, clusters with n in the range 1–15 were observed.

In addition, ion signals corresponding to hydrocarbon fragments were also observed. These ions are believed to be covalently bonded hydrocarbon fragments formed as a result of metal ion induced catalytic polymerization, as previously reported by Schwarz and co-workers for the case of Fe^+.[73,163,172] It should be noted that the intensity of the observed hydrocarbon ions increases when the metal target is placed closer to the nozzle as shown in the mass spectrum of $Co^+(C_2H_2)_n$ displayed in Figure 56. This suggests that excited state ions could be responsible for the reactions leading to the generation of these hydrocarbon ions.

TM ions are characterized by a large number of low-lying electronic states that can be easily accessed under the typical LVI conditions as was recently studied using ion mobility.[106] In fact, the geometry of the ion source plays an important role in the extent of excited state ions generated by the LVI process.[106] By placing the metal target very close to the nozzle, the gas expansion pulse overlaps efficiently with the laser plume where the density of the excited state

TM metal ions is high. This increases the probability of excited state metal ion reactions with the acetylene clusters. The possible role of excited state ions in the generation of the observed hydrocarbon ions will be addressed later. For $Co^+(C_2H_2)_n$ and $Ni^+(C_2H_2)_n$ clusters (Figure 57), a sharp drop in ion intensity is observed following the n = 3 cluster while for $Fe^+(C_2H_2)_n$, enhanced intensity is observed for n = 4 with a drop in ion signal for clusters with n>4. A significant enhanced ion intensity is observed for the n=3 of the $Cu^+(C_2H_2)_n$ clusters with no side-products assigned to hydrocarbon fragments as shown in

Figure 58. Similarly, with Zn^+ the major ions observed belong to the $Zn^+(C_2H_2)_n$ cluster series although the overall clusters' ion signal is much weaker compared to other TM ions (Figure 59).

6.3.2 Fe+, Co+ and Ni+ ions in large acetylene clusters

Large $Fe^+(C_2H_2)_n$, $Co^+(C_2H_2)_n$ and $Ni^+(C_2H_2)_n$ clusters were generated to study their magic numbers trends, which indicates exceptional stability of certain clusters within a series. The large cluster generation was facilitated by increasing both the seed ratio of acetylene and the stagnation pressure of the He carrier gas during the supersonic beam expansion, which leads larger than usual neutral acetylene clusters. The laser delay was also increased to optimize the interaction of the LVI generated TM cations with the larger acetylene clusters by selecting the best laser delay which ensures that the portion of the gas pulse having the largest neutral clusters are reacting and then pulsing the repeller plate at appropriate delay times to detect the corresponding cluster ions. The mass spectra of the large $Fe^+(C_2H_2)_n$, $Co^+(C_2H_2)_n$ and $Ni^+(C_2H_2)_n$ clusters ion complexes are shown in Figure 60-62, respectively.

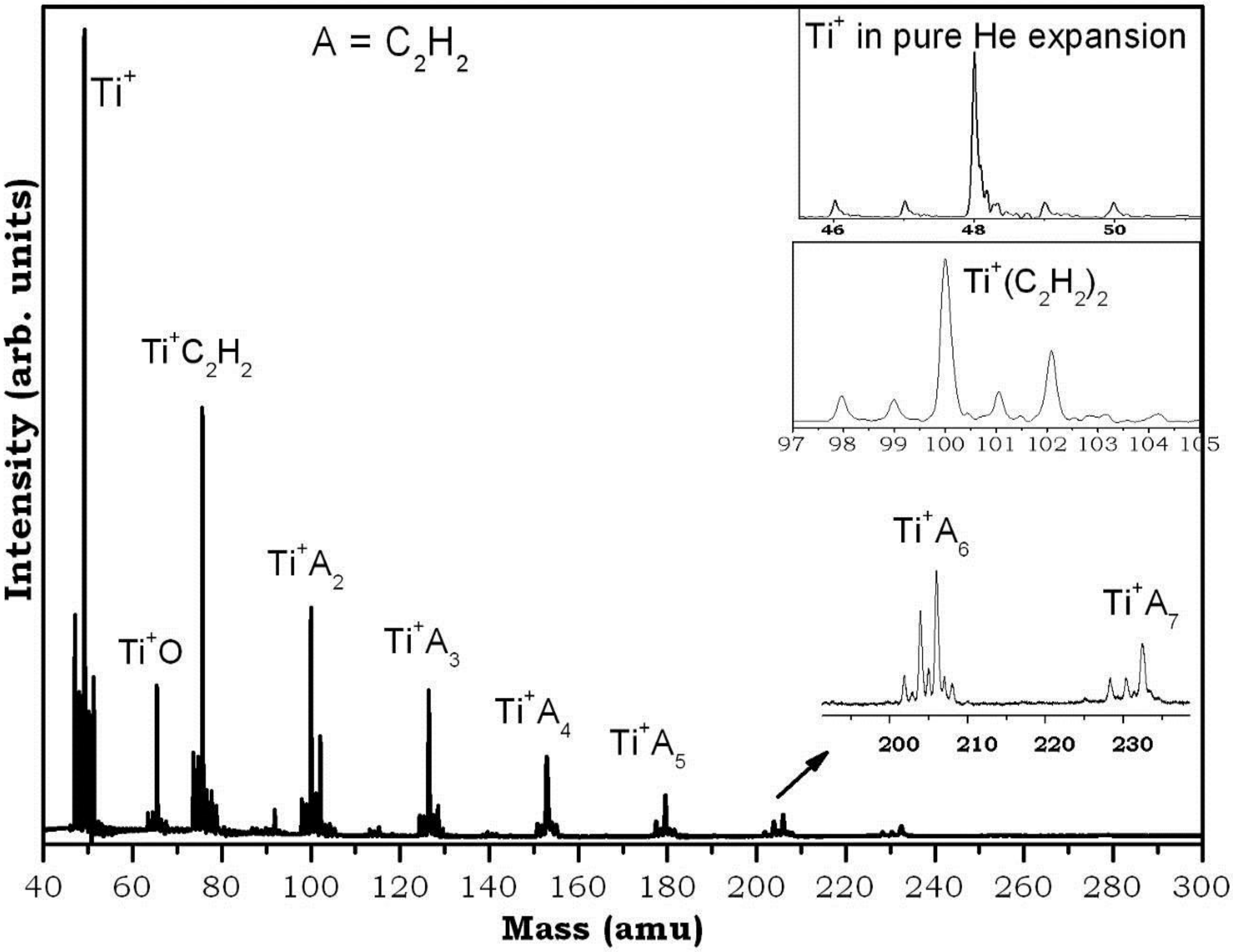

Figure 50:TOF mass spectrum of $Ti^+(C_2H_2)_n$ clusters. Insets show the mass spectra of different isotopes of Ti^+ generated in pure helium expansion (no acetylene) and $Ti^+(C_2H_2)_2$ cluster (high resolution).

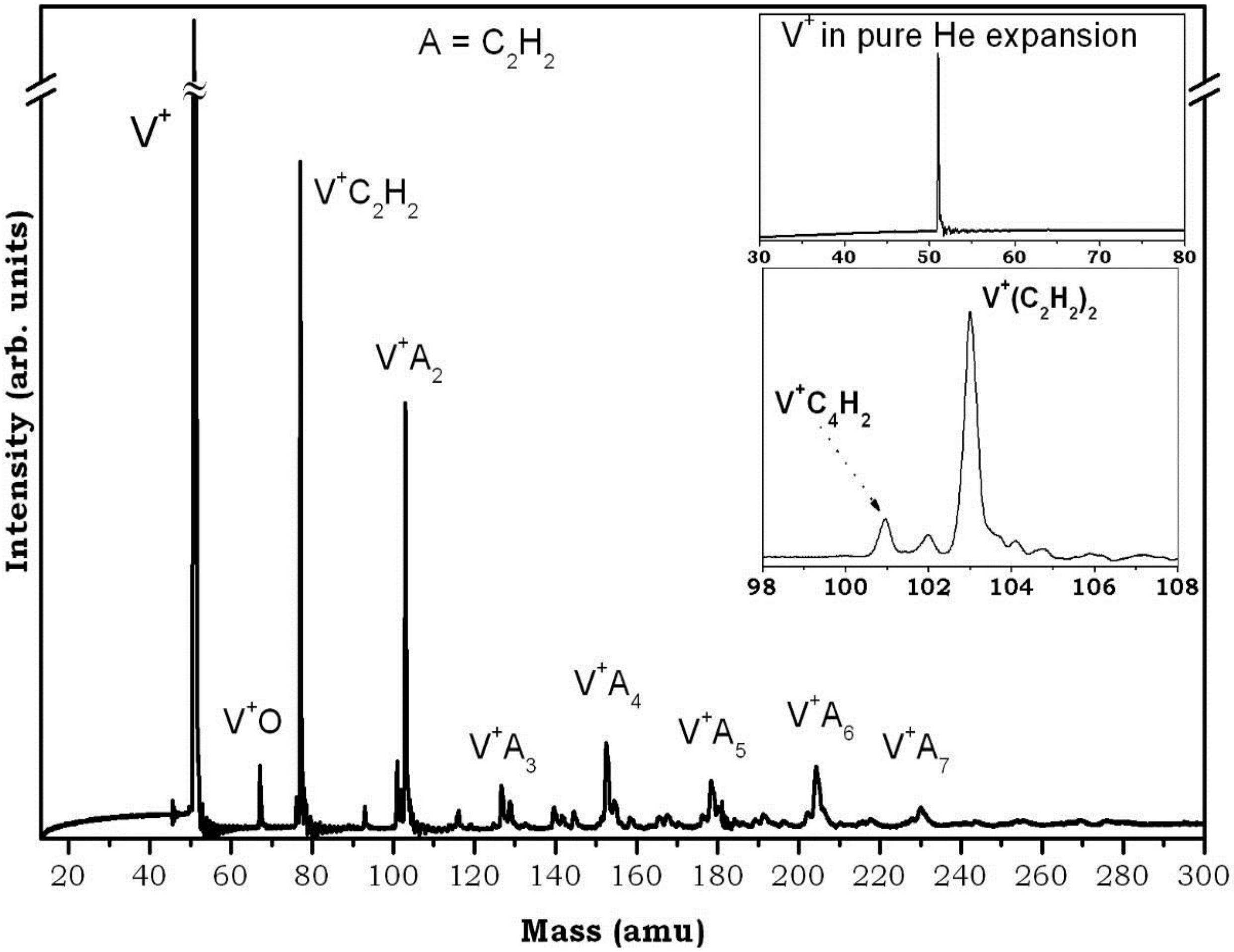

Figure 51: TOF mass spectrum of $V^+(C_2H_2)_n$ clusters. Insets show the mass spectra of V^+ in pure helium expansion (no acetylene), and $V^+(C_2H_2)_2$ cluster (high resolution).

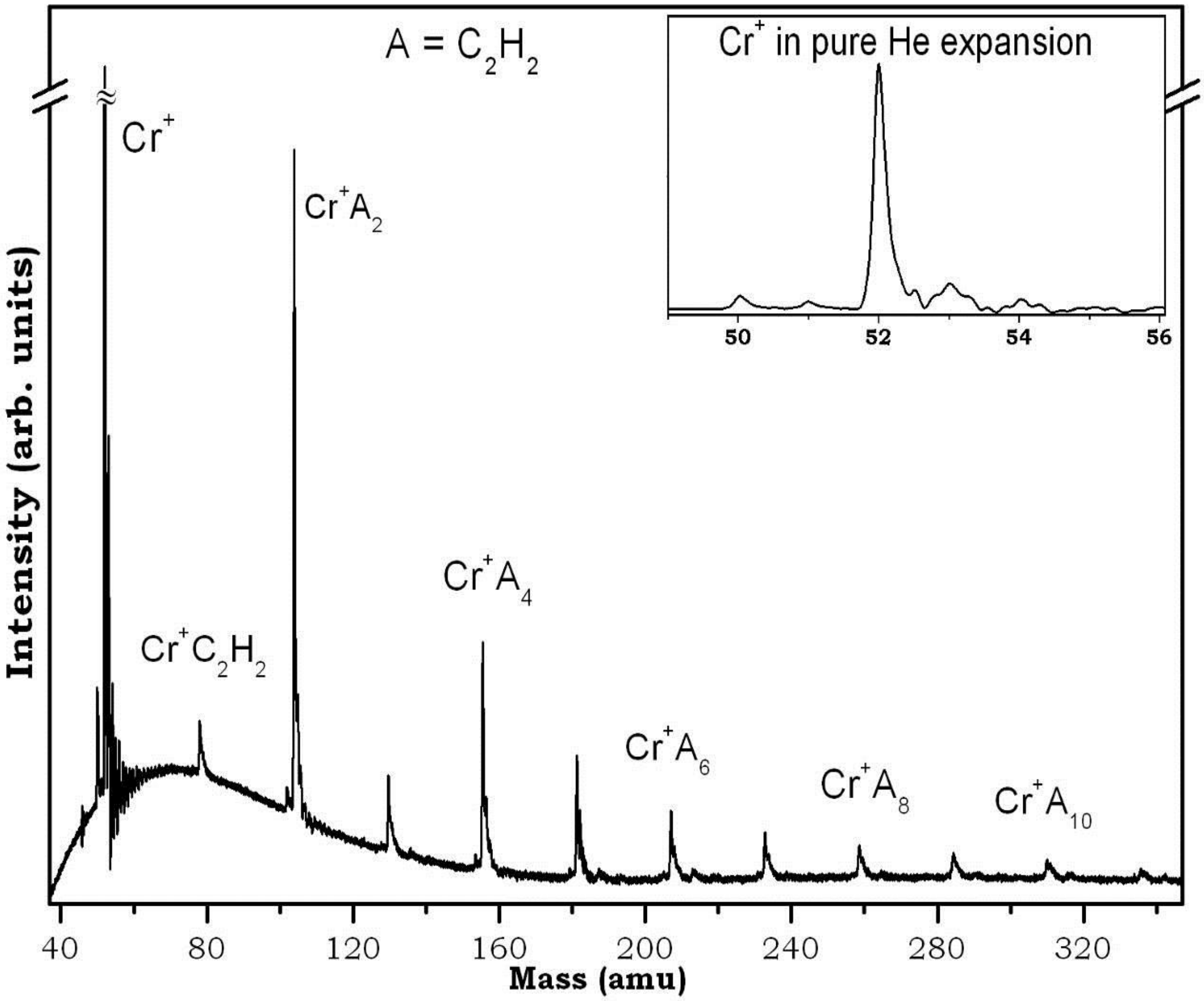

Figure 52:TOF mass spectrum of $Cr^{+}(C_2H_2)_n$ clusters. Inset shows the mass spectrum corresponding to different isotopes of Cr^{+} generated in pure helium expansion (no acetylene).

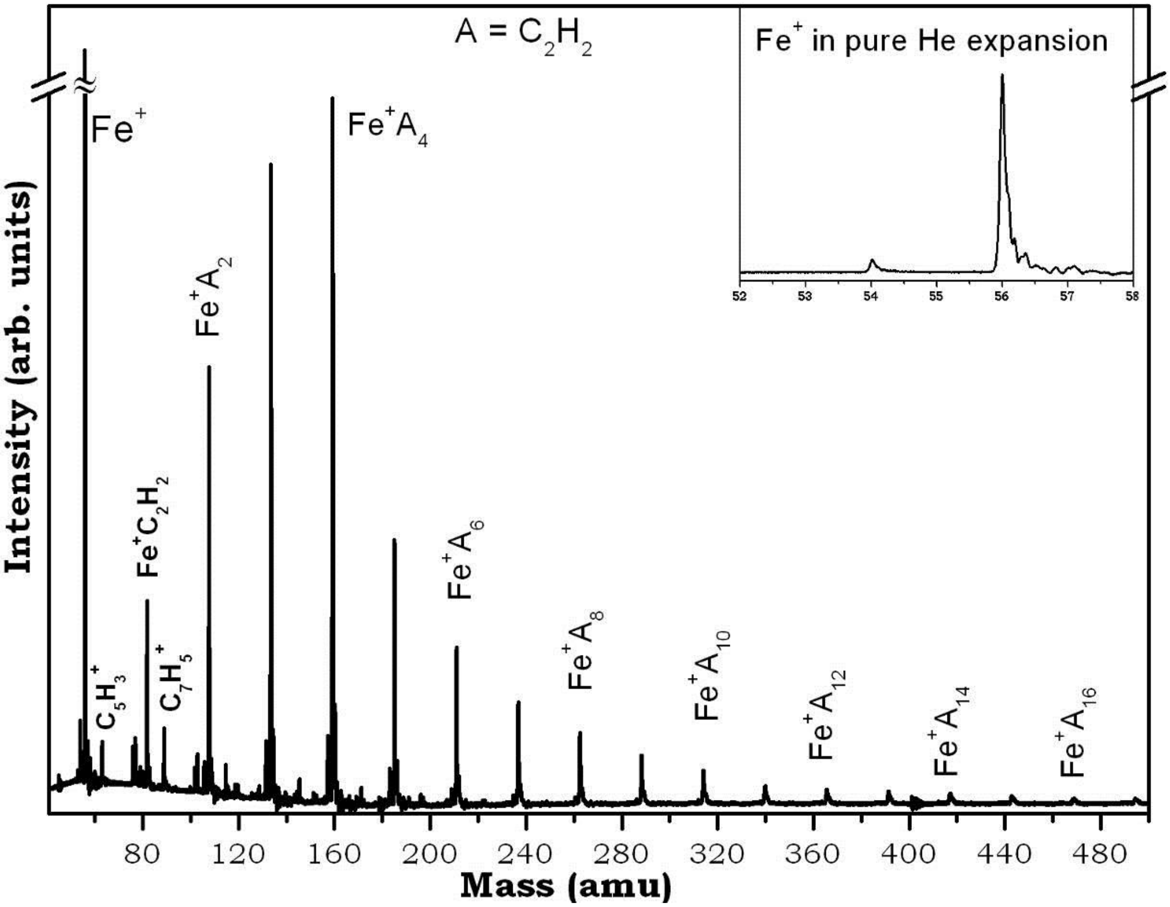

Figure 53: TOF mass spectrum of $Fe^+(C_2H_2)_n$ clusters. Inset shows the mass spectrum of Fe^+ in pure helium expansion (no acetylene).

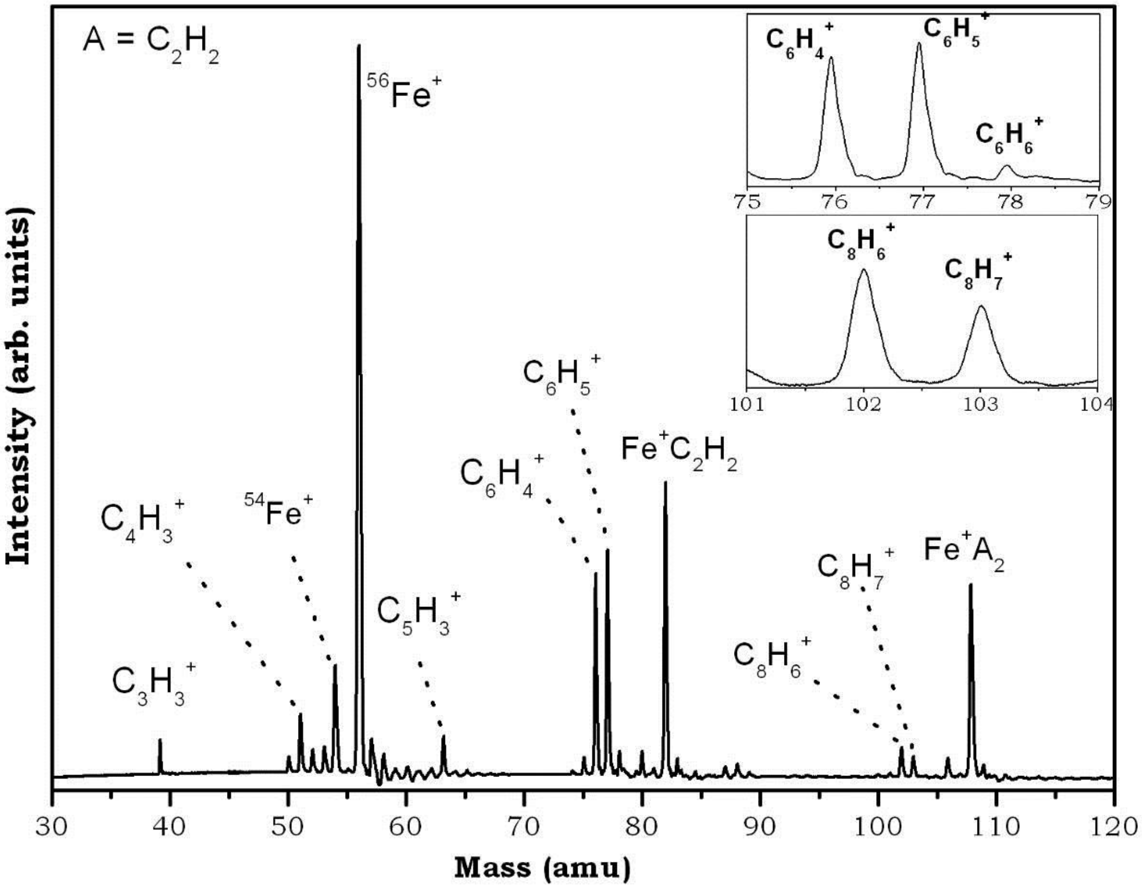

Figure 54: TOF mass spectrum of the hydrocarbon ions generated from the $Fe^+(C_2H_2)_n$ clusters. Insets show mass spectra of the $C_6H_4^+$, $C_6H_5^+$, $C_6H_6^+$, $C_8H_6^+$, and $C_8H_7^+$ ions (high resolution).

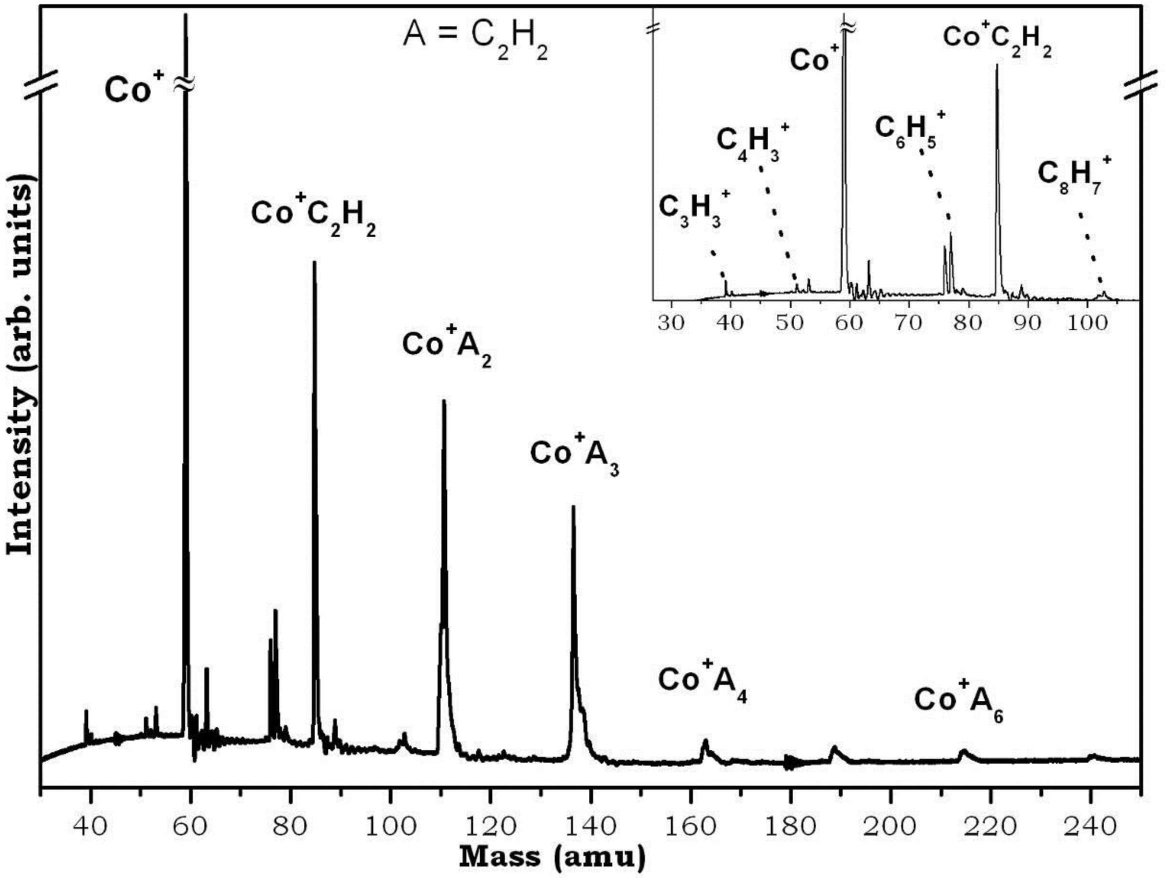

Figure 55: TOF mass spectrum of $Co^+(C_2H_2)_n$ clusters. Inset shows the mass spectrum of the hydrocarbon ions generated from the $Co^+(C_2H_2)_n$ clusters.

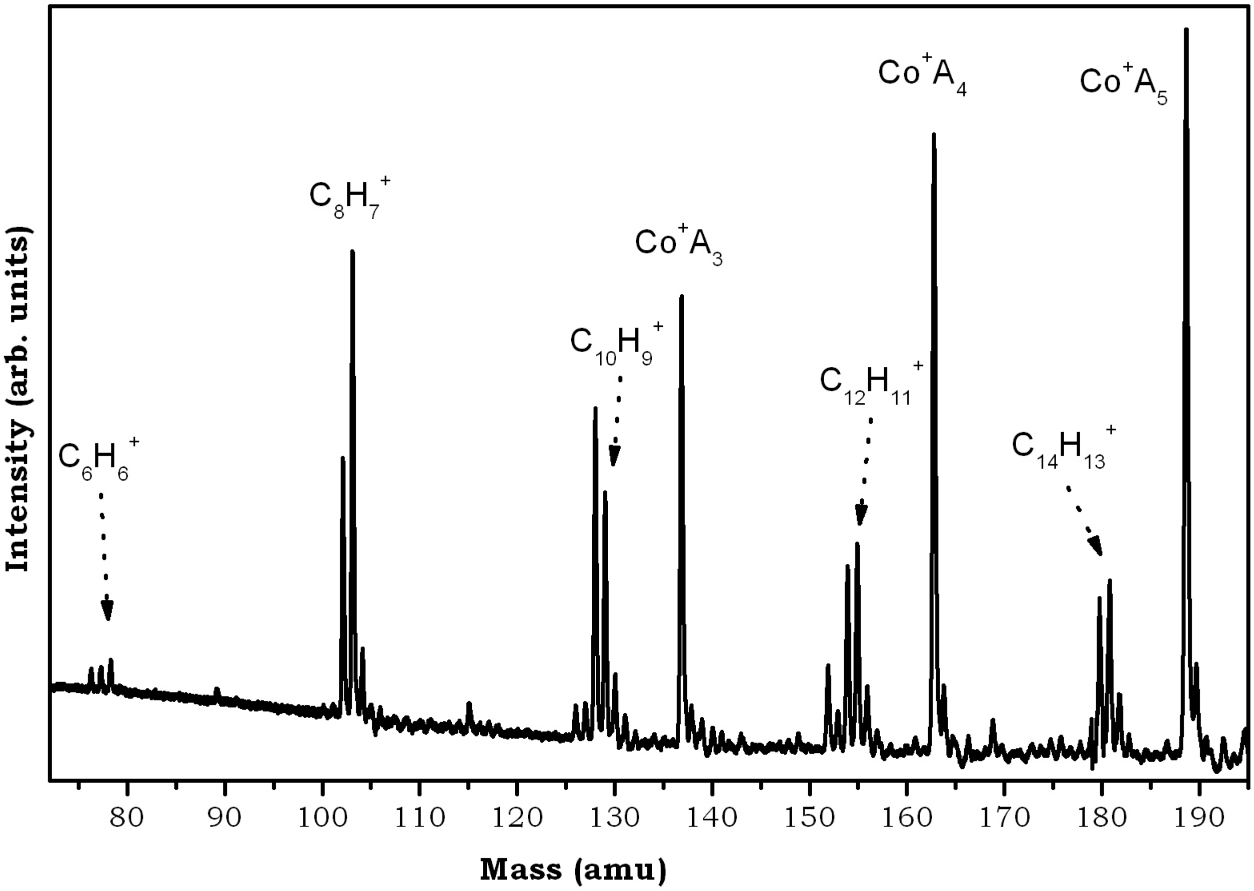

Figure 56: TOF mass spectrum of hydrocarbon ions generated from the $Co^+(C_2H_2)_n$ clusters when the Co target is placed closer to the nozzle generating the $(C_2H_2)_n$ clusters .

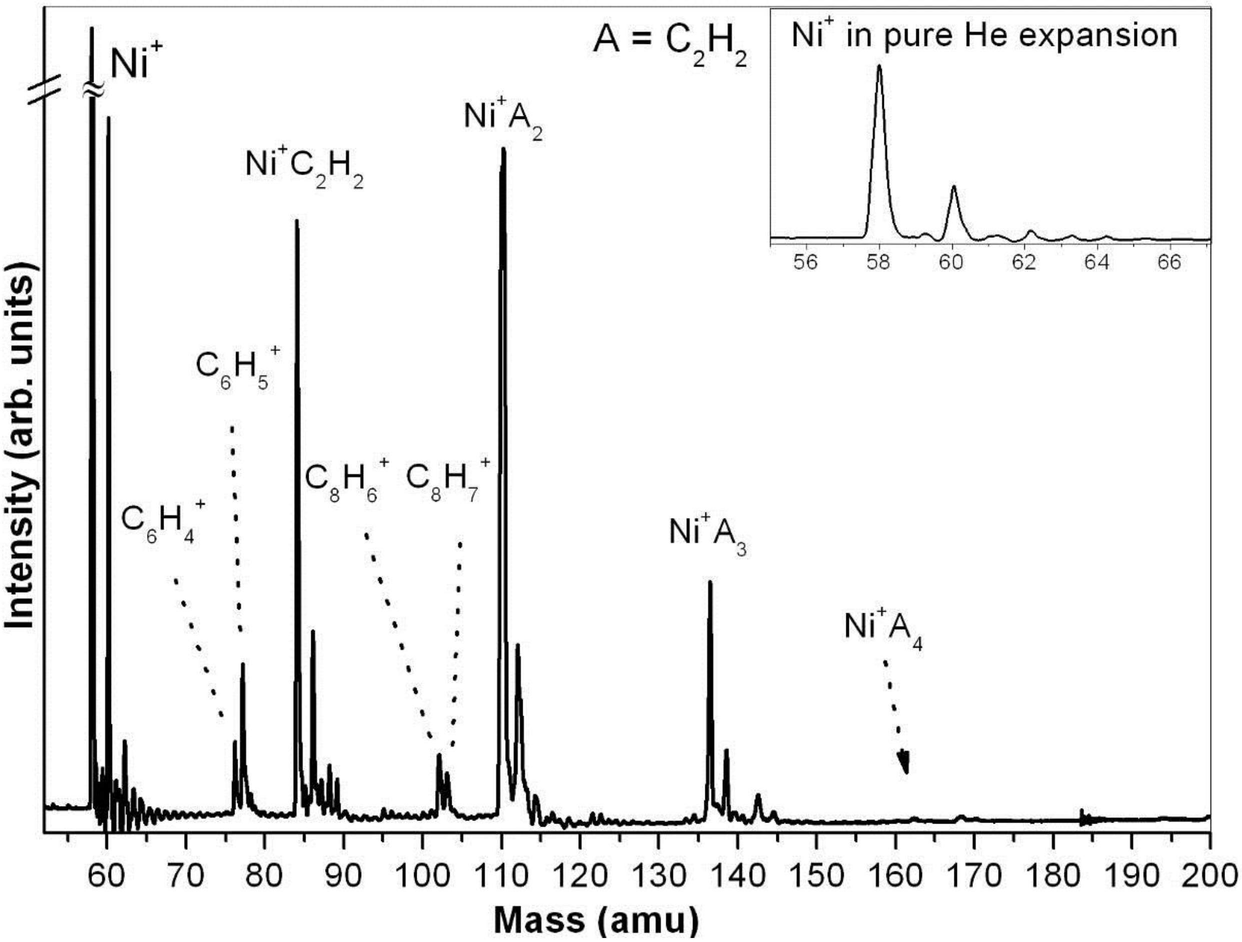

Figure 57: TOF mass spectrum of Ni$^+$(C_2H_2)$_n$ clusters. Inset shows the mass spectrum of Ni$^+$ in pure helium expansion (no acetylene).

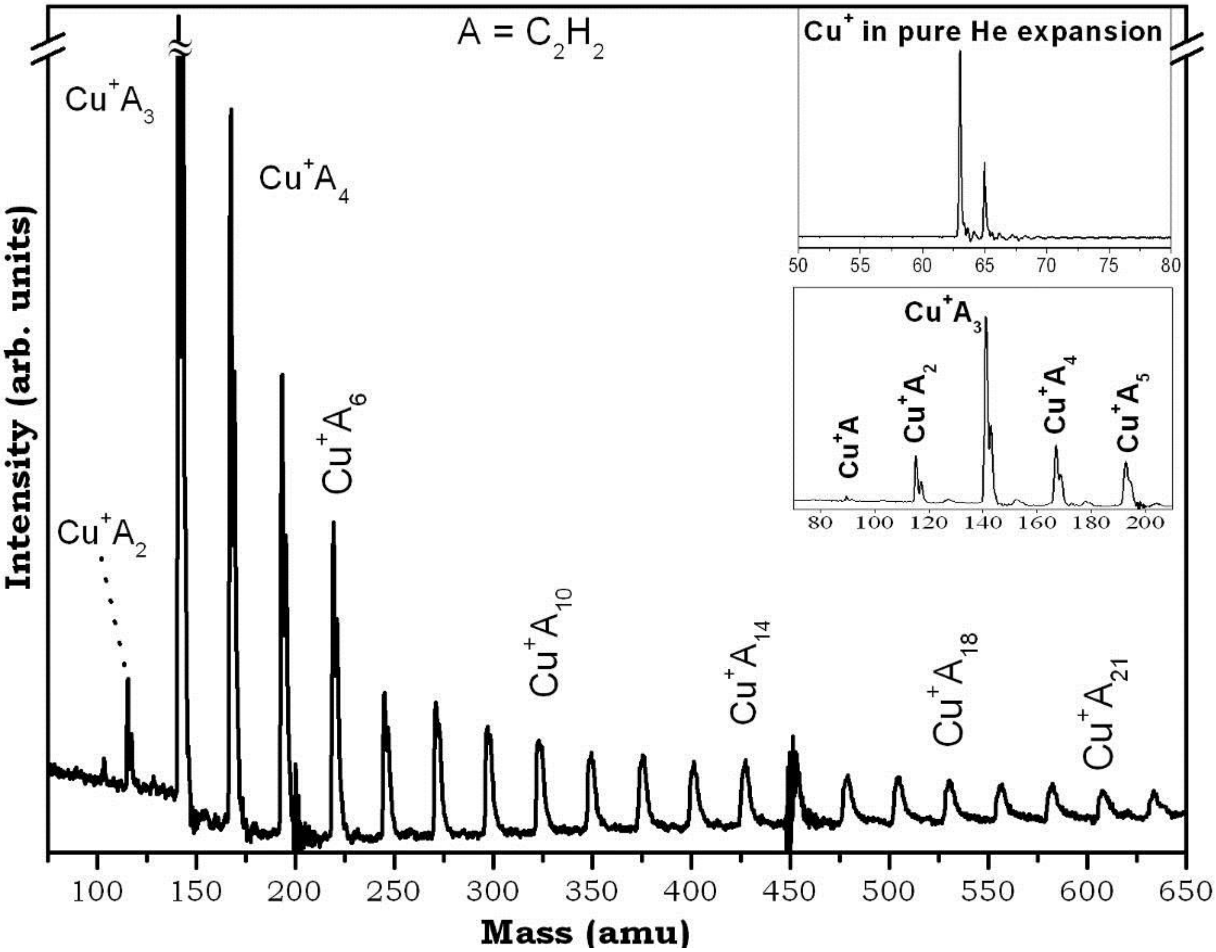

Figure 58: TOF mass spectrum of $Cu^+(C_2H_2)_n$ clusters. Insets show the mass spectra of Cu^+ in pure helium expansion (no acetylene), and $Cu^+(C_2H_2)_3$ cluster (suggested magic number).

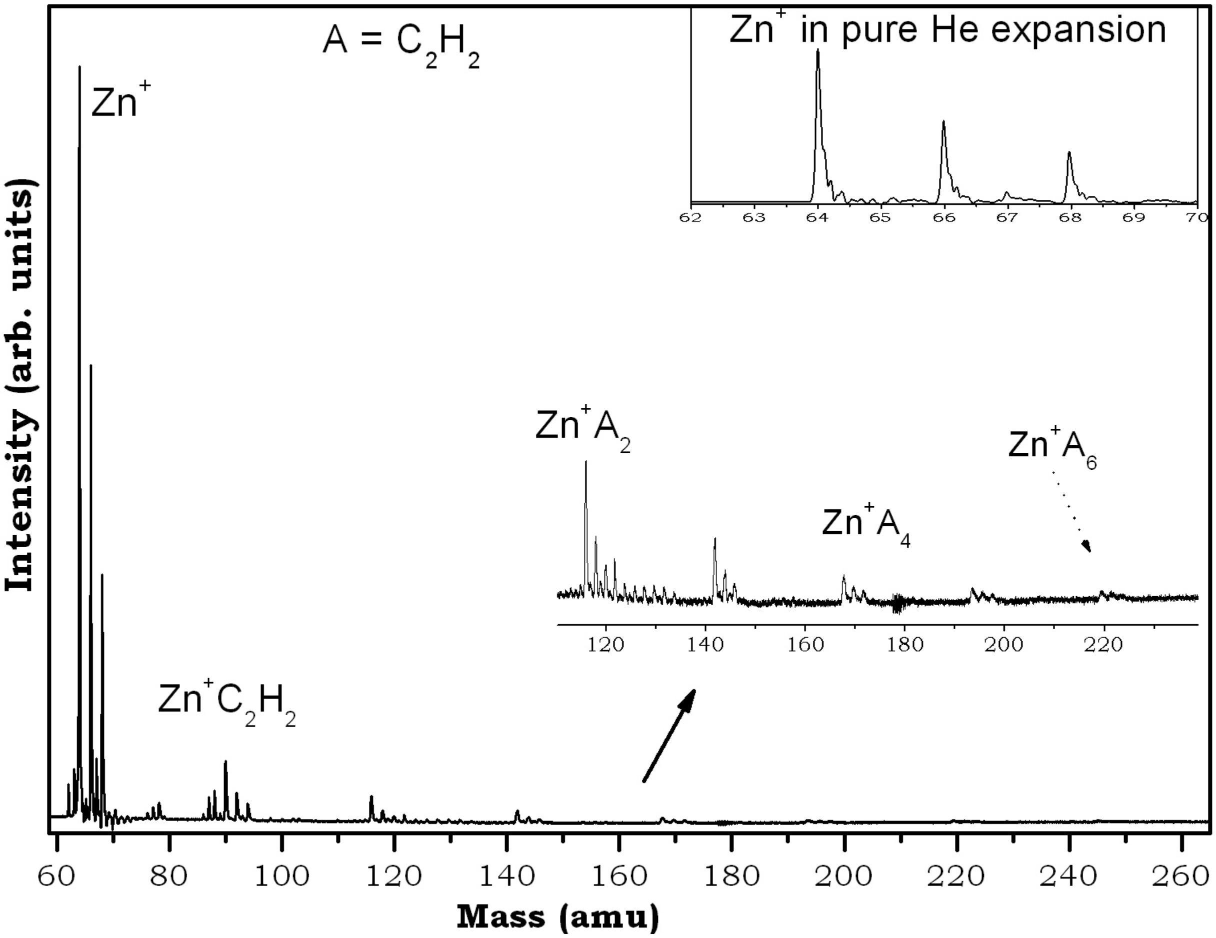

Figure 59: TOF mass spectrum of $Zn^+(C_2H_2)_n$ clusters. Inset shows the mass spectra of Zn^+ in pure helium expansion (no acetylene).

The insets display the corresponding intensity plots. The observed features in the small $Fe^+(C_2H_2)_n$ clusters (Figure 53) are more pronounced within the larger acetylene clusters. For example, the mass spectrum displayed in Figure 62 shows enhanced intensity for the Fe+(C2H2)2 and $Fe^+(C_2H_2)_4$ clusters. The enhanced intensity of the $Fe^+(C_2H_2)_2$ cluster could suggest stabilization of the acetylene dimer by a highly symmetric Fe+-bis-acetylene arrangement or formation of a covalent Fe+-dimer complex, i.e., $Fe^+C_4H_4$. As will be discussed later, DFT calculations suggest the Fe^+-bisacetylene geometry to be more stable than the $Fe^+C_4H_4$ complex. The intensity of the $Fe^+(C_2H_2)_4$ cluster ion peak is very much enhanced and can possibly be attributed to four acetylene molecules being required to close the first solvation shell of the Fe^+ cation, although this does not imply the n = 4 cluster is necessarily the coordination number for the Fe^+ cation, but merely stability from efficient ligand packing. A close look at the mass spectrum of the larger $Co^+(C_2H_2)_n$ clusters (Figure 61) shows an astonishing and highly reproducible trend; oscillatory magic numbers for the n = 3, 6, 9, and 12 clusters. A similar trend is also seen within the distribution of the small $Co^+(C_2H_2)_n$ clusters which shows a sharp drop in ion intensity after the n = 3 cluster (Figure 55). It is tempting to speculate that a Co^+-mediated multiple intracluster reaction process could be occurring in which a benzene ring and other covalent C_6H_6 products (perhaps multiple cyclic rings $Co^+(C_6H_6)_n$, n = 1–4) are formed. This possibility is of interest since it provides further evidence for intracluster reactions enhanced by interactions among the packed reactive molecules in the cluster.

Schwarz and Wesendrup, using FT-ICR mass spectrometry, reported that the Co^+ was unreactive toward the mediation of the acetylene cyclotrimerization reaction.[172]

Similarly, most late first-row transition metal cations are expected to show the same non-reactive nature towards the facilitation of the cyclotrimerization reaction, with the exception of iron. This could indicate that the Co^+- mediated cyclotrimerization reaction could be as a result of excited state Co^+ ions reacting with the acetylene molecules within the $Co^+(C_6H_6)_n$ large clusters. This is possible since the excited state ions possess the extra energy required to overcome the barrier involved in the isomerization of the $Co^+(C_6H_6)_3$ cluster species into the more stable Co^+-benzene structure. Dissipation of excess energy resulting from the exothermic cyclotrimerization reaction occurs via evaporative loss of neutral acetylene molecules, a process that is favored in a large cluster distribution.[173] It is well established that a cluster environment, much like the condensed phase, increases the rate of certain termolecular processes which may otherwise be inefficient under gas phase conditions.[173-175] It should be mentioned that at the experimental pressures ($<< 5\times10^{-8}$ bar) utilized by Wesendrup and Schwarz,[172] the probability of orientational collisions amenable to efficient Co+-mediated trimerization reaction kinetics might be too low.

Cluster size-specific TM-mediated intracluster reactions may also be responsible for the observed magic numbers.[176] For the large $Ni^+(C_2H_2)_n$ clusters (Figure 62), the n = 3 cluster shows enhanced intensity consistent with the spectrum of the small clusters (Figure 56) which could suggest a particularly stable structure for this cluster. The n = 3 cluster could be due to efficient packing of three acetylene molecules around the Ni^+ ion. Another possibility is a Ni^+-mediated intracluster cyclization reaction resulting in the formation of a Ni^+(benzene) structure similar to the suggested process in the $Co^+(C_2H_2)_n$ clusters. Duncan and co-workers, utilizing IR dissociation experiments, have proposed the $Ni(C_2H_2)_n$ geometry to be analogous to that of the tris(ethylene)platinum complex.[176] They suggested that four acetylene molecules are needed to close the Ni^+ first solvation shell, and proposed that the Ni- cyclobutadiene π-complex ($Ni^+C_4H_4$) is formed in larger clusters from a size-specific intracluster reaction.[176]

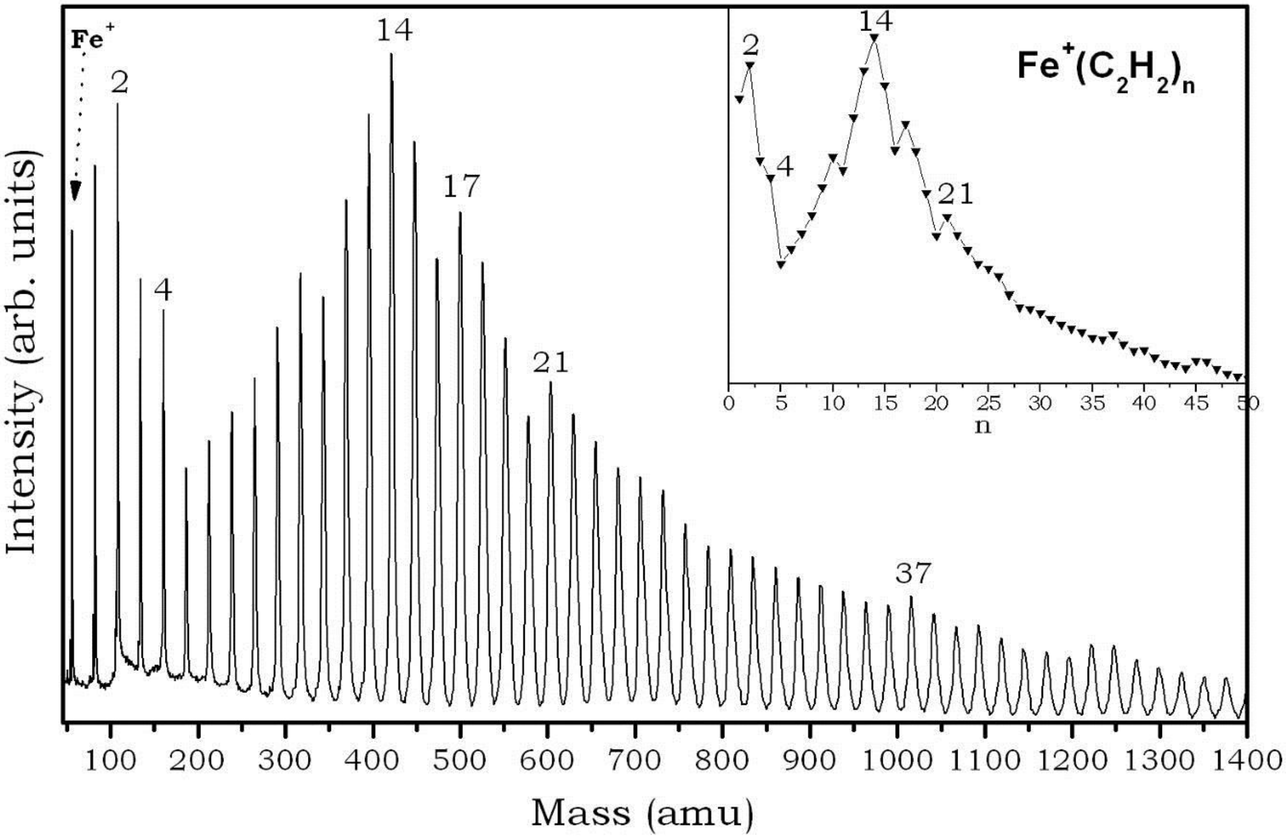

Figure 60: TOF mass spectrum of large $Fe^{+}(C_2H_2)_n$ clusters. The neutral acetylene clusters were generated by the supersonic beam expansion of 3% acetylene/helium mixture (100 PSI). Laser fluence at the Fe target surface was ≈ 10^7 Wcm^{-2}. Inset shows the corresponding intensity plot suggesting magic numbers at n = 2, 4 and 14.

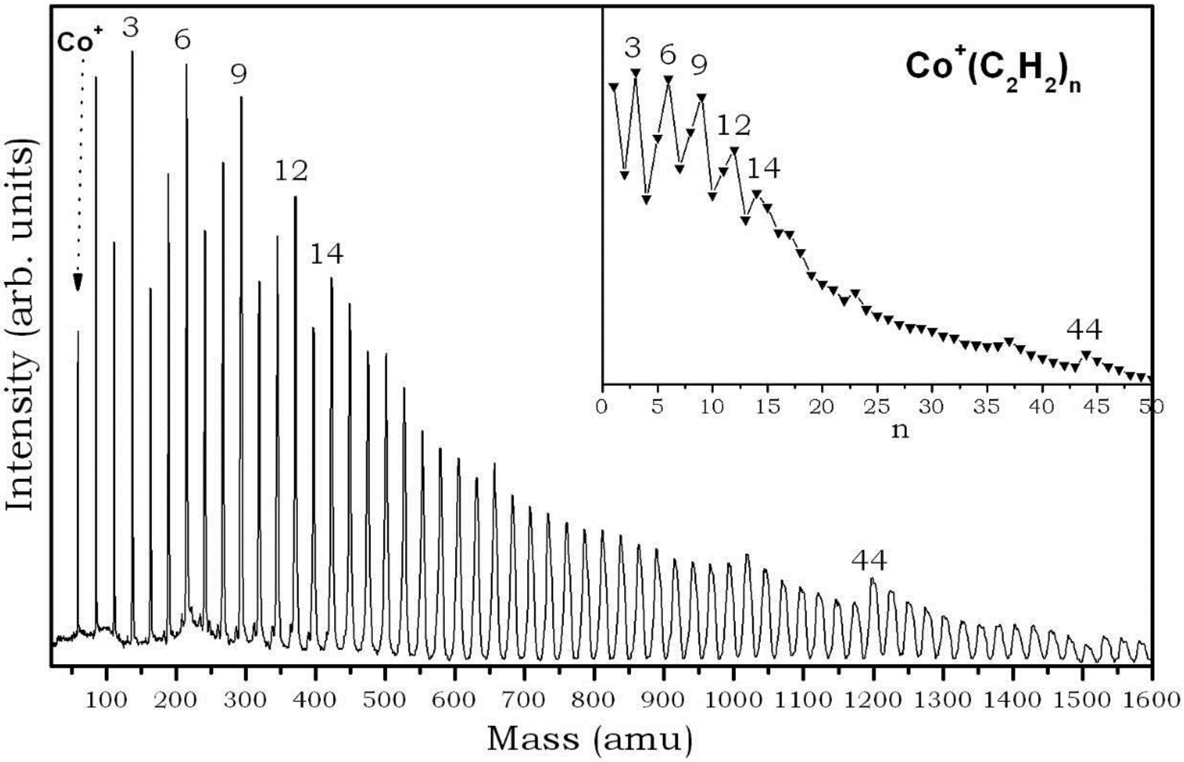

Figure 61: TOF mass spectrum of large $Co^+(C_2H_2)_n$ clusters. The neutral acetylene clusters were generated by the supersonic beam expansion of 3% acetylene/helium mixture (100 PSI). Laser fluence at the Co target surface was $\approx 10^7$ Wcm^{-2}. Inset shows the corresponding intensity plot suggesting intriguing magic numbers at n = 3, 6, 9 and 12.

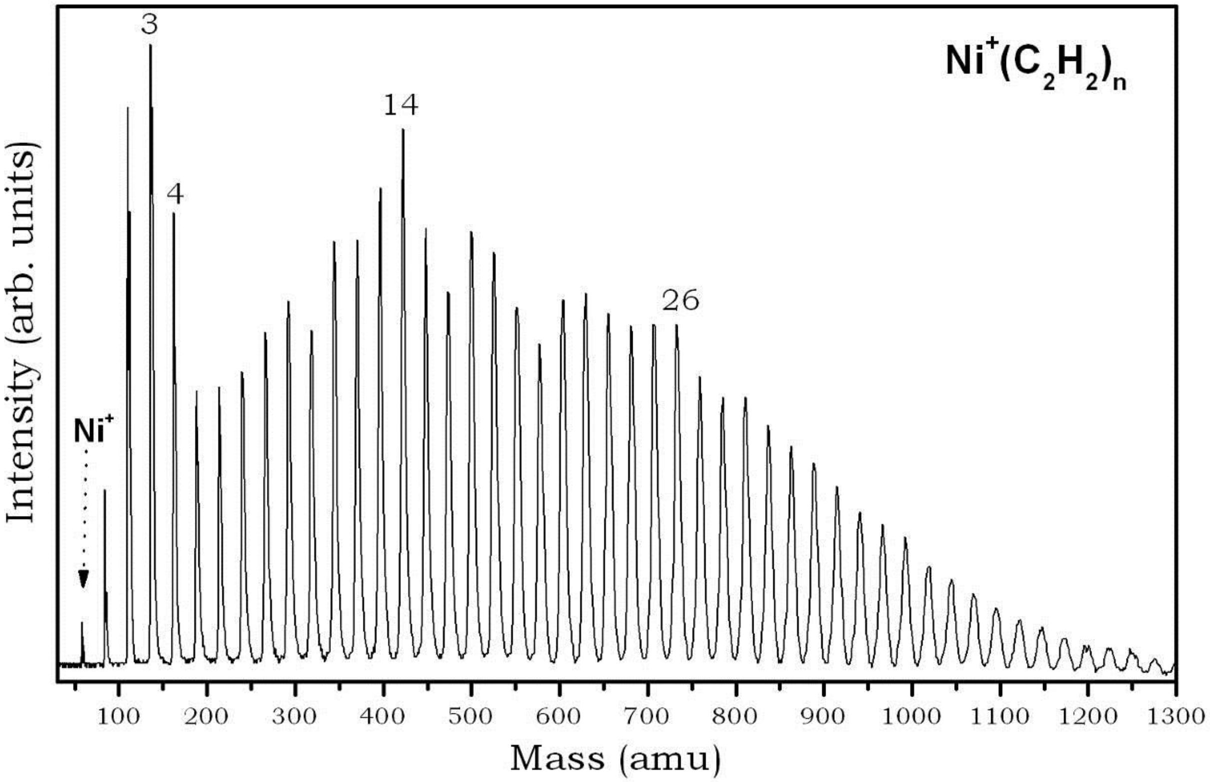

Figure 62: TOF mass spectrum of large $Ni^+(C_2H_2)_n$ clusters. The neutral acetylene clusters were generated by the supersonic beam expansion of 3% acetylene/helium mixture (100 PSI). Laser fluence at the Ni target surface was ≈ 10^7 Wcm^{-2}.

These suggestions are in full agreement with our mass spectra data where an enhanced intensity peak for $Ni^+(C_2H_2)_4$ is observed (Figure 62). Another observation common to the $Fe^+(C_2H_2)_n$, $Co^+(C_2H_2)_n$ and $Ni^+(C_2H_2)_n$ clusters and other metal ions containing acetylene clusters as well is the appearance of a magic number at n=14(Figure 60-62).

This magic number is attributed to an icosahedral structure, composed of a strongly bound central $M^+(C_2H_2)_2$ cation surrounded by 12 neutral acetylene molecules in an icosahedral arrangement consisting of two staggered 5-membered rings along the equator with each pole capped by another molecule.[177,178] This assumption is consistent with the observed strongly bound $M^+(C_2H_2)_2$ clusters as confirmed by the theoretical calculations. It should be noted that extensive evaporation of acetylene molecules is expected upon the interaction of the hot metal ions and the cold acetylene clusters. Intracluster exothermic reactions induced by the metal ions also result in neutral evaporation. These evaporation events result in magnifying the small differences in the binding energies among the cluster ions since relatively strong bound clusters experience less evaporation. In the present system, the binding of the “outer” acetylene molecules is expected to be by mere van der Waals interaction approximately similar to the binding energy of the neutral acetylene dimer (≈1.16 kcal/mol).[179]

Although the assumption of a strongly bound $M^+(C_2H_2)_n$ core ion surrounded by 12 neutral acetylene molecules is appealing and provides a plausible explanation of the observed n = 14 magic number for the $M^+(C_2H_2)_2$ clusters, it lacks direct experimental and theoretical evidence.

6.3.3 Structural calculations of $M^+(C_2H_2)_n$ clusters for M= Fe, Co and Ni, and n = 1–3

DFT calculated structures of the $M^+(C_2H_2)_n$ clusters for M= Fe, Co and Ni, and n = 1–3 are shown in Figure 63. The calculated binding energies, vibrational frequencies (C-H symmetric and asymmetric stretch), bond lengths and angles are given in Table 6, along with corresponding values predicted from previous calculations.[67,169,180] The optimized geometries show all monomer complexes possess C2v symmetry and $^nB_1$ ground electronic state (Table 6). Comparison of the calculated structures, energies and vibrational frequencies to those computed by Klippenstein and Yang,[67,169] Duncan and co-workers,[67] and Sicilia and Russo[180] show reasonable agreement (Table 6). The only discrepancy is the calculated ground state of $Fe^+(C_2H_2)$ to be $^4B_1$ and not $^4B_2$ as with previous investigations.[169,181] Also, our calculated binding energy for this complex (50.0 kcal/mol) is larger than previously predicted (42.6 kcal/mol, Table 6). We attribute this discrepancy to the failure of the basis set (Wachters + f) to properly describe the iron cation tendency to change electronic state (spin) in going from the bare ion to the complexed form. Klippenstein and Yang[169] using a different basis set described a similar problem. For the other metals (i.e. Co^+ and Ni^+) where spin is conserved, the Wachters + f basis set yields satisfactory results. It should be pointed out that calculations by Duncan and co-workers[67] using the 6-311+G(3df,2p) basis set also arrived at the same ground electronic state ($^4B_1$) as predicted by the (Wachters + f) basis set here. As expected, DFT calculations predict planar bis-acetylene geometry for Fe^+, Co^+, and Ni^+/acetylene dimer clusters (Figure 63). This was expected based on the enhanced intensities observed for the three $M^+(C_2H_2)_n$ clusters (see Figure 60-62 for RTOF mass spectra). Several experimental and theoretical investigations have confirmed the bis-acetylene geometry to be the most stable for iron and nickel/acetylene complexes.[73,176,180] An increase in the magnitude of the C-H stretching frequency red shift(compared to that of the neutral acetylene molecule), similar to what was observed for the monomer, from Ni^+ to Fe^+ due to increasing π-electron donation from acetylene into the d-orbitals of the metal ion and back-donation of π-electron density to the π*-orbital of the acetylene molecule. The reduction in binding energy, compared to the M^+(monomer) complexes

M^+	$M^+ (C_2H_2)$	$M^+(C_2H_2)_2$	$M^+(C_2H_2)_3$
Fe^+	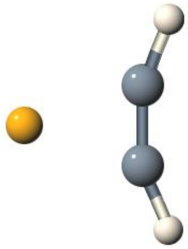	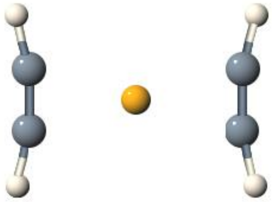	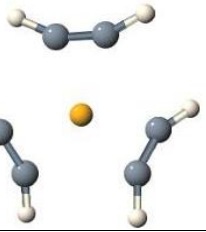 
Co^+	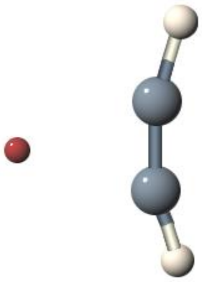	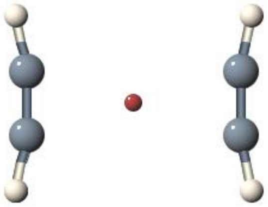	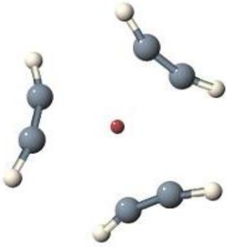 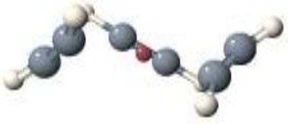
Ni^+	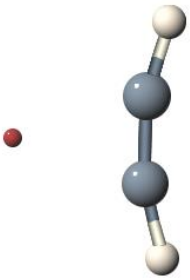	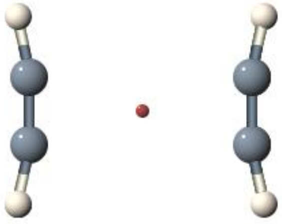	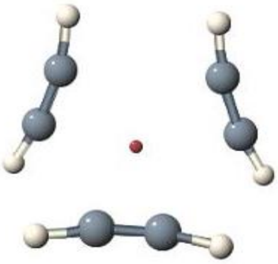 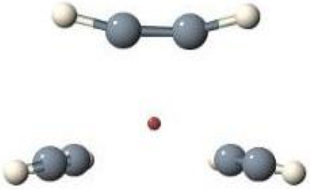

Figure 63: DFT optimized structures for $M^+(C_2H_2)_n$ complexes (n=1-3). Optimizations were performed with B3LYP utilizing the Wachters+f basis set.

Table 6: Comparison of calculated $M^+(C_2H_2)$ binding energies, bond lengths and angles, and C-H stretch frequency to literature values.

M^+	State (Symm)	Binding Energy (kcal/mol)			C-C (Å)		C-H (Å)	M^+-L (Å)		CCH Angle		Frequencies, C-H stretch, (cm^{-1})[b]		
		a	c	d	a	d	a	a	c	a	d	a	c	d
Fe	$^4B_1$ (C_{2v})	46.5	42.6		1.26		1.08	1.86	1.91	157.7		3144, 3207	3163, 3233	
Co	$^3B_1$ (C_{2v})	45.9	47.4		1.25		1.08	1.90	1.90	163.0		3166, 3241	3174, 3252	
Ni	$^2B_1$ (C_{2v})	47.4	48.0	47.0	1.24	1.23	1.08	1.88	1.87	165.0	165.8	3172, 3251	3192, 3273	3156, 3204

[a] Current work.

[b] Vibrational frequencies scaled by 0.96.

[c] Reference 171.

[d] Reference 67.

is attributed to the interactions between the acetylene molecules. Optimized geometries for the $M^+(C_2H_2)_3$ clusters for Fe^+ and Co^+, show a pseudo-cyclic structure with each acetylene molecule distorted from planarity (Figure 63) to reduce repulsive interaction between ligands (predicted symmetries were D_3 and C_3 for $Fe^+(C_2H_2)_3$ and $Co^+(C_2H_2)_3$, respectively). The predicted geometry for the Ni^+ trimer complex differs markedly from those of Fe^+ and Co^+. Instead of the pseudo-cyclic structure, the $Co^+(C_2H_2)_3$ geometry (C_S) is basically an addition of a third acetylene molecule to the "puckered" geometry predicted for the dimer complex. The third acetylene molecule is located above the dimer plane with CCH angles (165.4◦) different from the other two acetylene molecules (167.4◦/168.8◦)

For all three TM ion trimer complexes $Fe^+(C_2H_2)_3$, $Co^+(C_2H_2)_3$ and $Ni^+(C_2H_2)_3$, the metal cation is embedded in a "cage" created by the three acetylene molecules.

6.4 Discussion

The generation of hydrocarbon fragments with different composition and intensity from the reactions of TM ions and acetylene clusters could suggest a varying order of catalytic activity of the TM ions towards polymerization of acetylene. Since in the mass spectra we also observe hydrogen abstracted acetylene clusters (catalyzed by metal ion), it can be assumed that the fragment ions are produced upon reactions of the TM ions within the clusters followed by evaporation from the clusters. Based on the abundance of the ions namely $C_6H_4^+$, $C_6H_5^+$, $C_8H_6^+$ and $C_8H_7^+$ it can be concluded that these ions are covalently bonded hydrocarbons and not simply composed of acetylene clusters bound by ion-induced dipole and dispersion interactions. These fragment ions are suspected products of TM cation induced cyclotrimerization of acetylene to form the benzene ion, $C_6H_6^+$, and its fragment product ions, $C_6H_5^+$ and $C_6H_4^+$, as previously reported by Schwarz and co-workers in the case of Fe^+.[73,163,172] We have shown in earlier studies that EI ionization of large acetylene clusters produces a prominent ion signal at $(C_2H_2)_3^+$ with a structure identical to that of the benzene cation generated as a result of intracluster ion–molecule reactions.[173] Another study, based on vibrational predissociation spectroscopy, has suggested the presence of multiple isomers of the $(C_2H_2)_3^+$ ion including a contribution from the benzene type ion in cationic acetylene clusters $(C_2H_2)_n^+$ formed by charge-transfer collisions of Ar^+ with neutral acetylene clusters.[182] We have also reported new reactions of the benzene radical cation with acetylene over a wide temperature range from 120K to 680 K, showing that acetylene undergoes sequential additions onto the benzene cation with two different mechanisms operating at low and high temperatures.[23] Interestingly, under ordinary conditions at 300 K, the benzene cation does not react with acetylene as reported by another study.[183] However, at low temperatures (120 K) associative charge transfer reactions of acetylene onto the benzene cation catalyze the conversion of acetylene molecules into cyclic/polymerized ions. At high temperatures (680 K) addition/elimination reactions lead to the generation of possible naphthalene-type ions.[182] Since in the present work the major hydrocarbon ions observed are due to $C_6H_4^+$, $C_6H_5^+$, $C_8H_6^+$ and $C_8H_7^+$, it appears that the observation of these ions in the mass spectra is a signature of a metal ion catalyzed polymerization process distinct from the reactions observed in cationic acetylene clusters $(C_2H_2)_n^+$.[23,173,182,183] Previous studies dealing with gas phase reactions of TM cations with acetylene have reported cyclotrimerization of acetylene resulting in the formation of $C_6H_6^+$. [73,163,172] In the present study, $C_6H_6^+$ is not a major ion but the related ions $C_6H_4^+$ and $C_6H_5^+$ and the higher analogs $C_8H_6^+$ and $C_8H_7^+$ are observed following the reactions of laser-generated Fe^+, Co^+ and Ni^+ ions with neutral acetylene clusters. Based on previous studies on the reactivity of TM ions with small organic molecules, it has been inferred that first row group 8–10 metal ions are more active towards C-C bond activation, whereas the metal ions early in the transition series, as well as the second- and third-row metal ions preferentially activate the C-H bonds.[184] This is also clearly evident from the mass spectra of the $V^+(C_2H_2)_n$ clusters (Figure 51) which shows significant hydrogen abstraction of the type $(VC_{2n}H_{2(n-m)})^+$, thus suggesting that these species are produced by the C-H bond activation of the metal ion–acetylene complexes. This observation suggests that the mechanism responsible for TM initiated polymerization of acetylene clusters, under our experimental conditions proceeds via C-H bond activation.

6.4.1 Mechanism for catalytic polymerization of acetylene

Under the current experimental conditions, we were unable to detect any ion signal when the focused laser beam was allowed to directly interact with the supersonic jet of acetylene clusters. However, strong ion signals corresponding to the metal–acetylene cluster ions and other hydrocarbon fragments were readily observed when the produced clusters interacted with metal cations generated by LVI. The observation of dehydrogenated acetylene cluster ions of the type $C_{2n}H_{2(n-m)}{}^+$ in the mass spectra suggests that these ions originate from the metal–acetylene cluster ions and are produced as a result of a cluster evaporation process. Also since the observation of hydrocarbon ions depends on the nature of the TM cation under identical experimental conditions, the possibility of acetylene polymerization by EI ionization of neutral clusters using energetic electrons produced by LVI process is unlikely. It is well known that TM ions are characterized by a large number of low-lying electronic states that can be easily accessed under the typical LVI conditions.[106,185,186] Since most of the low-lying electronic states of first-row TM cations have either a $3d^n$ or a $4s^1 3d^{n-1}$ electronic configuration, most of the transitions between these states are parity forbidden. Therefore, the radiative life times of the excited states can be on the order of milliseconds or even seconds which allow the experimental observation of these states.[187] In fact, ion mobility measurements for most of the laser generated transition metal cations reveal the presence of two or three mobility peaks that correspond to ground and excited states of different electronic configurations.[106] It has been shown that the LVI process under conditions similar to the current experimental conditions can easily access excited states with energies in the range of 1–1.5 eV. [106] It is interesting that the observed reactivity of the TM cations towards acetylene cluster polymerization correlates with the presence of low-lying electronic states. For example, the TM cations V^+, Fe^+, Co^+ and Ni^+ have several excited states lying within 1.2 eV of their ground states as shown in Table 5. [106,56] In the present work, hydrogen abstraction reactions (Equation 6.1) are observed in $V^+(C_2H_2)_n$ (Figure 51 inset), and efficient generation of hydrocarbon ions is observed within $Fe^+(C_2H_2)_n$, $Co^+(C_2H_2)_n$ and $Ni^+(C_2H_2)_n$ clusters (Figures 53-55). On the other hand, no reactivity is observed in acetylene clusters containing Cr^+, Cu^+ and Zn^+ ions where their first excited states energies are 1.52, 2.81 and 7.9 eV, respectively.[185] This correlation suggests that the observed C-H bond activation is driven by electronically excited TM ions possessing low-lying excited states that can be reached under the current LVI conditions. In our experiments, the $M^+(C_2H_2)_n$ clusters are generated by the pickup method, and it is expected that the excited metal ion would reside on the surface of the acetylene clusters for significant duration for the C-H activation to take place. Based on the observed fragmentation pattern, it is clear that the fragment $C_4H_3^+$ is an essential link to the generation of species such as $C_6H_4^+$, $C_6H_5^+$, $C_8H_6^+$ and $C_8H_7^+$. The catalytic process could be initiated by C-H bond activation of a surface acetylene molecule on the cluster by the excited metal ion via the formation of an insertion intermediate within the $M^+(C_2H_2)_n$ cluster by oxidative addition. The activated acetylene molecule adds further acetylene units leading to the formation of higher acetylene polymeric ions as shown in Scheme 2. Scheme 2 qualitatively explains the mechanism of acetylene polymerization resulting in formation of the hydrocarbon fragments $C_4H_3^+$, $C_6H_5^+$ and $C_8H_7^+$ upon cluster evaporation. This mechanism explains the important role of the $C_4H_3^+$ intermediate in the metal ion-assisted acetylene polymerization. The generation of species like $C_6H_4^+$ and $C_8H_6^+$ could be ascribed to β-H abstraction upon activation of additional C-H bond by the metal ion. Also these ions could be produced if the condensation ion is formed with excess energy.[188] Previously, Walch has theoretically investigated the minimum energy pathway for the ring closure reaction of C_4H_3 with C_2H_2 using RHF calculations and concluded that the ring closure reaction leading to phenyl radical formation is thermodynamically favorable.[189] Similarly, Bauschlicher et al. investigated the mechanism of

$$
\begin{aligned}
&M^{*+}(C_2H_2)_n \rightarrow [H-M-C_2H....(C_2H_2)_{n-1}]^+ \rightarrow [H-M-C_4H_3....(C_2H_2)_{n-2}]^+\\
&\rightarrow [H-M-C_6H_5....(C_2H_2)_{n-3}]^+ \rightarrow [H-M-C_8H_7....(C_2H_2)_{n-4}]^+
\end{aligned}
$$

Scheme 2.

polycyclic hydrocarbon growth by computing the barriers and heats of reactions for the conversion of benzene to naphthalene upon acetylene addition using the B3LYP level of theory.[190] In their study it was inferred that the cationic synthesis mechanism is thermodynamically more favored. Based on analogy with the two studies above, which predict ring closure to be thermodynamically favorable, we can infer that under our experimental conditions the polymeric species generated $C_6H_4^+$, $C_6H_5^+$, $C_8H_6^+$ and $C_8H_7^+$ have structures equivalent to benzene and styrene derivatives. However, further theoretical studies are essential to justify this proposition.

6.5 Conclusions

The present study explores the feasibility of utilizing acetylene clusters as model reactors for screening the catalytic activity of laser-generated transition metal ions towards polymerization of acetylene. A sequential addition of acetylene molecules to a metal activated acetylene monomer within the clusters is proposed as a possible mechanism initiated by C-H bond activation. The proposed mechanism suggests the intermediacy of $C_4H_3^+$ in the generation of higher hydrocarbon species such as $C_6H_4^+$, $C_6H_5^+$, $C_8H_6^+$ and $C_8H_7^+$. Based on thermodynamic considerations it is expected that the observed hydrocarbon ions would have cyclic structures equivalent to benzene and styrene fragments. Enhanced ion intensities have been observed for $V^+(C_2H_2)_2$, $Cr^+(C_2H_2)_2$, $Fe^+(C_2H_2)_4$, $Co^+(C_2H_2)_3$, $Ni^+(C_2H_2)_3$, and $Cu^+(C_2H_2)_3$ consistent with the formation of stable covalent products formed by metal ion catalyzed polymerization of acetylene clusters. DFT calculations identify the structures of the initially formed trimer ion clusters $Fe^+(C_2H_2)_3$, $Co^+(C_2H_2)_3$ and $Ni^+(C_2H_2)_3$ where the metal cation is embedded in a “cage” created by the three acetylene molecules. Isomerization of these cluster ions into the more stable metal ion–benzene adducts is suggested and the energy needed to surpass the isomerization barriers is likely to come from the laser-generated excited state metal ions. A remarkable even–odd alternation has been observed for $Co^+(C_2H_2)_n$ clusters with enhanced ion intensities for n = 3, 6, 9 and 12, which could be explained by multiple isomerization events resulting in the formation of $Co^+(\text{benzene})_n$ clusters with n = 1–4. The combination of the excited state energy of the TM ions and the unique cluster environment which promotes concerted multi-monomer interactions with the metal ions could lead, under favorable conditions, to TM ion-mediated cyclotrimerization of acetylene molecules resulting in the formation of benzene and other polycyclic aromatic hydrocarbons. In addition to the formation of covalent adducts, a magic number behavior has been observed for

$M^+(C_2H_2)_n$ clusters for M= Fe, Co and Ni and n = 14 suggesting the possibility of a cage structure containing a strongly bound $M^+(C_2H_2)_2$ cation core surrounded by 12 neutral acetylene molecules in an icosahedral arrangement. Further experimental and theoretical investigations focusing on the structures of the observed magic numbers are needed to shed more light on metal ion-containing acetylene clusters.

CHAPTER 7. Probing the Catalytic Activity of 2nd Row TM Ions with Acetylene Clusters

7.1 Introduction

The chemistry and physics of transition metals has fascinated a lot of researchers for the past seven decades due to their wide application in many industrial processes. Most obvious is their versatile application in the field of catalysis[141,191], highly engineered materials[192], and renewable energy generation[193-195].

This field attracted the attention of scientist in the 1940's and 50's when several organic chemists aimed at developing theories to elucidate the nature of bonding in metal –alkene π-complexes which had been observed experimentally in several compounds such as the Zeise's salt, which led to the Dewar-Chatt-Duncanson model.[196,197] In the same period of time, Ziegler[198] and Natta[199] discovered the Ziegler-Natta catalyst which has had a tremendous impact on the material industry. Since then, the mechanism of C-H and C-C bond activation by transition metal centers has remained an active field of study.

Gas-Phase investigations of the interactions between transition metal ions and small hydrocarbons molecule has also boomed due to the fact that properties and characteristics of the bare transition metal ions, their neutrals and ligated complexes that are observed in these studies can give valuable insight on the mechanism of catalysis in the condensed phase and their stoichiometry.[150]

A lot of theoretical and experimental investigations have been conducted on understanding the interactions of specific transition metals cations with the small hydrocarbon molecules,[162,172,180,194,200-212] but most have focused on the first row transition metal ions.[201] For example, Guo and Castleman probed the reactivity of Ti^+ towards olefin polymerization using a selected ion drift tube mass spectrometer with a laser vaporization source, by examining the dehydrogenation and polymerization of ethylene and propylene.[203] They concluded that Ti^+ showed significant reactivity towards the polymerization of olefins. Carpenter *et.al*[202] also used product kinetic energy release distribution to study the energy requirement for the reaction between the first-row transition metal cations (Fe^+, Co^+, and Ni^+) with acetone, leading to the formation of C_2H_6 and CO through C-C activation. They found that all the three cations showed low reactivity towards acetone due to the existence of a rate-limiting tight transition state along the reaction coordinate, which has to do with the initial C-C bond activation by the metal ion. Relatively less work has been done on the interaction of the second and third row transition metal ions with small hydrocarbon molecules in comparison with the first row. A few studies have been conducted on transition metal atom congeners in the same periodic group to assess the variation in oxidative C-H/C-C activation as you go down the group.[210,211] Interestingly, not much work has been done to understand the general periodic trend on the activity of transition metal ions towards C-H/C-C activation, under similar experimental conditions because most of the work done have not been systematic, but look at specific metal ions.[184,200,209,213-215] This is necessary since these transition metal cations could show variable catalytic activity, under different experimental conditions. For example, P. B. Armentrout[200] found Mo^+ to be almost as unreactive towards C_2H_6 and C_3H_8 under thermal conditions, just as its first row congener Cr^+, whereas Schilling *et.al*[216] concluded that Mo^+ exhibited alkane-activation activity, unlike Cr^+.

Here we report experimental and complimentary Density Functional Theory computational work done on the goal of probing the reactivity of laser vaporization ionization generated transition metal(TM) ions towards acetylene clusters generated through supersonic expansion. The resulting product ions are analyzed using a reflectron time of flight mass spectrometer. The aim of this series of experiments is to investigate the catalytic activity of these TM ions towards acetylene polymerization under the same experimental conditions, giving us the general periodic trend of the TM ions. In a previous publication[207], we presented results from work done on the first row TM ions under the similar conditions towards acetylene polymerization. It was found that the later first row TM ions, (Fe^+, Co^+, and Ni^+ respectively) showed activity towards C-H bonds cleavage leading to polymerization of the acetylene clusters resulting in the formation of hydrocarbon fragment ions. V^+ also showed intra-cluster dehydrogenation, but did not result in the formation of the hydrocarbon fragment ions. In this study we present on the interaction of the second row TM ions with acetylene polymerization. Acetylene as a molecule gives us the ability to study the possible interaction between transition metal ions with more complex unsaturated molecules, where acetylene serves as a prototype for the unsaturated bonds in the complex unsaturated molecule, in this study. The simplicity of this molecule also gives us an idea about the competition of C-H vs. C-C activation by the TM ions, in that there is only one unsaturated C-C bond and two identical C-H bonds per acetylene molecule.

7.2 Experimental and Computational Methods

The experiments were done using the VCU RTOF-MS shown in figure 2 in the experimental section, which is based on a single stage ion mirror and 2nd order space focusing principle[95]. The system consists of two differentially pumped vacuum chambers. The first chamber, pumped by a Varian VHS-6 diffusion pump (3000 L/s in He), houses a 250μm supersonic nozzle (General valve, series 9) for cluster production as well as a metal target for cation generation by LVI (source chamber). The second chamber (RTOF-MS chamber), pumped by a Varian VHS-4 diffusion pump (1500 L/s in He), contains the acceleration plates, flight tube, ion mirror and a micro channel-plate detector (MCP). The typical operating pressure of the source chamber and the TOF chamber are 1.0×10^{-5} Torr and $\leq 2\times10^{-6}$ Torr, respectively. For a typical experiment, the metal target is placed 0.5–1.5cm from the nozzle face and displaced 0.5–1.2cm from the beam axis. Acetylene clusters formed by supersonic expansion of a mixture of ≈ 1% acetylene (BOC GASES®) in helium (ultrahigh purity, Spectra Gases, 99.99%, 4–5 atm, 250–350_s pulse widths, 8 Hz) are interacted with transition metal cations produced by LVI of a metal target utilizing the second harmonic (532 nm) of a Nd-YAG laser (Continuum-Surelite SSP-I, 8–10 ns pulse width). For experiments with a higher seed ratio of acetylene to helium (>5%), acetylene vapor is passed over a dry ice/methanol cooled trap to remove the acetone stabilizer prior to the expansion. Under our experimental conditions the cluster generation source, as well as the laser used to generate the ions are pulsed. In addition, a pulsed high voltage is applied to the repeller plate to accelerate ions towards the detector. Hence synchronization of these different events in space as well as in time is very essential. A typical sequence begins with opening of the nozzle (t_0) which results in the generation of neutral acetylene clusters $(C_2H_2)_n$. After a certain delay (≈ 490–550μs), the laser Q-switch is triggered to initiate lasing, resulting in the generation of metal cations (M^+) along with anions (M^-), electrons and neutral particles. The ions subsequently interact with the neutral cluster beam forming charged clusters, $M^+(C_2H_2)_n$. The charged clusters are collimated by a 3mm conical skimmer placed at a distance of about 4–7cm coaxial to the nozzle. Approximately 1.05 ms after t_0, the pulse generator is triggered to supply voltage (100μs pulses) to the repeller plate to accelerate the ions (300 V/cm) through the ion mirrors guided by the ion optics towards the MCP detector. Signal intensity is maximized by timing the laser delay so that the cations interact with the portion of the gas pulse having maximum cluster intensity and timing the pulse-generator to pulse the repeller plate at appropriate delay times. The delay generator utilized here is a BNC, model 555 generator. Data acquisition is carried out on a digital storage oscilloscope (Lecroy 9350A, 500 MHz), averaged and transferred to a computer for further processing.

All theoretical work done in this study to obtain the lowest energy structures and the binding energies of the cluster complex ions ($-\Delta H^{o}_{n-1,n}$) were done with B3LYP hybrid density functional method[217-219] using the GAUSSIAN 03 suite of programs. [139] All thermochemistry reported here is corrected for zero-point energy (ZPE) effects. The 6-311++G (d,p) basis set is used for carbon and hydrogen, and Hay-Wadt (*n*+1) ECP VDZ .[119]This level of theory has been shown to yield sufficiently accurate results.[200,201,209] The figures shown in figures xxx

7.3 Results

The interactions of selected 2nd row transition metal ions generated by laser vaporization ionization with acetylene clusters were probed using a Reflectron-Time of Flight mass spectrometer, and the results are presented here.

7.3.1 Positive Ions

Figure 64 shows a RTOF-MS generated from the interaction between zirconium cations and acetylene clusters. In the spectra, we observe the zirconium-acetylene cluster complex ions as the major product ion series with up to six additions of acetylene unto the zirconium ion. A closer examination of the zirconium-acetylene cluster complex series reveals intracluster dehydrogenation processes being catalyzed by the Zr^+ ion after the second and sixth additions of acetylene to the complex ion, leading to the formation of a zirconium-carbide complex according to the reaction,

$$\text{i)}\ ZrC_2H_2^+ + C_2H_2 \longrightarrow ZrC_4H_2^+ + H_2 \qquad (7.1)$$

$$\text{ii)}\ ZrC_{10}H_8^+ + C_2H_2 \longrightarrow ZrC_{12}H_8^+ + H_2. \qquad (7.2)$$

We observe an increase in intensity on going from the $ZrC_2H_2^+$ to $ZrC_4H_2^+$, which could suggest an increase in stability, indicating an enhanced interaction upon the second addition between the zirconium ion and the acetylene ligands through the formation of a carbide complex with 2 Zr^+-C . We also observe hydrocarbon fragment ion formation as another reaction channel, which can be explained as the result of the insertion of the Zr^+ into C-H /C-C bonds of acetylene, leading to the activation /cleavage of the covalent bond in acetylene. The fragment ions $C_4H_3^+$, $C_6H_4^+$, $C_6H_5^+$, $C_8H_6^+$, $C_8H_7^+$are due to C-H bond insertion of the transition metal ion, whereas $C_5H_3^+$, $C_7H_3^+$, $C_7H_4^+$, are from C-C insertion.

These hydrocarbons are believed to be covalently bonded hydrocarbon ions formed by metal-ion induced catalytic polymerization of acetylene. This phenomenon has been previously observed by many researchers both theoretically and experimentally, and is well documented in literature.[73,163-165,172]

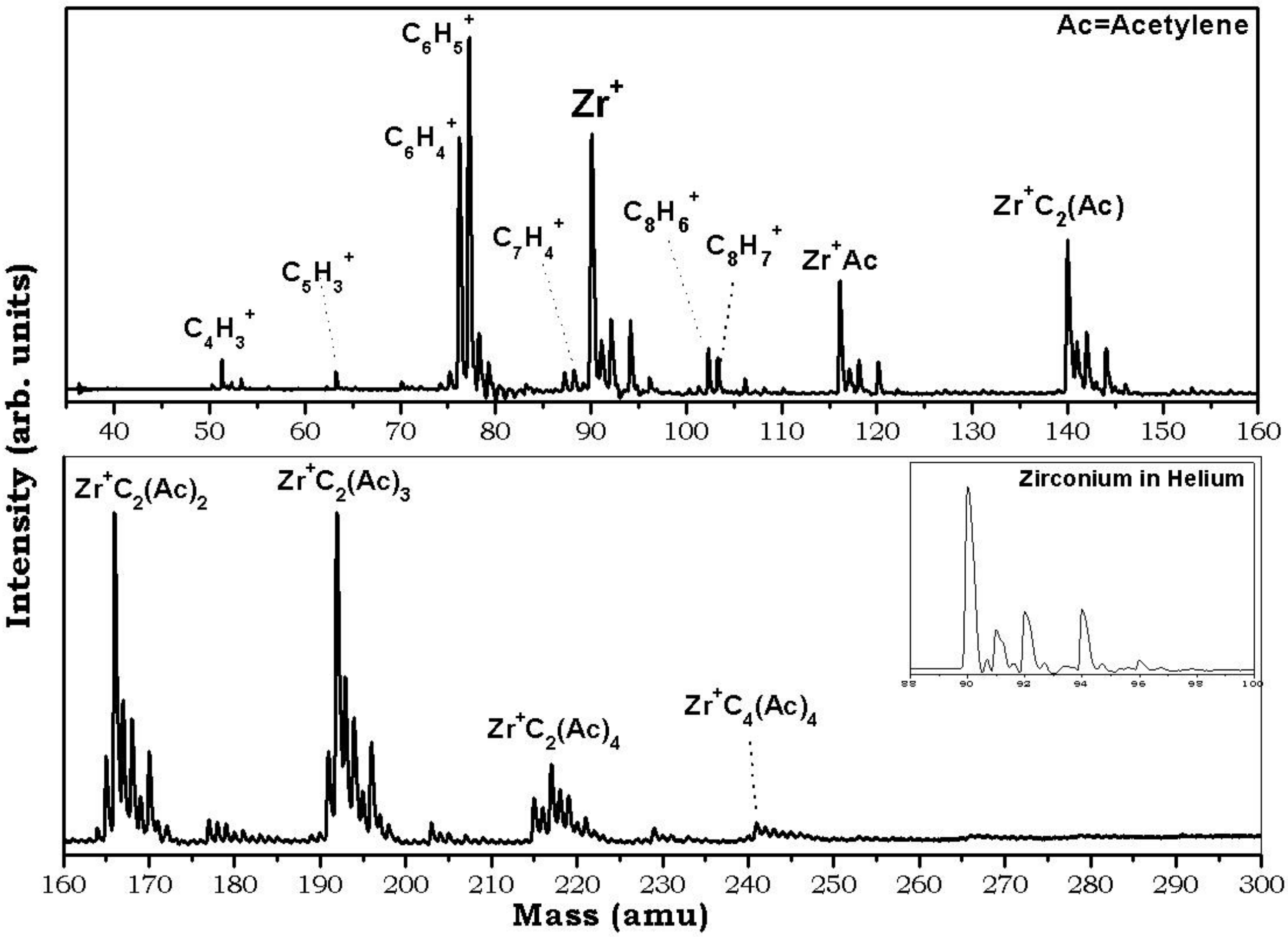

Figure 64: TOF mass spectrum of $Zr^+(C_2H_2)_n$ clusters. Inset shows the mass spectrum of Zr^+ isotope(s) in pure helium expansion.

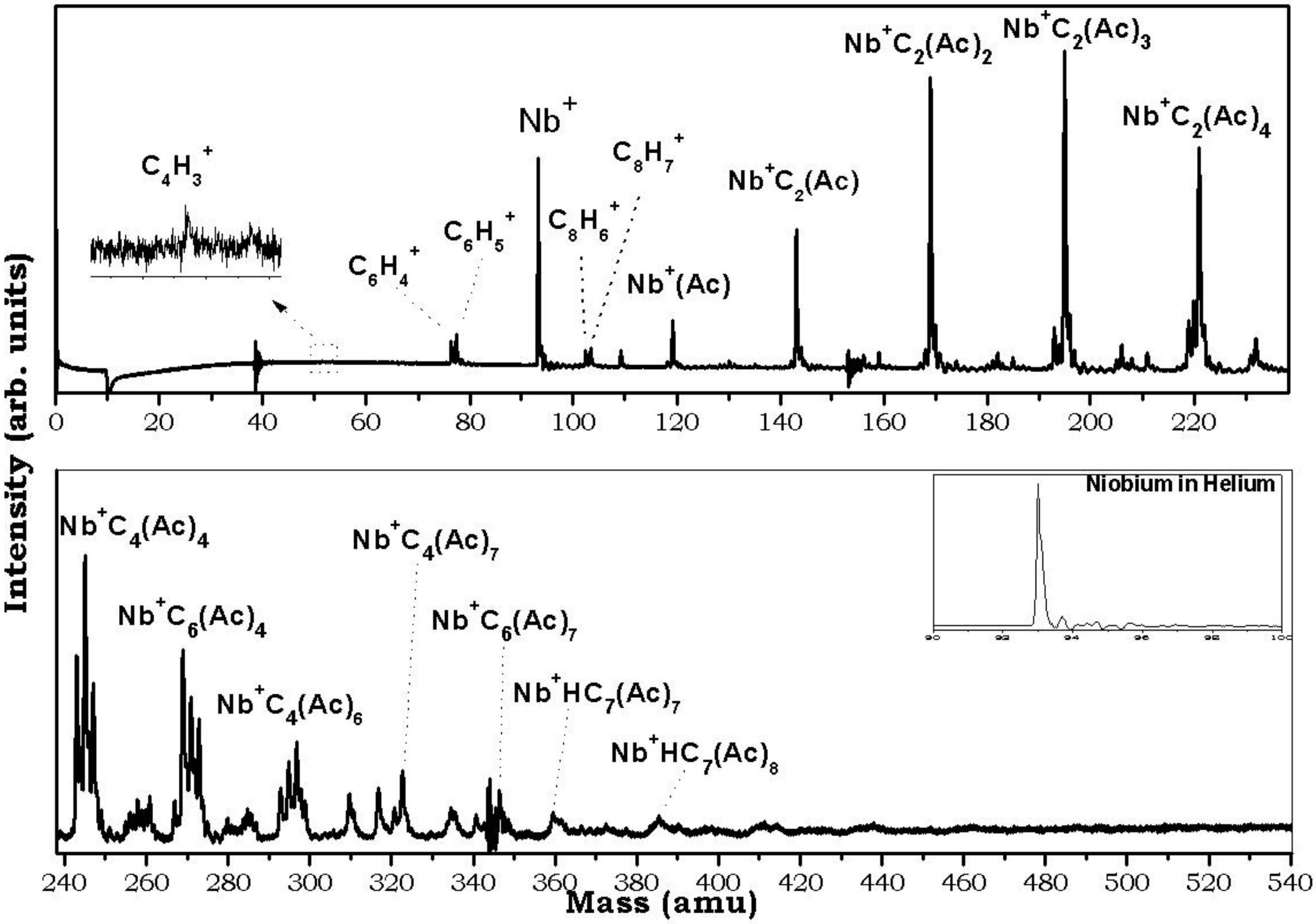

Figure 65: TOF mass spectrum of Nb $^+$ $(C_2H_2)_n$ clusters. Inset shows the mass spectrum of Nb $^+$ isotope(s) in pure helium expansion.

Figure 65 shows the RTOF-MS generated from the interaction of niobium cations with acetylene clusters. Niobium-acetylene cluster complex ions are the major product ion series, with $NbC_8H_6^+$ (a carbide complex with 2 Nb^+-C bonds) as the magic cluster. We see a steady increase in peak intensity from the first addition of acetylene unto the Nb^+, till $NbC_8H_6^+$ and then a steady decrease throughout the subsequent additions. The first intra-cluster dehydrogenation occurs after the second addition of acetylene as observed for Zr^+ and the second dehydrogenation of an acetylene molecule within the cluster, after the 6th addition of acetylene to the metal ion. Although not obvious in the Zr^+ spectrum due to possible overlapping of isotopic peak, the Nb^+ removes several hydrogen atoms from the bound acetylene cluster, but we only point out the dehydrogenated species that have the highest intensity. We observe different numbers of Nb^+-C bonds being required to stabilize the niobium-acetylene cluster complex ions. For example upon the sixth acetylene to Nb^+ to form $NbC_{12}H_8^+$ (4 Nb^+-C bonds), we observe $NbC_{14}H_8^+$ (6 Nb^+-C bonds) as the more stable carbide complex formed, but with the eight addition to the Nb^+ ion, the more stable product ion $NbC_{16}H_{12}^+$ (4 Nb^+-C bonds) requires less Nb^+-C bonds to form the most stable niobium-carbide complex.

In Figure 65, we also observe hydrocarbon fragments being formed, as was in the case for zirconium. However, we do not see any hydrocarbon fragments formed via C-C insertion. The only fragments observed here are $C_4H_3^+$, $C_6H_4^+$, $C_6H_5^+$, $C_8H_6^+$, and $C_8H_7^+$.

Figure 66 represents a RTOF-MS of Molybdenum ions interacting with acetylene clusters. The spectrum is similar to the first two spectra described for zirconium and niobium, with just a few differences. One of these differences is that we observe the first dehydrogenation of acetylene within the cluster after the 3rd addition. In the Mo^+- acetylene metal-acetylene cluster complex ion series the most stable species is a Mo^+- carbide complex $MoC_{10}H_8^+$, with 2 Mo^+-C bonds.

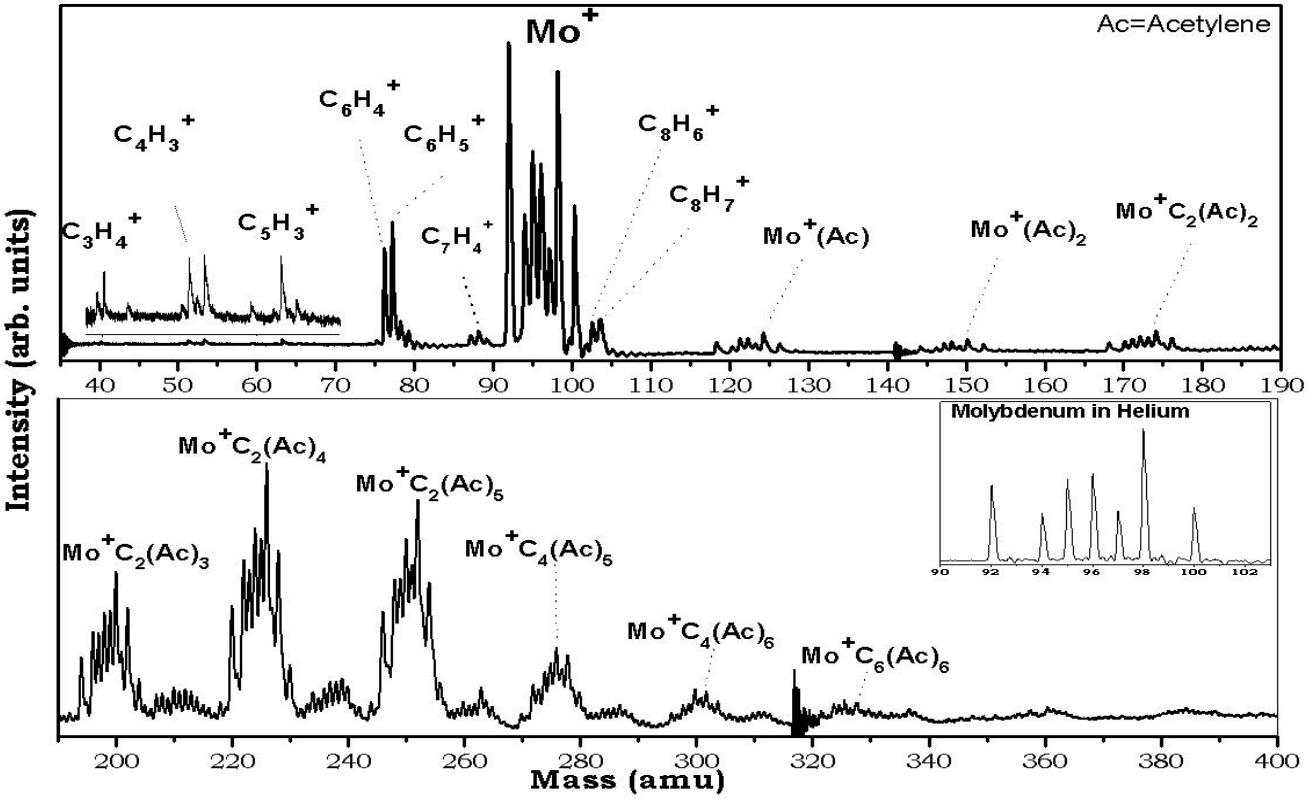

Figure 66: TOF mass spectrum of Mo $^+$ $(C_2H_2)_n$ clusters. Inset shows the mass spectrum of Mo $^+$ isotope(s) in pure helium expansion.

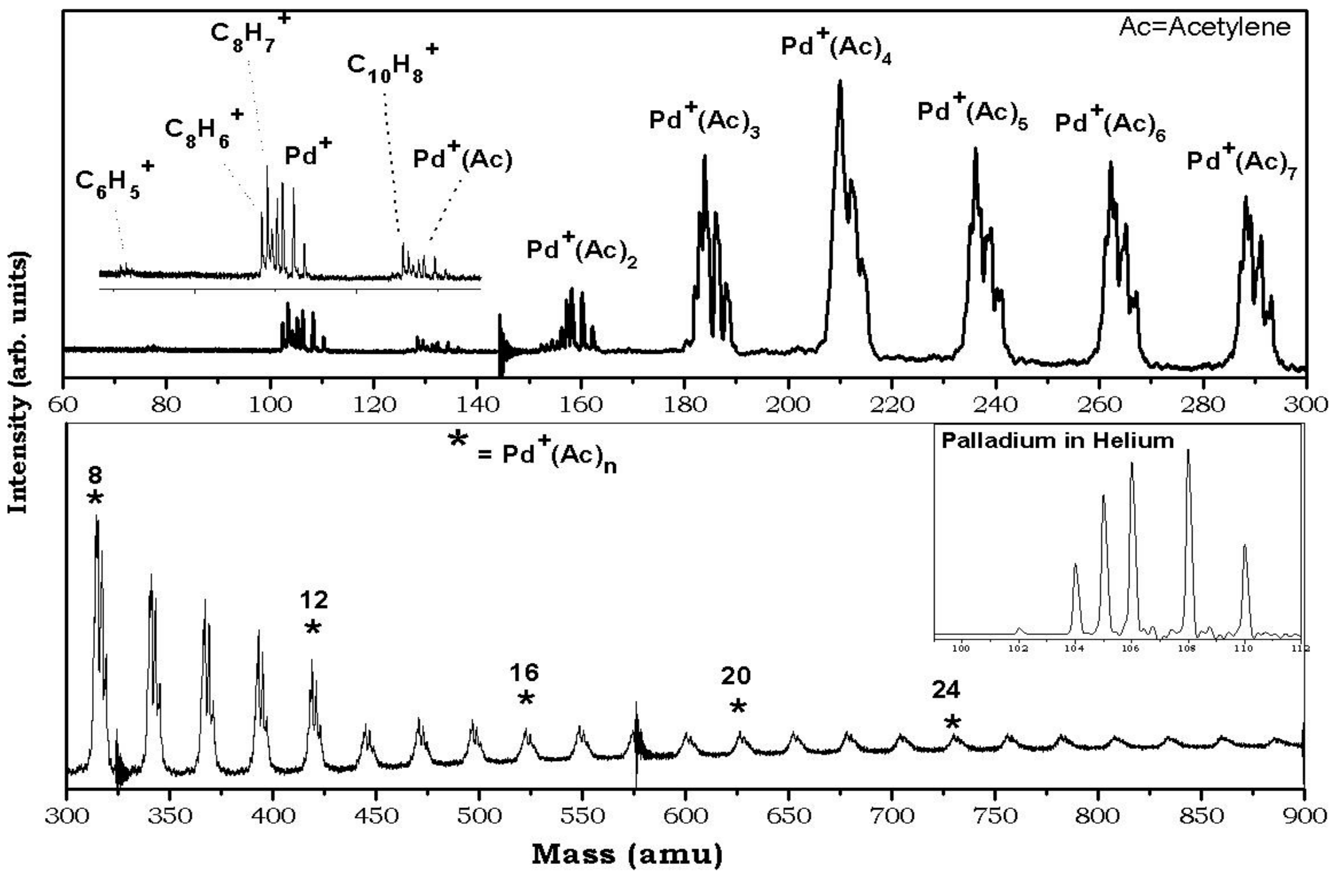

Figure 67: TOF mass spectrum of $Pd^+ (C_2H_2)_n$ clusters. Inset shows the mass spectrum of Pd^+ isotope(s) in pure helium expansion.

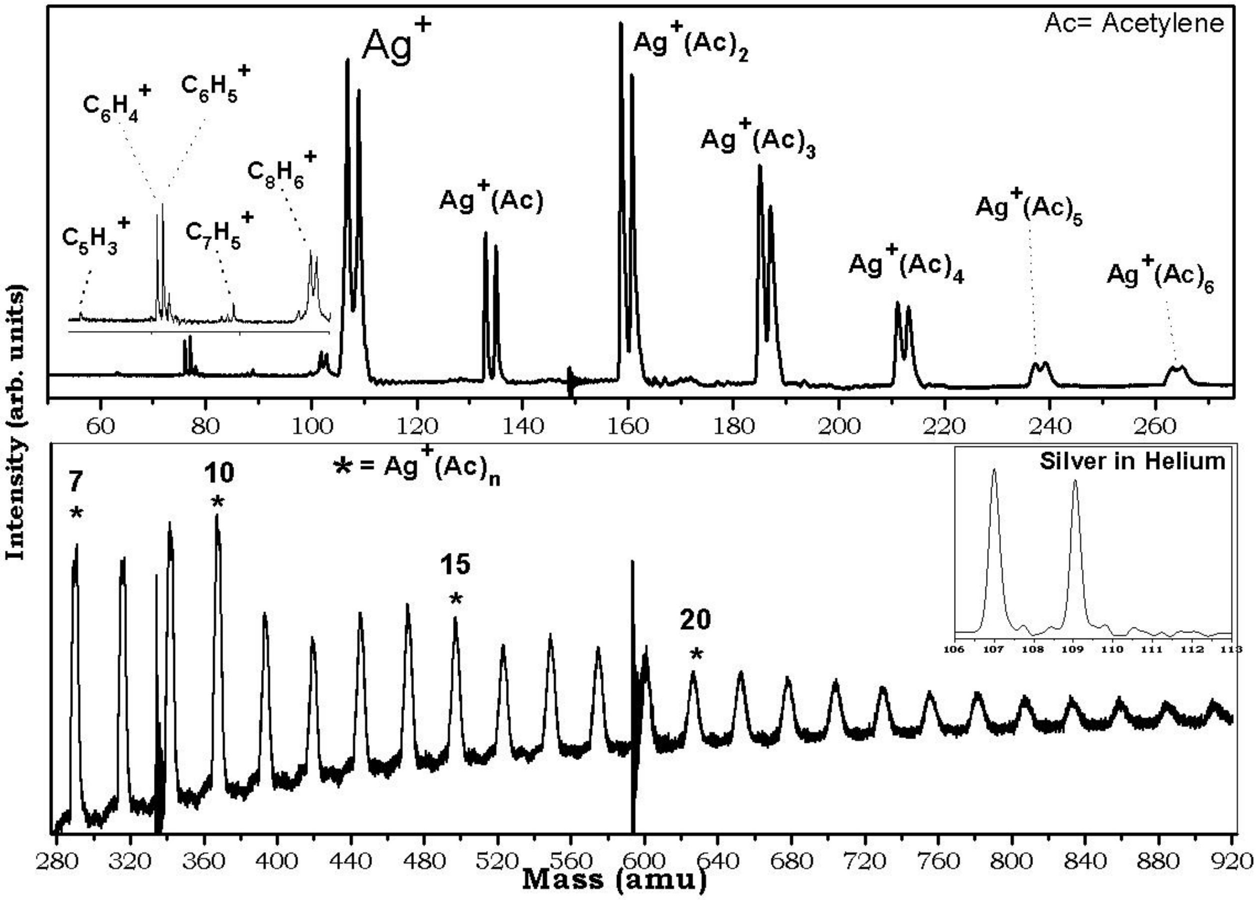

Figure 68: TOF mass spectrum of $Ag^+ (C_2H_2)_n$ clusters. Inset shows the mass spectrum of Ag^+ isotope(s) in pure helium expansion.

We see an increase in the Mo^+-C bonds required to stabilize the metal ion- acetylene complex as the number of acetylene increases. Hydrocarbon fragment ions are also observed in this spectrum, and here we see evidence of both C-C and C-H bond insertion by Mo^+. The RTOF-MS shown if Figures 67-69 represents the interactions of acetylene clusters with palladium, silver, and cadmium respectively and we observe M^+-$(Ac)_n$ as the dominant species in all 3 spectra. In all 3 spectra, we see n values in the range $1 \leq n \leq 30$. The value of n seen in these 3 spectra are higher than what was observed in figures 1-3 for Zr^+, Nb^+, and Mo^+ respectively. This difference in behavior in the second row transition metal ions towards acetylene clusters will be discussed in detail in the next section. In the Pd^+-$(Ac)_n$ series shown in Figure 66, Pd^+-$(Ac)_4$ is the magic cluster observed. In Figures 68 and 69, Ag^+-$(Ac)_2$and Cd^+-$(Ac)_2$ are observed to be the magic clusters in the M^+-$(Ac)_n$ series. In Figures 67-69, we also see ion signals corresponding to hydrocarbon fragment. The nature of the fragment ions in these 3 spectra suggest that Pd^+ favors only C-H bond activation, whereas Ag^+ and Cd^+ both show C-C and C-H activation.

7.3.2 Negative Ions

Figures 70 and 71 display the negative ion RTOF-MS of the interaction of acetylene cluster with zirconium and niobium respectively. We observe a distribution of pure carbon cluster series, and a hydrogenated carbon cluster series, namely C_n^- and C_nH^- respectively, with n values in the range 1 to 8 for Zr and 1 to 6 for Nb. The interesting feature in these two spectra is the presence of ion peaks corresponding to pure metal carbides. ZrC_2^-,ZrC_4^-, and ZrC_6^-, are seen in the zirconium spectra, whereas NbC^-,NbC_2^-,NbC_3^-, are seen for niobium. We also see peaks indicating oxide formation by niobium.

In Figure 72, we show a representative negative ion RTOF-MS for molybdenum with acetylene clusters. We do not show the negative ion spectra for palladium, silver, and cadmium because they comprise of a distribution of pure carbon clusters, and their hydrogenated forms, as shown for molybdenum in figure. In all these spectra, we do not observe any other peaks suggesting metal carbide formation.

Negative carbon clusters C_n^- and their hydrogenated analogues C_nH^- have been widely studied.[220-223] Since the positive acetylenic ions and their fragments are observed, their negative counterparts could also be formed from the interactions of the metal ions and electrons created in the plasma plume during laser ablations, leading to the formation of these negative carbon ions.

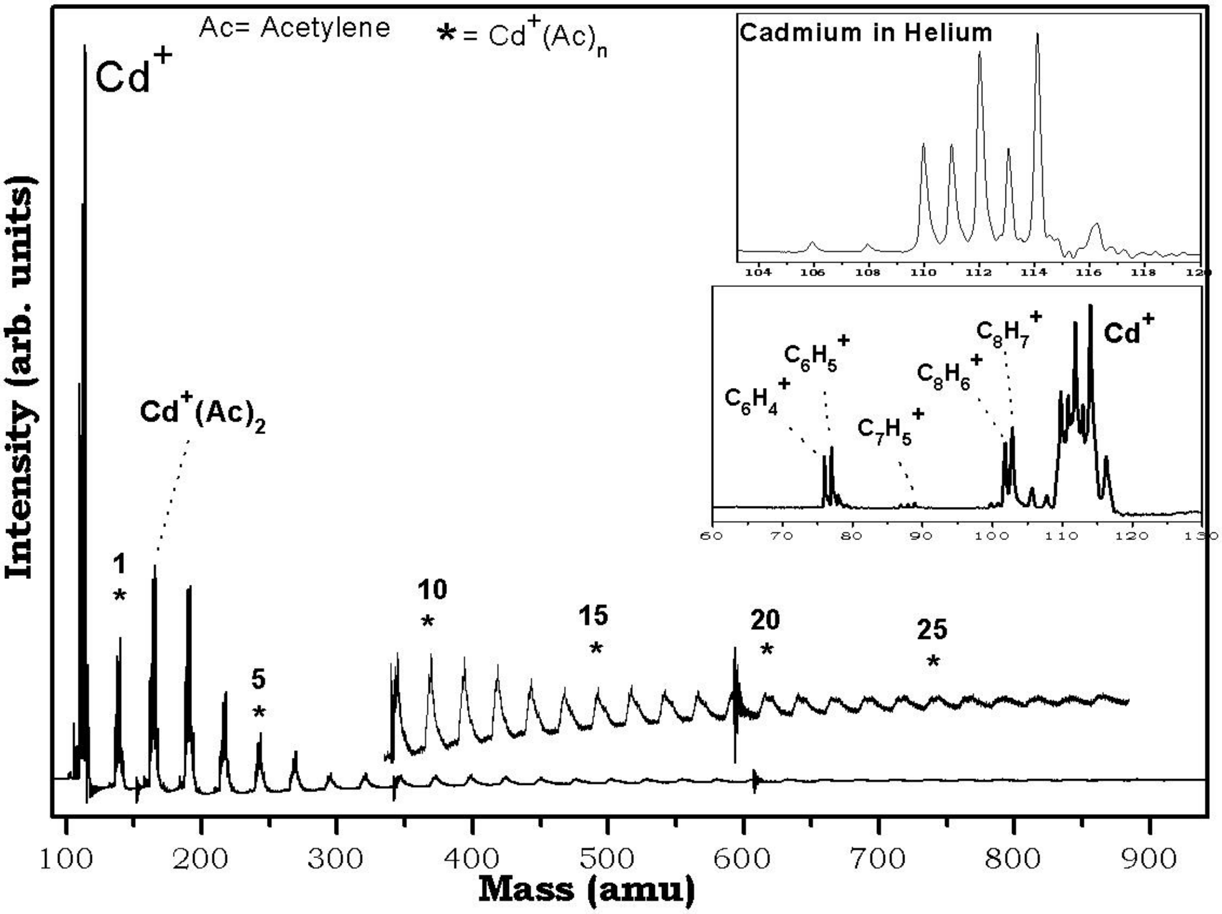

Figure 69: TOF mass spectrum of Cd $^+$ (C_2H_2) $_n$ clusters. Inset shows the mass spectrum of Cd $^+$ isotope(s) in pure helium expansion.

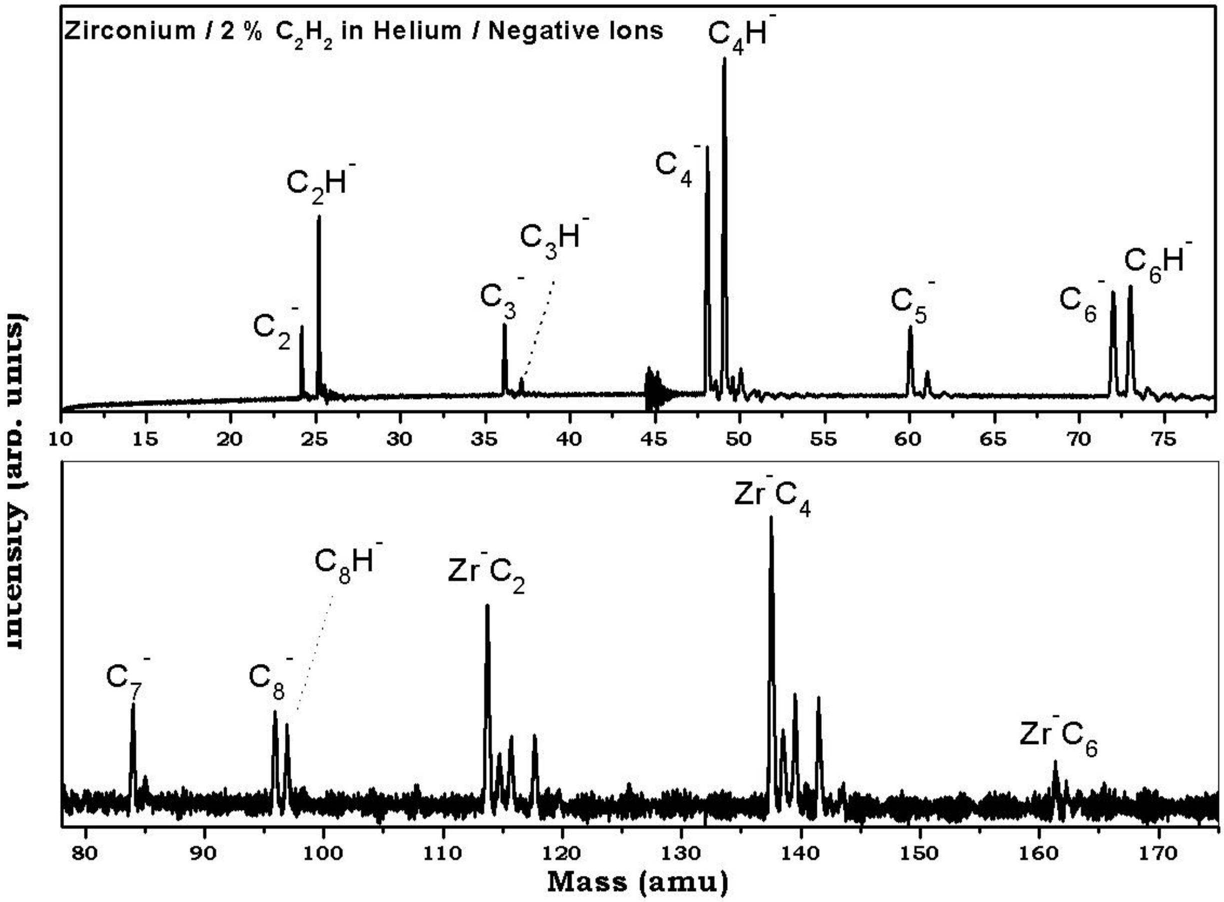

Figure 70: TOF mass spectrum of $Zr^-(C_2H_2)_n$ clusters.

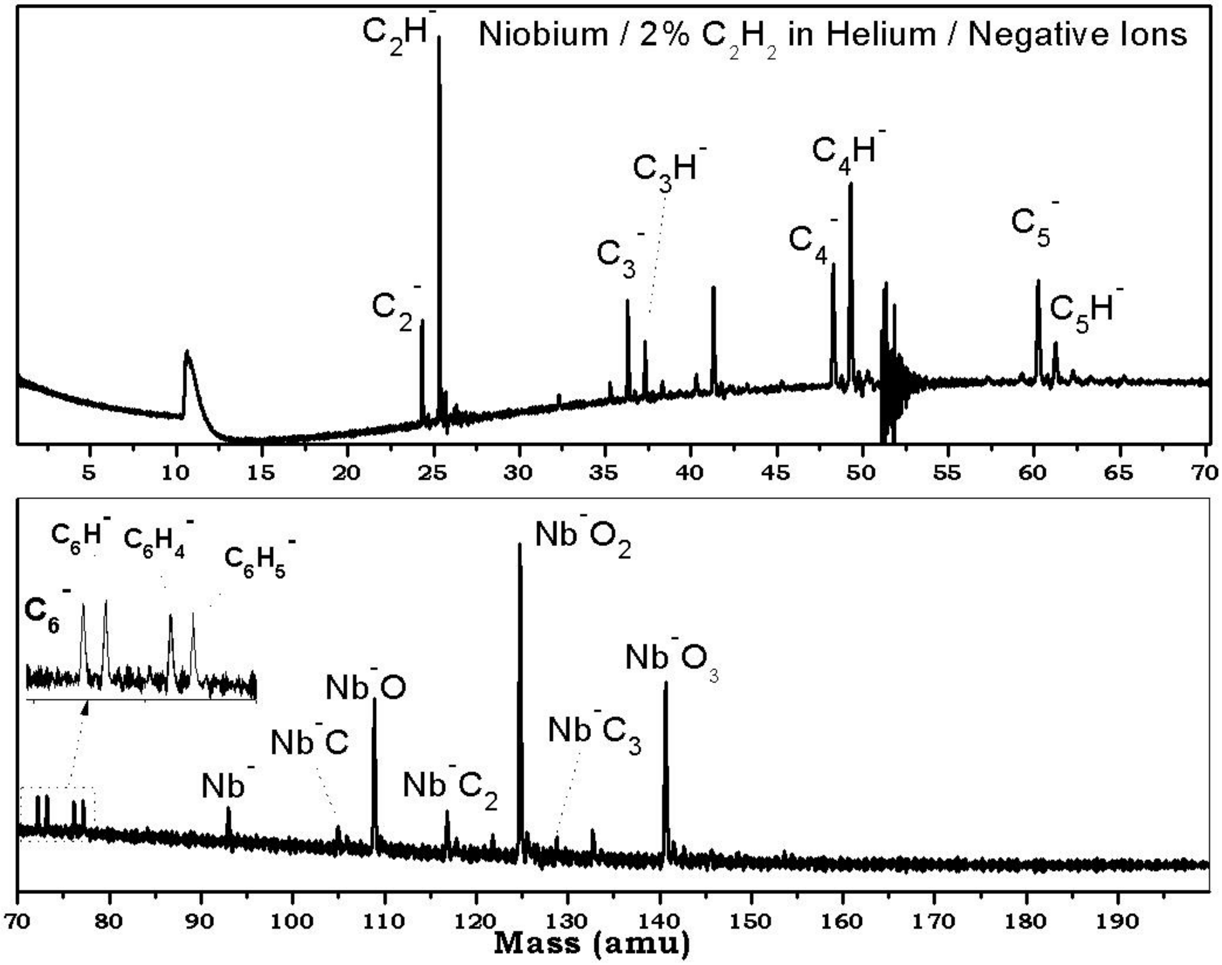

Figure 71: TOF mass spectrum of $Nb^-(C_2H_2)_n$ clusters.

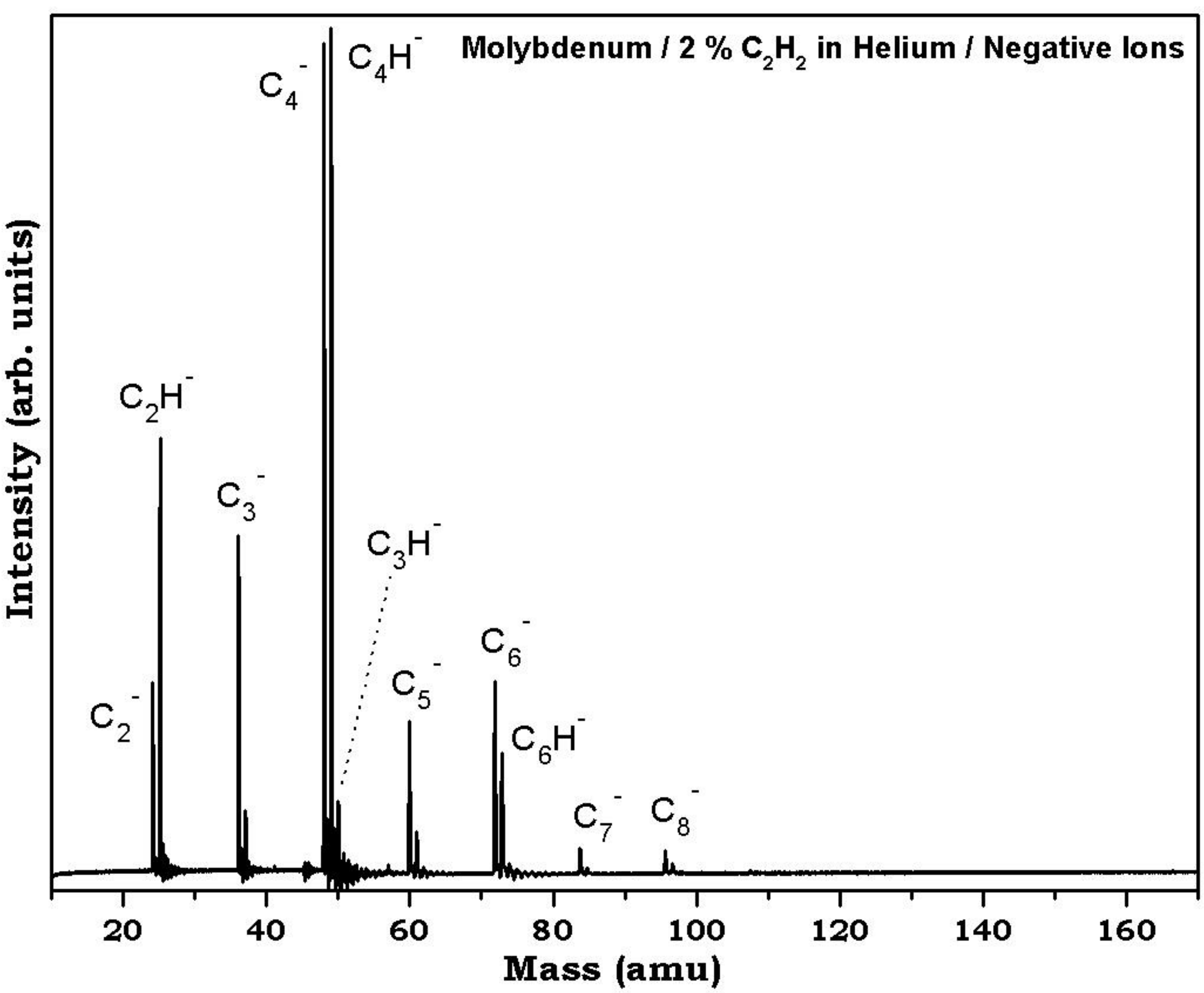

Figure 72: TOF mass spectrum of Mo $^-$ $(C_2H_2)_n$ clusters.

7.4 Structures and binding energies for the DFT calculated M-$(Ac)_n^+$ cluster ion complexes.

7.4.1 M-$(Ac)^+$

The optimized lowest energy structures for the most dominant series shown mass scans in Figures 64, 65, 66, and 67 are given in Tables 7 and 8, along with the computed binding energies ($-\Delta H^o_{n-1,n}$),for the addition, and relative energies of each metal ion-acetylene cluster ion in reference to the lowest energy congener for each acetylene addition respectively. The computed binding energies for the metal ion-acetylene complexes, compared to the complex ion forming a carbide complex are also shown in Tables 9 and 10.

Figure 73 shows the DFT optimized structures of the M-$(Ac)_n^+$ cluster ions (M=Zr, Nb, Pd, and Ag respectively) and also the optimized structures of neutral acetylene and ethene molecules. The bond lengths given in angstrom (Å) and bond angles given in degrees (º) for each molecule are also given in Figure 73.

Zr^+ and Nb^+ form insertion complexes with the first acetylene molecule as shown in Table 7, whereas Pd and Ag form π complexes respectively. A further confirmation of this trend is seen in figure 11. Zr^+ forms a bond with each carbon of the bound acetylene molecule with a bond length of 2.3Å. The structure of the acetylene molecule is slightly altered in forming this complex. The C≡C bond length changes from the 1.20Å in the neutral acetylene molecules to 1.24 Å, indicating a slight increase. The C-H bond length also increases slightly from1.06Å, to 1.08. The insertion of Zr^+ into the C≡C π bond also pushed the hydrogen away from the Zr^+ cation, causing a decrease in the CCH bond angle from 177.3 º in neutral acetylene to 157.8º in the Zr^+ (Ac) complex ion. The calculated binding energy for the formation of the Zr^+ (Ac) complex ion is 66.07 Kcal/mol.

Nb^+ binds to the acetylene molecule with a computed energy of 104.48Kcal/mol. This high binding energy is explained when the binding geometry between the Nb^+ and the acetylene complex in considered. Nb^+ forms a bond each with the two carbon atoms of the acetylene molecule with a bond length of 2.01Å. This close interaction between the two species creates a C≡C bond length of 1.33Å in the bound acetylene, 0.18Å more than the C≡C bond length in neutral acetylene and similar to the C=C bond length in neutral ethene. This is a very clear indication of the change in nature of the C-C bond of the acetylene molecule, from the sp-sp triple bond character as found in H-C≡C-H to the sp^2 character found in H_2-C=C-H_2. The CCH bond angle in the Nb^+ (Ac) complex ion is 138.9 º, 38º less than what is found in neutral acetylene.

The palladium cation binds electrostatically to the acetylene molecule through an ion-π interaction with a non-covalent bond distance of 2.25Å to form Pd $(Ac)^+$. The bound acetylene is observed to change slightly in nature compared to the neutral acetylene molecule, indicating that the molecule retains its sp character, and binds only with its π electrons. The C≡C bond length barely increases from 1.20Å to 1.22Å, and the C-H bond length also increases by just 0.01Å. The CCH bond angle changes from 177.3º in neutral acetylene to 169.4º found in the bound acetylene in the Pd $(Ac)_n^+$. The computed binding energy for the formation of the Pd $(Ac)_n^+$ cluster ion complex is 51.48Kcal/mol.

The Ag^+ (Ac) cluster ion complex forms between the silver cation and the acetylene molecule with an ion-π interaction similar to what is observed for Pd $(Ac)^+$, but with a non-covalent bond length of 2.45Å. Both the C≡C and C-H bond lengths of the bound acetylene molecules increase by only 0.01Å, compared to the unbound neutral acetylene molecule. The CCH bond angle also increases by a mere 5º, all this again indicating the retention of the sp character similar to the neutral unbound acetylene molecule.

7.4.2 M-(Ac)$_2^+$

The second acetylene molecule is observed to bind to the Zr$^+$ (Ac) forming a nonsymmetrical Zr$^+$ (Ac)$_2$ cluster ion. The Zr$^+$ is seen to insert itself into the second acetylene molecule it binds to. The binding energy drops by 39% upon the second addition as shown in table 2. The formation of Nb$^+$ (Ac)$_2$ upon the addition of a second acetylene molecule to Nb$^+$ (Ac),unlike Zr$^+$ (Ac)$_2$, leads to a symmetrical cluster ion. The binding energy is calculated to drop by 23% upon forming the di-acetylene complex. The Nb$^+$ also insets itself into the second acetylene molecule in forming the Nb$^+$ (Ac)$_2$, just as was observed for the Zr$^+$ (Ac)$_2$.

The lowest energy structure for the Pd$^+$ (Ac)$_2$ cluster ion shows the second acetylene molecule oriented at a 90º with respect to the first acetylene molecule. This could be necessary to reduce the interactions between the acetylene molecules. The binding energy decreases by 18% on adding the second acetylene molecule. Both the first and second acetylene molecules are seen to retain their C≡C bonds, and are bound electrostatically to the Pd$^+$ cation. The Ag$^+$ (Ac)$_2$ geometry is calculated to be of a similar nature to what is observed for Pd$^+$ (Ac)$_2$, with both acetylene molecules retaining the acetylenic character, and the two molecules being oriented in space around the Ag$^+$ ion at a 90º with respect to each other. The binding energy is also computed to drop by just 6% upon the second addition of acetylene.

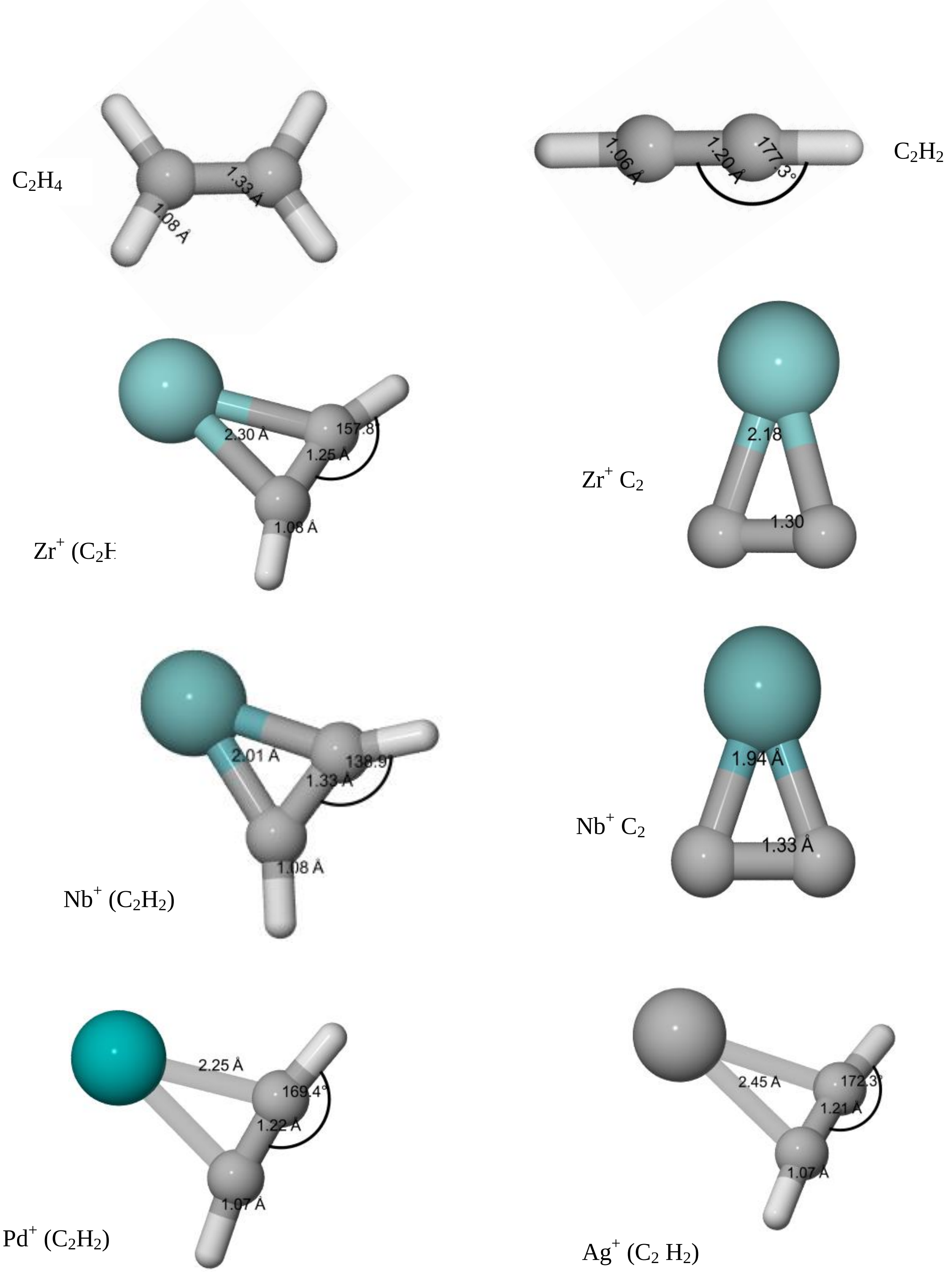

Figure 73: Density Functional theoretical optimized lowest energy structures showing the bond lengths and bond angles for the M-$(Ac)^+$and M-C_2^+.

Table 7: Density Functional theoretical optimized lowest energy structures with the computed binding energies ($-\Delta H^{o}_{n-1,n}$),for the addition to form M-$(Ac)_n^+$, n= 1, 2 along with relative energies of each metal ion-acetylene cluster ion in reference to the lowest energy congener for each acetylene addition. B. E = Binding Energy for $[M^+(Ac)_{n-1,n}]$, Rel. E = Relative Energy for the different ion clusters

n	$Zr^+ (Ac)_n$	$Nb^+ (Ac)_n$	$Pd^+ (Ac)_n$	$Ag^+ (Ac)_n$
1	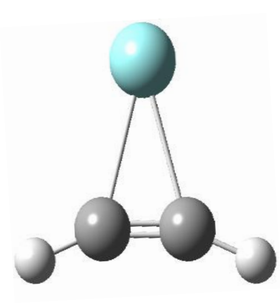	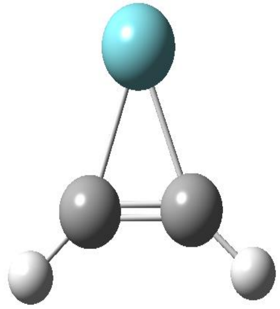	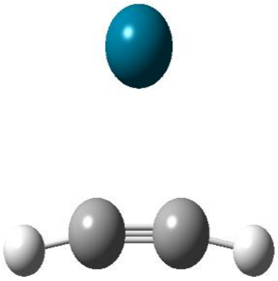	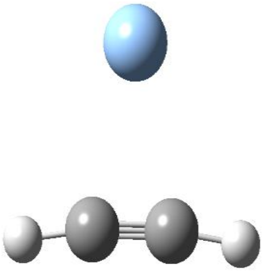
B. E. ($-\Delta H^{o}_{n-1,n}$, Kcal/mol)	**66.07042261**	**104.4840136**	**51.47832832**	**38.99278175**
Rel. E	38.41359	0	53.00569	65.49123
2	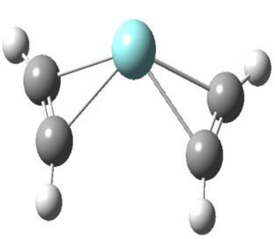	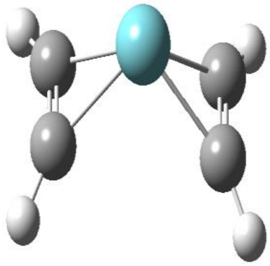	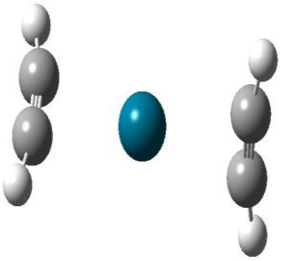	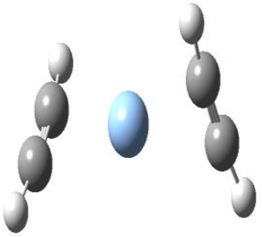
B. E ($-\Delta H^{o}_{n-1,n}$, Kcal/mol)	**40.53080631**	**80.24145836**	**42.21629548**	**36.69045123**
Rel. E	39.71065	0	38.02516	43.55101

7.4.3 M-$(Ac)_3^+$

The lowest energy structures and binding energies for the 3rd acetylene addition to the M-$(Ac)_2^+$to form M-$(Ac)_3^+$ [M= Zr, Nb, Pd, and Ag] is shown in Table 9. One interesting feature observed for the third addition series is that the binding energy increases in the formation of $Zr(Ac)_3^+$by 7%, whereas a similar addition to the $Nb(Ac)_2^+$, $Pd(Ac)_2^+$, and $Ag(Ac)_2^+$ to yield $Nb(Ac)_3^+$, $Pd(Ac)_3^+$, and $Ag(Ac)_3^+$ causes the calculated binding energies to drop by 61%, 43%, and 44% respectively. This anomaly could be attributed to symmetry effect in the M-$(Ac)_3^+$ cluster ions formed. The Zr $(Ac)_3^+$goes from a nonsymmetrical bi-acetylenic covalently bonded cluster ion complex to a more symmetric non-covalent tri-acetylenic complex with the Zr^+ ion in the center. The three acetylene molecule bound to the Nb^+ ion in Nb $(Ac)_3^+$do not bind symmetrically. The symmetric binding between the two covalently bonded acetylene molecules in the Nb $(Ac)_2^+$is retained, with the third acetylene molecules electrostatically binding above the $Nb(Ac)_2^+$plane. This apparent distortion in symmetry leads to the huge decrease in the binding energy, from 80.24Kcal/mol to 31.36Kcal/mol in the formation of the Nb $(Ac)_3^+$. $Pd(Ac)_3^+$forms with two acetylene molecules binding to the Pd^+ just below the Pd^+ plane ,on opposite sides of the cation, and the third acetylene molecule is added above the Pd $(Ac)_2^+$ plane. The third acetylene molecule is oriented 90^o with respect to the other two acetylene molecules. The Ag cation in forming the Ag $(Ac)_3^+$ cluster ion, orients the three acetylene molecules in space around itself such that no two molecules are aligned in the same plane.

7.4.4 M-$(Ac)_4^+$

The lowest energy geometry for the fourth addition of acetylene to the $Zr(Ac)_3^+$cluster ion to form $Zr(Ac)_4^+$shows the distortion of the initial $Zr(Ac)_3^+$geometry, and this leads to a 37% decrease in binding energy on going from the tri-acetylene cluster complex ion to the tetra-acetylene cluster complex ion. Nb $(Ac)_3^+$ adds the fourth acetylene molecule to form Nb $(Ac)_4^+$, by retaining the geometry of the tri-acetylene complex ion as shown if Table 8, which leads to a 14% decrease in binding energy. The calculated lowest energy Pd $(Ac)_4^+$ and Ag $(Ac)_4^+$cluster ion complexes are also shown in Table 8. All the four acetylene molecules are oriented in space around the metal cations to reduce the interaction between the acetylene molecules, whilst enhancing the individual interactions between the metal cation and each acetylene molecule.

Table 8: Density Functional theoretical optimized lowest energy structures with the computed binding energies ($-\Delta H^{o}_{n-1,n}$),for the addition to form M-(Ac)$_n^+$, n= 3, 4 along with relative energies of each metal ion-acetylene cluster ion in reference to the lowest energy congener for each acetylene addition. B. E = Binding Energy for [M$^+$(Ac)$_{n-1,n}$], Rel. E = Relative Energy for the different ion clusters

N	Zr$^+$ (Ac)$_n$	Nb$^+$ (Ac)$_n$	Pd$^+$ (Ac)$_n$	Ag$^+$ (Ac)$_n$
3	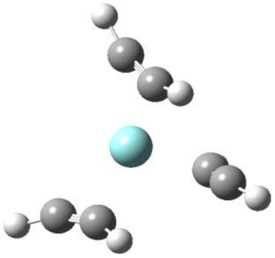	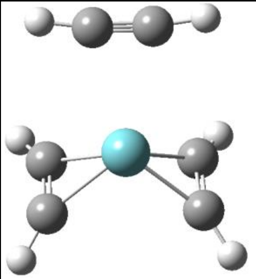	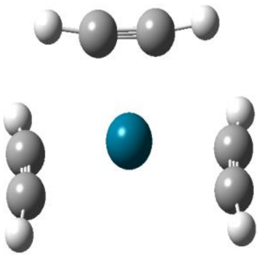	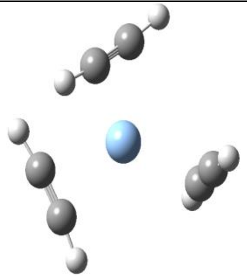
B. E. ($-\Delta H^{o}_{n-1,n}$, Kcal/mol)	**43.64764351**	**31.36415484**	**24.25573289**	**20.4360856**
Rel. E	0	12.28349	19.39191	23.21156
4	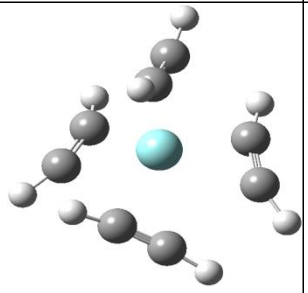	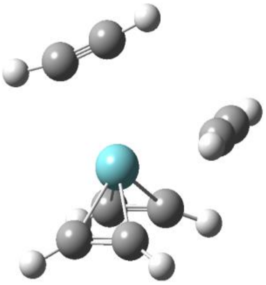	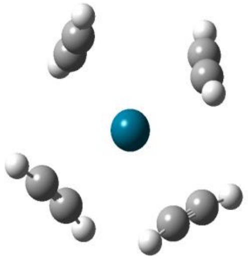	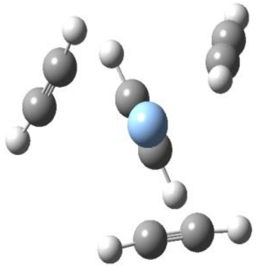
B. E. ($-\Delta H^{o}_{n-1,n}$, Kcal/mol)	**27.16800215**	**27.13411667**	**18.7832269**	**17.12221057**
Rel. E	0	0.033885	8.384775	10.04579

7.5 Prudent Thermodynamics; $[M\text{-}(Ac)(Ac)_{n-1}]^+$ or $[M\text{-}C_2(Ac)_{n-1}]^+$

The presence of metal acetylene cluster ion peaks that corresponds to dehydrogenated complexes in both positive and negative ion spectra of the early row transition metal was very interesting. The formation of a carbide complex was obviously the more favorable reaction channel leading to the formation of the most stable complex since it was observed that except for Mo^+ which formed Mo $(Ac)_2^+$ but forms the carbide complex upon the third addition of an acetylene molecule, both Zr^+ and Nb^+ formed the carbide complex upon the addition of the second acetylene molecule to the cluster complex.

To further understand this phenomenon, DFT studies were carried out to investigate the thermodynamic implications of forming the carbide cluster complex over the non-dehydrogenated cluster complex. Niobium was studied due to its relatively less complex spectra due to its isotopic distribution, compared to zirconium or Molybdenum.

The lowest energy geometries with bond length and angles are shown in Figure 73. Tables 9 and 10 also display the structures and binding energies for $M\text{-}(Ac)(Ac)_{n-1}^+$ $M\text{-}C_2(Ac)_{n-1}^+$, where n=1-3 for Nb and n=0 for Zr respectively.

The geometry of the NbC_2^+ and ZrC_2^+ show a more enhanced interaction between the dehydrogenated acetylene molecule and the metal cation. Nb $^+$in the NbC_2^+ ion binds to the carbide carbon atoms with a covalent bond 1.94Å in length, compared to 2.01Å. The bond length of the C≡C bond remains the same in length. The computed geometry of a similar carbide formed by Zr^+ in ZrC_2^+ shows that the bond length reduces from 2.30Å in the hydrogenated complex, to 2.18Å in the carbide complex, again showing an enhanced interaction between the two entities. The DFT calculated binding energies shows and almost two fold (85%) increase in binding energy when the carbide complex is formed compared to the acetylene complex for Nb^+.

A 124% increase in binding energy is observed when the carbide complex is formed, compared to the hydrogenated complex in ZrC_2^+.

In forming NbC_2 $(Ac)^+$, the binding energy drops drastically by 74%, compared to 23% in $Nb(Ac)_2^+$. This huge decrease in binding energy could be attributed to the non-symmetry introduced by the second acetylene molecule, compared to the geometry of the lowest energy structure of Nb $(Ac)_2^+$ cluster ion complex. This situation is reversed in forming the tri-acetylene complex, where the third acetylene complex adding to NbC_2 $(Ac)^+$ introduces a more symmetrical binding, thus causes only a 13% drop in binding energy, compared to a 61% decrease when the third acetylene molecule binds to $Nb(Ac)_2^+$ to form $Nb(Ac)_3^+$. The fourth addition of acetylene to NbC_2 $(Ac)_2^+$ and $Nb(Ac)_3^+$ cluster ions cause a decrease in the binding energies as shown in Table 10.

Table 9: Density Functional theoretical optimized lowest energy structures with the computed binding energies ($-\Delta H^o_{n-1,n}$),for the addition to form $[M\text{-}(Ac)(Ac)_{n-1}]^+$or $[M\text{-}C_2(Ac)_{n-1}]^+$, n= 1, 4 along relative energies of each metal ion-acetylene cluster ion in reference to the lowest energy congener for each acetylene addition. B. E = Binding Energy for $[M^+(Ac)_{n-1,n}]$, Rel. E = Relative Energy for the different ion clusters

N	Nb^+ (Ac)(Ac)$_n$	Nb^+ C_2(Ac)$_n$	Zr^+ (Ac)(Ac)$_n$	Zr^+ C_2(Ac)$_n$
0	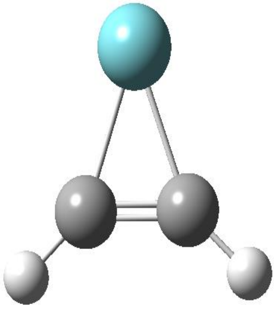	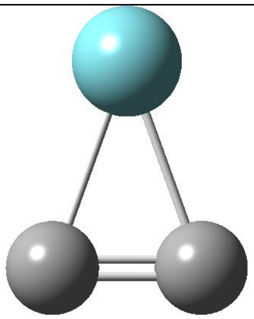	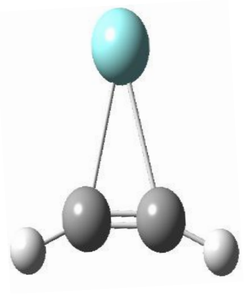	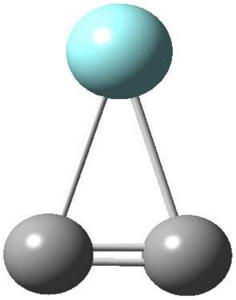
B. E. ($-\Delta H^o_{n-1,n}$, Kcal/mol)	**104.4840136**	**193.3210902**	**66.07042261**	**148.0569835**
Rel. E	88.83708	0	81.98656	0
1	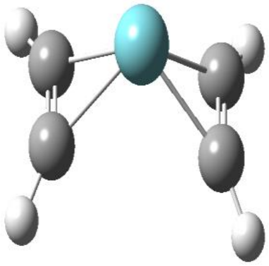	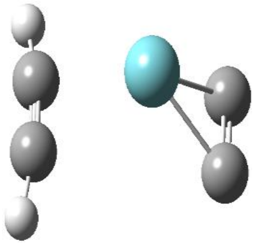		
B. E ($-\Delta H^o_{n-1,n}$, Kcal/mol)	**80.24145836**	**48.57484418**		
Rel. E				

Table 10: Density Functional theoretical optimized lowest energy structures with the computed binding energies ($-\Delta H^{o}_{n-1,n}$),for the addition, and relative energies of each metal ion-acetylene cluster ion in reference to the lowest energy congener for each acetylene addition. B. E = Binding Energy for $[M^{+}(Ac)_{n-1,n}]$, Rel. E = Relative Energy for the different ion clusters

n	Nb^{+} (Ac)$(Ac)_n$	Nb^{+} $C_2(Ac)_n$
3	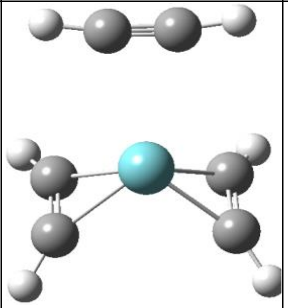	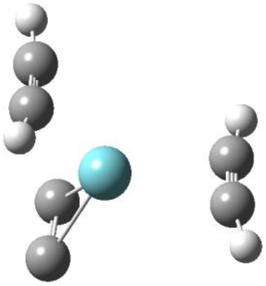
B. E. ($-\Delta H^{o}_{n-1,n}$, Kcal/mol)	**31.36415484**	**42.46416154**
Rel. E		
4	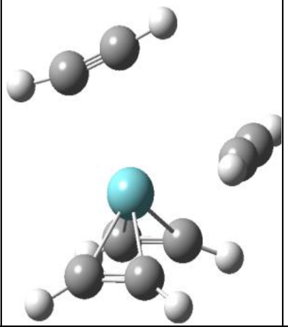	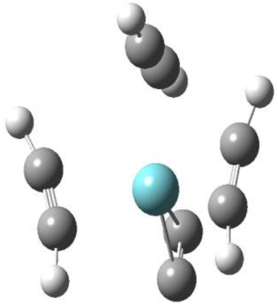
B. E ($-\Delta H^{o}_{n-1,n}$, Kcal/mol)	**27.13411667**	**28.57550484**
Rel. E		

7.6 Discussion

7.6.1 Nature of bonding in M^+-$(Ac)_n$ across the 2nd row transition metals ions (TM) of the periodic table

To explain the difference in the bonding between the TM ions and the acetylene clusters shown in the results section, we will briefly review the nature of interaction between the metal ion and the acetylene for clarity. The idea that an unsaturated molecule could use its π electrons to form a dative bond with electron acceptors was suggested by Michael Dewar in 1945.[224] In 1951 he provided a scheme to explain this observation, where he indicated that such coordination is possible if the acceptor group has filled p or d orbitals whose electrons could be back donated into the empty π antibonding orbitals of the unsaturated group. The result of this two-way charge transfer leads to a "double bond" – like coordination between the two groups and an overall stronger bond between them in the resultant π-complex.

In the gas phase, the TM ion (acceptor) will interact with an acetylene molecule (donor) in close proximity due to collision or will attract it through electrostatic forces. For an efficient association between these two species, the acetylene molecule donates electrons from its π bonding orbitals into the acceptor orbitals of the metal (5s and dσ orbitals in the 2nd row TM ions) and then the metal ion back-donates electrons from its dπ orbitals into the π* orbitals of the acetylene molecule.[149]

Based on this analogy, it is evident that the later row TM ion in the second row will meet both requirements (being able to receive the donated electrons from acetylene, and back-donate their dπ electrons from doubly occupied d orbitals into the π* of acetylene), provided that they have the right electronic configuration, where the acceptor orbitals are not filled. The early TM ions however, will not meet these requirements since they have no doubly occupied d orbitals which could be used to back-donate dπ electrons to into the π* of acetylene.[225]

The later 2nd row TM ions form strong π-coordination complexes with the acetylene molecule since it is able to efficiently donate electrons into the π* of acetylene. Thus the resultant nature of the interaction between these TM ions with acetylene is seen to be electrostatic in character. This character is clearly seen in the mass spectra of $Pd^+(Ac)_n$, $Ag^+(Ac)_n$, and $Cd^+(Ac)_n$, and also in figure 11 for $Pd^+(Ac)_n$, and $Ag^+(Ac)_n$. The early TM ions however due to the inability to efficiently bind to the acetylene molecule through electrostatic π-coordination interactions, binds to acetylene molecule by inserting itself into one of the C-C π bonds on the acetylene molecule leading to the formation of covalent bonds between the metal ion and acetylene. This causes the bond length of the C≡C bond to increase from the bond length in acetylene towards the bond length of the C=C double bond in ethylene, indicating the breaking of one of the π bonds. This behavior was observed in the mass spectra of $Zr^+(Ac)_n$, $Nb^+(Ac)_n$, and $Mo^+(Ac)_n$, as well as in the lowest energy DFT optimized geometries of $Zr^+(Ac)_n$, $Nb^+(Ac)_n$, shown in Figure 73. A decrease in the HCC angle from the value in acetylene is also observed. Similar observations have been reported previously where several research groups have exploited the dehydrogenation of ethylene by the early transition metal ions leading to the formation of metal ion-acetylene complex to study the nature of bonding between these TM ions and acetylene. [150,162,203,206,214]

In our experiment, we observe the dehydrogenation of an acetylene molecule upon the second addition in the case of Zr^+, and Nb^+, and the third addition of acetylene in Mo^+. However we do not observe any dehydrogenation of acetylene molecules in the M^+-$(Ac)_n$, when M is Pd, Ag, and Cd.

In the negative ion spectra discussed in the results section, we also observe the formation of metal carbides for only Zr and Nb. The formation of a metal carbide bond after the 3rd addition of acetylene to the molybdenum cation, and also the absence of a metal carbide in the negative ion study of molybdenum is possible confirmation of the fact that the nature of its bonding with acetylene is in-between the extreme covalent bonding nature of the ions that come before it in the 2ndrow and the electrostatic bonding nature of the ions on its right in the 2nd row of the periodic table.

One interesting observation is why Zr^+, Nb^+, and Mo^+ dehydrogenates acetylene molecules after a specific number of the molecules are added to the complex, and raises the question if for example, in the case of $ZrC_4H_2^+$ does the dehydrogenation occur in the first bound acetylene, or the incoming molecule. Based on the DFT computed thermodynamic binding energies, we can conclude that the formation of the carbide complex occurs through the dehydrogenation of the bound acetylene in the M^+-(Ac) complex for Zr^+ (Ac) and Nb^+ (Ac). This phenomenon could however be facilitated by a second incoming acetylene ligand. van Koppen *et. al.* observed this phenomenon and termed it as the cluster assisted σ-bond activation. [208]They observed that Ti^+ ions, translationally and electronically thermalized through collisions with methane, reacted to form adduct products for the first and second additions of methane. They however observed that upon the third addition of methane to the adduct complex, sigma bond activation of the methane C-H bond became a competitive channel, with respect to adduct formation. The driving force behind the new reaction channel was attributed to the increased methane binding in the inserted product compared to the $Ti^+ (CH_4)_n$. This observation was interesting because methane dehydrogenation by 1st row TM ions is endothermic, and does not occur at thermal energies.

Similar observations were made by in the same group where H-H bond activation by Sc^+ was also observed only after the third addition of H_2.[226]

7.6.2 Mechanism of Hydrocarbon Fragment Ion Formation.

The observation of hydrocarbon fragment molecules formation as a result of the catalytic polymerization of smaller hydrocarbon by transition metal atoms, ions and complexes has been widely studied and reported on in literature.[71,73,163,164,172] In the case of acetylene polymerization, it has been shown that these fragment ions are covalently bonded hydrocarbons, and not clusters of hydrocarbon fragment ions held together by ion-induced forces. The fragment ions $C_6H_4^+$, and $C_6H_5^+$, are also believed to be fragments of benzene formed through the cyclotrimerization of 3 acetylene molecules, as has been previously reported, using TM ion catalysis,[172] and electron impact[22]. Intra-cluster dehydrogenation processes involving the TM ions and the bound acetylene clusters give a possible clue that the transition metal centers could be the site for the initiation of the polymerization process that leads to the formation of these hydrocarbon fragment ions. This also raises two possible routes for the formation of the hydrocarbon fragment ion;

1) when a TM ion encounters an acetylene cluster, a C-H/C-C bond of a monomer is activated by the metal ion, and this activated monomer goes on to sequentially add on other acetylene molecules from the cluster, leading to the formation of a polymer while it still remains bound to the metal ions, but is evaporated from the cluster complex, leading to its detection as a fragment ion.

2) a monomer molecule is activated, but does not remain bound to the TM ion. This activated monomer then interacts with an acetylene cluster, leading to polymerization.

Most studies of covalent bond activation in hydrocarbons using transition metal ions identify oxidative insertion of the transition metal into the covalent bond to be activated as the initial crucial step.[194,227] The process of bond activation by transition metals is explained in terms of a simplified donor-acceptor model.[205] The metal ion in this model has to have an electronic configuration in which the acceptor orbitals are unoccupied, which will be used to receive the donated electrons from the covalent bond to be broken, and must also have electrons in its π-like symmetry d orbitals which can be back-donated into the anti-bonding orbital of the bond to be broken. When the acceptor orbitals are occupied by electrons in the TM ion, 5s orbital in the case of the 2nd row transition metal ions, there is repulsion between the metal ion and the approaching acetylene ligand, thus decreasing the efficiency of the reaction by introducing a higher energy barrier. A few research groups have used ion-mobility chromatography to separate the different electronic states of transition metal ions generated by laser vaporization ionization,[80] and electron impact of transition metal complexes,[185] by making use of the principle that the electronic states with fully filled or half-filled valence s-orbitals will have more repulsive interactions with the $1s^2$electrons of helium (buffer gas in the mobility cell) and thus have a higher mobility than those with empty valence s-orbitals. This relatively higher ion mobility of the ions which have filled valence s-orbitals is because the s orbital has larger spatial extent [185], and thus faces more repulsion when approaching the $1s^2$electrons in helium. This prevents capture collision and thus increases the mobility of these ions in the mobility cell.[80]

Other research groups have investigated the effect of the electronic configuration of transition metal ions on their reactivity. For example, Armentrout and Beauchamp [228]using the guided ion beam tandem mass spectrometry to study the reactivity of transition metal ions with dihydrogen and simple alkanes reported that the reactivity of the transition metal ions depended very much on the electronic configuration of the ion, where the favorable electronic state (unoccupied valence s-orbital) will lead to one channel of products, whilst the unfavorable electronic state(occupied valence s-orbital)will lead to different reaction channels, or the reaction does not proceed at all.

These two experiments emphasize the importance of the electronic configuration in the activation of the C-H/C-C bonds of acetylene to initiate the polymerization of acetylene. Table 11 shows the electronic configuration of the atoms used in this study and the electronic states of their singly charged cations. Zr^+ has a (^4F, $5s^14d^2$) ground state, and the first excited state (^4F, $4d^3$) 0.312eV above the ground state. We can expect that the first excited state will be the more favorable state because of its electronic configuration, and thus more reactive than the ground state. In the case of Pd^+, the ground state (^2D, $4d^9$) has the desired electronic configuration for the cation to be most reactive in C-H/C-C bond activation but the next four higher excited states have unfavorable electronic configuration ($5s^14d^8$) for optimum reactivity. We however observe hydrocarbon fragment ions being generated as a result of the interactions between the transition metal ion and the acetylene clusters. Previous work done in this group has shown that most of the low-lying electronic states that characterize transition metal ions are accessible using laser vaporization ionization. Thus it could be argued that both ground state and excited state transition metal ions are involved in the catalytic polymerization of acetylene for the different metal ions.

Of course we cannot rule out the participation of excitation energies that the ions bear, which could overcome the energy barriers, involved in the reaction of the electronic states of the TM ions having unfavorable electronic configuration. This behavior has been reported by several transition metal ion studies. For example, Buckner *et. al.* reported that LVI generated Nb^+

reacted with methane and *n*-hexane to yield $NbCH_3^+$, and $NbCH_2^+$ for methane, and also observed 6 reaction channels for the reaction with *n*-hexane. However after thermalization of the Nb^+ using argon, it was observed not to react with methane, and resulted in only 2 reaction channels in the reaction with *n*-hexane.[184] In our experimental setup, there is no prior "cooling" before the TM ion interacts with the acetylene clusters, since the acetylene is expanded with helium, which serves to help create the clusters, as well as thermalize the "hot" transition metal ions created from the LVI of the metal target. Therefore we could have all the low-lying electronic states contributing substantially to the C-H/C-C bond activation reaction due to their high electronic energies.

7.6.3 Relative catalytic activity of 1st and 2nd row TM ions towards acetylene polymerization

The previous study that assessed the 1st row transition metal ions towards C-C and C-H activation of C_2H_2 showed that all the metal ions studied except for Fe^+, Co^+, and Ni^+ did not show any C-C and C-H activity, albeit they formed metal ion- acetylene cluster complexes. V^+ was observed to undergo intracluster hydrogen abstraction reactions from with the $V^+(C_2H_2)_n$ cluster formed, indicating C-H activity, although not as strongly as the three active ions mentioned. With the exception of Fe^+, Co^+, and Ni^+, no other 1st row TM ion was able to catalyze the formation of hydrocarbon fragment ions $C_6H_4^+$, $C_6H_5^+$, $C_8H_6^+$ and $C_8H_7^+$. Although a mixtures of the excited and ground states of the TM ions are relevant in the thermodynamics of C-C and C-H activation, we still do not observe all the ions showing this activity, even though it has been clearly proven that these electronic states are accessible using the laser vaporization ionization, which was used in the production of these metal ions.

All the 2nd TM ions studied here show C-H activity leading to the formation of $C_4H_3^+$, $C_4H_4^+$, $C_6H_4^+$, $C_6H_5^+$, $C_6H_6^+$, $C_8H_6^+$, and $C_8H_7^+$. The ion Zr^+, Mo^+, Ag^+, and Cd^+ also showing C-C activity leading to $C_3H_3^+$, $C_3H_4^+$, $C_5H_3^+$, $C_7H_3^+$, $C_7H_4^+$, and $C_7H_5^+$. This suggests that the C-C/C-H activity of these ions is not only dependent on the electronic energy of the ions, but other factors could be involved. Obviously, the electronic configuration, and the size of the d orbitals of the ions could be important. As previously discussed, the TM ions interact with the acetylene ligand by accepting the electrons from the ligand's π bonding orbitals into its acceptor orbitals (4s and 3dσ in 1st row, 5s and 4dσ in 2nd row TM ions respectively) and then the metal ion back-donates electrons from its dπ orbitals into the π* orbitals of the acetylene molecule. In the case of the early 1st row TM ions, the absence of dπ electrons, coupled with the relatively smaller orbital size the orbitals makes the C-C/C-H activation by these ions inefficient. However, Fe^+, Co^+, and Ni^+ possess dπ electrons, and are thus able to activate the C-H bond in C_2H_2 through efficient overlap of their atomic orbitals. Both Cu^+ and Zn^+ are $3d^{10}$ ions, and thus are seen to be labile towards C-C/C-H activation. The early 2nd row TM ions also lack the dπ electrons for back donation, and thus prefer to form covalent bonds with the C_2H_2 ligand by breaking a pi bond in the ligand.

This infers that the ability of the 2nd row TM ions to activate the C-C/C-H bonds of acetylene indicates a more efficient overlap between the relevant orbitals of the metal ion with that of the ligand, compared to the 1st row TM ions.

7.7 Conclusions

In this study, we have presented the catalytic C-C/C-H activation of the 2nd row transition metal ions generated using laser vaporization ionization towards acetylene, leading to the polymerization of the acetylene molecules which leads to the formation of hydrocarbon fragment ions. We observe that all the metal ions studied show C-H bond activation capability, however only Zr^+, Mo^+, Ag^+, and Cd^+ are C-C active. Contrary to the early 1st row TM ions which are not able to activate C-H or C-C bonds, the early second row TM ions are observed to be active. This has been attributed to their bigger valence orbital size, which ensures efficient overlap with the orbitals of the acetylene ligand. The availability of excited electronic states for some transition metal ions, along with ground states electronic configuration and energies is shown to be relevant in the energetics of C-C and C-H activation.

Table 11: Low-lying electronic states for the second-row transition metal ions used in this study. Ground states are in bold. Energies are statistically averaged over J-levels from Reference 229.

Ion	State	Configuration	Energy (eV)
Zr(0)	^3F	$5s^24d^2$	
Zr(+1)	**^4F**	**$5s4d^2$**	**0.094**
	^4F	$4d^3$	0.406
	^2D	$5s4d^2$	0.546
	^2P	$5s4d^2$	0.742
	^2F	$5s4d^2$	0.764
	^4P	$5s4d^2$	0.974
	^2G	$4d^3$	0.993
	^2P	$4d^3$	1.218
	^2H	$4d^3$	1.511
Nb(0)	^6D	$5s4d^4$	
Nb(+1)	**^5D**	**$4d^4$**	**0.096**
	^5F	$5s3d^3$	0.421
	^3P	$4d^4$	0.833
	^3F	$5s4d^3$	0.990
	^3H	$4d^4$	1.225
	^3G	$4d^4$	1.319
	^5P	$5s4d^3$	1.368

Mo(0)	^{7}S	5s 4d^{5}	
Mo(+1)	**^{6}S 4d^{5}**		0.000
^{6}D	5s 4d^{4}		1.587
^{4}G	4d^{5}		1.906
^{4}P	4d^{5}		1.950
^{4}D	4d^{5}		2.210
^{2}D	4d^{5}		2.804
^{2}I	4d^{5}		2.867
^{4}F	4d^{5}		2.964
Pd(0)	^{1}S	4d^{10}	
Pd(+1)	**^{2}D4d^{9}**		0.176
^{4}F	5s 4d^{8}		3.369
^{2}F	5s 4d^{8}		4.116
^{2}P	5s 4d^{8}		4.589
^{2}D	5s 4d^{8}		5.027

Ion	State	Configuration	Energy (eV)
Ag(0)	^2S	$5s4d^{10}$	
Ag(+1)	**^1S**	$4d^{10}$	**0.000**
^3D	$5s4d^9$		5.034
^1D	$5s4d^9$		5.709
Cd(0)	^1S	$5s^24d^{10}$	
Cd(+1)	**^2S**	$5s4d^{10}$	**0.096**
^2P	$5p4d^{10}$		0.421
^2D	$5s^24d^9$		0.833

Moore, C. E. *Atomic Energy Levels as Derived from the Analyses of Optical Spectra*; U.S. National Bureau of Standards; U.S. Govt. Print. Off.: <Washington>, 1971.[229]

CHAPTER 8. Production of Organic Ions Relevant to Astrochemistry by Plasma Discharge Ionization of Molecular Clusters

8.1 Introduction

For the past few decades, the study of the chemistry and physics of carbon clusters has intensively engaged the scientific community[230-235], yielding several new discoveries such as the single atomic layer sp^2 carbon sheet graphene[236,237], and a family of closed and semi closed cage fullerenes[1,235,238,239]. It is worth mentioning that the discovery of fullerene was as a result of attempts to create carbon cluster ions of the nature C_nHN, observed in the interstellar medium, where n = 5,7,9 or 11.[239] In the same way, this field has also led to more questions, which makes the field still as engaging as when it begun. These studies have found importance in several fields including, but not limited to soot and combustion chemistry[1,240,241], catalysis[237,242], nano-engineering[240], and all sciences of the interstellar medium (ISM)[230,238,241,243]. The intriguing chemistry of carbon is attributed to its ability form hybridized orbitals.[1]

Interstellar chemistry started in the 1930's with the detection of the simple diatomic molecules CH, CH^+, and CN,[1,2] but since the discovery of complex organic molecules in the late 1960's [3], a lot of research has been conducted to gain insight into the origin and occurrence of these molecules in outer space. Although the chemistry of formation of these molecules in the ISM is still not well understood,[4] several mechanisms have been proposed by research groups for interstellar molecule formation[5-7]. These mechanisms include among others radiative association, dissociative recombination, and exothermic ion-molecule reactions.[244] Such postulations have only been confirmed by the identification and isolation of the precursors, intermediates and products in these proposed mechanisms. Indeed the most difficult task is to recognize these molecules in the ISM. However, this can only be achieved by isolation of the species in high enough density in laboratory experiments followed by concrete spectroscopic characterization.[245] This is then correlated to the diffuse interstellar bands[246] (DIB) which is the absorption spectrum of the interstellar medium. For example, the interstellar spectral lines of HCO^+ were detected in 1970 by Buhl *et al*.[247] but remained ambiguous till the laboratory characterization of this molecule 6 years later by Kramer and Diercksen using microwave spectroscopy. [248]

In 1977, Douglas[249] proposed that carbon chains are possible carriers of some of these DIBs. He based this argument on the unique photo-physical and spectroscopic characteristics of these compounds. This has attracted further attention to the study of carbon clusters in the attempt to understand the marveling chemistry that goes on in the ISM. The heterogeneous nature of the interstellar and circumstellar media leads to a large variety of chemistry.[2] Gas-phase experiments designed to investigate ISM chemistry are generally effective, in that it is possible to achieve the steady-state time scale conditions of the ISM.[1] Conducting current research using steady-state conditions is important since the estimated average time of particle collision in the diffuse interstellar clouds is measured in decades, whereas this time could be reduced to a few hours in the dense interstellar clouds. It will be difficult to study such time frames in the current laboratory setting.[1]

Carbon clusters have been produced in the laboratory environment using various ionization techniques[233] to study their chemical and physical properties, whereas other groups have focused on efforts to create the possible candidate molecules linked to DIBs. A few of such techniques are direct ablation of a carbonaceous material, [238]fragmentation of a large carbon molecule through collision or an incident photon,[250] gas-phase chemical reactions,[250] dissociative ionization of bigger carbon cluster molecules such as C_{60},[233, 250] etc. Several research groups[7,232,235,238,243,250,251],[252,253] have reported on the gas-phase chromatography[254] of positive and negative carbon clusters produced using by laser ablation of graphite rods, by far the most popular ionization technique for making these molecules. Even though the mechanism of the formation of the carbon cluster ions is still not well understood, [242, 250] plasma processes are believed to be involved in most of the ionization processes. Many plasma ionization techniques have been employed in the production of carbon cluster ions. For example, Maier *et al*.[255] and A. N. Pargellis[256] have both used cesium sputtering ionization source to produce carbon cluster ions. In our lab, we currently have 2 home-made electrical plasma discharge ionization sources, a two brass plate assembly or a two needle assembly separated by teflon in both cases. We have used these ionization sources in the plasma discharge of several small organic molecules seeded in a carrier gas and the mass scans reveal the formation of several interstellar and circumstellar relevant molecules, both positive and negative ions. To the best of our knowledge, not much work has been reported in literature using this ionization technique. There is only a handful of publication known to us, where similar ionization sources have been used in the generation of carbon clusters which may or may not contain other elements.[257,258]. Plasma in space is a very widely known phenomenon, where it is believed that most of the visible part of the universe is in the form of plasma.[259] This coupled with the known occurrence of acetylene and several other organic molecules in parts of the ISM[244] makes our ionization approach a very interesting route to pursue in the study of the formation of hetero-carbonaceous cluster and molecular ions related to ISM chemistry.

8.2 Experimental Section

Positive and negative carbon cluster ions were generated by plasma discharge ionization (plate plasma discharge and needle plasma discharge shown in Figures 3 and 4 respectively) of the sample vapor (acetylene, methanol, acrylonitrile, HCN/DCN, or binary clusters) in helium. The best mixing ratio of sample in Helium carrier gas was found to be between 1- 3% of sample in Helium mixture. To generate the sample mixture for methanol and acrylonitrile, the pick-up method was used, where helium carrier gas is passed over the liquid compound kept at a specific temperature, and the vapor above the liquid then mixes with the carrier gas before expansion. To obtain the right vapor pressure of the liquid samples, we utilized Antoine's equation[260-262] and parameters for each liquid compound to determine the temperature at which sufficiently enough vapor pressure is available in the bubbler. This study was performed on the VCU R-TOF mass spectrometer (details of this setup are given in the experimental section).

The sample mixture is expanded into the chamber by supersonic adiabatic expansion using pulsed nozzle (general valve, *series 9*) in the first chamber. The flow of a combustible gas through the two electrodes of the plasma discharge ionizer creates a plasma discharge. This is due to the potential difference on the electrodes of the plasma discharge assembly as a result of the applied voltages. The ions created in this plasma are then transported to the second chamber, through a 3mm skimmer, which collimates the ion beam. The ions are extracted at the ion source by a pulsed repeller plate, controlled by a pulse generator, and accelerated into the ion mirror assembly, travelling through a field free flight tube. The ions are then "pushed out" towards the detector through a second field free flight tube. The ions strike the MCP detector and the current generated is collected by an oscilloscope (LeCroy 9350A) and converted into a spectrum as a function of the time of flight (from ion source till the detector) if the ions. The spectrum is then transferred to a computer for further analysis. One important factor considered in this experiment is the delay timing of the system, in that the pulse generator has to be set at such a time (in reference to the pulsed nozzle) that it coincides with the largest packet of ions being directly above repeller plate.

8.3 Results and Discussion

The positive and negative ion spectra collected from the plasma discharge ionization of the molecular clusters of acetylene, hydrogen cyanide, methanol, and binary molecular clusters of acetylene/acrylonitrile, and acetylene /methanol are presented here.

8.3.1 Positive Carbon Cluster Ions from the plasma discharge ionization of acetylene

Figure 74 shows a positive ion R-TOF mass spectrum of carbon cluster ions from the plate plasma discharge ionization of acetylene in helium. In the spectra we observe a series of pure carbon cluster ions C_n^+, and hydrogenated carbon clusters $C_nH_m^+$, $(1= n \geq 15, 0 \leq m \geq 6)$.

In our experiment, we observed that the positive hydrogenated species $C_nH_m^+$ exhibited higher intensities than C_n^+ when ≤ 4 n≤ 13 (where n is the number of carbons and m the number of hydrogen atoms). Above n=13, C_n^+ becomes the dominant species in the range of $0 \leq m \geq 5$, where m is the number of hydrogen in the series. For the C_2 series, $C_2H_2^+$ has the highest intensity, similar to what is observed for ≤ 4 n≤ 13. The $C_nH_2^+$ series showed the highest intensity for $2 \leq n \geq 15$, except for n=3. The magic number peaks in our spectra are assigned $C_5H_2^+$ and $C_7H_2^+$ for the $C_nH_2^+$ series and C_3H^+ for the C_nH^+ series.

We also observed an even/odd intensity alternation for the $C_nH_2^+$ ions, where abundance is higher when n is odd than when n is even.

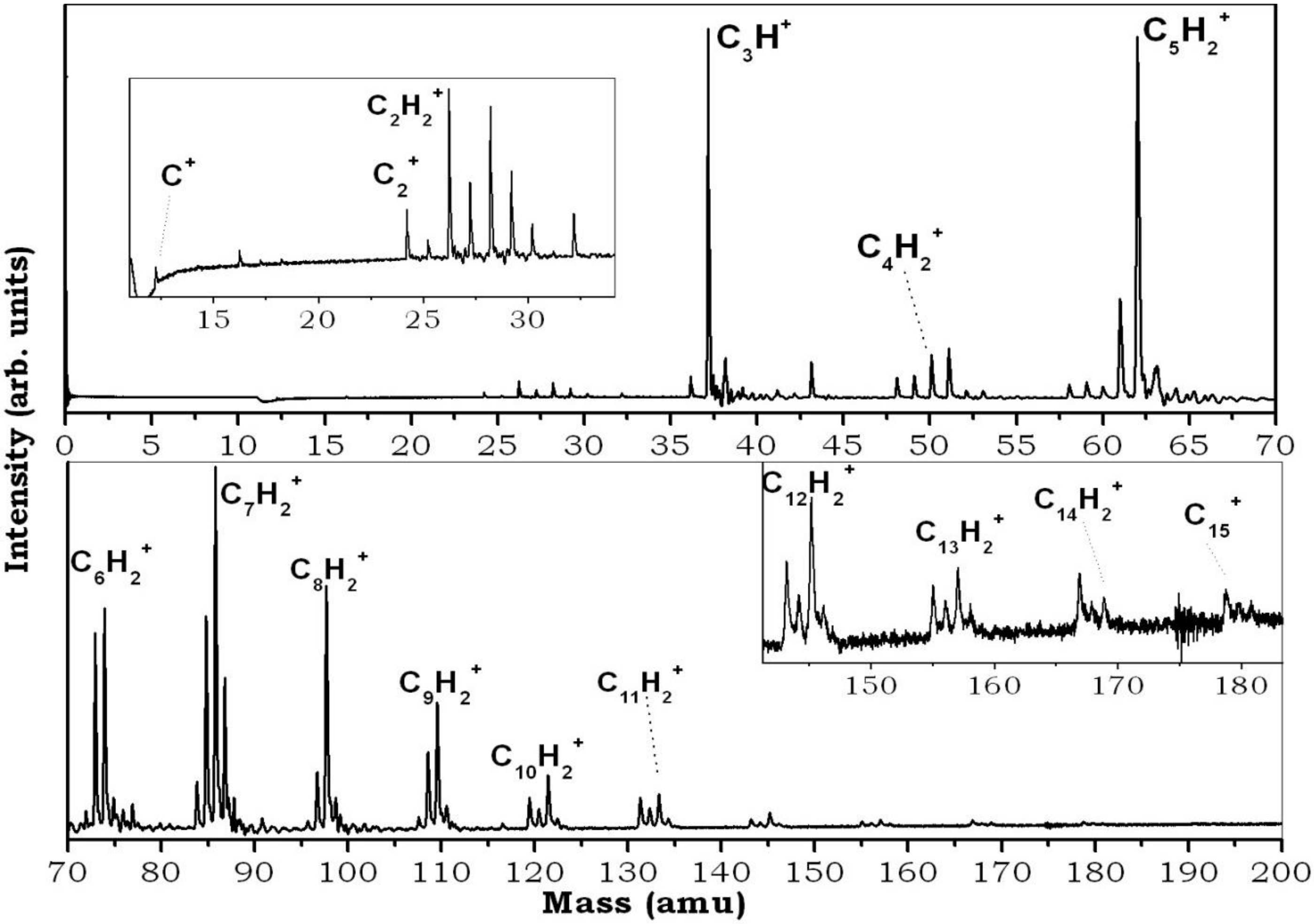

Figure 74: A positive R-TOF spectrum of carbon cluster ions. Ions were generated from plate plasma discharge ionization of acetylene gas seeded in helium.

A large variety of in *vacuo* laser ablation experiments produced hydrogenated carbon cluster by ablating carbonaceous materials and obtained similar spectra, with differences in magic numbers and trends in the even/odd alternation.[239,263] For example, E. A. Rohlfing[263] observed extensive hydrogenation of carbon clusters produced by laser ablation when he used a hydrogen/ helium (0.5 – 4.0 % H_2 in He) mixture as the expansion gas. For $C_nH_m^+$ ions, he observed values of m, which ranged from $0 = m \geq 9$ when 4% H_2/He was used, compared to $m \leq 2$ in pure He. In his study using 4% H_2/He, he also observed C_nH_2 and C_nH_4 to be the magic clusters in the hydrogenation series $C_nH_m^+$ of a given n when n was even, and $C_nH_3^+$ when n was odd.

Heath *et al* [7] also observed an even/odd alternation trend in a similar experiment as done by Rohlfing, but mainly focusing on the low mass range, and observed that only even n clusters of $C_nH_2^+$ were abundant, with odd n being almost absent. It must be mentioned albeit, that under their experimental conditions (using H_2/He for expansion), Heath and co-workers found $C_nH_2^+$ to be the most prominent peak for the even n hydrogenated carbon peaks. Although we observed the same peaks as our most prominent ion, contrary to this observation, the mass spectra in our experiments shows the odd n peaks in the $C_nH_2^+$ cluster series as being the most prevalent species.

Both groups concluded that the formation of $C_nH_2^+$ species by even n clusters could be due to the formation of linear poly-acetylenic ions with the structure $H\text{-}(C{\equiv}C)_{n/2}\text{-}H$. Not much is known about the structure of $C_nH_2^+$ when n is odd, but have been shown to exist in several isomeric forms. C_n^+ ions are hypothesized to have a cumulene structure, :C=C=C=C=C: . Peaks corresponding to C_nH^+ are also observed with intensities higher than the pure Cn^+ ions. Figure 75 shows an R-TOF mass spectrum of positive carbon cluster ions from the needle plasma discharge ionizer. The spectra shows a pure carbon cluster ions series C_n^+, and also the hydrogenated

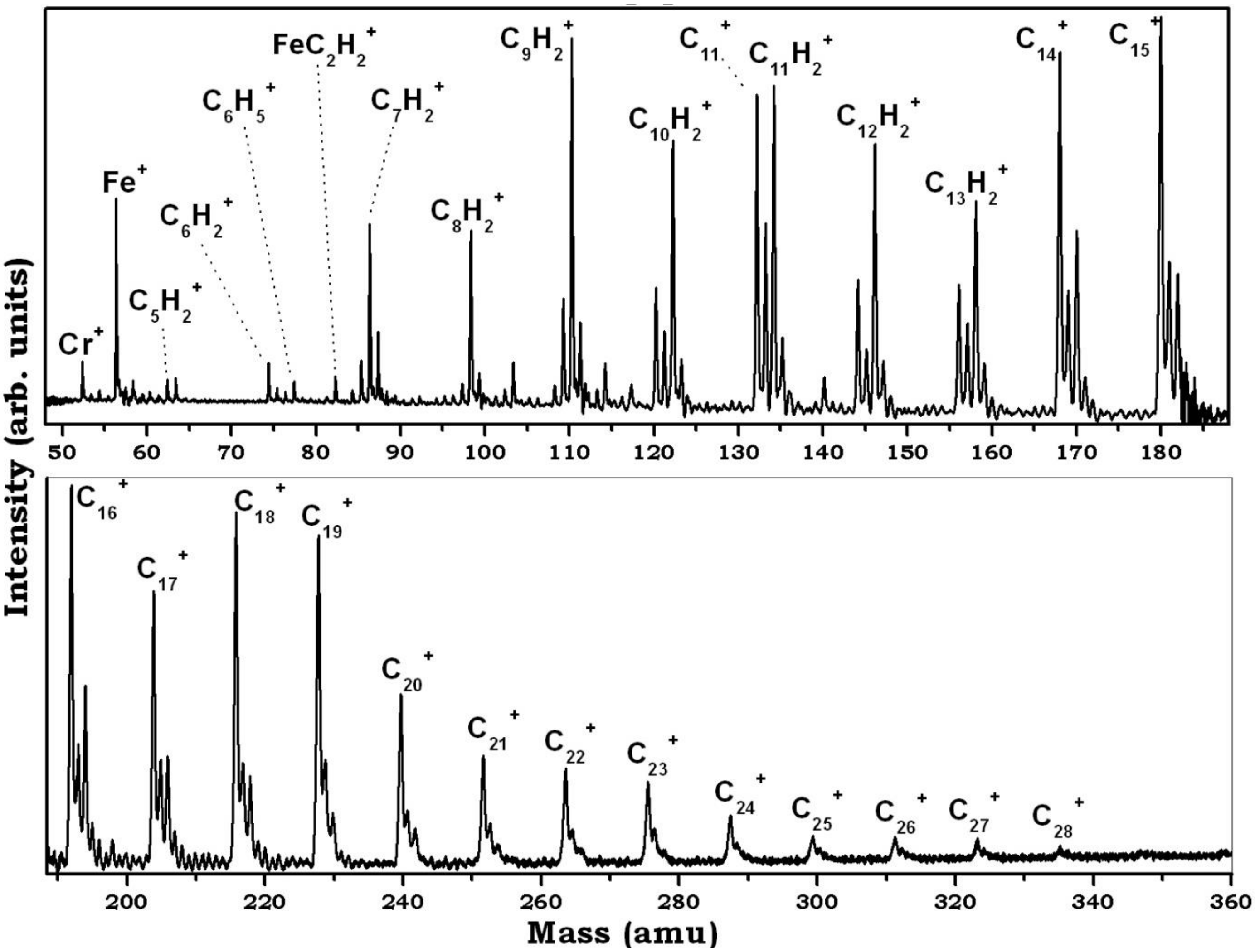

Figure 75: A positive R-TOF spectrum of carbon cluster ions. Ions were generated from needle plasma discharge ionization of acetylene gas seeded in helium.

carbon clusters $C_nH_m^+$, ($5= n \geq 28$, $0 \leq m \geq 5$). As mentioned previously, we observe the $C_nH_2^+$ ion signal to have the highest abundance from $5\leq n \leq 13$. After n = 13, the m = 0 peaks (i.e. pure C_n^+ clusters) have the highest abundance in the hydrogenation series for each n. The two main features of this spectra different from the spectra in Figure 74 is the presence of the transition metal cations Fe^+ and Cr^+ and the higher mass clusters observed using this ionization method. The appearance of the metal ions is as a result of the thermal decomposition of the stainless steel needles used in the plasma discharge process, due to the high temperature associated with the plasma process. The higher clusters observed could indicate a higher efficiency of the NPDI compared to the PPDI, probably due to its high voltage to electrode surface area ratio. It could also be attributed to the Fe+ and Cr+ ions formed in the plasma process, which could catalyze a metal-ion induced polymerization process.[207] The presence of $Fe^+C_2H_2$ and enhanced intensity of $C_6H_5^+$ could suggest that the second assumption made above cannot be disregarded. A lot of studies have been conducted on the polymerization of acetylene by transition metals ions in the gas phase.[207, 67, 264] It has been found that Fe^+ is able to catalyze the polymerization of acetylene molecule clusters into different hydrocarbon fragment ions, of which the most studied is the polymerization of 3 acetylene molecules into hydrocarbons synonymous to benzene. The $Fe^+C_2H_2$ ion is the first member of the $M^+ (C_2H_2)_n$ series in the interaction of transition metal ions with acetylene clusters, in this case iron.

The spectrum in Figure 75 shows an even/odd alternation in intensity for the $C_nH_2^+$ peaks, with the odd n having the higher intensity. Here we observe $C_7H_2^+$, $C_9H_2^+$, and $C_{11}H_2^+$ as the magic clusters in going from n=5 to n=13. The second noticeable difference between the two spectra from PPDI and NPDI is the relative abundance of the C_n^+ ions. NPDI produces a higher abundance of these ions relative to PPDI. We observe a gradual increase in abundance from C_5^+

till C_{10}^+. From n= 10 till n ≥ 28, C_n^+ has comparable intensities to $C_nH_2^+$ and becomes the most abundant in the m series for each n.

8.3.2 Positive Cluster Ions from the plasma discharge ionization of Methanol

Figure 76 shows an R-TOF mass spectrum obtained from the plasma discharge ionization of pure methanol clusters using the plate plasma discharge ionizer with an applied potential difference of 500V. The observed ion peaks correspond to a protonated methanol series $H^+(MeOH)_n$. in our study we observe this series up to n=13. The magic cluster in the $H^+(MeOH)_n$ series is the protonated trimer ion, $H^+(MeOH)_3$. We also observe two distinct inter cluster reactions occurring in this system as shown in the spectrum. The formation of a protonated dimethyl ether (m/z 47), occurring from and intra cluster reaction which results in a water molecule being expunged, according to the equation;

$$CH_3OH_2^+ + CH3OH \longrightarrow H^+ (CH_3)_2O + H_2O \qquad (8.1)$$

The dimethyl ether ion then adds neutral methanol molecules to form a new series, though obviously not as stable as the pure protonated clusters, as seen in the mass spectrum in figure 8. Several groups have previously reported on the protonated methanol cluster ion series.[265-270] They all reported the observation of the relative stability of the protonated methanol trimer, with respect to the rest of the series. The unusual stability has been attributed to the hydrogen bonded structure of the trimer, with the protonated methanol as the center.[265]

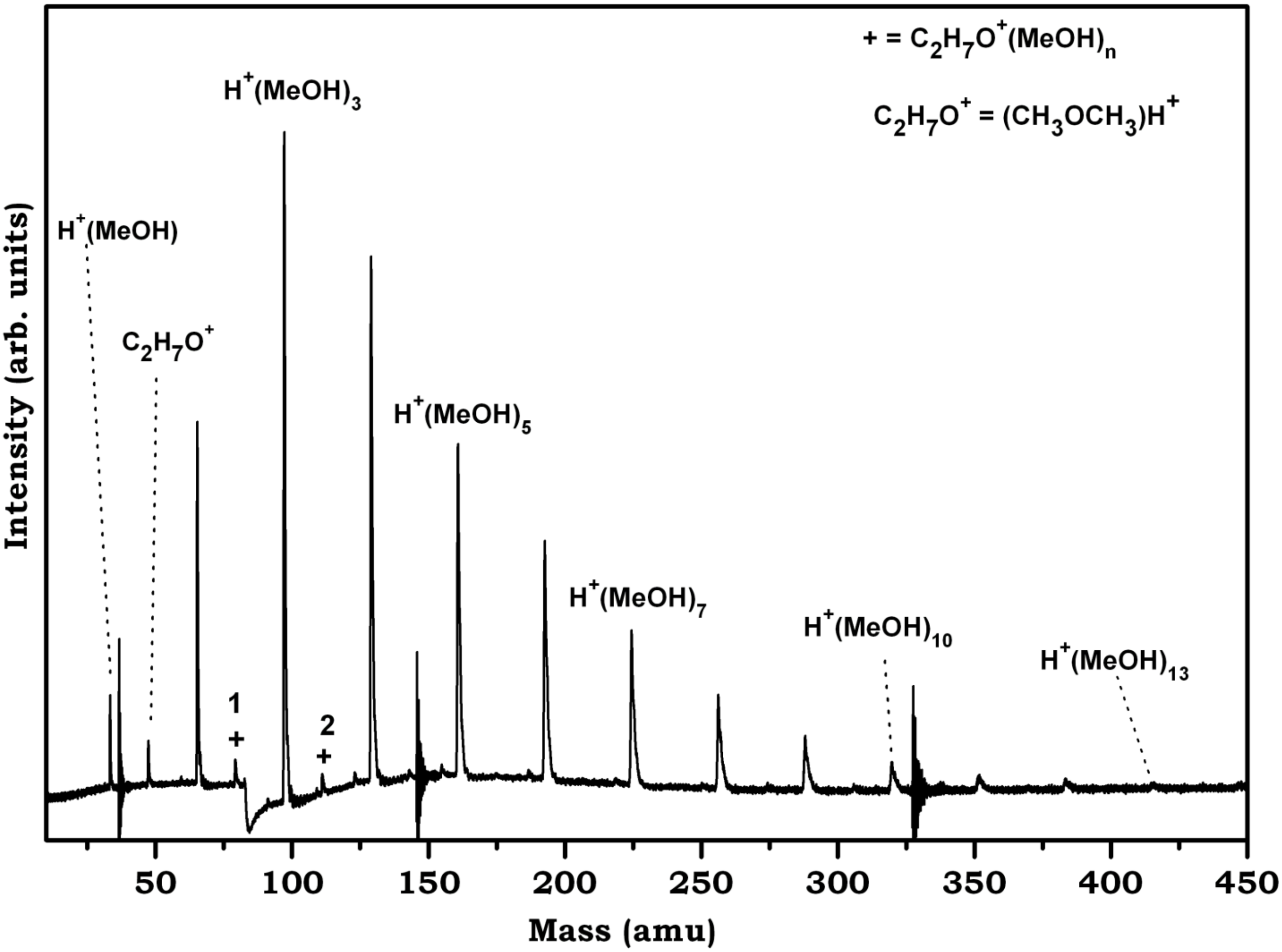

Figure 76: R-TOF mass spectrum obtained from the plasma discharge ionization of pure methanol clusters using the plate plasma discharge ionizer with an applied potential difference of 500V.

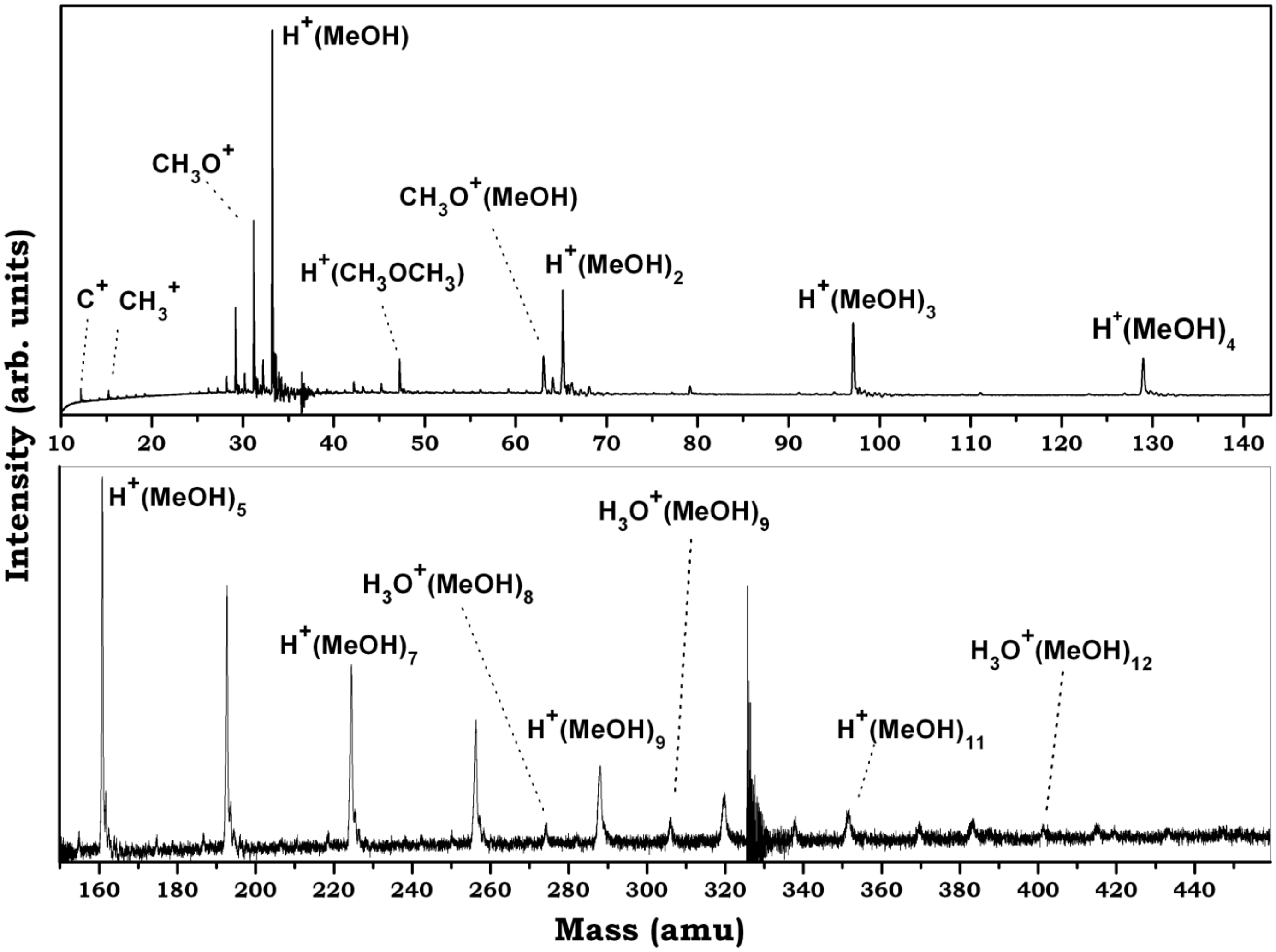

Figure 77: R-TOF mass spectrum obtained from the plate plasma discharge ionization of pure methanol clusters with applied potential difference of 700V.

Figure 77 displays an R-TOF mass spectrum obtained from the plate plasma discharge ionization of pure methanol clusters similar to the spectrum obtained in Figure 76, but with applied potential difference of 700V. Again the protonated methanol cluster ion series is the most prominent series observed in this spectrum. The applied potential is however more than required to create the methanol clusters, and this leads to fragmentation products of the methanol monomer being observed. The intracluster dehydration reaction of the protonated clusters are also observed in

this spectrum. Interestingly, a size controlled intracluster reaction which leads to the removal of a neutral ether molecule is also observed after the formation of $H^+(MeOH)_n$, with $n \geq 8$, leading to a hydronium ion/methanol cluster complex possibly with an H_3O^+ center. This intracluster reaction is given by the equation;

$$H^+(CH_3OH)_n \longrightarrow H_3O^+ (CH_3OH)_n + (CH_3)_2O \qquad (8.2)$$

This observation of the intracluster ether removal has also been reported in literature.[265,267-269]

8.3.3 Positive Cluster Ions from the plasma discharge ionization of Hydrogen Cyanide

The R-TOF mass spectrum obtained of plate plasma discharge ionized DCN is clusters is shown in the spectrum shown if Figure 78. We observe the formation of the dehydrogenated hydrogen fragment CN^+, the radical cation of DCN, and the deuterated DCN. The other fragments observed in the spectrum are C^+, N^+, and O^+. All the above mentioned fragments form cluster complexes with the neutral DCN clusters formed through supersonic expansion. Most prominent of all these series is the radical DCN cation series $(DCN)_n^+$ till $n < 6$. From $n \geq 7$, the dehydrogenated form series $CN^+(DCN)_n$ becomes the more stable from of the ion in the series.

The chemistry of CN^+ has been previously, and has been reported to be essential to interstellar chemistry.[271-274] One very interesting feature of this spectrum is the formation and relative stability of the ion DC_4N^+. The neutral molecule of this ion we observe in our spectrum has been observed in the IRC +10216 by Cernicharo *et. al*.[275] Several of the other ions, along with their neutral and anionic forms have been proposed in interstellar chemical models to be present in the interstellar media.[276]

8.3.4 Positive Cluster Ions from the plasma discharge ionization of Acrylonitrile

Figure 79 displays the R-TOF mass spectrum of the plate plasma discharge ionization of acrylonitrile, obtained by passing He carrier gas over a bubbler of liquid acrylonitrile(ACN) kept at -20° to achieve the right mixing ratio for efficient dilution of the sample vapor, and an applied potential difference of 800V. The spectrum show some interesting fragment ions being produced through plasma discharge ionization. Fragments of the parent ion corresponding to C_3H_3-CN bond cleavage yielding the cyano cation and the vinyl radical. We also observe the C-N of $C_2H_3C{\equiv}N$ cleaved to yield the propynyl cation and the N radical. We observe fragment ions corresponding to further dehydrogenation of the propynyl cation $C_3H_3^+$, although they are comparatively less stable. Ions corresponding to the dehydrogenated parent molecule, the radical cation, and the protonated molecular ion are also observed. Another hydrogenation series of ions are observed, with the composition of $C_4H_nN^+$, with n=0 – 4. The most stable of this series is $C_4H_2N^+$. All the above mentioned ions in the spectrum go on to add neutral ACN molecules to form cluster complex ions. For additions of up to 3 ACN molecules, the protonated series has the highest intensity for all the ions. From the fourth addition and upwards, the radical cluster ion of

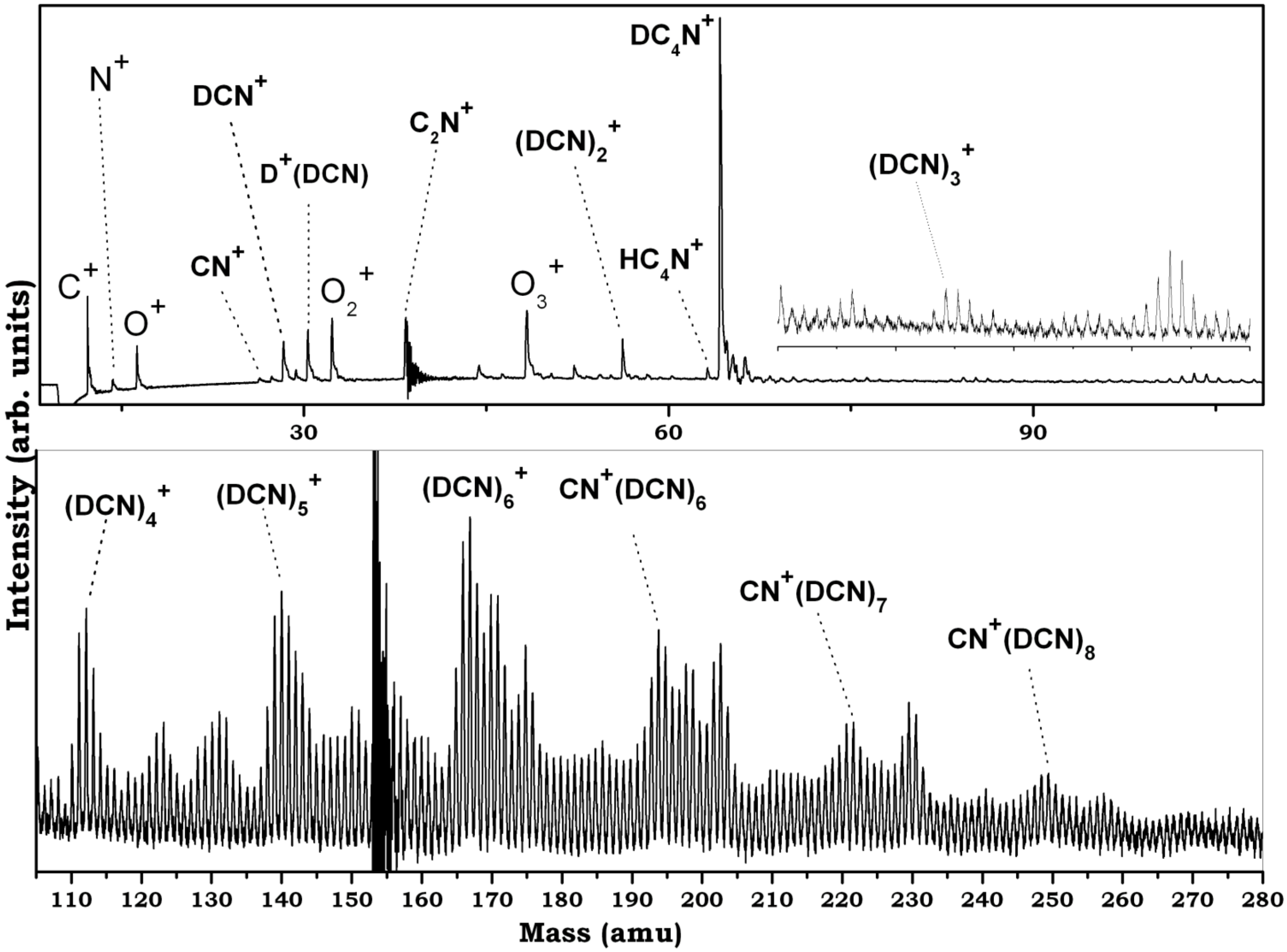

Figure 78: R-TOF mass spectrum obtained from plate plasma discharge ionized DCN is clusters

ACN has the highest intensity among all ion-cluster complex series, as shown in the spectrum in Figure 79.

8.3.5 Positive Cluster Ions from the plasma discharge ionization of Acetylene/Methanol Binary clusters

The positive spectra obtained from the plate plasma discharge ionization of acetylene/methanol binary clusters are shown in Figures 80 and 81. Figure 80was obtained by ionizing binary clusters of both compounds, which was obtained by passing 2% acetylene in helium mixture over methanol liquid in a bubbler at room temperature. The spectra looks very much like what is obtained from the plasma discharge of 2% pure acetylene in helium. A close inspection of both Figures 74, 77 and 80 reveal that there is overlap of peaks corresponding to either pure acetylene or the lower m/z section of pure methanol spectrum. There is however not much corresponding to a possible inter-cluster complexation. All the observed ions have been previously identified in their mono molecular discharge ionization spectra respectively. Figure 81 shows the plasma discharge ionization of the binary clusters of acetylene and methanol obtained by passing 1% acetylene in helium mixture over methanol at room temperature. This spectrum is similar to what is observed in Figure 77, but have a few differences. The most prominent series observed is the protonated methanol series, where $n \geq 15$ is observed for the $H^+(CH_3OH)_n$. Ions corresponding to $CH_3O^+(CH_3OH)_n$, and $CH_3OH^+(CH_3OH)_n$ are also observed. The hydronium core with methanol solvent shell $H_3O^+(CH_3OH)_n$, formed by the intra cluster removal of a dimethyl ether is seen with $n \geq 6$. Ion peaks corresponding to acetylene/ methanol binary cluster complexes are also observed. We observe a cluster complex ion series assigned to $[CH_3O^+ (CH_3OH)_n(C_2H_2)]$, $[H^+ (CH_3OH)_n(C_2H_2)]$, and $[H^+ (CH_3OH)_n(C_2H_2)_2]$. The observation that these ion-methanol-acetylene cluster complex ions appear after specific number of methanol molecules add to the

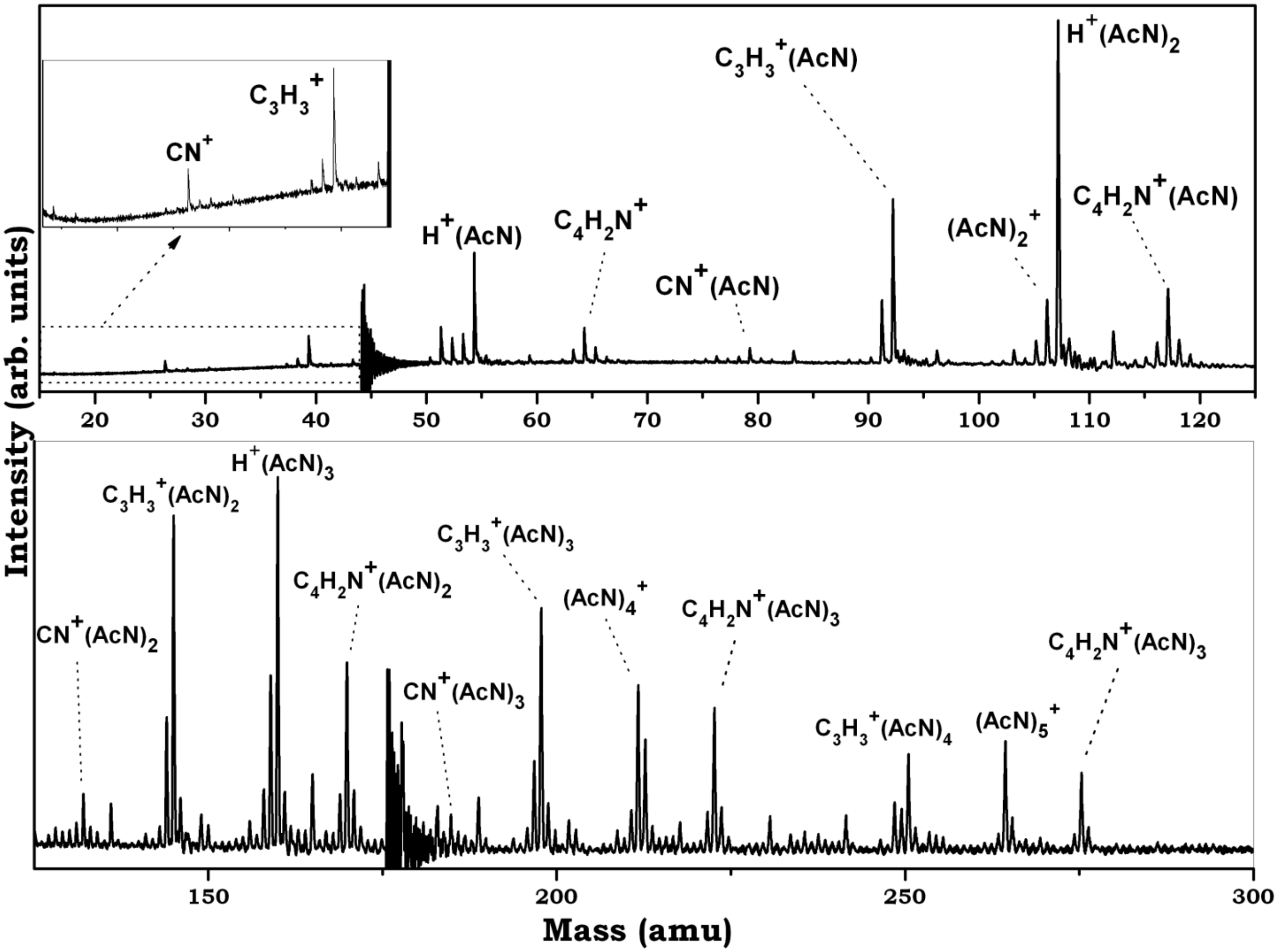

Figure 79: R-TOF mass spectrum of the plate plasma discharge ionization of acrylonitrile at an applied potential difference of 800V. The bubbler of liquid acrylonitrile (ACN) was kept at -20°.

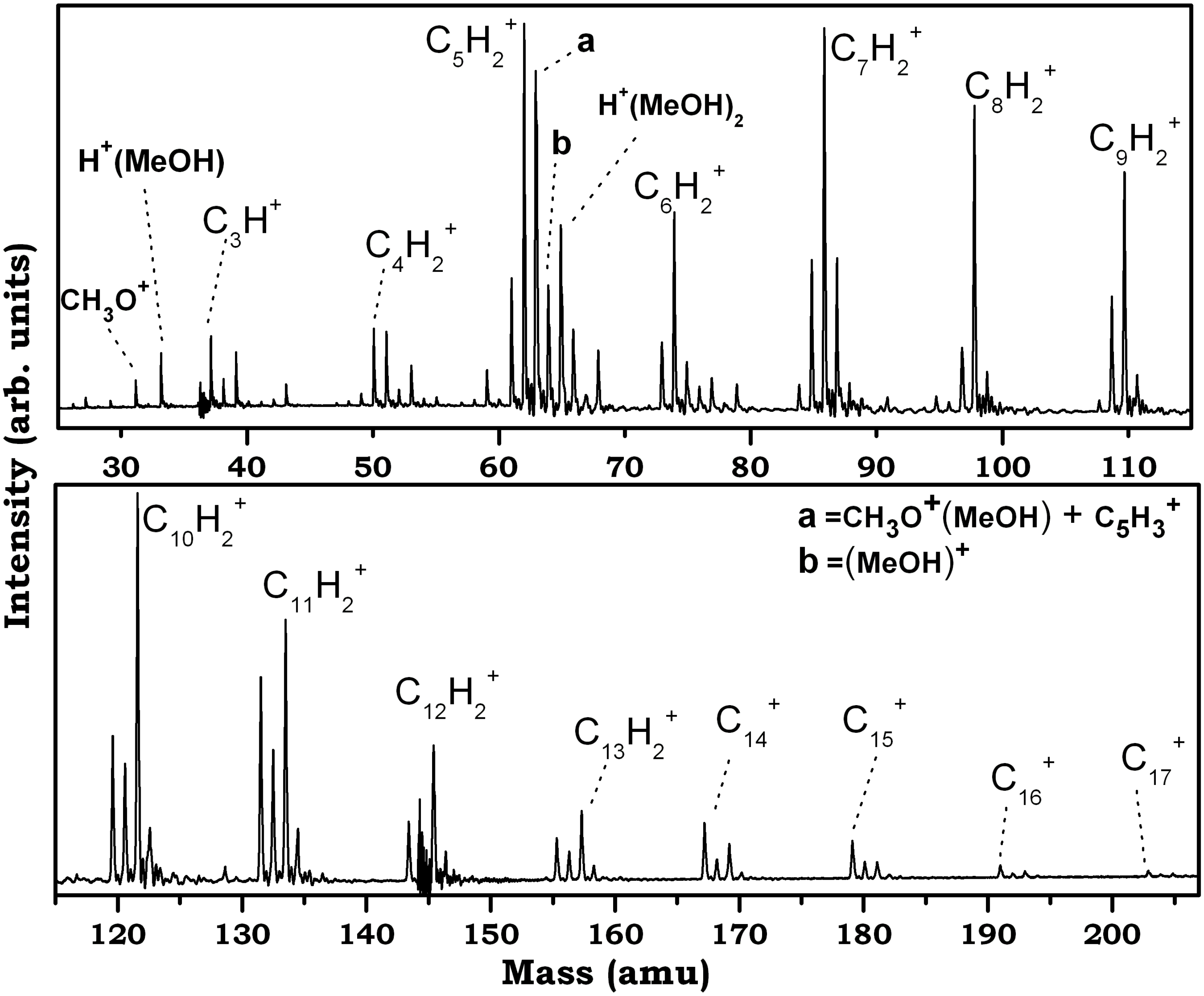

Figure 80: R-TOF mass spectrum of plate plasma discharge ionization of acetylene/methanol binary clusters obtained by passing 2% acetylene in helium mixture over methanol liquid in a bubbler at room temperature.

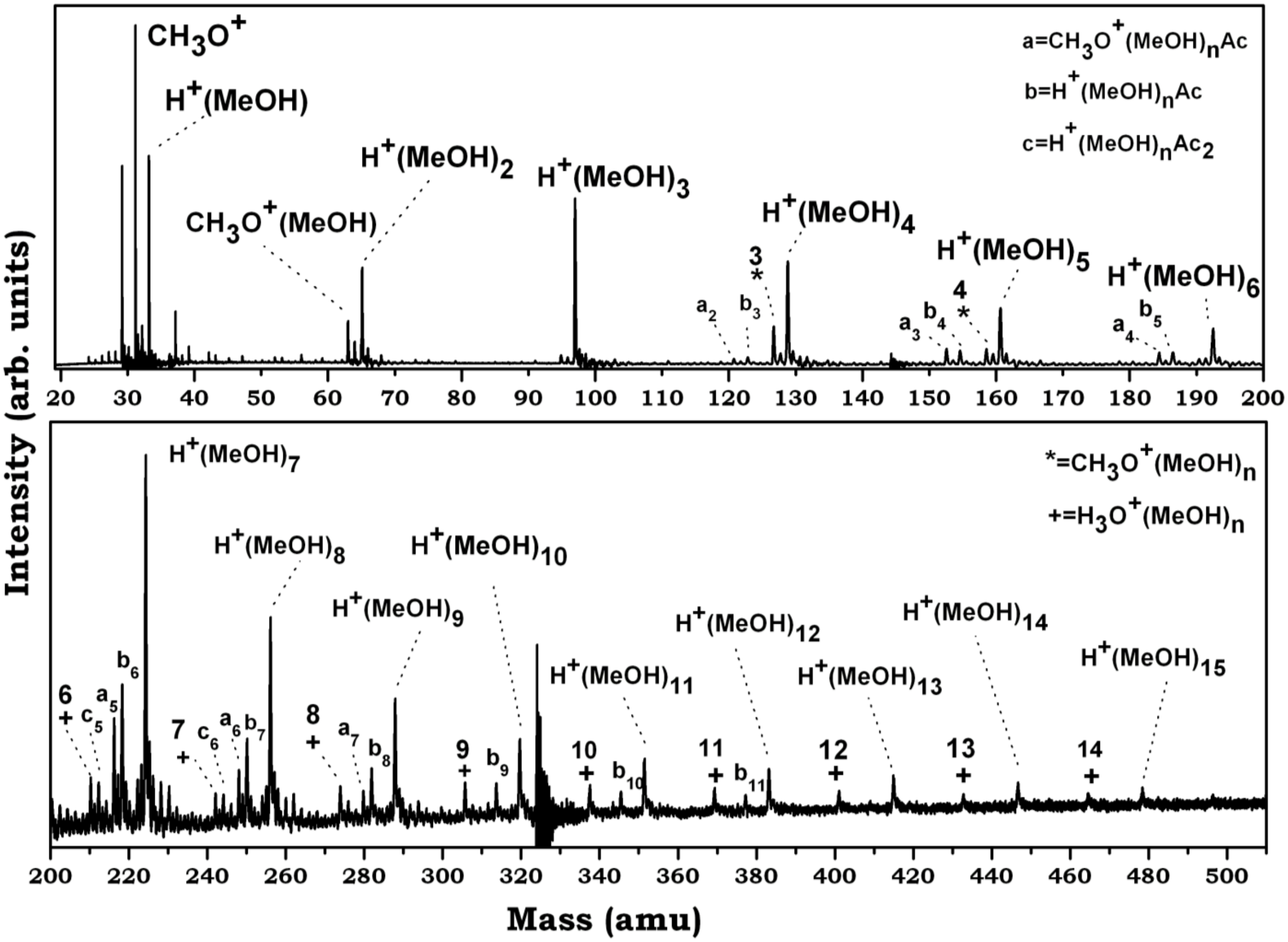

Figure 81: : R-TOF mass spectrum of plate plasma discharge ionization of acetylene/methanol binary clusters obtained by passing 2% acetylene in helium mixture over methanol liquid in a bubbler at room temperature.

complex could suggest that there is a size dependent stabilization effect required to efficiently host the acetylene molecule. For example, the $[CH_3O^+ (CH_3OH)_n(C_2H_2)]$ complex ion appears only for n ≥ 2, $[H^+ (CH_3OH)_n(C_2H_2)]$ shows only after n ≥ 3, and $[H^+ (CH_3OH)_n(C_2H_2)_2]$ after n ≥ 5. Among these three binary cluster complex ions, $[H^+ (CH_3OH)_n(C_2H_2)]$ seems to be comparatively the most stable ion, as seen in the spectrum in Figure 81.

8.3.6 Negative Cluster Ions from the plasma discharge ionization of Acetylene

Figure 82 shows a negative ion cluster spectrum of acetylene/Helium mixture using Plate Plasma Discharge Ionization. It shows pure carbon cluster ions, C_n^-, and hydrogenated carbon cluster ions, $C_nH_m^-$, where n is the number of carbon atoms, and m is the number of hydrogen atoms.

We observe for C_n^- ion, values of n as $3 \leq n \geq 24$. Values of m also ranges from 0 to 8, where hydrogenation is lower for the smaller mass ranger, and the value of m increases as n increases. For example, m values for n = 3 is 0, 1. From n = 4 to n = 8, m values are 0, 1, 2, and 3. m increases further after n = 8.

This could be attributed to the fact that the carbon cluster structure is able to coordinate to more hydrogen atoms as it gets larger. Cn^- ions for which m = 0 have the highest abundance for values of n from 3 to 9. From $10 \leq n \leq 16$, m = 1, i.e. C_nH^- ion signal have the highest abundance. After n =16, we observe an even/odd alternation for the highest intensity peak between m = 3 and m = 1, where m = 3 is highest in the m series for n if n is odd, and m = 1 is highest in intensity if n is even. C_3^- has a low intensity compared to the average abundance of the higher mass ions. The reason could be due to the time delay for this spectrum being optimum for the higher masses in the series.

Figure 83 shows a second negative ion cluster spectrum of acetylene/Helium mixture using Needle Plasma Discharge Ionization. It shows the hydrogenation series of carbon anions with $n \geq 27$. We also do not observe C_3^- in the spectrum. A negative ion cluster spectrum of acetylene/Helium mixture using Needle Plasma Discharge Ionization is shown in Figure 84.

There are a few differences between Figure 8 and Figure 10. Close inspection of both spectra reveals that the extent in hydrogenation is different in the two ionization techniques. In the NPDI process, the spectrum shows the highest value of m to be 3, compared to 8, in the case of PPDI. The reason could be that the ions created using NDPI could have a slightly higher energy, and thus relax to the ground state, or a more favorable energy state by evaporating the hydrogen atoms attached to the ion.

This conclusion can be drawn since all the ions in this spectra exhibit the same trend. Most work done on negative ion clusters previously used carbon cluster anions created through laser ablation of graphite[277] or other carbonaceous compounds such as coal[278], organic compounds[235,279,280]. All the above research groups observed similar trends of carbon cluster anion formation, with different hydrogenation trends as reported here.

Structure of negative carbon cluster ions of the form C_nH^- with n values between 5 and 13, have also been studied, and are reported to be linear, with no isomeric forms within this range of carbon atoms.[281] Another group also reported these ions to have long linear chains for carbon clusters with carbon atoms of $2 \leq n \leq 29$ in a UPS of carbon anions.[282] von Helden *et.al.*[283] using the same cluster ion source with ion mobility measurement and backed by theoretical calculations, concluded that linear clusters exist up to carbon cluster cations with n= 10, and monocyclic rings exist for cations with n values of 7 and above.

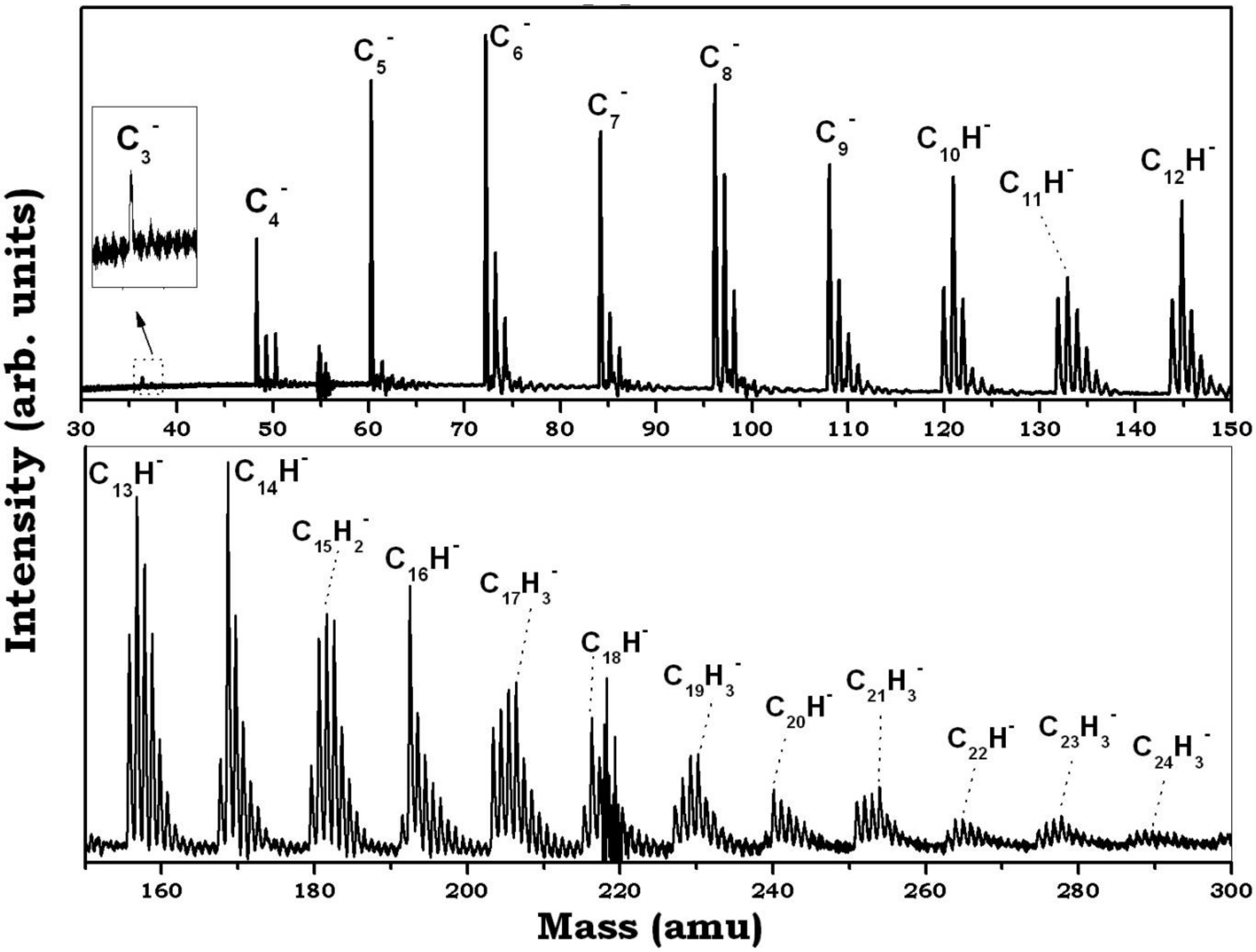

Figure 82: A negative R-TOF spectrum of carbon cluster ions. Ions were generated from plate plasma discharge ionization of acetylene gas seeded in helium.

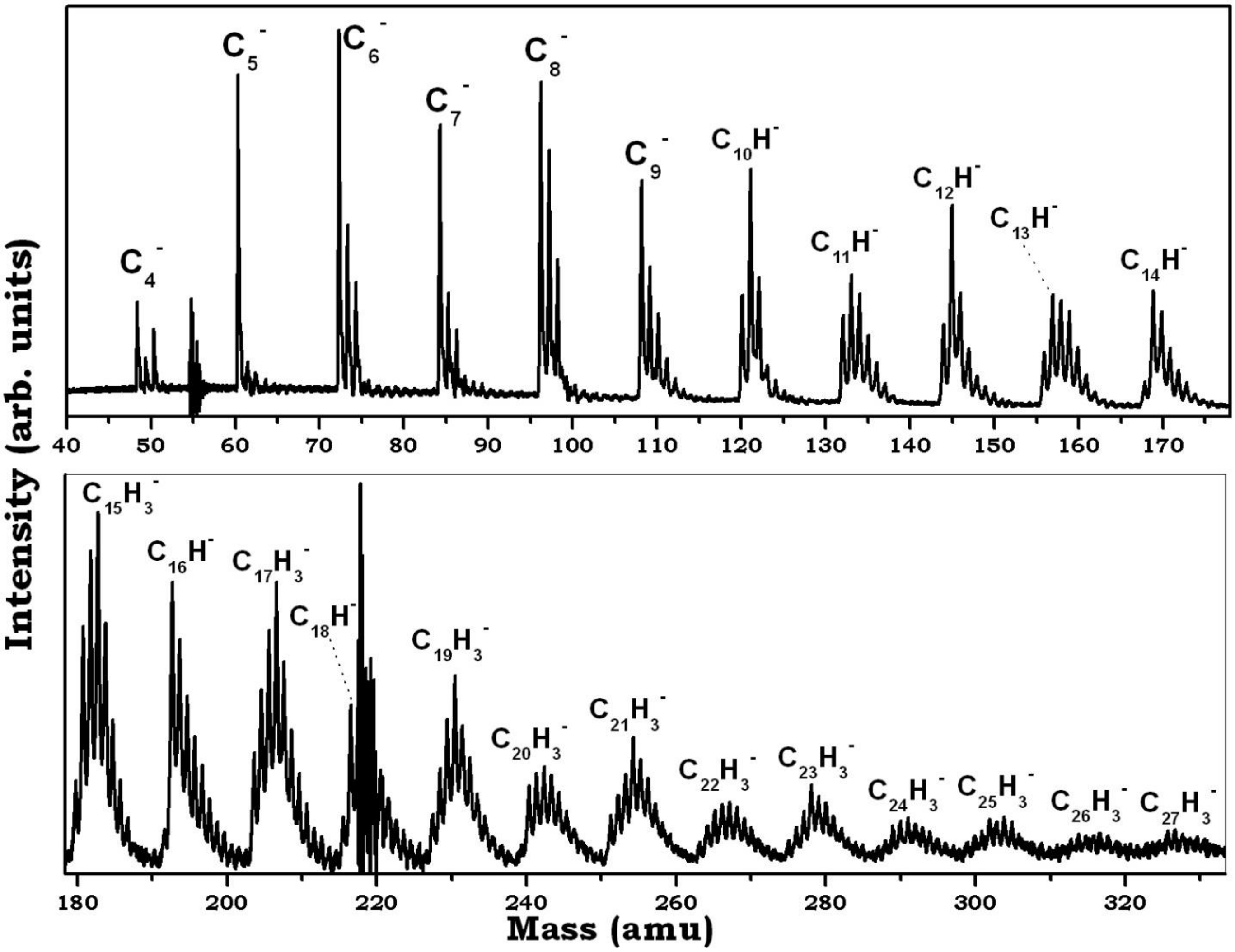

Figure 83: A negative R-TOF spectrum of carbon cluster ions. Ions were generated from plate plasma discharge ionization of acetylene gas seeded in helium.

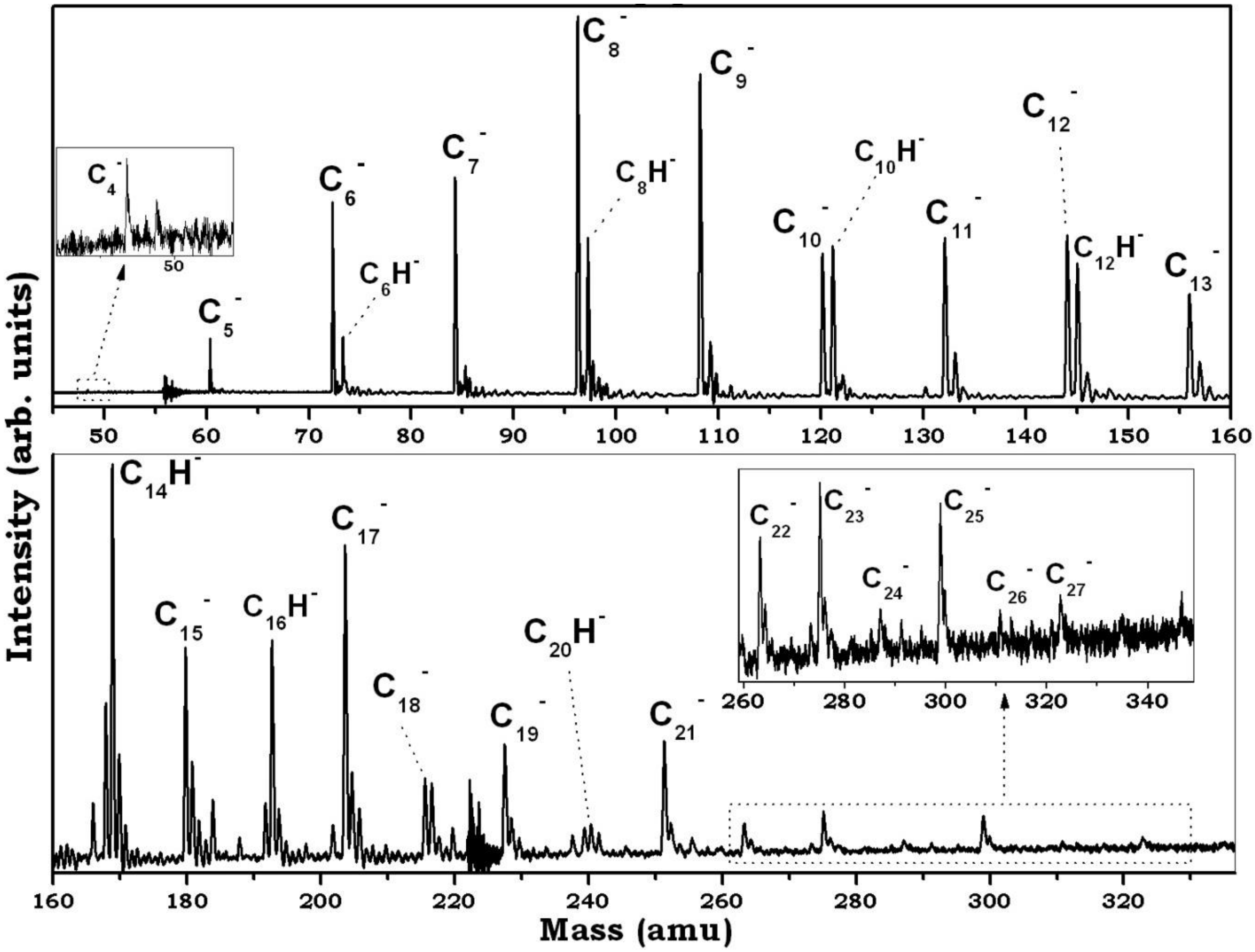

Figure 84: A negative R-TOF spectrum of carbon cluster ions. Ions were generated from needle plasma discharge ionization of acetylene gas seeded in helium.

Another observation made in the negative cluster ion analysis is the absence of the negatively charged transition metal ions, as we observe in the positive cluster ion analysis. This could be attributed to the relative difficulty of electron binding /attachment to the transition metal atoms created in the plasma process using the NPDI under our experimental conditions

8.3.7 Negative Cluster Ions from the plasma discharge ionization of Acrylonitrile

Displayed in Figure 85 is the negative R-TOF mass spectrum of the plate plasma discharge ionization of acrylonitrile at a potential difference of 680V. Several stable cluster complex ion series are observed in this spectrum, some formed through possible rearrangement of different fragments of the acrylonitrile molecule, and others through adduct formation between fragment ions and neutral ACN molecular clusters, which could get to a stable ground state possibly through covalent and non-covalent interactions. The most stable complex ion series resulting from rearrangement of the fragments of the ACN molecule include pure carbon cluster anions C_n^- (n=2-8), cyano polyynes C_mN^- (m=1-7), and hydrogenated cyano polyynes C_mHN^- (m=3-9). We also observe the fragment ions C^-, C_3^-, C_6^-, CN^-, and C_mH^-, all adding ACN molecules to form the adduct complex. The radical anion cluster $(ACN)_n^-$ is also observed with values of n between 2 and 7. Several of the molecular ions mentioned above have been the focus of extensive experimental and theoretical research, [258,284-289] with several of them being detected in the interstellar, circumstellar media[258,290-298].

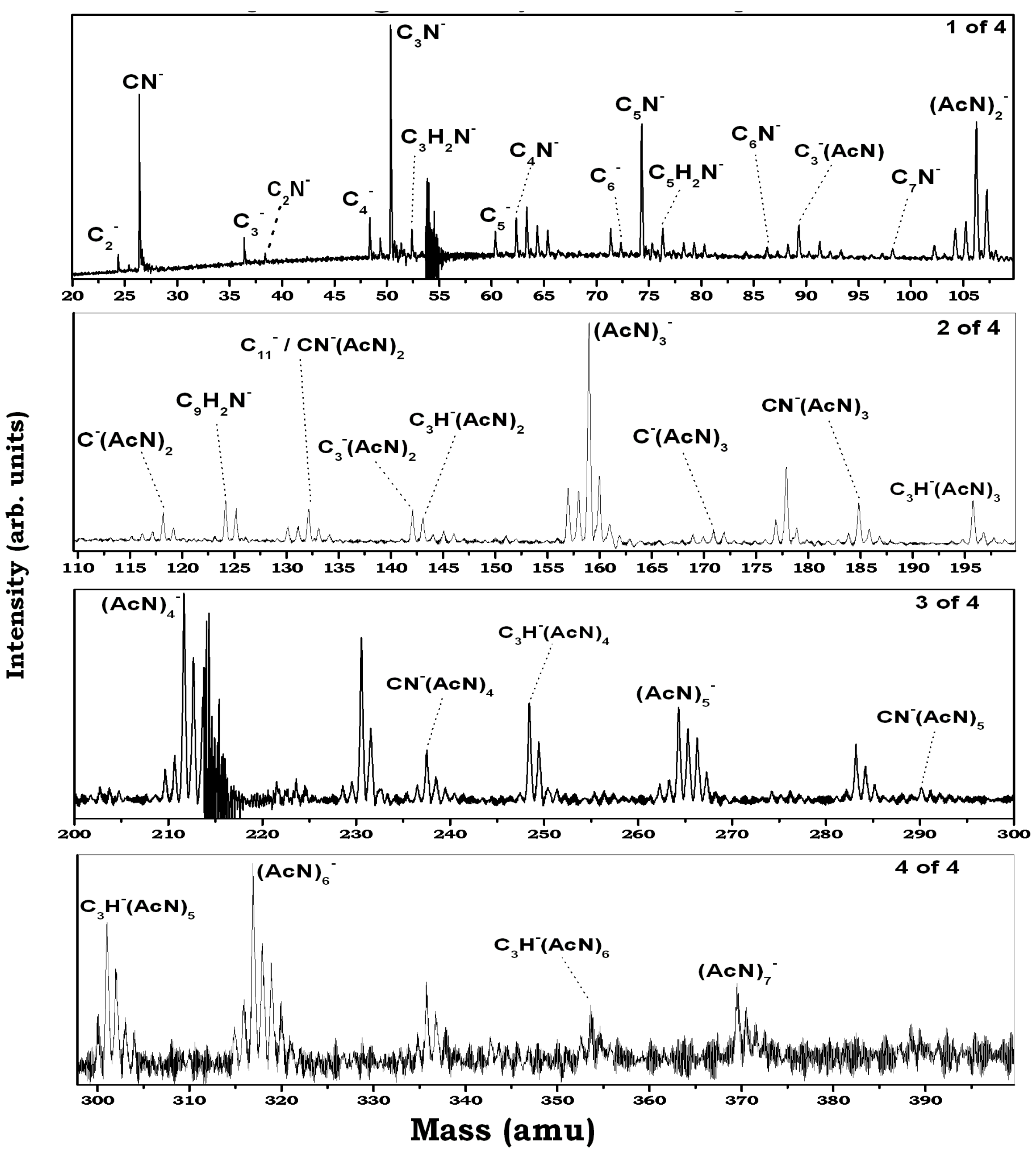

Figure 85: R-TOF mass spectrum of the plate plasma discharge ionization of acrylonitrile at a potential difference of 680V.

The efficient production and study of these ions is essential to the understanding of the mechanism of their formation, and their eventual detection in the interstellar and circumstellar media. Also equally important is the study of the mechanism of formation of these ions in the interstellar and circumstellar media, which is obviously too complex to decipher, and thus a step by step analysis of each single molecule or ion in the laboratory is the most realistic approach to understanding the chemistry of the interstellar and circumstellar media.[299] Information on structure of ions and molecules could be useful for insight into their formation and reaction mechanism.[281]

Study of the ions is essential since they could be a possible pathway to the formation of several of the identified neutral molecules by electron capture/recombination reactions by cationic species, and electron detachment for anionic species respectively. Alternatively, the neutrals can form these ions through radiative electron attachment to form anions,[300] and dissociative ionization to from cations[301].

Several of these molecules can only be identified in space if they are produced in high enough densities to enable high spectral resolution studies in the laboratory, which is essential for unambiguous astronomical search. [302,303]

8.4 Conclusion

We have presented here a novel inexpensive ionization technique that has been applied generate molecular and adduct ions relevant to the interstellar and circumstellar media, some of which have previously been identified through their rotational transitions. These ions have been produced in relative high densities through the plasma discharge ionization of precursor organic molecules such as acetylene, methanol, acrylonitrile, HCN/DCN, and binary clusters of acetylene/methanol, and are shown to be relatively stable, compared to the other ions observed in their respective mass spectra. This ionization technique coupled with a mass selection instrument could be useful in the characterization of each of the ionic species formed. Spectroscopic and chemical information of these ions could be very valuable in understanding the nature of their occurrence in the interstellar and circumstellar media.

CHAPTER 9. **Summary and Future Outlook**

The research presented in this dissertation has covered a few interesting fields in astrochemistry, especially relating to the formation mechanism and growth of several types of carbonaceous compounds through different ionization methods. In this work, we have addressed the question of what the effect of the presence the second nitrogen in the pyrimidine molecule will have on the formation of a possible covalent bond between the benzene radical cation and the neutral pyrimidine molecule. This investigation was made necessary after the evidence of the formation of a stable covalent (Benzene•Pyridine)$^{\bullet+}$ adduct bonded by a C-N bond between benzene radical cation and neutral pyridine using the ion mobility mass spectrometry technique. [24] It was found that the two most stable isomers of the covalently bonded dimer had a the displaced hydrogen of the benzene ring on the para position of the rings on either the benzene or the pyridine ring, with the isomer having the hydrogen on the pyridine ring almost 7 kcalmol^{-1} lower in energy. Undoubtedly, the positioning of the displaced hydrogen at this position will disrupt the π aromaticity of the pyridine ring. This incited the curiosity of whether a similar stable covalent bonded adduct could be formed between the benzene radical cation and pyrimidine.

Here we found a stable covalent (Benzene•Pyrimidine)$^{\bullet+}$ adduct bonded by a C-N bond between benzene radical cation and neutral pyrimidine, and the presence of the second nitrogen further stabilizes the covalent dimer formed by hosting the displaced hydrogen. In fact, the (Benzene•Pyrimidine)$^{\bullet+}$ adduct formed here is found to have a BDE of 40.7 kcalmol^{-1}, almost 6 kcalmol^{-1} lower than the (Benzene•Pyridine)$^{\bullet+}$ adduct when both are calculated at the same level of theory and basis set for the atoms.

Further work on this subject will look to generate these stable covalent adducts and investigate their chemistry, such as their covalent and non-covalent binding to other aromatic systems such as acetylene, benzene, pyridine, and pyrimidine, etc. to gain insight into their growth mechanism. Another area will look into their solvation by interstellar relevant organic molecules such as water, acetylene, ammonia, and acetonitrile.

The solvation of substituted benzenes by HCN was also investigated using the ion mobility technique and DFT computations to access the effect of the presence of electron-withdrawing substituents on the benzene ring, and the findings were compared to previous work done to determine the solvation chemistry of benzene[60] and phenylacetylene[114]. In this work, we used fluorobenzene, 1,4 di-fluorobenzene, and benzonitrile. We observed a slight increase in the binding of the HCN molecule to the aromatic ring as the electronegativity of the substituent increases due to the electron-withdrawing substituents increasing the partial positive charge on the ring hydrogens that form $CH^{\delta+}$---N bonds, and by creating positive charge centers on the fluorinated ring carbons for electrostatically bonded isomers. In the electrostatically bonded isomers the HCN is perpendicular to the ring and its dipole points to a positively charged ring carbon. In the fluorobenzenes these vertical isomers, and in benzonitrile a hydrogen bonded planar isomer have the lowest energy.

Although in these isomers HCN interacts with different sites of the ionized benzenes, vertical electrostatic and the planar hydrogen bonded structures were found to have similar calculated binding energies within 1 kcal•mol^{-1} in these isomers, which is thermodynamically insignificant. The thermochemistry suggests that the observed cluster populations are mixtures of the vertical and planar isomers. Further HCN molecules can bond directly to unoccupied ring CH hydrogens or bond to the first-shell HCN molecules to form linear HCN---HCN--- hydrogen bonded chains.

The next step of this study will be to look at the solvation of the substituted rings using electron donating groups such as methyl–benzene, aniline and hydroxybenzene.

The catalytic activity of the 1st and 2nd row TM ions towards the polymerization of acetylene was studied and reported in this work using the reflectron time of flight mass spectrometry and DFT calculations. The nature of the interaction of the TM ions with acetylene ligand occurs through a process where the ion accepts the electrons from the acetylene π bonding orbitals into its acceptor orbitals (4s and 3dσ in 1st row, 5s and 4dσ in 2nd row TM ions respectively) and then the metal ion back-donates electrons from its dπ orbitals into the π* orbitals of the acetylene molecule. The early 1st row TM ions do not possess electrons and also have relatively smaller orbital size the orbitals, and this makes C-C/C-H activation by these ions inefficient, and almost inexistent.[25] However, Fe^+, Co^+, and Ni^+ possess dπ electrons, and are thus able to activate the C-H bond in C_2H_2 through efficient overlap of their atomic orbitals. Both Cu^+ and Zn^+ are $3d^{10}$ ions, and thus are seen to be labile towards C-C/C-H activation. The early 2nd row TM ions which also lack the dπ electrons for back donation, however possessing larger orbitals prefer to form covalent bonds with the C_2H_2 ligand by breaking a pi bond in the ligand, and are also observed to facilitate the polymerization of C_2H_2. The later second row TM ions interact with the C_2H_2 molecules through ion-π electrostatic interaction, and are observed to also efficiently catalyze the polymerization of C_2H_2. The ability of the 2nd row TM ions to activate the C-C/C-H bonds of acetylene indicates a more efficient overlap between the relevant orbitals of the metal ion with that of the ligand, compared to the 1st row TM ions.

The next step in this work is to study the same system with the 3rd row transition metal ions, and also to investigate the activity of the TM ions towards the polymerization of other organic molecules.

Finally, we reported a novel ionization technique that has been used to generate ISM relevant ions using the reflectron time of flight mass spectrometry. The prospects of this ionization technique is exciting because it opens the pathway to producing several stable molecular ions and adducts in high enough density in the laboratory, that can be characterized spectroscopically which could lead to the identification of several molecules and ions that have yet to be assigned to unidentified infrared (UIR) bands and diffuse interstellar bands (DIB) due to the lack of their laboratory characterization.

References

(1) Petrie, S.; Bohme, D. K. *Mass Spectrometry Reviews* **2007**, *26*, 258.

(2) Klemperer, W. *Proceedings of the National Academy of Sciences* **2006**, *103*, 12232.

(3) Heath, J. R. S., R. J., *Science* **1996**, *274*, 1489.

(4) Ochsenfeld, C.; Kaiser, R. I.; Lee, Y. T.; Suits, A. G.; Head-Gordon, M. *The Journal of Chemical Physics* **1997**, *106*, 4141.

(5) Herbst, E. L., C. M., *Astrophys. J. Suppl. Ser.* **1989**, *69*, 271.

(6) Savic, I.; Gerlich, D. *AIP Conference Proceedings* **2006**, *876*, 415.

(7) Heath, J. R.; Zhang, Q.; O'Brien, S. C.; Curl, R. F.; Kroto, H. W.; Smalley, R. E. *Journal of the American Chemical Society* **1987**, *109*, 359.

(8) Henning, T.; Salama, F. *Science* **1998**, *282*, 2204.

(9) Héctor Alvaro, G.; Jos, O. *The Astrophysical Journal* **2012**, *746*, 83.

(10) Sloan, G. C.; Hayward, T. L.; Allamandola, L. J.; Bregman, J. D.; DeVito, B.; Hudgins, D. M. *The Astrophysical Journal Letters* **1999**, *513*, L65.

(11) Allamandola, L. J. T., A. G. G. M.; Barker, J. R.

Astrophysical Journal **1985**, *290*, L25.

(12) Leger, A. P., J. L. *Astronomy and Astrophysics* **1984**, L5.

(13) Ruiterkamp, R.; Peeters, Z.; Moore, M. H.; Hudson, R. L.; Ehrenfreund, P. *A&A* **2005**, *440*, 391.

(14) Klemperer, W. *Annual Review of Physical Chemistry* **2011**, *62*, 173.

(15) Nikolaou, K.; Masclet, P.; Mouvier, G. *Science of The Total Environment* **1984**, *32*, 103.

(16) Tokiwa, H.; Ohnishi, Y.; Rosenkranz, H. S. *Critical Reviews in Toxicology* **1986**, *17*, 23.

(17) Atkinson, R. A., J.: *Environ Health Perspect.* **1994**, *102*, 117.

(18) Boffetta, P.; Jourenkova, N.; Gustavsson, P. *Cancer Causes Control* **1997**, *8*, 444.

(19) Smith, L. E.; Denissenko, M. F.; Bennett, W. P.; Li, H.; Amin, S.; Tang, M.-s.; Pfeifer, G. P. *Journal of the National Cancer Institute* **2000**, *92*, 803.

(20) Rybicki, B. A.; Neslund-Dudas, C.; Bock, C. H.; Rundle, A.; Savera, A. T.; Yang, J. J.; Nock, N. L.; Tang, D. *Clinical Cancer Research* **2008**, *14*, 750.

(21) Rogan, E. G.; Devanesan, P. D.; RamaKrishna, N. V. S.; Higginbotham, S.; Padmavathi, N. S.; Chapman, K.; Cavalieri, E. L.; Jeong, H.; Jankowiak, R.; Small, G. J. *Chemical Research in Toxicology* **1993**, *6*, 356.

(22) Momoh, P. O.; Abrash, S. A.; Mabrouki, R.; El-Shall, M. S. *Journal of the American Chemical Society* **2006**, *128*, 12408.

(23) Momoh, P. O.; Soliman, A.-R.; Meot-Ner, M.; Ricca, A.; El-Shall, M. S. *Journal of the American Chemical Society* **2008**, *130*, 12848.

(24) El-Shall, M. S.; Ibrahim, Y. M.; Alsharaeh, E. H.; Meot-Ner, M.; Watson, S. P. *J. Am. Chem. Soc.* **2009**, *131*, 10066.

(25) Sharma, P.; Attah, I.; Momoh, P.; El-Shall, M. S. *International Journal of Mass Spectrometry* **2011**, *300*, 81.

(26) Soliman, A.-R.; Hamid, A. M.; Attah, I.; Momoh, P.; El-Shall, M. S. *Journal of the American Chemical Society* **2012**.

(27) Meot-Ner, M. *Chem. Rev.* **2012**, *112*, PR22.

(28) Dougherty, D. A. *Science* **1996**, *271*, 163.

(29) Cerny, J.; Hobza, P. *Phys. Chem. Chem. Phys.* **2007**, *9*, 5291.

(30) Garand, E.; Kamrath, M. Z.; Jordan, P. A.; Wolk, A. B.; Leavitt, C. M.; McCoy, A. B.; Miller, S. J.; Johnson, M. A. *Science* **2012**, *335*, 694.

(31) Tsuzuki, S. In *Intermolecular Forces and Clusters I*; Wales, D. J., Ed.; Springer Berlin Heidelberg: 2005; Vol. 115, p 149.

(32) Ugozzoli, F.; Arduini, A.; Massera, C.; Pochini, A.; Secchi, A. *New Journal of Chemistry* **2002**, *26*, 1718.

(33) Liou, C. C.; Wu, H. F.; Bradbelt, J. S. *J. Am. Soc. Mass Spectrom.* **1994**, *5*, 260.

(34) Chung, S.; Hippler, M. *J. Chem. Phys.* **2006**, *124*, 214316.

(35) Tarakeshwar, P.; Kim, K. S.; Brutschy, B. *J. Chem. Phys.* **1999**, *110*, 8501.

(36) Ben-Naim, A. *Hydrophobic interactions*; Plenum: New York, 1980.

(37) Tanford, C. *The Hydrophobic Effect: Formation of Micelles and*

Biological Membranes; Wiley: New York,: New York, 1980; Vol. 2.

(38) Conway, B. E. *Ionic Hydration in Chemistry and Biophysics*; Elsevier: New York, 1981.

(39) Jeffrey, G. A. *An Introduction to Hydrogen Bonding*; University Press: Oxford, U.K, 1997.

(40) Tsuzuki, S. A., F. *Phys. Chem. Chem. Phys.* **2008**, *10*, 2584.

(41) Mabrouki, R.; Ibrahim, Y.; Xie, E.; Meot-Ner, M.; El-Shall, M. S. *J. Phys. Chem. A* **2006**, *110*, 7334.

(42) Raju, R. K.; Bloom, J. W. G.; An, Y.; Wheeler, S. E. *ChemPhysChem* **2011**, *12*, 3116.

(43) McMahon, T. B.; Kebarle, P. *Journal of the American Chemical Society* **1986**, *108*, 6502.

(44) K. M. Lee, H.-C. C., J.-C. Jiang, J. C. C. Chen, H.-E. Kao, S. H. Lin,; and I. J. B. Lin *J. Am. Chem. Soc.* **2003**, *125*, 12358.

(45) P. Asselin, P. S., B. Madebene, M. E. Alikhani, and M. Lewerenz, *Phys. Chem. Chem. Phys.* **2006**

8, 1785

(46) Pribble, R. N.; Zwier, T. S. *Science* **1994**, *265*, 75.

(47) Miyazaki, M.; Fujii, A.; Ebata, T.; Mikami, N. *Chemical Physics Letters* **2001**, *349*, 431.

(48) Suzuki, S.; Green, P. G.; Bumgarner, R. E.; Dasgupta, S.; Goddard, W. A.; Blake, G. A. *Science* **1992**, *257*, 942.

(49) Ibrahim, Y. M.; Meot-Ner, M.; Alshraeh, E. H.; El-Shall, M. S.; Scheiner, S. *J. Am. Chem. Soc.* **2005**, *127*, 7053.

(50) Shibasaki, K.; Fujii, A.; Mikami, N.; Tsuzuki, S. *The Journal of Physical Chemistry A* **2006**, *110*, 4397.

(51) Pribble, R. N.; Zwier, T. S. *Faraday Discussions* **1994**, *97*, 229.

(52) Tarakeshwar, P.; Choi, H. S.; Lee, S. J.; Lee, J. Y.; Kim, K. S.; Ha, T.-K.; Jang, J. H.; Lee, J. G.; Lee, H. *The Journal of Chemical Physics* **1999**, *111*, 5838.

(53) Solcà, N.; Dopfer, O. *The Journal of Physical Chemistry A* **2003**, *107*, 4046.

(54) Solcà, N.; Dopfer, O. *Chemical Physics Letters* **2001**, *347*, 59.

(55) Miyazaki, M.; Fujii, A.; Ebata, T.; Mikami, N. *Physical Chemistry Chemical Physics* **2003**, *5*, 1137.

(56) Miyazaki, M.; Fujii, A.; Ebata, T.; Mikami, N. *Chem. Phys. Lett.* **2004**, *399*, 412.

(57) Miyazaki, M.; Fujii, A.; Mikami, N. *The Journal of Physical Chemistry A* **2004**, *108*, 8269.

(58) Enomoto, S.; Miyazaki, M.; Fujii, A.; Mikami, N. *J. Phys. Chem. A* **2005**, *109*, 9471.

(59) Mizuse, K.; Suzuki, Y.; Mikami, N.; Fujii, A. *The Journal of Physical Chemistry A* **2011**, *115*, 11156.

(60) Hamid, A. M.; Soliman, A. R.; El-Shall, M. S. *The journal of physical chemistry. A* **2012**, *117*, 1069.

(61) Momoh, P. O.; Xie, E.; Abrash, S. A.; Meot-Ner, M.; El-Shall, M. S. *J. Phys. Chem. A* **2008**, *112*, 6066.

(62) Ibrahim, Y.; Mabrouki, R.; Meot-Ner, M.; El-Shall, M. S. *J. Phys. Chem. A* **2007**, *111*, 1006.

(63) Momoh, P. O.; Hamid, A. M.; Abrash, S. A.; El-Shall, M. S. *J. Chem. Phys.* **2011**, *134*, 204315.

(64) Momoh, P. O.; El-Shall, M. S. *Chem. Phys. Lett.* **2007**, *436*, 25.

(65) Li, Q.; Jacob, D. J.; Yantosca, R. M.; Heald, C. L.; Singh, H. B.; Koike, M.; Zhao, Y.; Sachse, G. W.; Streets, D. G. *J. Geophys. Res.* **2003**, *108*, 8827.

(66) Herbst, E.; van Dishoeck, E. F. *Annu. Rev. Astron. Astrophys.* **2009**, *47*, 427.

(67) Walters, R. S.; Pillai, E. D.; Schleyer, P. v. R.; Duncan, M. A. *Journal of the American Chemical Society* **2005**, *127*, 17030.

(68) Mecking, S. *Angewandte Chemie International Edition* **2001**, *40*, 534.

(69) Hettich, R. L.; Jackson, T. C.; Stanko, E. M.; Freiser, B. S. *Journal of the American Chemical Society* **1986**, *108*, 5086.

(70) Bauschlicher, C. W.; Partridge, H.; Langhoff, S. R. *The Journal of Physical Chemistry* **1992**, *96*, 3273.

(71) Chretien, S.; Salahub, D. R. *The Journal of Chemical Physics* **2003**, *119*, 12291.

(72) Ma, Y.-P.; Xue, W.; Wang, Z.-C.; Ge, M.-F.; He, S.-G. *The Journal of Physical Chemistry A* **2008**, *112*, 3731.

(73) Schroeter, K.; Schalley, C. A.; Wesendrup, R.; Schröder, D.; Schwarz, H. *Organometallics* **1997**, *16*, 986.

(74) Meyer, F. K., Farooq A.; Armentrout, P. B. *Journal of the American Chemical Society* **1995**, *117*, 9740.

(75) Chert, Z. Y.; Guo, B. C.; May, B. D.; Cartier, S. F.; Castleman Jr, A. W. *Chemical Physics Letters* **1992**, *198*, 118.

(76) Bettens, R. P. A. H., Eric *Astrophysical Journal* **1996**, *468*, 68.

(77) Comita, P. B.; Brauman, J. I. *Science* **1985**, *227*, 863.

(78) El-Shall, M. S. *Acc. Chem. Res.* **2008**, *41*, 783.

(79) Rusyniak, M. J.; Ibrahim, Y. M.; Wright, D. L.; Khanna, S. N.; El-Shall, M. S. *J.Am. Chem. Soc.* **2003**, *125*, 12001.

(80) Rusyniak, M.; Ibrahim, Y.; Alsharaeh, E.; Meot, N.; El-Shall, M. S. *The Journal of Physical Chemistry A* **2003**, *107*, 7656.

(81) Stein, G. D. *The Physics Teacher* **1979**, *17*, 503.

(82) Bernstein, E. R. *Atomic and Molecular Clusters*, 1990; Vol. 68.

(83) Momoh, P. O.; Hamid, A. M.; Soliman, A.-R.; Abrash, S. A.; El-Shall, M. S. *J. Phys. Chem. Lett.*, *2*, 2412.

(84) Elshall, M. S. S., K. E.; Whetten, R. L.; Meotner, M. *Journal of Physical Chemistry* **1989**, *93*.

(85) Gibson, J. K. *The Journal of Physical Chemistry* **1994**, *98*, 6063.

(86) Gibson, J. K. *The Journal of Physical Chemistry* **1996**, *100*, 15688.

(87) Yang, Y.; Saoud, K. M.; Abdelsayed, V.; Glaspell, G.; Deevi, S.; El-Shall, M. S. *Catalysis Communications* **2006**, *7*, 281.

(88) Caldwell, R.; Wright, D.; El-Shall, M. S. *Z Phys D - Atoms, Molecules and Clusters* **1993**, *26*, 189.

(89) Vann, W.; El-Shall, M. S. *Journal of the American Chemical Society* **1993**, *115*, 4385.

(90) Daly, G. M.; El-Shall, M. S. *The Journal of Physical Chemistry* **1995**, *99*, 5283.

(91) Hercules, D. M.; Day, R. J.; Balasanmugam, K.; Li, C. P. *Analytical Chemistry* **1982**, *54*, 280A.

(92) El-Shall, M. S. L., S. **Advances in Metal and Semiconductor Clusters. 1998**, *4*, 115.

(93) Alsharaeh, E. H.; Ibrahim, Y. M.; El-Shall, M. S. *J. Am. Chem. Soc.* **2005**, *127*, 6164.

(94) Extrel., E. A. N. R. B. A. A. I. A. D.-. **2003**.

(95) Heer, W. A. d.; Milani, P. *Review of Scientific Instruments* **1991**, *62*, 670.

(96) Wiley, W. C.; McLaren, I. H. *Review of Scientific Instruments* **1955**, *26*, 1150.

(97) Guilhaus, M. *Journal of Mass Spectrometry* **1995**, *30*, 1519.

(98) Jarrold, M. F.; Bower, J. E. *J. Chem. Phys.* **1992**, *96*, 9180.

(99) Mesleh, M. F.; Hunter, J. M.; Shvartsburg, A. A.; Schatz, G. C.; Jarrold, M. F. *The Journal of Physical Chemistry* **1996**, *100*, 16082.

(100) Kanu, A. B.; Dwivedi, P.; Tam, M.; Matz, L.; Hill, H. H., Jr. *J. Mass Spectrom.* **2008**, *43*, 1.

(101) Mason, E. A.; McDaniel, E. W. *Transport Properties of Ions in Gases*; John Wiley & Sons: New York, 1988.

(102) Kemper, P. R.; Bowers, M. T. *J. Am. Soc. Mass Spectrom.* **1990**, *1*, 197.

(103) Van Koppen, P. A. M.; Kemper, P. R.; Bowers, M. T. *Understanding Chemical Reactivity* **1996**, *15*, 157.

(104) Revercomb, H. W.; Mason, E. A. *Anal. Chem.* **1975**, *47*, 970.

(105) Kaneko, Y.; Megill, L. R.; Hasted, J. B. *Journal of Chemical Physics* **1966**, *45*, 3741.

(106) Ibrahim, Y.; Alsharaeh, E.; Mabrouki, R.; Momoh, P.; Xie, E.; El-Shall, M. S. *J. Phys. Chem. A* **2008**, *112*, 1112.

(107) Krishnamurthy, M.; de Gouw, J. A.; Bierbaum, V. M.; Leone, S. R. *J. Phys. Chem.* **1996**, *100*, 14908.

(108) Mesleh, M. F.; Hunter, J. M.; Shvartsburg, A. A.; Schatz, G. C.; Jarrold, M. F. *Journal of Physical Chemistry* **1996**, *100*, 16082.

(109) Shvartsburg, A. A.; Jarrold, M. F. *Chemical Physics Letters* **1996**, *261*, 86.

(110) Wyttenbach, T.; Helden, G. v.; Batka Jr., J. J.; Carlat, D.; Bowers, M. T. *Journal of the American Society for Mass Spectrometry* **1997**, *8*, 275.

(111) Logan, S. R. **Fundamentals of Chemical Kinetics;Longman Group Limited 1996**.

(112) Jarrold, M. F. *J. Phys. Chem.* **1995**, *99*, 11.

(113) Soliman, A.-R.; Hamid, A. M.; Abrash, S. A.; El-Shall, M. S. *Chemical Physics Letters* **2012**, *523*, 25.

(114) Hamid, A. M.; Soliman, A.-R.; Samy El-Shall, M. *Chem. Phys. Lett.* **2012**, *543*, 23.

(115) Keesee, R. G.; Castleman, A. W., Jr. *J. Phys. Chem. Ref. Data* **1986**, *15*, 1011.

(116) Zhang, B.; Cai, Y.; Mu, X.; Lou, N.; Wang, X. *J. Chem. Phys.* **2002**, *117*, 3701.

(117) Yamabe, S.; Fukuda, T.; Yamazaki, S. *J. Phys. Chem. A* **2012**, *116*, 1289.

(118) Lavorato, D.; Terlouw, J.; McGibbon, G.; Dargel, T.; Koch, W.; Schwarz, H. *Int. J. Mass Spectrom.* **1998**, *179-180*, 7.

(119) Hay, P. J.; Wadt, W. R. *The Journal of Chemical Physics* **1985**, *82*, 299.

(120) Wright, J. S.; Rowley, C. N.; Chepelev, L. L. *Mol. Phys.* **2005**, *103*, 815.

(121) Bohme, D. K. In *Dusty Objects in the Universe*; Bussoletti, E., Vittone, A. A., Eds.; Springer Netherlands: 1990; Vol. 165, p 69.

(122) El-Shall, M. S.; Ibrahim, Y. M.; Alsharaeh, E.; Dias, K.; Meot-Ner, M. *Abstracts, 56th Southeast Regional Meeting of the American Chemical Society, Research Triangle Park, NC, United States*, **2004**.

(123) Mesleh, M. F.; Hunter, J. M.; Shvartsburg, A. A.; Schatz, G. C.; Jarrold, M. F. *J. Phys. Chem.* **1996**, *100*, 16082.

(124) Wright, M. R. *Introduction to Chemical Kinetics*; John Wiley & Sons, 2005.

(125) Luis G Arnaut, S. J. F., Hugh Burrows *Chemical Kinetics: From Molecular Structure to Chemical Reactivity*; Elsevier, 2006.

(126) Wren, S. W.; Vogelhuber, K. M.; Garver, J. M.; Kato, S.; Sheps, L.; Bierbaum, V. M.; Lineberger, W. C. *Journal of the American Chemical Society* **2012**, *134*, 6584.

(127) M. Mautner, I. T. D. i. N. C. W., NIST Standard Reference Database Number 69, Eds. P.J. Linstrom and W.G. Mallard, National Institute of Standards and Technology, Gaithersburg MD, 20899, http://webbook.nist.gov, (retrieved March 14, 2013).

(128) Meot-Ner, M.; Hamlet, P.; Hunter, E. P.; Field, F. H. *Journal of the American Chemical Society* **1978**, *100*, 5466.

(129) Von Helden, G.; Wyttenbach, T.; Bowers, M. T. *Science* **1995**, *267*, 1483.

(130) Meot-Ner, M. *Journal of the American Chemical Society* **1992**, *119*, 3312.

(131) Taylor, E. C.; American

Chemical Society: Washington, DC, , 1974.

(132) Norrman, K.; McMahon, T. B. *Journal of the American Chemical Society* **1996**, *118*, 2449.

(133) Sloan, E. D. M. D. *Clathrate Hydrates of Natural Gases*; CRC Press: Florida, 2008; Vol. 3.

(134) Meot-Ner, M.; Hamlet, P.; Hunter, E. P.; Field, F. H. *J. Am. Chem. Soc.* **1978**, *100*, 5466.

(135) Meot-Ner, M. M.; El-Shall, M. S. *J. Am. Chem. Soc.* **1986**, *108*, 4386.

(136) El-Shall, M. S.; Ibrahim, Y. M.; Mabrouki, R. M.; Meot-Ner, M. *Abstracts of Papers, 229th ACS National Meeting, San Diego, CA, United States, March 13-17, 2005* **2005**, PHYS.

(137) Momoh, P. O.; El-Shall, M. S. *Phys. Chem. Chem. Phys.* **2008**, *10*, 4827.

(138) Wheeler, S. E.; Houk, K. N. *Journal of the American Chemical Society* **2008**, *130*, 10854.

(139) Frisch, M. J.; Trucks, G. W.; Schlegel, H. B.; Scuseria, G. E.; Robb, M. A.; Cheeseman, J. R.; Montgomery, J. A.; Vreven, T.; Kudin, K. N.; Burant, J. C.; Millam, J. M.; Iyengar, S. S.; Tomasi, J.; Barone, V.; Mennucci, B.; Cossi, M.; Scalmani, G.; Rega, N.; Petersson, G. A.; Nakatsuji, H.; Hada, M.; Ehara, M.; Toyota, K.; Fukuda, R.; Hasegawa, J.; Ishida, M.; Nakajima, T.; Honda, Y.; Kitao, O.; Nakai, H.; Klene, M.; Li, X.; Knox, J. E.; Hratchian, H. P.; Cross, J. B.; Bakken, V.; Adamo, C.; Jaramillo, J.; Gomperts, R.; Stratmann, R. E.; Yazyev, O.; Austin, A. J.; Cammi, R.; Pomelli, C.; Ochterski, J. W.; Ayala, P. Y.; Morokuma, K.; Voth, G. A.; Salvador, P.; Dannenberg, J. J.; Zakrzewski, V. G.; Dapprich, S.; Daniels, A. D.; Strain, M. C.; Farkas, O.; Malick, D. K.; Rabuck, A. D.; Raghavachari, K.; Foresman, J. B.; Ortiz, J. V.; Cui, Q.; Baboul, A. G.; Clifford, S.; Cioslowski, J.; Stefanov, B. B.; Liu, G.; Liashenko, A.; Piskorz, P.; Komaromi, I.; Martin, R. L.; Fox, D. J.; Keith, T.; Laham, A.; Peng, C. Y.; Nanayakkara, A.; Challacombe, M.; Gill, P. M. W.; Johnson, B.; Chen, W.; Wong, M. W.; Gonzalez, C.; Pople, J. A. 2003.

(140) Teng, Y.-L.; Xu, Q. *The Journal of Physical Chemistry A* **2009**, *113*, 12163.

(141) Böhme, D. K.; Schwarz, H. *Angewandte Chemie International Edition* **2005**, *44*, 2336.

(142) Michelini, M. d. C.; Russo, N.; Sicilia, E. *Inorganic Chemistry* **2004**, *43*, 4944.

(143) Irigoras, A.; Fowler, J. E.; Ugalde, J. M. *Journal of the American Chemical Society* **1999**, *121*, 8549.

(144) Y.B. Pithawalla, M. S. E.-S. In,*in: M.O. Hunt, T.E. Long (Eds.)* 1998; Vol. Solvent-Free Polymerizations and Processes,ACS Symposium Series, p 232.

(145) Daly, G. M.; Pithawalla, Y. B.; Yu, Z.; El-Shall, M. S. *Chemical Physics Letters* **1995**, *237*, 97.

(146) Daly, G. M.; El-Shall, M. S. *The Journal of Physical Chemistry* **1994**, *98*, 696.

(147) van Koppen, P. A. M.; Bowers, M. T.; Haynes, C. L.; Armentrout, P. B. *Journal of the American Chemical Society* **1998**, *120*, 5704.

(148) Armentrout, P. B. *Accounts of Chemical Research* **1995**, *28*, 430.

(149) Armentrout, P. B. *Annual Review of Physical Chemistry* **1990**, *41*, 313.

(150) Eller, K.; Schwarz, H. *Chemical Reviews* **1991**, *91*, 1121.

(151) Katz, T. J.; Lee, S. J. *Journal of the American Chemical Society* **1980**, *102*, 422.

(152) Johnson, L. K.; Killian, C. M.; Brookhart, M. *Journal of the American Chemical Society* **1995**, *117*, 6414.

(153) J. Allison *Prog. Inorg. Chem.* **1986**, *34*, 627.

(154) Buckner, S. W.; Freiser, B. S. *Polyhedron* **1988**, *7*, 1583.

(155) Bowers, M. T. *Accounts of Chemical Research* **1994**, *27*, 324.

(156) Freiser, B. S. *Accounts of Chemical Research* **1994**, *27*, 353.

(157) Holthausen, M. C.; Fiedler, A.; Schwarz, H.; Koch, W. *Angewandte Chemie International Edition in English* **1995**, *34*, 2282.

(158) Holthausen, M. C.; Koch, W. *Journal of the American Chemical Society* **1996**, *118*, 9932.

(159) Weisshaar, J. C. *Accounts of Chemical Research* **1993**, *26*, 213.

(160) Magnera, T. F.; David, D. E.; Michl, J. *Journal of the American Chemical Society* **1987**, *109*, 936.

(161) Schilling, J. B.; Beauchamp, J. L. *Journal of the American Chemical Society* **1988**, *110*, 15.

(162) Mourgues, P.; Ferhati, A.; McMahon, T. B.; Ohanessian, G. *Organometallics* **1997**, *16*, 210.

(163) Schröder, D.; Sülzle, D.; Hrušák, J.; Böhme, D. K.; Schwarz, H. *International Journal of Mass Spectrometry and Ion Processes* **1991**, *110*, 145.

(164) Gevorgyan, V.; Radhakrishnan, U.; Takeda, A.; Rubina, M.; Rubin, M.; Yamamoto, Y. *The Journal of Organic Chemistry* **2001**, *66*, 2835.

(165) Martinez, M.; del Carmen Michelini, M.; Rivalta, I.; Russo, N.; Sicilia, E. *Inorganic Chemistry* **2005**, *44*, 9807.

(166) Abbet, S.; Sanchez, A.; Heiz, U.; Schneider, W. D.; Ferrari, A. M.; Pacchioni, G.; Rösch, N. *Journal of the American Chemical Society* **2000**, *122*, 3453.

(167) Kohn, W.; Sham, L. J. *Physical Review* **1965**, *140*, A1133.

(168) Bytheway, I.; Wong, M. W. *Chemical Physics Letters* **1998**, *282*, 219.

(169) Klippenstein, S. J.; Yang, C.-N. *International Journal of Mass Spectrometry* **2000**, *201*, 253.

(170) Lebrilla, C. B.; Schulze, C.; Schwarz, H. *Journal of the American Chemical Society* **1987**, *109*, 98.

(171) Rosi, M.; Bauschlicher Jr, C. W. *Chemical Physics Letters* **1990**, *166*, 189.

(172) Wesendrup, R.; Schwarz, H. *Organometallics* **1997**, *16*, 461.

(173) Momoh, P. O.; Abrash, S. A.; Mabrouki, R.; El-Shall, M. S. *J. Am. Chem. Soc.* **2006**, *128*, 12408.

(174) Castleman, A. W.; Wei, S. *Annual Review of Physical Chemistry* **1994**, *45*, 685.

(175) Castleman, A. W., Jr.; Bowen, K. H., Jr. *Journal of Physical Chemistry* **1996**, *100*, 12911.

(176) Walters, R. S.; Jaeger, T. D.; Duncan, M. A. *The Journal of Physical Chemistry A* **2002**, *106*, 10482.

(177) Ingolfsson, O.; Wodtke, A. M. *The Journal of Chemical Physics* **2002**, *117*, 3721.

(178) Martin, T. P.; Bergmann, T.; Goehlich, H.; Lange, T. *The Journal of Physical Chemistry* **1991**, *95*, 6421.

(179) Alberts, I. L.; Rowlands, T. W.; Handy, N. C. *The Journal of Chemical Physics* **1988**, *88*, 3811.

(180) Sicilia, E.; Russo, N. *Journal of Molecular Structure: THEOCHEM* **2004**, *709*, 167.

(181) Sodupe, M.; Bauschlicher, C. W. *The Journal of Physical Chemistry* **1991**, *95*, 8640.

(182) Relph, R. A.; Bopp, J. C.; Roscioli, J. R.; Johnson, M. A. *The Journal of Chemical Physics* **2009**, *131*, 114305.

(183) Bohme, D. K.; Wlodek, S.; Zimmerman, J. A.; Eyler, J. R. *International Journal of Mass Spectrometry and Ion Processes* **1991**, *109*, 31.

(184) Buckner, S. W.; MacMahon, T. J.; Byrd, G. D.; Freiser, B. S. *Inorganic Chemistry* **1989**, *28*, 3511.

(185) Kemper, P. R.; Bowers, M. T. *The Journal of Physical Chemistry* **1991**, *95*, 5134.

(186) Michael T. Bowers, P. R. K., Gert von Helden, and Petra A. M. van Koppen *Science* **1993**, *4*, 1446.

(187) Elkind, J. L.; Armentrout, P. B. *The Journal of Physical Chemistry* **1985**, *89*, 5626.

(188) Anicich, V. G.; Sen, A. D.; Wesley T. Huntress, J.; McEwan, M. J. *The Journal of Chemical Physics* **1990**, *93*, 7163.

(189) Walch, S. P. *The Journal of Chemical Physics* **1995**, *103*, 8544.

(190) Bauschlicher Jr, C. W.; Ricca, A. *Chemical Physics Letters* **2000**, *326*, 283.

(191) Bergman, R. G. *Nature* **2007**, *446*, 391.

(192) Godula, K.; Sames, D. *Science* **2006**, *312*, 67.

(193) Schröder, D.; Schwarz, H. *Proceedings of the National Academy of Sciences* **2008**, *105*, 18114.

(194) Di Santo, E.; Michelini, M. d. C.; Russo, N. *Organometallics* **2009**, *28*, 3716.

(195) Bergman, R. G. *Nature* **22 March 2007**, *446*, 391.

(196) D.Michael P, M. *Journal of Organometallic Chemistry* **2001**, *635*, 1.

(197) Labinger, J. A.; Bercaw, J. E. *Nature* **2002**, *417*, 507.

(198) Ziegler, K.; Holzkamp, E.; Breil, H.; Martin, H. *Angewandte Chemie* **1955**, *67*, 426.

(199) Natta, G. *Journal of Polymer Science* **1955**, *16*, 143.

(200) Armentrout, P. B. *Organometallics* **2007**, *26*, 5473.

(201) Armentrout, P. B.; Sievers, M. R. *The Journal of Physical Chemistry A* **2003**, *107*, 4396.

(202) Carpenter, C. J.; van Koppen, P. A. M.; Bowers, M. T. *Journal of the American Chemical Society* **1995**, *117*, 10976.

(203) Guo, B. C.; Castleman, A. W. *Journal of the American Chemical Society* **1992**, *114*, 6152.

(204) Musaev, D. G.; Morokuma, K. *The Journal of Physical Chemistry* **1996**, *100*, 11600.

(205) Parke, L. G.; Hinton, C. S.; Armentrout, P. B. *The Journal of Physical Chemistry A* **2008**, *112*, 10469.

(206) Ranasinghe, Y. A.; Freiser, B. S. *Chemical Physics Letters* **1992**, *200*, 135.

(207) Sharma, P.; Attah, I.; Momoh, P.; El-Shall, M. S. *International Journal of Mass Spectrometry* **2011**, *300*, 81.

(208) Van Koppen, P. A. M.; Kemper, P. R.; Bushnell, J. E.; Bowers, M. T. *Journal of the American Chemical Society* **1995**, *117*, 2098.

(209) Armentrout, P. B. *The Journal of Physical Chemistry A* **2006**, *110*, 8327.

(210) Cho, H.-G.; Andrews, L. *The Journal of Physical Chemistry A* **2010**, *114*, 10028.

(211) Cho, H.-G.; Kushto, G. P.; Andrews, L.; Bauschlicher, C. W. *The Journal of Physical Chemistry A* **2008**, *112*, 6295.

(212) Quintal, M. M.; Karton, A.; Iron, M. A.; Boese, A. D.; Martin, J. M. L. *The Journal of Physical Chemistry A* **2005**, *110*, 709.

(213) Chen, Y.-M.; Armentrout, P. B. *Journal of the American Chemical Society* **1995**, *117*, 9291.

(214) Gee, C.; Boissel, P.; Ohanessian, G. *Chemical Physics Letters* **1998**, *298*, 85.

(215) Glendening, E. D. *The Journal of Physical Chemistry A* **2004**, *108*, 10165.

(216) Schilling, J. B.; Beauchamp, J. L. *Organometallics* **1988**, *7*, 194.

(217) Becke, A. D. *The Journal of Chemical Physics* **1993**, *98*, 5648.

(218) Lee, C.; Yang, W.; Parr, R. G. *Physical Review B* **1988**, *37*, 785.

(219) Stephens, P. J.; Devlin, F. J.; Chabalowski, C. F.; Frisch, M. J. *The Journal of Physical Chemistry* **1994**, *98*, 11623.

(220) Watts, J. D.; Bartlett, R. J. *The Journal of Chemical Physics* **1992**, *97*, 3445.

(221) Arnold, C. C.; Zhao, Y.; Kitsopoulos, T. N.; Neumark, D. M. *The Journal of Chemical Physics* **1992**, *97*, 6121.

(222) Naaman, A.; Bhushan, K. G.; Pedersen, H. B.; Altstein, N.; Heber, O.; Rappaport, M. L.; Moalem, R.; Zajfman, D. *The Journal of Chemical Physics* **2000**, *113*, 4662.

(223) Gotts, N. G.; von Helden, G.; Bowers, M. T. *International Journal of Mass Spectrometry and Ion Processes* **1995**, *149-150*, 217.

(224) Dewar, M. J. S.; Ford, G. P. *Journal of the American Chemical Society* **1979**, *101*, 783.

(225) Siegbahn, P. E. M.; Blomberg, M. R. A.; Svensson, M. *Journal of the American Chemical Society* **1993**, *115*, 1952.

(226) Bushnell, J. E.; Kemper, P. R.; Maitre, P.; Bowers, M. T. *Journal of the American Chemical Society* **1994**, *116*, 9710.

(227) Hinrichs, R. Z.; Schroden, J. J.; Davis, H. F. *Journal of the American Chemical Society* **2002**, *125*, 860.

(228) Armentrout, P. B.; Beauchamp, J. L. *Accounts of Chemical Research* **1989**, *22*, 315.

(229) Moore, C. E. *U.S. National Bureau of Standards; U.S. Govt. Print. Off.: <Washington>* **1971**.

(230) Rohlfing, E. A. *J. Chem. Phys* **1990**, *11*, 7851.

(231) von Helden, G.; Hsu, M.-T.; Kemper, P. R.; Bowers, M. T. *Journal of Chemical Physics* **1991**, *95*, 3835.

(232) Jiao, C. Q. P., D. K.; Lee, S.; Huang, Y.; Freiser, B. S. *Rapid Comm. Mass Spec.* **1993**, *7*, 404.

(233) Sun, J. G., H.; Lifshitz, C., *J. Am. Chem. Soc.* **1993**, *115*, 8382.

(234) Parent, D. C. M., S. W., **1989**, *111*, 2393.

(235) Shibagaki, K.; Takada, N.; Sasaki, K.; Kadota, K. *Journal of Applied Physics* **2002**, *91*, 2449.

(236) Marcano, D. C. K., D. V.; Berlin, J. M.; Sinitskii, A.; Sun, Z.; Slesarev, A.; Alemany, L. B.; Lu, W.; Tour, J. M. , *ACS Nano* **2010**, *4*, 4806.

(237) Bernath, P. F. *Advances in space research : the official journal of the Committee on Space Research (COSPAR)* **1995**, *15*, 15.

(238) Szczepanski, J.; Ekern, S.; Vala, M. *The Journal of Physical Chemistry A* **1997**, *101*, 1841.

(239) Herod, A. A.; Kandiyoti, R.; Parker, J. E.; Johnson, C. A. F.; John, P.; Smith, G. P.; Li, C. Z. *Rapid Communications in Mass Spectrometry* **1993**, *7*, 360.

(240) Kaiser, R. I.; Belau, L.; Leone, S. R.; Ahmed, M.; Wang, Y.; Braams, B. J.; Bowman, J. M. *ChemPhysChem* **2007**, *8*, 1236.

(241) McElvany, S. W.; Dunlap, B. I.; O'Keefe, A. *The Journal of Chemical Physics* **1987**, *86*, 715.

(242) Campbell, E. E. B.; Ulmer, G.; Hasselberger, B.; Busmann, H.-G.; Hertel, I. V. *The Journal of Chemical Physics* **1990**, *93*, 6900.

(243) Pradel, P.; Monchicourt, P.; Laucagne, J. J.; Perdrix, M.; Watel, G. *Chemical Physics Letters* **1989**, *158*, 412.

(244) Kaiser, R. I. O., C.; Head-Gordon, M.; Lee Y. T.; Suits, A. G.; *Science* **1996**, *274*, 1508.

(245) Bunker, P. R. In *Molecular Astrophysics*; Diercksen, G. H. F., Huebner, W. F., Langhoff, P. W., Eds.; Springer Netherlands: 1985; Vol. 157, p 491.

(246) Terzieva, R.; Herbst, E. *International Journal of Mass Spectrometry* **2000**, *201*, 135.

(247) Buhl, D. S., L. E. *Nature* **1970**, *228*, 267.

(248) Kraemer, W. P. D. G. H. F. *Astrophys. J. Suppl. Ser.* **1976**, *205*, L97.

(249) Douglas. A.E. *Nature* **1977**, *269*, 130.

(250) Bae, C. H.; Park, S. M. *The Journal of Chemical Physics* **2002**, *117*, 5347.

(251) Helden, G. v.; Hsu, M.-T.; Kemper, P. R.; Bowers, M. T. *The Journal of Chemical Physics* **1991**, *95*, 3835.

(252) von Helden, G.; Kemper, P. R.; Gotts, N. G.; Bowers, M. T. *Science* **1993**, *259*, 1300.

(253) Howard S. Carman, J.; Compton, R. N. *The Journal of Chemical Physics* **1993**, *98*, 2473.

(254) Book, L. D.; Xu, C.; Scuseria, G. E. *Chemical Physics Letters* **1994**, *222*, 281.

(255) Forney, D.; Fulara, J.; Freivogel, P.; Jakobi, M.; Lessen, D.; Maier, J. P. *The Journal of Chemical Physics* **1995**, *103*, 48.

(256) Pargellis, A. N. *The Journal of Chemical Physics* **1990**, *93*, 2099.

(257) Miller, S. L. *Journal of the American Chemical Society* **1955**, *77*, 2351.

(258) McCarthy, M. C.; Gottlieb, C. A.; Gupta, H.; Thaddeus, P. *The Astrophysical Journal Letters* **2006**, *652*, L141.

(259) S. J. Schwartz, C. J. O. a. D. B. In *Astrophysical Plasmas Astronomy Unit, Queen Mary*; University of London: London, 2004, p 35.

(260) Thomson, G. W. *Chemical Reviews* **1946**, *38*, 1.

(261) Boublik, T.; Fried, V.; Hala, E. *The vapour pressures of pure substances*, 1984.

(262) Van Ness, H. C.; Byer, S. M.; Gibbs, R. E. *AIChE Journal* **1973**, *19*, 238.

(263) Rohlfing, E. A.; Cox, D. M.; Kaldor, A. *The Journal of Chemical Physics* **1984**, *81*, 3322.

(264) Meyer, F.; Khan, F. A.; Armentrout, P. B. *Journal of the American Chemical Society* **1995**, *117*, 9740.

(265) El-Shall, M. S.; Marks, C.; Sieck, L. W.; Meot-Ner, M. *The Journal of Physical Chemistry* **1992**, *96*, 2045.

(266) Fujii, A.; Enomoto, S.; Miyazaki, M.; Mikami, N. *The Journal of Physical Chemistry A* **2004**, *109*, 138.

(267) Morgan, S.; Castleman, A. W. *Journal of the American Chemical Society* **1987**, *109*, 2867.

(268) Morgan, S.; Castleman, A. W. *The Journal of Physical Chemistry* **1989**, *93*, 4544.

(269) Morgan, S.; Keesee, R. G.; Castleman, A. W. *Journal of the American Chemical Society* **1989**, *111*, 3841.

(270) Tono, K.; Kuo, J.-L.; Tada, M.; Fukazawa, K.; Fukushima, N.; Kasai, C.; Tsukiyama, K. *The Journal of Chemical Physics* **2008**, *129*, 084304.

(271) S.S. Prasad and W.T. Huntress *Astrophys. J. Suppl. Ser.* **1980**, *43*.

(272) McEwan, M. J.; Anicich, V. G.; Huntress Jr, W. T.; Kemper, P. R.; Bowers, M. T. *International Journal of Mass Spectrometry and Ion Physics* **1983**, *50*, 179.

(273) Capone, L. C. P., S.S; Huntress,W.T.; Whitten, R. C.;, Dubach, J.; Santhanam K.; *Nature*, *293*, 45.

(274) Raksit, A. B.; Schiff, H. I.; Bohme, D. K. *International Journal of Mass Spectrometry and Ion Processes* **1984**, *56*, 321.

(275) Cernicharo, J.; Guélin, M.; Pardo, J. R. *The Astrophysical Journal Letters* **2004**, *615*, L145.

(276) Vuitton, V.; Yelle, R. V.; McEwan, M. J. *Icarus* **2007**, *191*, 722.

(277) McElvany, S. W. *International Journal of Mass Spectrometry and Ion Processes* **1990**, *102*, 81.

(278) Greenwood, P. F. *Organic Mass Spectrometry* **1994**, *29*, 61.

(279) Shibagaki, K.; Takada, N.; Sasaki, K.; Kadota, K. *Journal of Applied Physics* **2003**, *93*, 655.

(280) Wallis, D.; Vasil'ev, Y. V.; Clipston, N. L.; Lobach, A. S.; Hirsch, A.; Boltalina, O. V.; Lenz, C.; Drewello, T. *International Journal of Mass Spectrometry* **2003**, *228*, 969.

(281) Parent, D. C.; Anderson, S. L. *Chemical Reviews* **1992**, *92*, 1541.

(282) Yang, S.; Taylor, K. J.; Craycraft, M. J.; Conceicao, J.; Pettiette, C. L.; Cheshnovsky, O.; Smalley, R. E. *Chemical Physics Letters* **1988**, *144*, 431.

(283) von Helden, G.; Hsu, M. T.; Gotts, N.; Bowers, M. T. *The Journal of Physical Chemistry* **1993**, *97*, 8182.

(284) Rienstra-Kiracofe, J. C.; Tschumper, G. S.; Schaefer, H. F.; Nandi, S.; Ellison, G. B. *Chemical Reviews* **2002**, *102*, 231.

(285) Gupta, H.; Brünken, S.; Tamassia, F.; Gottlieb, C. A.; McCarthy, M. C.; Thaddeus, P. *The Astrophysical Journal Letters* **2007**, *655*, L57.

(286) Botschwina, P.; Oswald, R. *Journal of Molecular Spectroscopy* **2009**, *254*, 47.

(287) Botschwina, P.; Oswald, R. *The Journal of Chemical Physics* **2008**, *129*, 044305.

(288) Stefano, M. D.; Rosi, M.; Sgamellotti, A.; Ascenzi, D.; Bassi, D.; Franceschi, P.; Tosi, P. *The Journal of Chemical Physics* **2003**, *119*, 1978.

(289) Heyl, A.; Botschwina, P.; Hirano, T. *The Journal of Chemical Physics* **1997**, *107*, 9702.

(290) Agúndez, M.; Cernicharo, J.; Guélin, M.; Kahane, C.; Roueff, E.; Kłos, J.; Aoiz, F. J.; Lique, F.; Marcelino, N.; Goicoechea, J. R.; González García, M.; Gottlieb, C. A.; McCarthy, M. C.; Thaddeus, P. *A&A* **2010**, *517*, L2.

(291) Cernicharo, J.; Guélin, M.; Agúndez, M.; Kawaguchi, K.; McCarthy, M.; Thaddeus, P. *A&A* **2007**, *467*, L37.

(292) Thaddeus, P.; Gottlieb, C. A.; Gupta, H.; Brünken, S.; McCarthy, M. C.; Agúndez, M.; Guélin, M.; Cernicharo, J. *The Astrophysical Journal* **2008**, *677*, 1132.

(293) Cernicharo, J.; Guélin, M.; Agúndez, M.; McCarthy, M. C.; Thaddeus, P. *The Astrophysical Journal Letters* **2008**, *688*, L83.

(294) Brünken, S.; Gupta, H.; Gottlieb, C. A.; McCarthy, M. C.; Thaddeus, P. *The Astrophysical Journal Letters* **2007**, *664*, L43.

(295) Anthony, J. R.; Hollis, J. M.; Lovas, F. J.; Cordiner, M. A.; Millar, T. J.; Markwick-Kemper, A. J.; Jewell, P. R. *The Astrophysical Journal Letters* **2007**, *664*, L47.

(296) Pety, J.; Gratier, P.; Guzmán, V.; Roueff, E.; Gerin, M.; Goicoechea, J. R.; Bardeau, S.; Sievers, A.; Le Petit, F.; Le Bourlot, J.; Belloche, A.; Talbi, D. *A&A* **2012**, *548*, A68.

(297) Kawaguchi, K. K., Yasuko; Ishikawa, Shin-Ichi; Ohishi, Masatoshi; Kaifu, Norio; Amano, Takayoshi *Astrophysical Journal* **1994**, *420*, L95.

(298) Oscar Martinez, J.; Lattanzi, V.; Thorwirth, S.; McCarthy, M. C. *The Journal of Chemical Physics* **2013**, *138*, 094316.

(299) Hagen, W.; Allamandola, L.; Greenberg, J. *Astrophysics and Space Science* **1979**, *65*, 215.

(300) Eric, H.; Yoshihiro, O. *The Astrophysical Journal* **2008**, *679*, 1670.

(301) Lifshitz, C.; Peres, T.; Agranat, I. *International Journal of Mass Spectrometry and Ion Processes* **1989**, *93*, 149.

(302) Hirota, E. *Chemical Reviews* **1992**, *92*, 141.

(303) Owrutsky, J.; Rosenbaum, N.; Tack, L.; Gruebele, M.; Polak, M.; Saykally, R. J. *Philosophical Transactions of the Royal Society of London. Series A, Mathematical and Physical Sciences* **1988**, *324*, 97.

Appendix

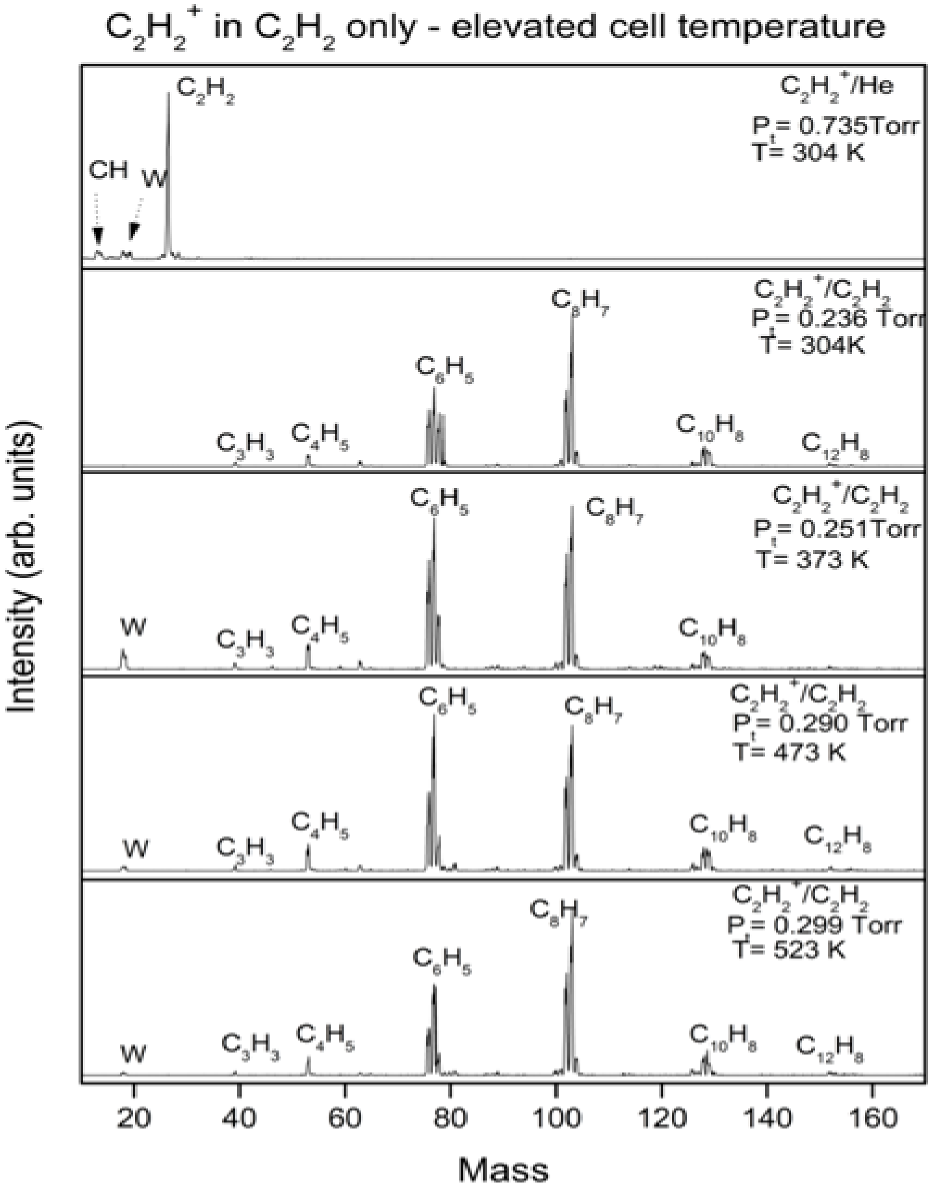

Figure 86: Mass spectrum of acetylene radical cation $(C_2H_2)^{\bullet+}$ injected into acetylene vapor in the drift cell collected at different temperatures. The ion injection energy is 12.8eV (lab. frame).

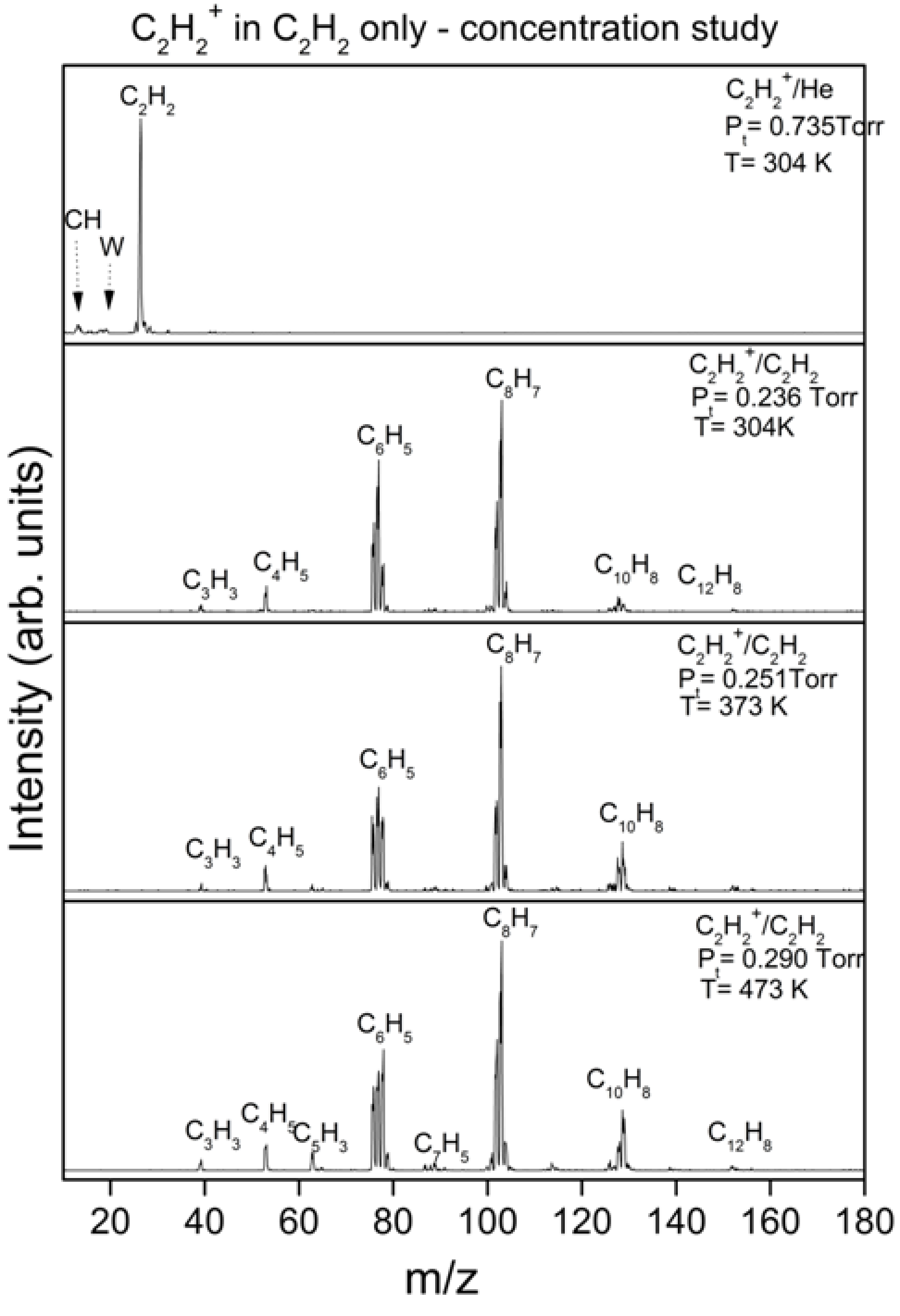

Figure 87: Mass spectrum of acetylene radical cation $(C_2H_2)^{\bullet+}$ injected into acetylene vapor in the drift cell collected at different temperatures. The ion injection energy is 12.8eV (lab. frame).

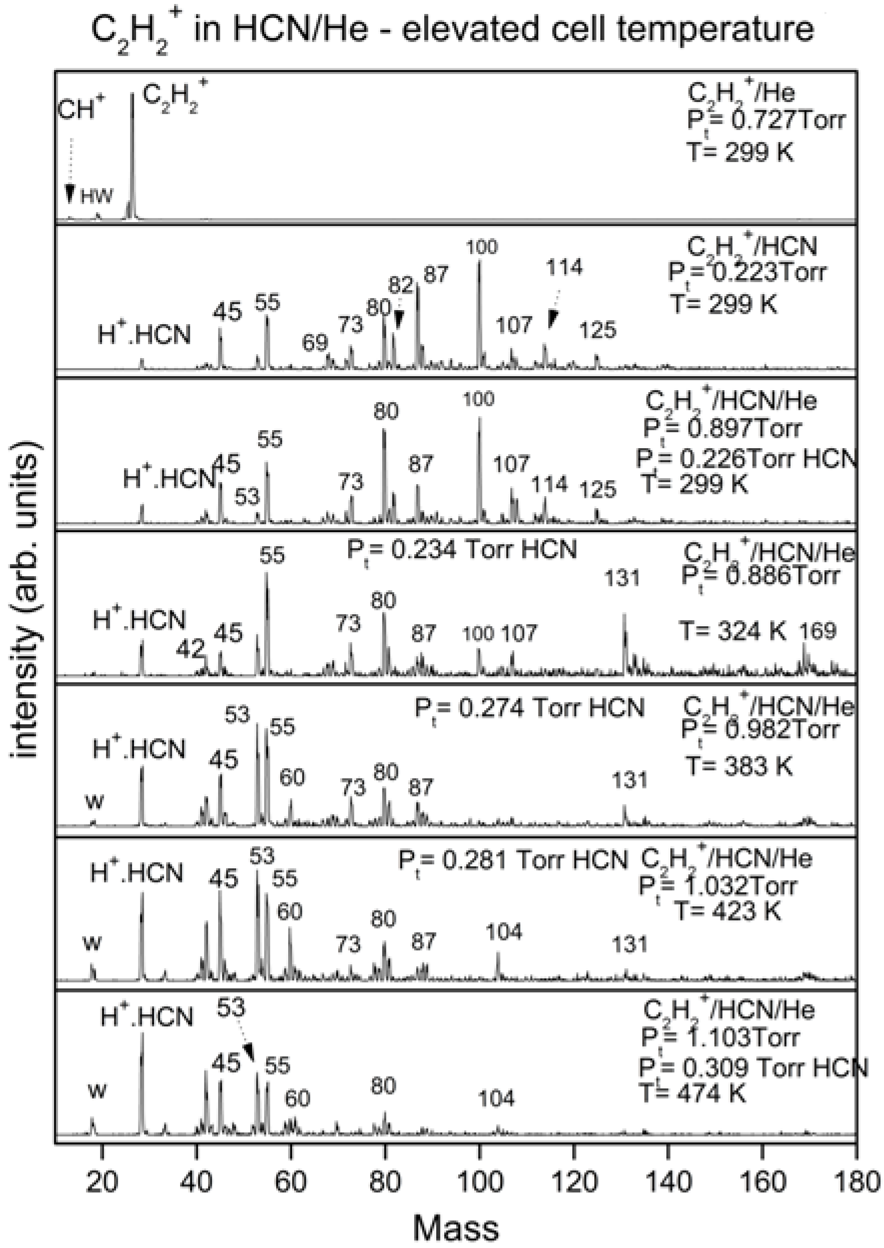

Figure 88: Mass spectrum of acetylene radical cation $(C_2H_2)^{\bullet+}$ injected into HCN vapor/ He in the drift cell collected at different temperatures as indicated. The ion injection energy is 12.8eV (lab. frame).

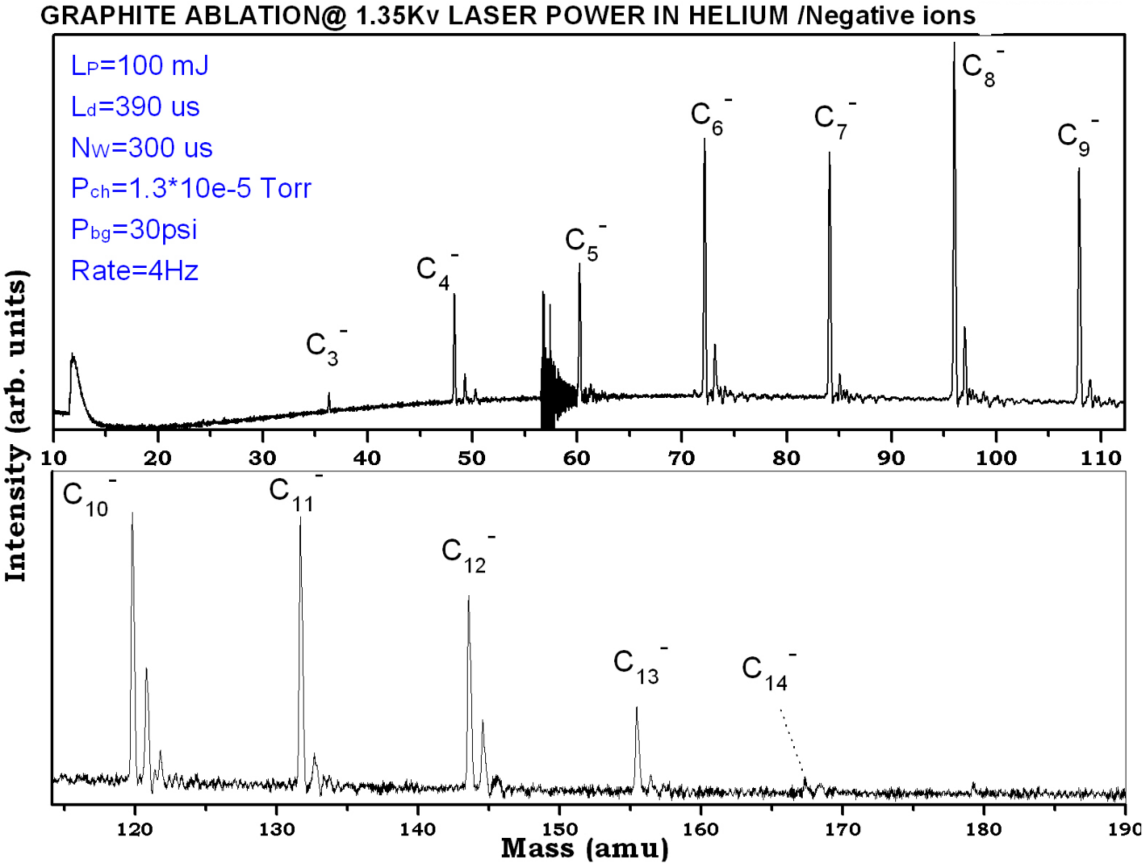

Figure 89: Negative ion TOF mass spectra of carbon cluster anion (C_n^-) generated through laser vaporization of graphite using as Helium carrier gas. Experimental conditions used are shown in blue.

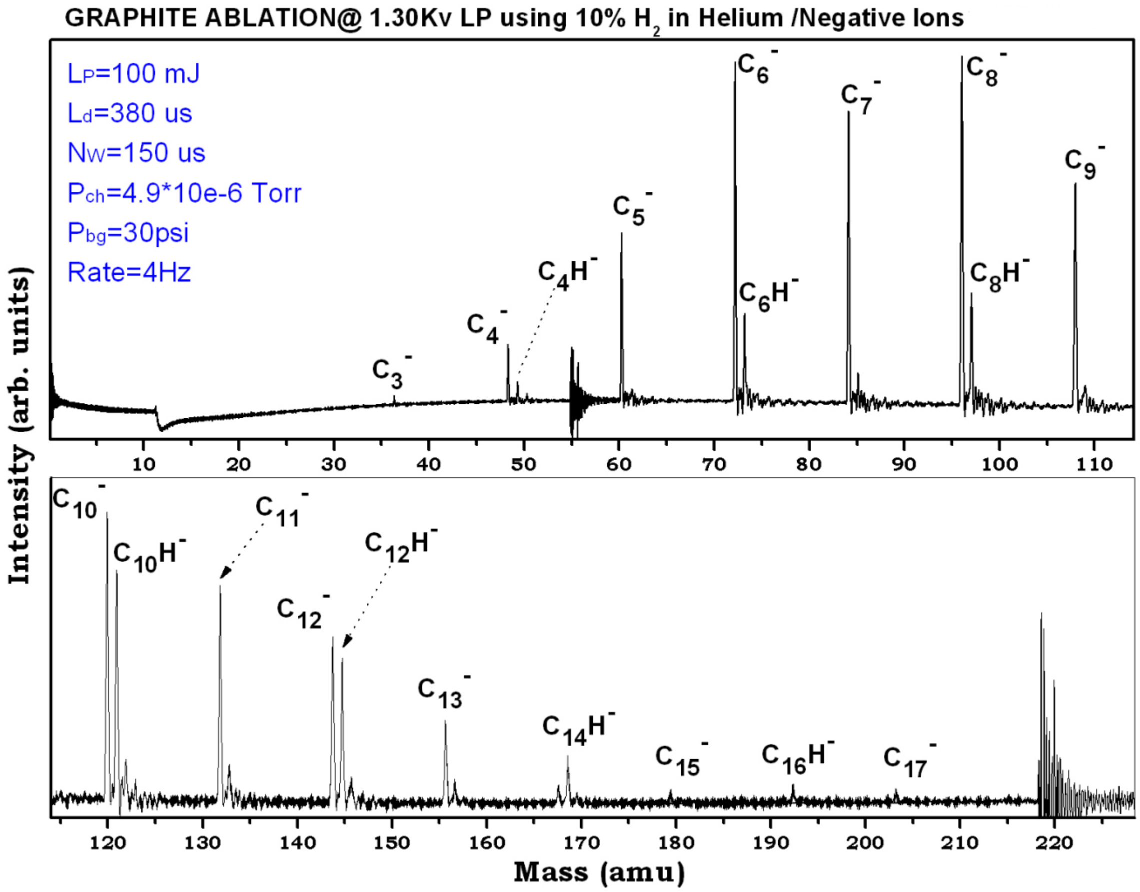

Figure 90: Negative ion TOF mass spectra of carbon cluster anion (C_n^-) generated through laser vaporization of graphite using 10% H_2/He as carrier gas. Experimental conditions used are shown in blue.

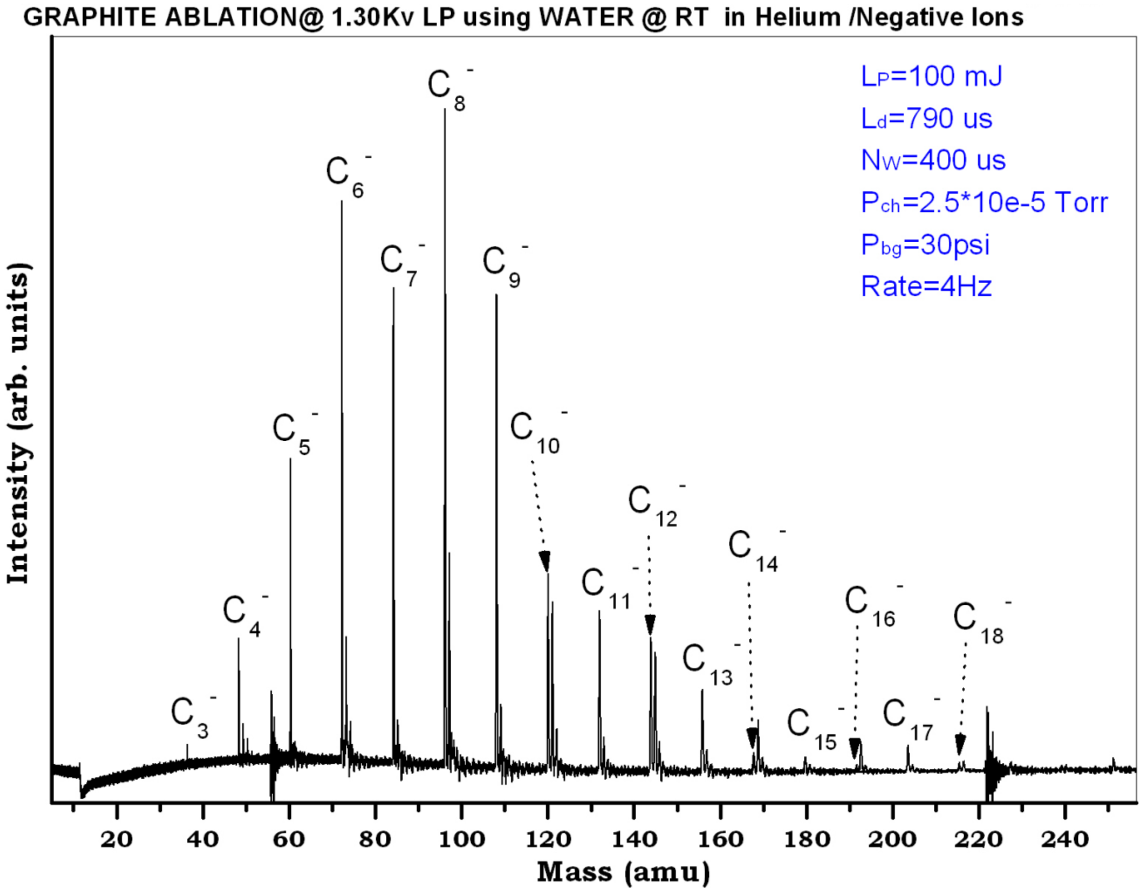

Figure 91: Negative ion TOF mass spectra of carbon cluster anion (C_n^-) generated through laser vaporization of graphite using H_2O vapor in He as carrier gas. Experimental conditions used are shown in blue.

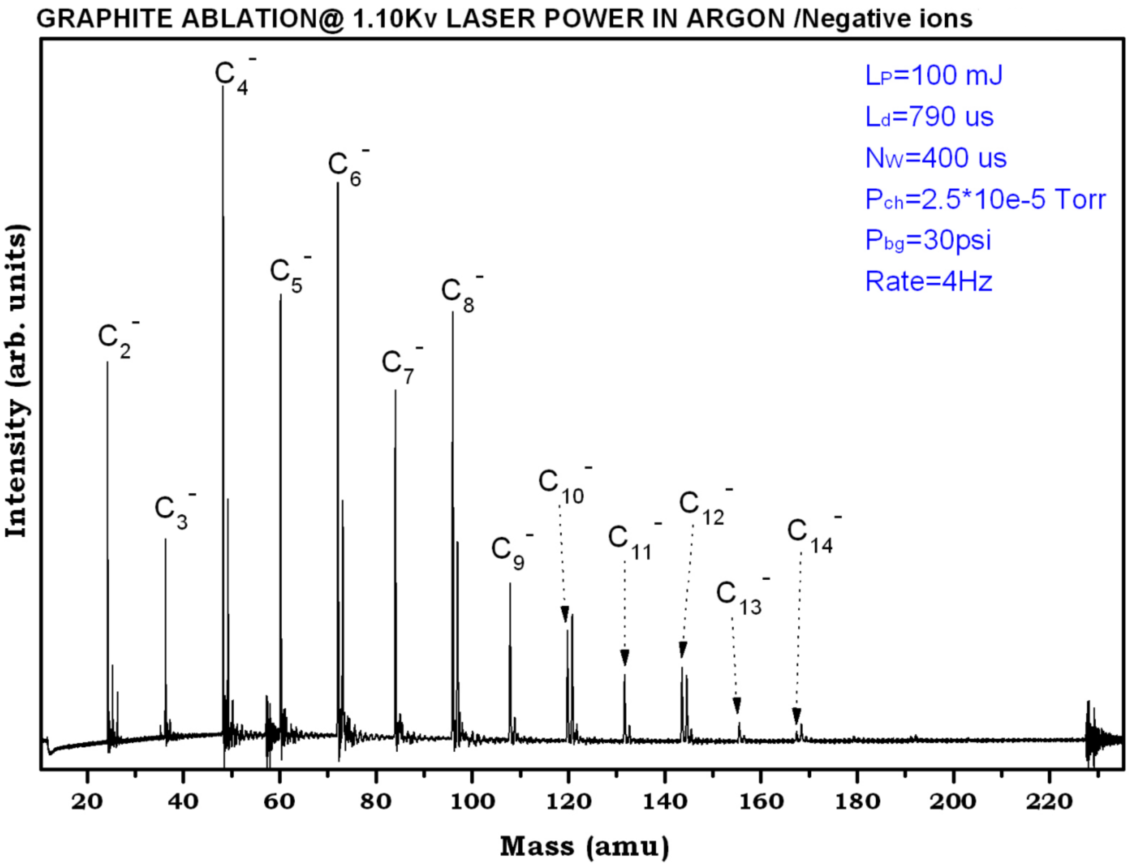

Figure 92: Negative ion TOF mass spectra of carbon cluster anion (C_n^-) generated through laser vaporization of graphite using Argon as carrier gas. Experimental conditions used are shown in blue.

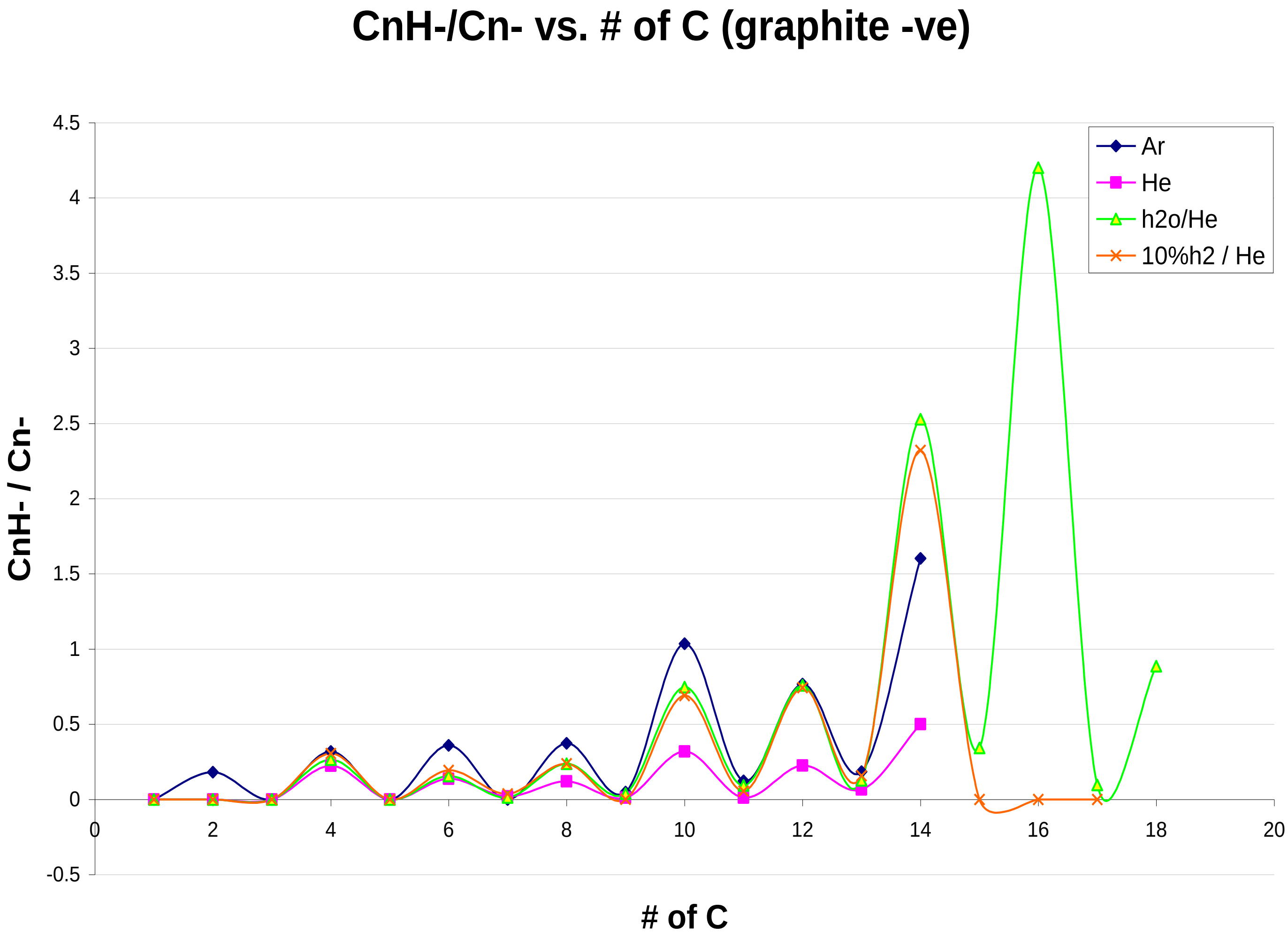

Figure 93: Plot of C_nH^-/C_n^- vs number of carbon atoms showing the level of incorporation of H into the carbon cluster anions generated from laser vaporization of graphite using different gases as carrier gas, as indicated.

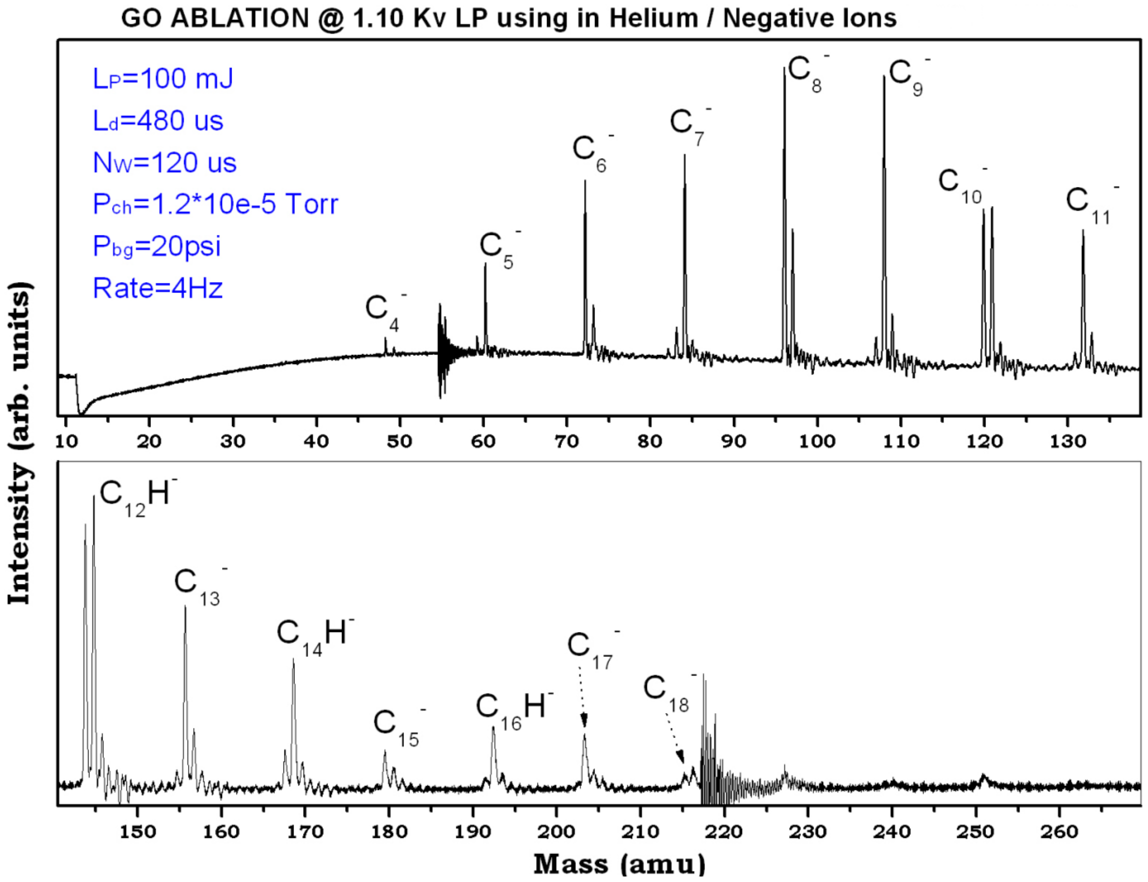

Figure 94: Negative ion TOF mass spectra of carbon cluster anion (C_n^-) generated through laser vaporization of graphite oxide using Helium as carrier gas. Experimental conditions used are shown in blue.

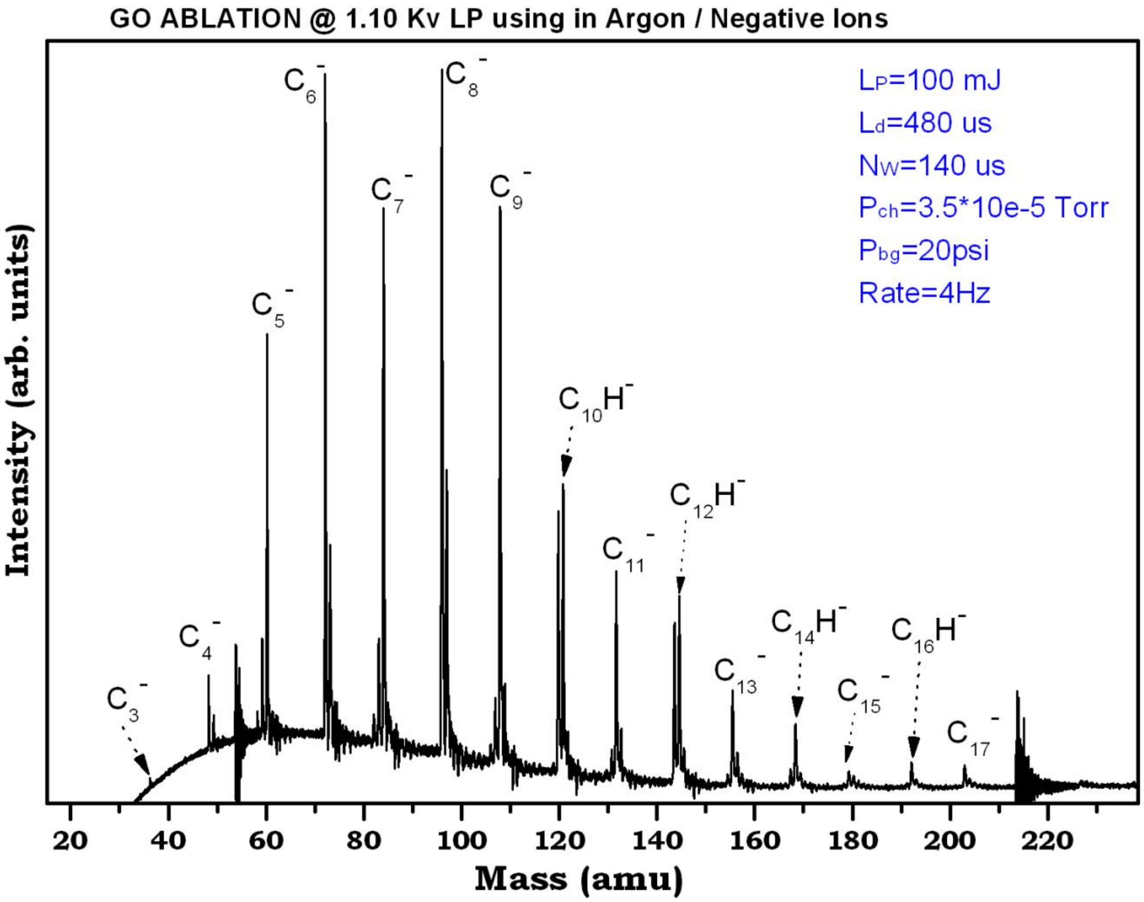

Figure 95: Negative ion TOF mass spectra of carbon cluster anion (C_n^-) generated through laser vaporization of graphite oxide using Argon as carrier gas. Experimental conditions used are shown in blue.

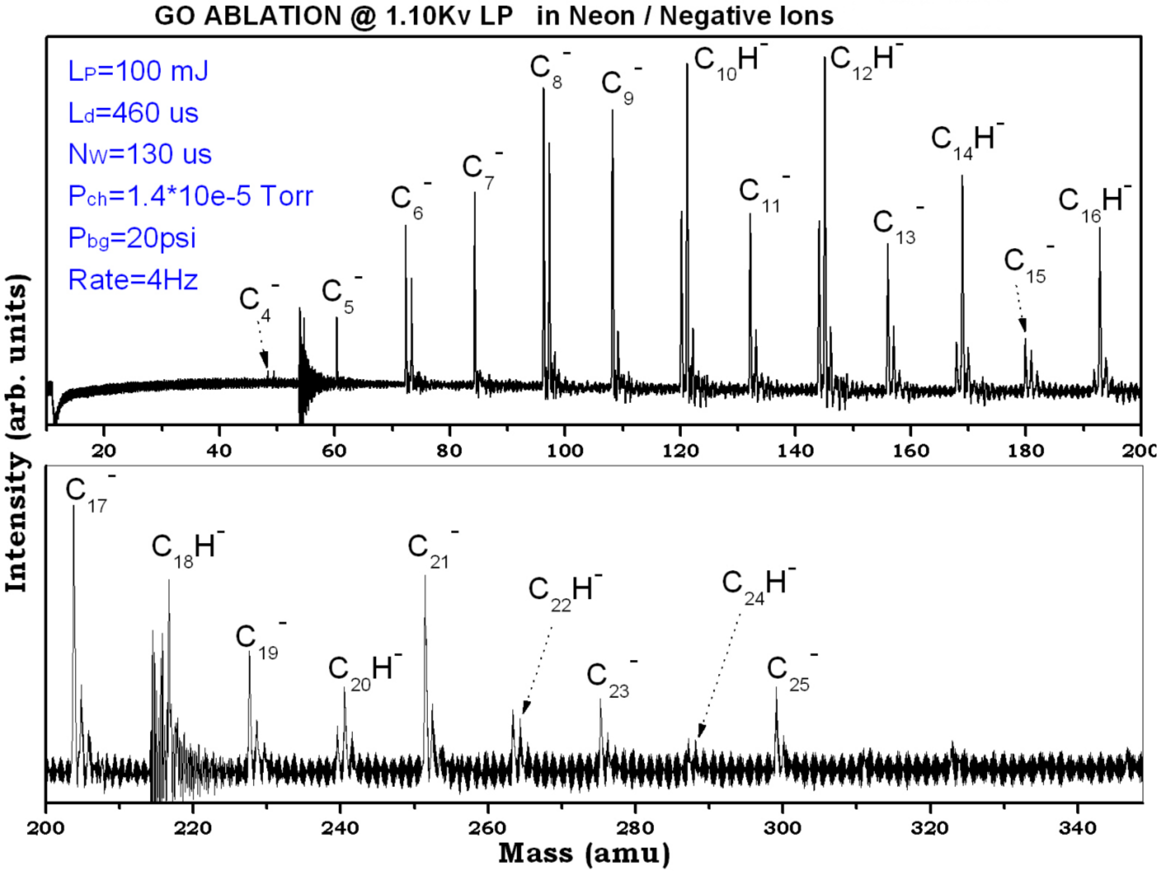

Figure 96: Negative ion TOF mass spectra of carbon cluster anion (C_n^-) generated through laser vaporization of graphite oxide using Neon as carrier gas. Experimental conditions used are shown in blue.

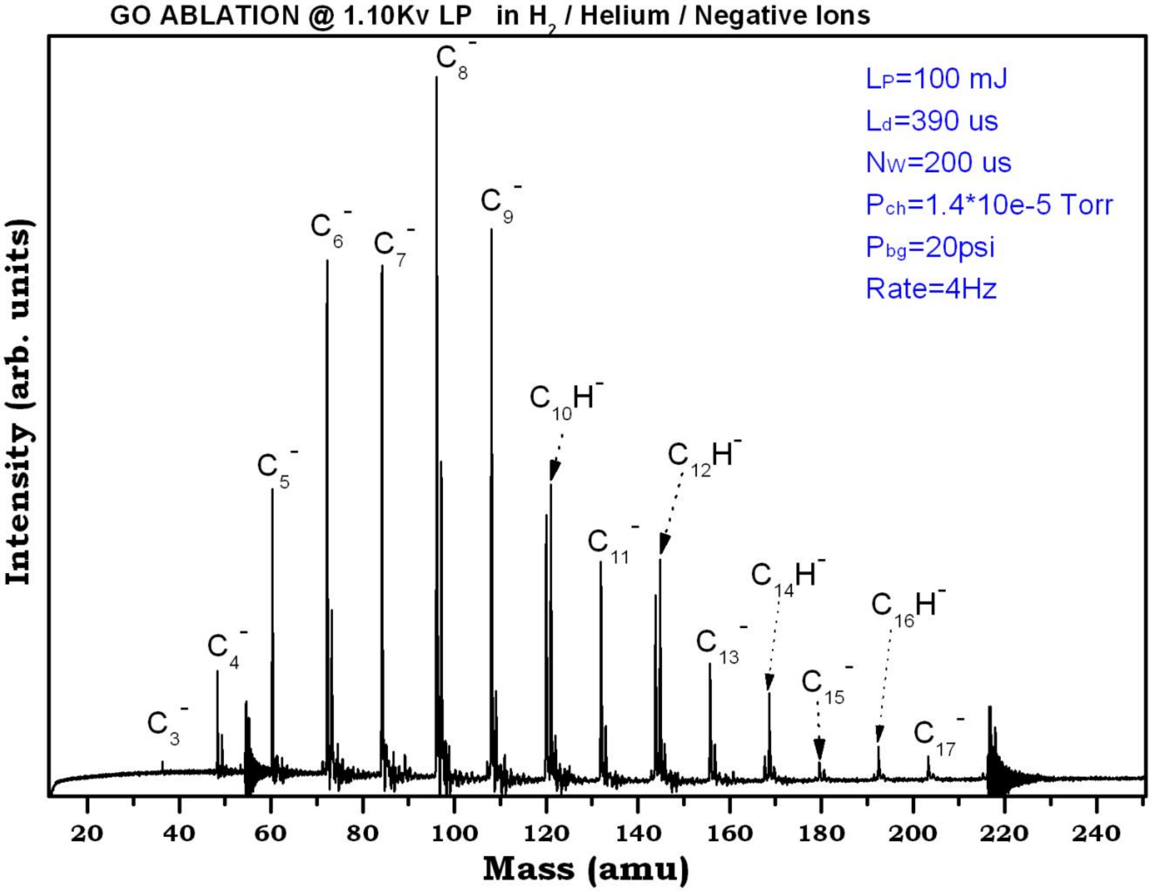

Figure 97: Negative ion TOF mass spectra of carbon cluster anion (C_n^-) generated through laser vaporization of graphite oxide using 10% H_2/He as carrier gas. Experimental conditions used are shown in blue.

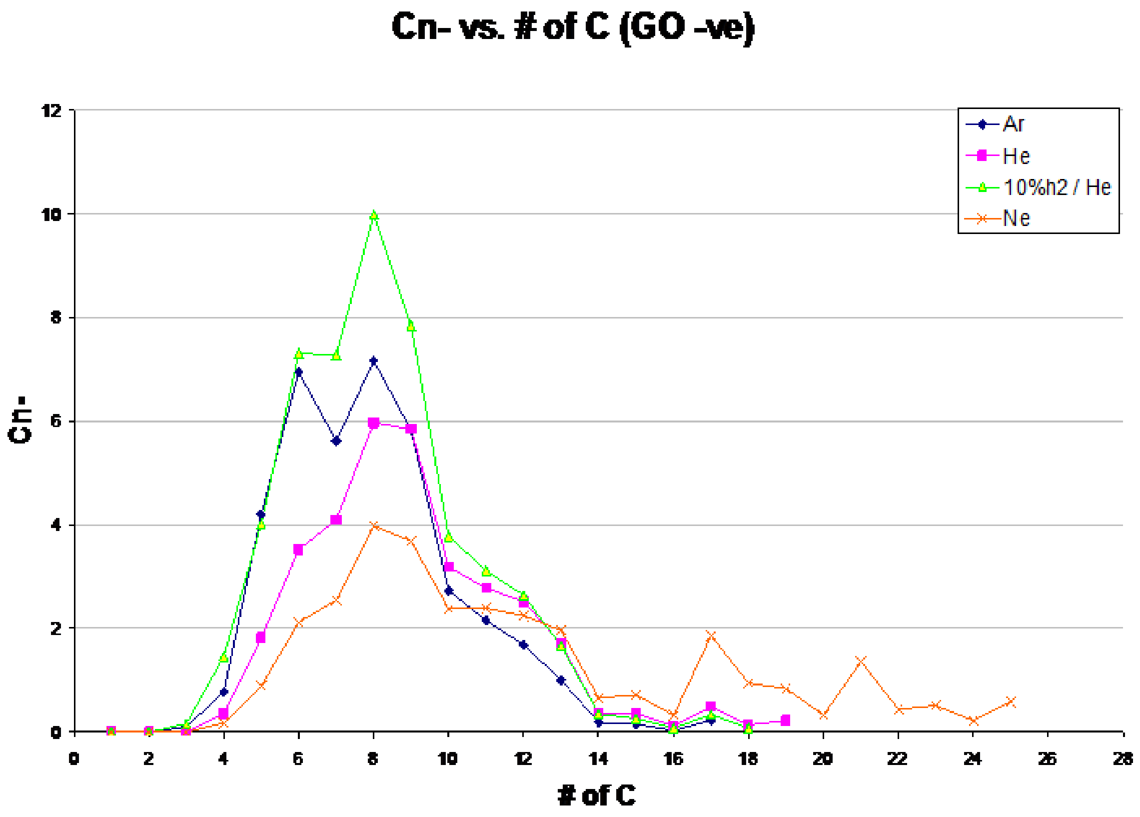

Figure 98:Plot of intensity of C_nH^-/Cn- vs number of carbon atoms showing abundance distribution of carbon cluster anions generated from laser vaporization of graphite oxide using different gases as carrier gas, as indicated.

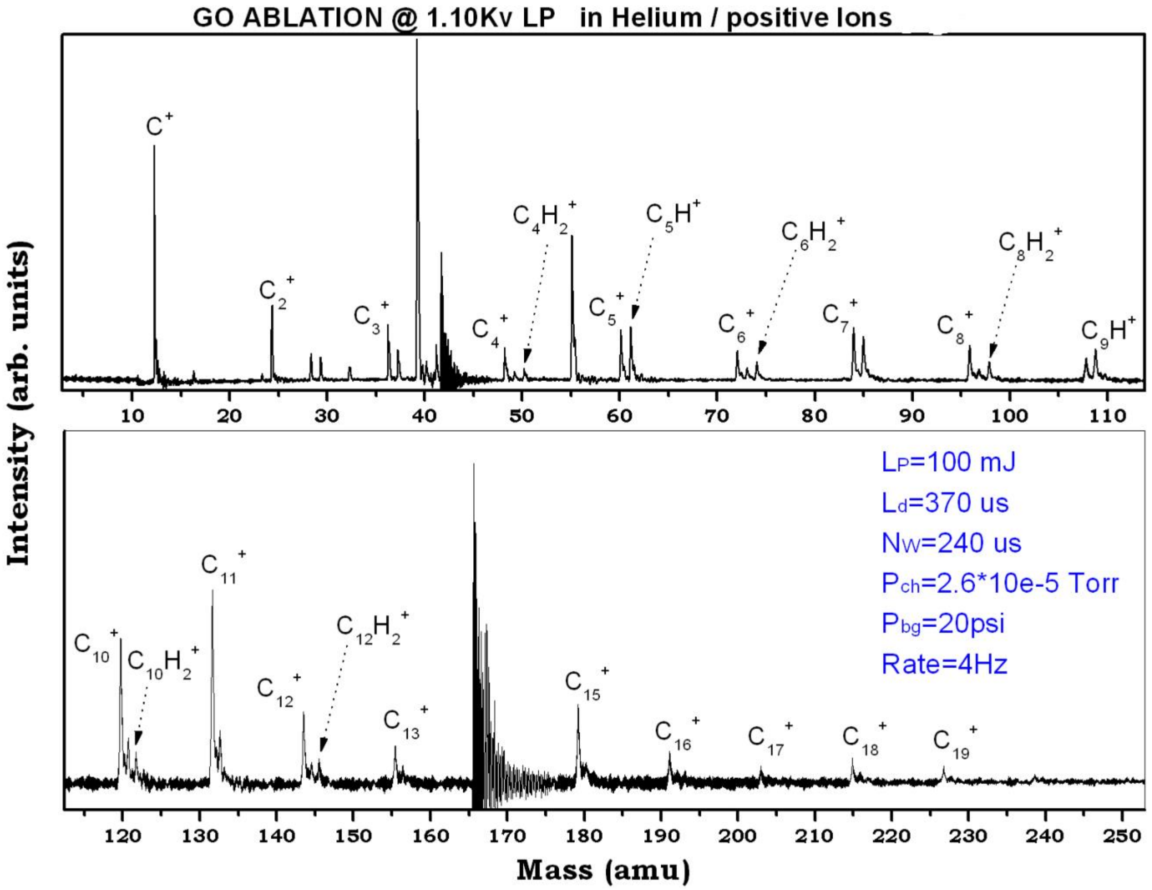

Figure 99: Positive ion TOF mass spectra of carbon cluster anion (C_n^+) generated through laser vaporization of graphite oxide using Helium as carrier gas. Experimental conditions used are shown in blue.

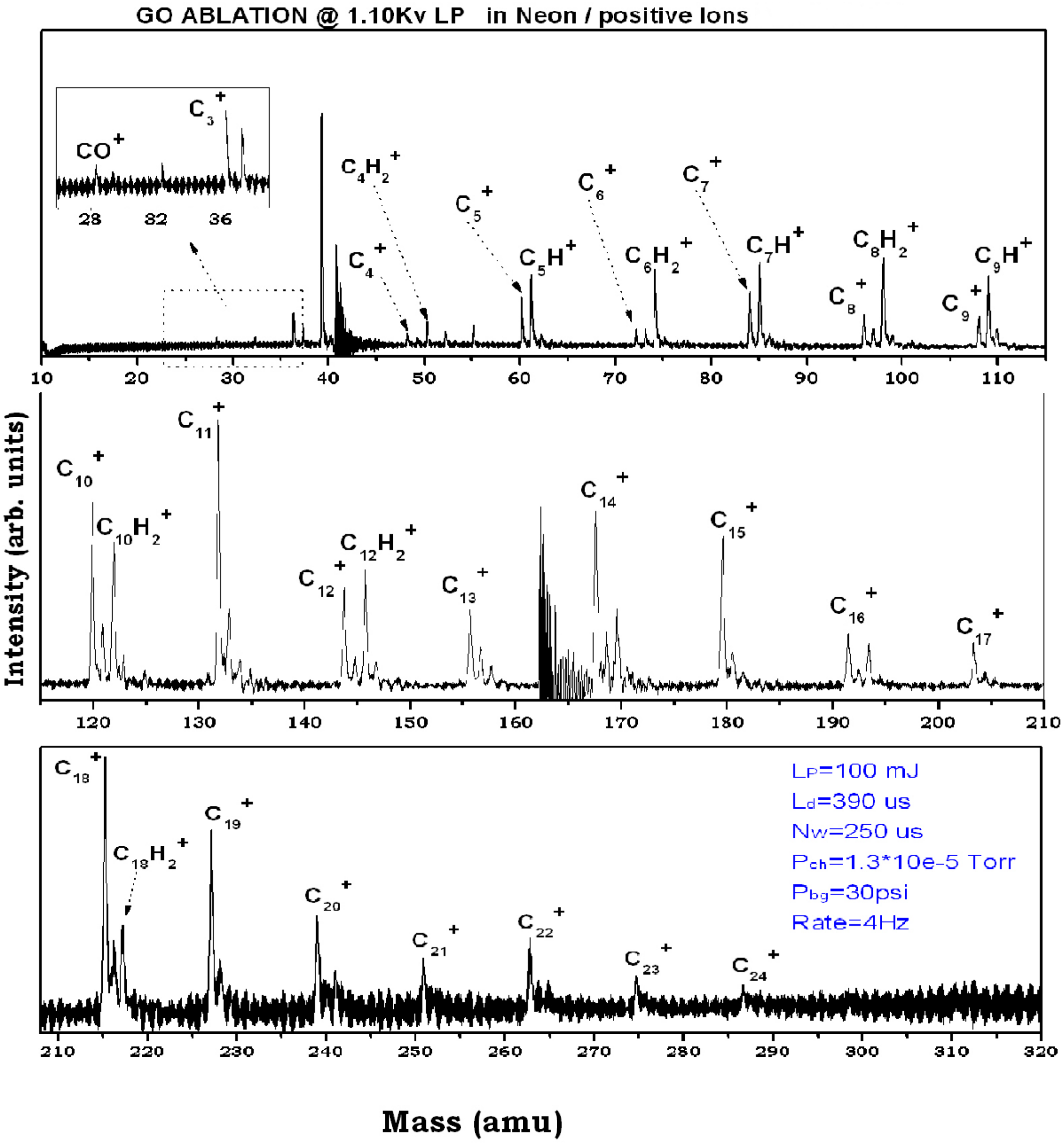

Figure 100: Positive ion TOF mass spectra of carbon cluster anion (C_n^+) generated through laser vaporization of graphite oxide using Neon as carrier gas. Experimental conditions used are shown in blue.

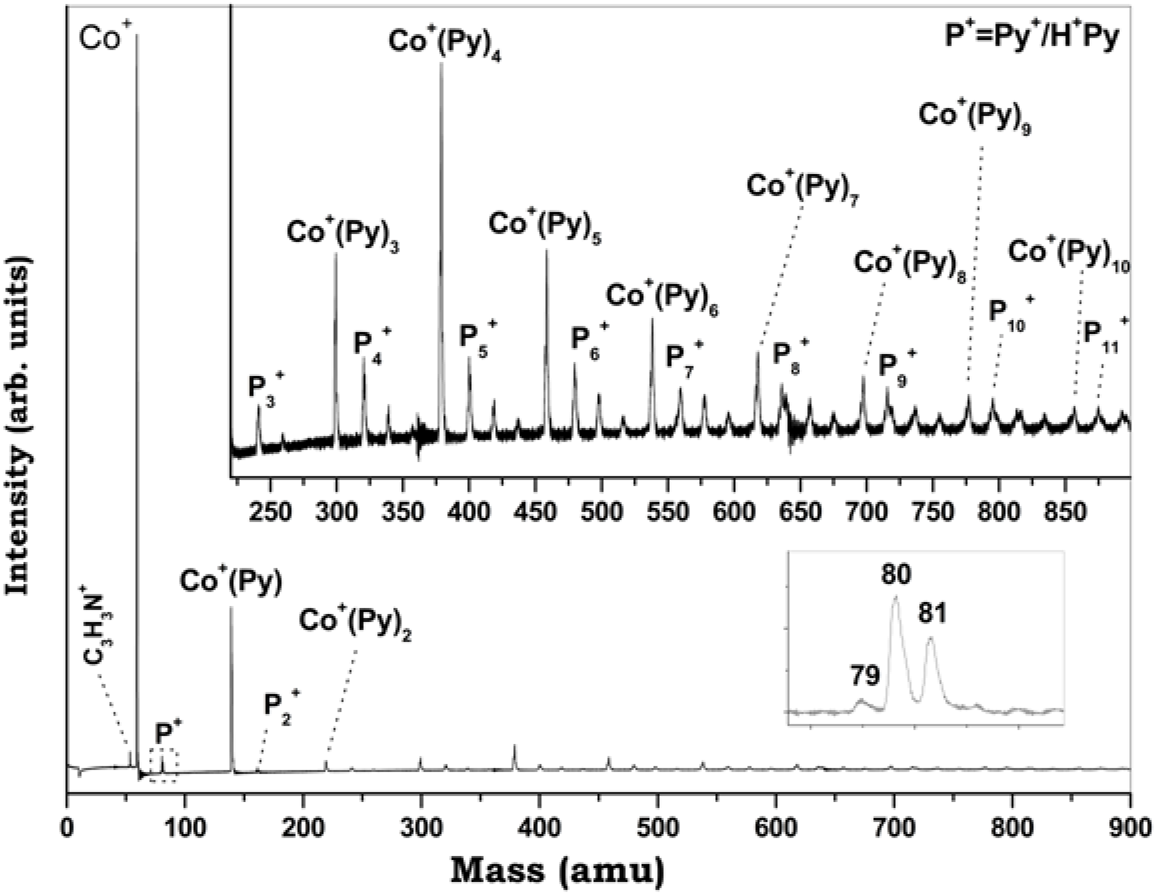

Figure 101: R-TOF mass spectrum of $Co^+(C_4H_4N_2)_n$ clusters obtained by interacting the neutral Pyrimidine clusters with LVI generated cobalt metal cations using 532nm Nd: YAG at 2.5 mJ/pulse energy. Metal target was ablated 650 μs after nozzle opened (t_0) and accelerating plates were pulsed 1.04 ms after t_0. Background pressure was 100 PSI (helium) passed over the liquid Pyrimidine in a glass bubbler. Pressure of the source chamber was 1.1×10^{-5} Torr.

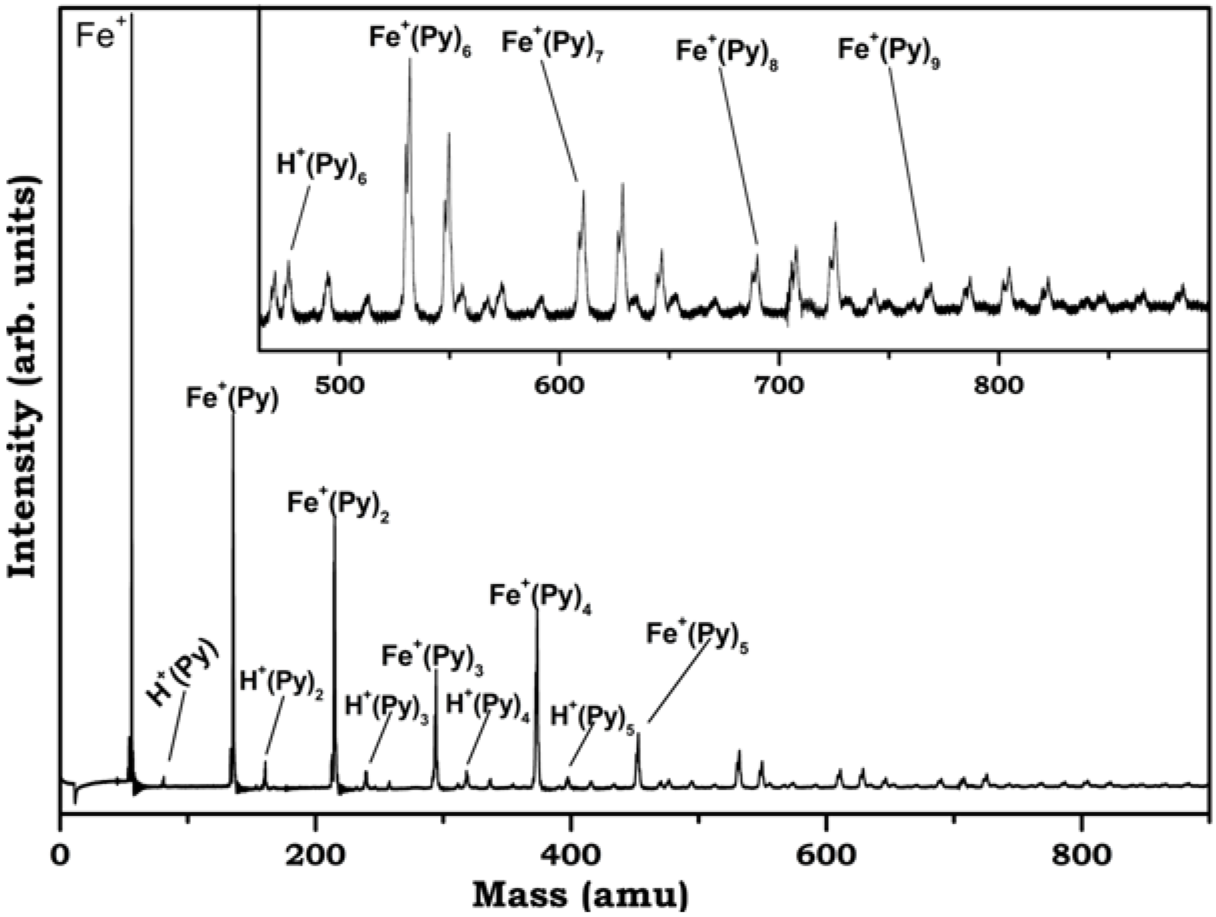

Figure 102: R-TOF mass spectrum of $Fe^+(C_4H_4N_2)_n$ clusters obtained by interacting the neutral Pyrimidine clusters with LVI generated iron metal cations using 532nm Nd: YAG at 2.5 mJ/pulse energy. Metal target was ablated 628 μs after nozzle opened (t_0) and accelerating plates were pulsed 1.04 ms after t_0. Background pressure was 50 PSI (helium) passed over the liquid Pyrimidine in a glass bubbler. Pressure of the source chamber was 5.0×10^{-5} Torr.

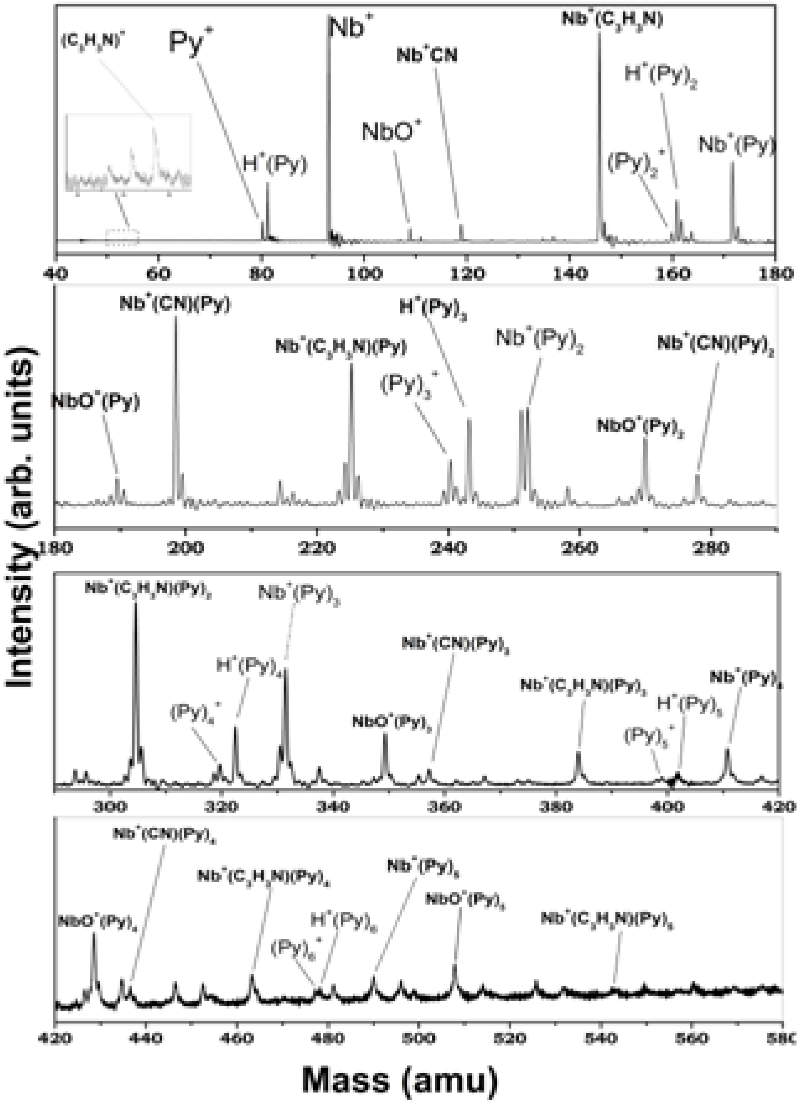

Figure 103: R-TOF mass spectrum of $Nb^+(C_4H_4N_2)_n$ clusters obtained by interacting the neutral Pyrimidine clusters with LVI generated niobium metal cations using 532nm Nd: YAG at 2.5 mJ/pulse energy. Metal target was ablated 628 μs after nozzle opened (t_0) and accelerating plates were pulsed 1.05 ms after t_0. Background pressure was 100 PSI (helium) passed over the liquid Pyrimidine in a glass bubbler. Pressure of the source chamber was 2.6×10^{-5} Torr.

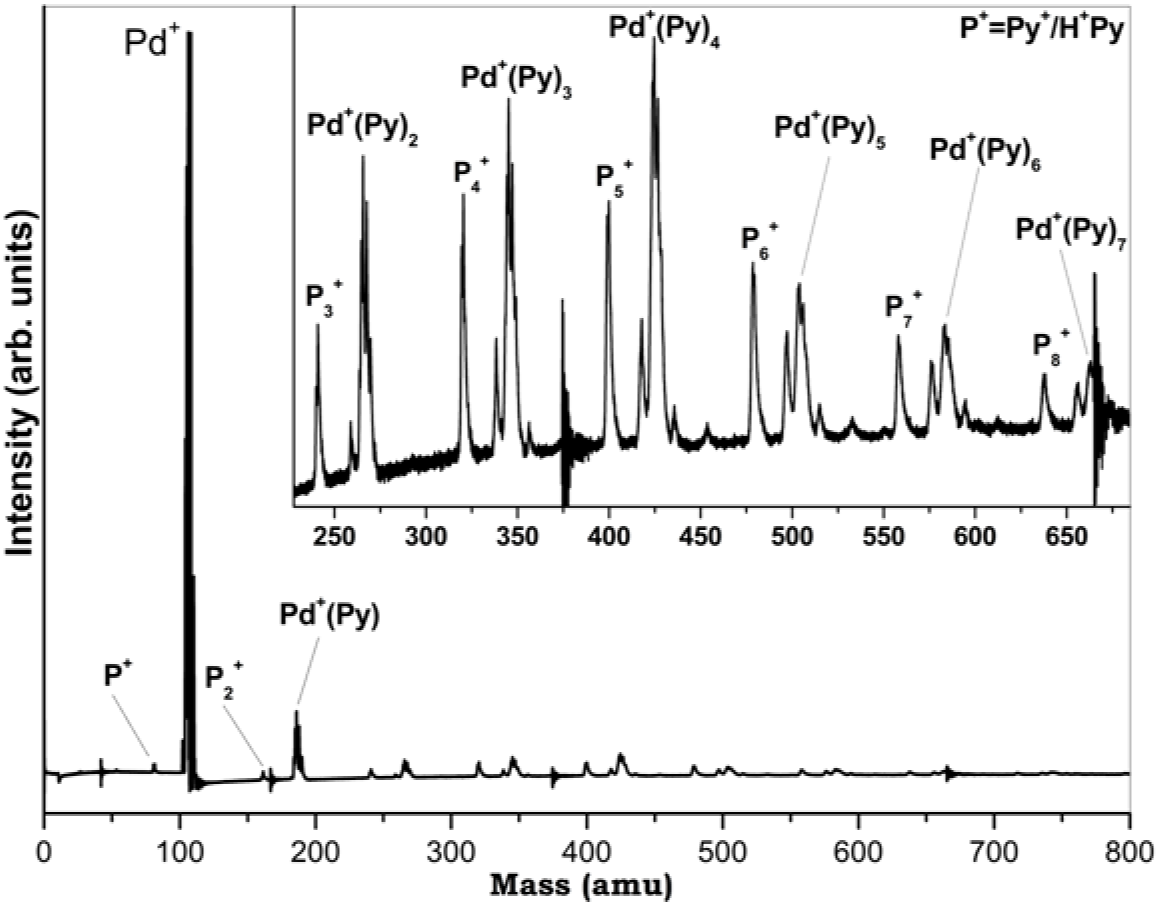

Figure 104: R-TOF mass spectrum of $Pd^+(C_4H_4N_2)_n$ clusters obtained by interacting the neutral Pyrimidine clusters with LVI generated palladium metal cations using 532nm Nd: YAG at 2.5 mJ/pulse energy. Metal target was ablated 607 µs after nozzle opened (t_0) and accelerating plates were pulsed 1.04 ms after t_0. Background pressure was 40 PSI (helium) passed over the liquid Pyrimidine in a glass bubbler. Pressure of the source chamber was 4.7×10^{-5} Torr.

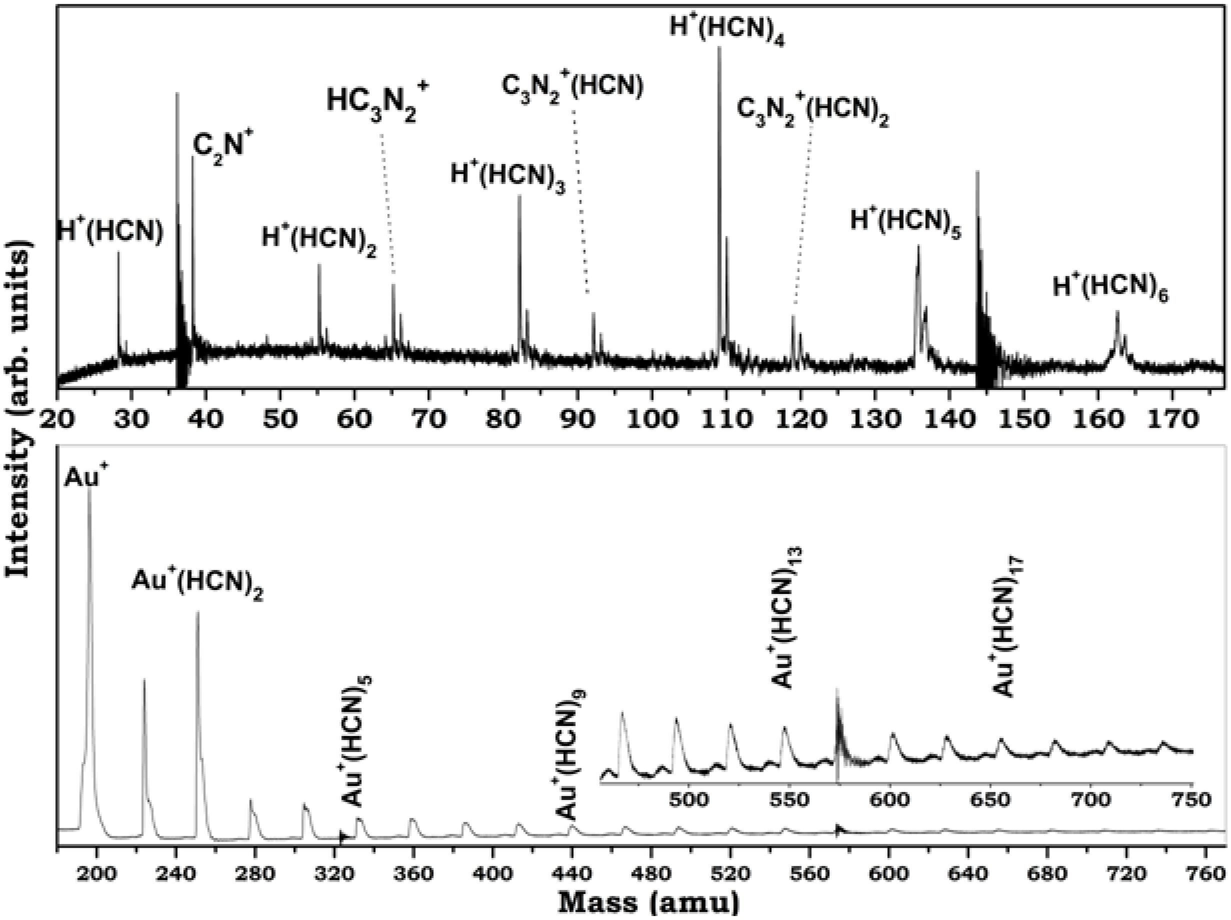

Figure 105: R-TOF mass spectrum of $Au^{+}(HCN)_n$ clusters obtained by interacting the neutral HCN clusters with LVI generated gold metal cations using 532nm Nd: YAG at 2.5 mJ/pulse energy. Metal target was ablated 260 µs after nozzle opened (t_0) and accelerating plates were pulsed 700 µs after t_0. Sample gas was 1% HCN in helium at a backing pressure of 100 PSI. Pressure of the source chamber was 6.2×10^{-6} Torr.

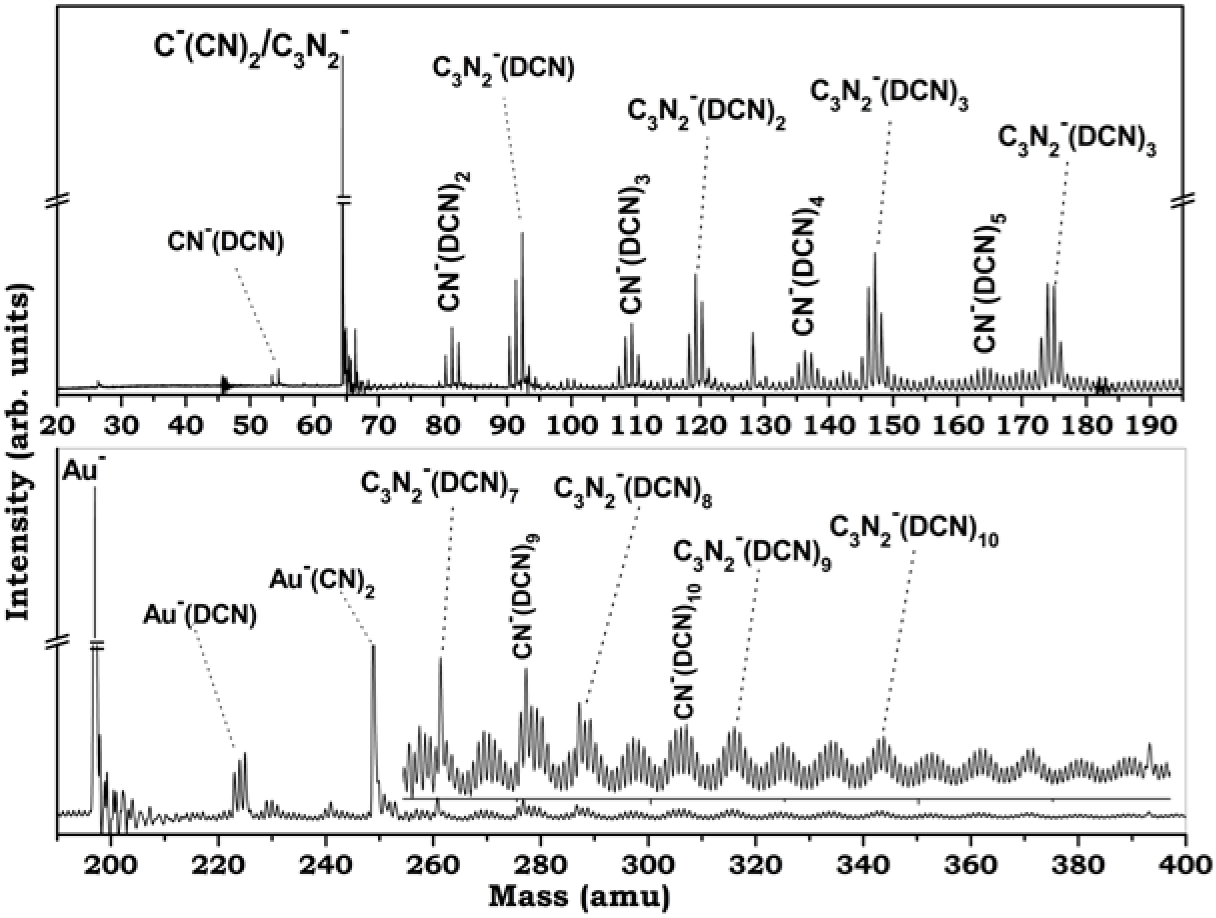

Figure 106: R-TOF mass spectrum of Au$^-$(DCN)$_n$ clusters obtained by interacting the neutral DCN clusters with LVI generated gold metal ions using 532nm Nd: YAG at 20.0 mJ/pulse energy. Metal target was ablated 220 μs after nozzle opened (t_0) and accelerating plates were pulsed 450 μs after t_0. Sample gas was 2% DCN in helium at a backing pressure of 60 PSI. Pressure of the source chamber was 3.6×10^{-6} Torr.

Vita

Isaac Kwame Attah was born on november13th, 1982 in Accra Ghana. He graduated form Ghana Secondary Technical School in 2000.He joined the Chemistry program in Kwame Nkrumah University of Science and Technology in 2002, and graduated in 2006 with his BSc in 2006. After working in the industry for almost 2 years, he joined the chemistry department of Virginia Commonwealth University, where is currently pursuing his PhD. in physical chemistry under the supervision of Professor M. Samy El-Shall.

Curriculum Vitae

Isaac Kwame Attah
PhD Candidate
Department of Chemistry
Virginia Commonwealth University
Richmond, VA 23284
Phone: 804-827-1112
e-mail: attahi@vcu.edu

Education

- **PhD Candidate**, Virginia Commonwealth University, Richmond, VA 8/ 2011 to Present
  Department of Chemistry
  Advisor: Prof M. S. El-Shall

- **B.S.** Kwame Nkrumah University of Science and Technology, Kumasi, Ghana. 9/ 2002 to 5/ 2006
  Department of Chemistry
  Chemistry Major

Employment History

- **Virginia Commonwealth University**
  Graduate Teaching Assistant 8/2008 to Present

Courses taught:
General Chemistry 100, 101 and 102
General Chemistry 101 Honors Class
General Chemistry Laboratory 101 and 102
Physical Chemistry Lab 303

- **Virginia Commonwealth University**
  Graduate Research Assistant 8/ 2008 to Present
  Responsibilities:
  Design and perform experimental and theoretical investigations of chemical systems for research purposes

- **Melgrep Company Ltd.**
  Management trainee 3/2008 to 7/2008
  Responsibilities:
  Training under the production manager to assume supervision of production team upon completions of training.

- **Aluworks Ltd.**
  National service personnel 6/2006 to 1/2008
  Responsibilities:
  In-situ analyses of chemical and physical standards of aluminum products, from molten aluminum to finished products.

<u>Technical Research Skills</u>

Quadrupole Mass Selector-Ion Mobility-Quadrupole Mass Spectrometer (QMS-IM-QMS)

Reflectron Time-Of-Flight Mass Spectrometry (R-TOF MS)

UV and Visible Laser operation for molecular sample ionization i.e. laser vaporization ionization and photo ionization

Good knowledge of vacuum systems, i.e. achieving and maintaining vacuum in home built mass spectrometers

Density Functional Theory calculations, a complimentary method used to support experimental findings

Publications

Metal acetylene cluster ions M+(C_2H_2)n as model reactors for studying reactivity of laser-generated transition metal cations ,; Sharma, Pramod; **Attah, Isaac**; Momoh, Paul; El-Shall, M. Samy; International Journal of Mass Spectrometry, **2011**, 300, 81-90.

Formation of Nitrogen-Containing Polycyclic Cations by Gas Phase and Intracluster Reactions of Acetylene with the Pyridinium and Pyrimidinium Ions,; Soliman, Abdel-Rahman; Hamid, Ahmed; **Attah, Isaac**; Momoh, Paul;. *J. Am. Chem. Soc.*, **2013** , 135, 155-66

Hydrogen-Terminated Graphene by Laser Vaporization-Controlled Condensation of Graphite Oxide. Observation of Hydrogen-Capped Carbon Chains C_nH^-, C_nH^+, and $C_nH_2^+$ (n = 2–30) in the Gas Phase,; Afshani , Parichehr ; **Attah , Isaac**; Moussa, Sherif; Terner , James ; El-Shall, M. Samy;, *J. Phys. Chem. C*, **2013**, 117 , 9485–9495

Reaction of laser-generated 2nd row transition metal cations with acetylene clusters in the gas phase,; **Attah, Isaac** ;Sharma, Pramod ; El-Shall, M. Samy;, Draft completed, to be submitted.

Sequential solvation of organic cations (Fluorobenzene, Difluorobenzene, Benzonitrile) with HCN in the gas phase and their implications to complex growth of organics in the interstellar medium; **Attah, Isaac**; Hamid, Ahmed; Meot-ner, Micheal; El-Shall, M. Samy

Draft completed, to be submitted

Conferences

- talks:

Reactions of transition metal cations with acetylene clusters in the gas phase

Attah, Isaac K.; El-Shall, M. Samy

63rd Southeast Regional Meeting of the American Chemical Society, Richmond, VA, October 26-29 (2011), SERM-38.

- Poster sessions:

Reactions of Transition Metal Ions with Acetylene and HCN Clusters

Attah, Isaac K.; El-Shall, Mohamed S.,

63rd Southeast Regional Meeting of the American Chemical Society, Richmond, VA, United States, October 26-29 (2011), SERM-158.

Reactions of Transition Metal Ions with Acetylene and HCN Clusters, Attah, Isaac and M. Samy El-Shall,

International Symposium on Clusters and Nano-Structures (Energy, Environment, and Health) November 7-10, 2011, Richmond VA.

Gas phase metal acetylene cluster ions as model reactors for studying reactivity of transition metal ions , Sharma, Pramod; Attah, Isaac; El-Shall, M. Samy,

240th ACS National Meeting, Boston, MA, August 22-26, 2010 (2010), PHYS-474.

Awards

James Quagliano scholarship (VCU chemistry department scholarship award) 5/ 2012

Professional Affiliations

American Chemical Society 8/2009 – Present